## Acknowledgement

I would like to express many thanks to my supervisor prof. Dr. Ing. Karel Pavelka for his obligingness, help and advice during writing this thesis as well as in the course of my doctoral study. My thanks goes to my colleagues Ing. Jan Holešovský, Ing. Marina Faltýnová, PhD., Ing. Vojtěch Hron, PhD for their valuable comments and technical consultations. I would also like to thank Mgr. Lucie Bubníková for English language corrections. After all the main thanks goes to my friends and family namely my partner Miroslav and son Eduard for their long time support and patience without which this thesis could not be written.

## Annotation

The goal of this thesis is to compare and evaluate various exact methods of historical material determination, with special interest to methods based on reflectance spectroscopy and hyperspectral imaging. These methods are non-invasive and therefore very interesting for historic preservation. The material decomposition was oriented to several historical objects like paintings, plasters and mortars, but biological contamination of stone was also tested. It was found that these methods can provide new information about historic materials and therefore help with object identification and restoration works. The key issue is the used spectral range where the visible near infrared spectral region gives information mainly for biological purposes and the short-wave for material determination. In this work, hyperspectral imaging was used in the spectral range 400-1000nm and reflectance spectroscopy in 900-2500nm. In the 1000 – 2500nm region, the new material spectral library was created for the material decomposition of historical plasters and mortars. This library is produced with respect to the Central Europe region and then applied for eleven historical samples analysis using various algorithms. Final results were then compared to the Scanning electron microscope findings. It was ascertained that classification analysis can be used for material decomposition of samples when a convenient spectral library is available, although the similarity of plaster and mortar mixture makes the task very challenging. Due to this fact, a decision tree approach was successfully tested.

## Keywords

Hyperspectral imaging, Reflectance spectroscopy, Spectral library, Cultural heritage, Material determination, Plaster, Mortar, Biological contamination of stone

## Anotace

Cílem práce je porovnání a zhodnocení využití několika metod používaných pro určení složení historických materiálů, zejména těch využívajících odrazivostní spektrometrii a hyperspektrálním snímkování. Tyto metody jsou ve své podstatě neinvazivní, a proto velmi zajímavé pro dokumentaci historických památek. Složení materiálů, jejich analýza a rozpoznání bylo zaměřeno zejména na historické objekty – konkrétně malby, omítky a malty. Dále bylo zkoumáno i biologické znečištění kamenů. Bylo zjištěno, že pomocí výše zmíněných metod lze získat nové informace o zkoumaných objektech, které mohou být následně použity například pro restaurátorské práce. Základní informací je použitý rozsah vlnových délek – rozmezí mezi viditelným a blízkým infračerveným pásmem je vhodné zejména pro analýzu biologických pokryvů, zatímco střední infračervená pásma se hodí spíše pro určení složení materiálů. V této práci bylo použito hyperspektrální snímkování v rozsahu 400 – 1000nm a metoda odrazivostní spektrometrie v rozsahu 900 – 2500nm. V rozsahu 1000 – 2500nm byla v rámci práce vytvořena spektrální knihovna materiálů nazvaná "CTU material spectral library", která je určena zejména pro určení složení historických malt a omítek. Knihovna byla vytvořena pro středoevropský region a následně využita pro analýzy jedenácti vzorků. Tyto výsledky byly pro kontrolu porovnány s výsledky z elektronového mikroskopu (Scanning Electron Microscope). Bylo zjištěno, že za pomoci vhodných analýz je možné určit složení neznámých vzorků, pokud je k dispozici vhodná spektrální knihovna. Vzhledem k vysoké míře podobnosti jednotlivých směsí malt a omítek je tento úkol velmi náročný, a proto byl pro tuto úlohu testován i přístup založený na tzv. rozhodovacím stromu.



## Klíčová slova

Hyperspektrální snímkování, Odrazivostní spektrometrie, Spektrální knihovna, Kulturní dědictví, určení složení materiálů, Omítka, Malta, Biologické znečištění kamene

## Acronym list

| | |
|---|---|
| ASCII | Americal Standard Code for Information Interchange |
| ASTER | Advance Spaceborne Thermal Emission and Radiance |
| AVIRIS | Airborne Visible / Infrared Imaging Spectrometer |
| BE | Binary Encoding |
| CCD | Charge-coupled device |
| CTU | Czech Technical University in Prague |
| EDS | Energy Dispersive Spectroscopy |
| ESA | European Space Agency |
| FCE | Faculty of Civil Engineering |
| FLAASH | Fast Line-of-sight Atmospheric Analysis of Hypercubes |
| GPS | Global Positioning System |
| HDPU | Hyperspec Data processing Unit |
| IMU | Inertial Measurement Unit |
| InGaAs | Indium Galium Arsen |
| KLUM | Karlsruhe Library of Urban Materials |
| LUMA-SLUM | London Urban Micromet data Archive - the Spectral Library of Impervious Materials |
| LWIR | Long Wave InfraRed |
| NAKI | Národní Kulturní Identita (National Cultural Identity) |
| NASA | National Aeronautics and Space Administration |
| NDVI | Normalized Difference Vegetation Index |
| NIR | Near InfraRed |
| NNLS | Non Negative Least Squares |
| PCA | Principal Component Analysis |
| PPI | Pixel Purity Index |
| SAM | Spectral Angle Mapper |
| SEM | Scanning Electron Microscope |
| SFF | Spectral Feature Fitting |
| SID | Spectral Information Divergence |
| SNR | Signal to Noice Ratio |
| SWIR | Short Wave Infrared |
| UAV | Unmanned Aerial Vehicle |
| USGS | United States Geological Survey |
| UV | Ultra-Violet |
| VGA | Video Graphics Array |
| VNIR | Very Near InfraRed |

# Table of content

# 1. Introduction

Hyperspectral imaging has been an area of active research and development in many different fields during past decades and its giant potential is getting more visible with technical development. Recently hyperspectral imaging data have started to be widely used among the public in a wide variety of applications. Different names were given to this field of study like hyperspectral imaging, imaging spectrometry, or imaging spectroscopy, but the output is similar – derive the set material's reflectance spectra in a given range.

Unlike the multispectral sensor which operates in a relatively low number of wide spectral bands hyperspectral scanners give full information across the electromagnetic spectrum in given spectral range, (Figure 1). This is done by collecting many (tens to hundreds) narrow, closely spaced spectral bands so that the resulting spectra appear to be continuous curves. Using these data one can enable the extraction of reflectance spectra at a pixel scale that can be directly compared with similar spectra measured in the field or in a laboratory. Although most hyperspectral sensors measure hundreds of wavelengths, it is not the number of measured wavelengths that define a sensor to be hyperspectral. It is rather the narrowness and contiguous nature of the measurements.

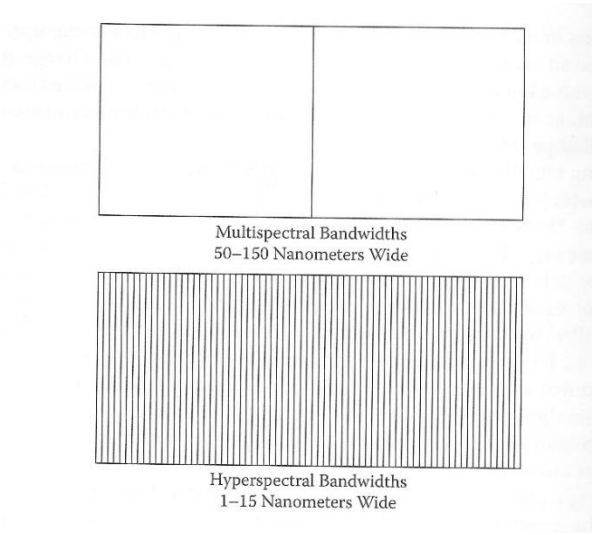


*Figure 1 - Number of hyperspectral bands compared to the number of hyperspectral bands in the same area [1].*

# 2. Aims and objectives

Historic object analysis and the knowledge of its composition play an important role in the restoration processes. Based on this information restoration works are conducted. The aim of this thesis was to gain knowledge of the hyperspectral imaging and reflectance spectroscopy use for historic object documentation. Diverse exact non-invasive methods of historical material determination and information identification were tested and analysed at various objects of interest.

The first objective is to explore and test possibilities of hyperspectral imaging on close-range analysis in the laboratory to prepare the CTU

hyperspectral system for future in-situ use at the Charles Bridge, Prague, the Czech Republic. The second objective is to create and examine spectral characteristics of selected materials that will be used for their determination in the Central Europe region using reflectance spectroscopy. Materials were carefully selected to include those that were and still are commonly used for plaster and mortar production.

# 3. Literature review

## 3.1. Basic principles of reflectance spectrometry

### 3.1.1. Spectral reflectance

Different surface features reflect and absorb the electromagnetic radiation of the sun in different ways. The reflectance properties of an object depend on the material and its physical and chemical state, the surface roughness as well as the angle of the sunlight. The reflectance of material also varies with the wavelength of the electromagnetic radiation. The amount of reflectance from a surface can be measured as a function of wavelength range, this is referred to as Spectral Reflectance. Spectral Reflectance is a measure of how much energy (as a percent) a surface reflects at a specific wavelength. Surfaces reflect a different amount of energy in different portions of the spectrum. These differences in reflectance make it possible to identify different earth surface features or materials by analysing their spectral reflectance signatures. Spectral reflectance curves graph the reflectance (in percent) of objects as a function of wavelengths [2] (Figure 2). Some materials reflect radiation of a certain wavelength, while other materials absorb the radiation of the same wavelength. These patterns of reflectance and absorption across wavelengths can uniquely identify certain materials.

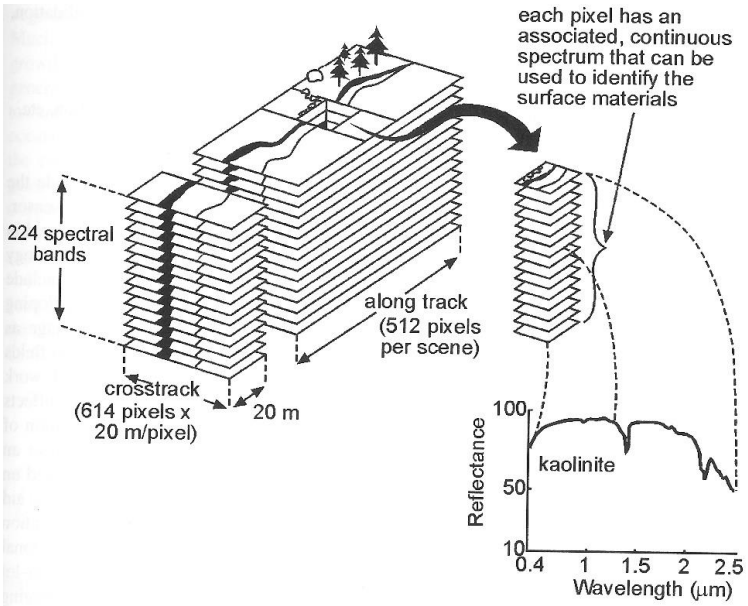


*Figure 2 - Hyperspectral data cube and spectral reflectance graph [3]*

### 3.1.2. Spectral libraries

Specific materials have their spectral curves measured in the laboratory and are stored in spectral libraries. Using these differences and comparisons with laboratory measurements one can compare spectral curves in order to detect measured material. Spectra from libraries can guide spectral classifications or define targets to use in spectral image analysis.

A spectral library can be created by a user for a specific topic (e.g. a tree or plant types, minerals, materials) or a public library can be used for the data analysis. For public use, there are several spectral libraries available for natural and man-made materials. Spectral signatures are measured in laboratories and are used for comparison with given reflectance spectra. More information about relevant spectral libraries dealing with building materials can be found in Chapter 8.1.

### 3.1.3. Instrument types

For various wavelengths different detector types have to be used. This is due to the nature/core of the operating spectral range. The two most common detectors are Si-CCD and InGaAs.

A silicon-based charge-coupled device (Si-CCD) is a standard detector used in UV-VIS-NIR cameras. The cost of these detectors is relatively low and cooling is not always compulsory. The operation range is 300 to 1100 nm, but the maximum quantum efficiency is highest in 420 – 560 nm (above 50%) but falls to less than 1% over 1000nm [4]. The higher quantum efficiency indicates higher sensitivity. Due to this fact, a powerful illumination source is required and the signal-to-noise (SNR) ratio is lower in boundary wavelengths. In order to gain more signal cooled Si-CCD detectors can be used. Generally, cooling allows longer exposure time and provides higher SNR but increases the cost of the spectral apparatus.

Indium Gallium Arsen (InGaAs) detectors are used for NIR-SWIR wavelengths from 1000 to 2600 nm, but usually only a part of this range is used to get high SNR. Cooling is a necessity in this case since a lot of heat is produced during detector operation time and noise increases with temperature. Quantum efficiency also varies over wavelengths depending on the detector type. More information can be found at a manufacturer website e.g. [5]. Costs of these detectors are much higher compared to Si-CCD and together with cooling it increases the NIR-SWIR spectrometer cost to several tens of thousands euro.

### 3.1.4. Reflectance spectrometer

Reflectance spectrometers are devices that measure light that is emitted by or reflected from materials and its variation in energy with wavelength range. One deals with sunlight or artificial illuminator that is diffusely reflected by measured materials. An optical dispersing element such as grating or prism in the spectrometer splits light into many narrow, adjacent wavelength bands and the energy in each band is measured by a separate detector. Using these detectors, the device can measure many spectral bands as narrow as hundreds of micrometres [6] over a wide wavelength range depending on the instrument.

For system explanation, an Ocean Optics NIRQuest modular spectrometer is used. This device is at the disposal at the department of

Geomatics, FCE, CTU in Prague and has been used for in-situ data measurements. Reflectance spectrometers give spectral information about one single point of interest. Information derived from this device is given in the form of a 2D spectral curve (Figure 3).

Radiance reflected from an object enters the device through the input optical fibre (1), it goes through a slit (2) that regulates the amount of light that enters the optical bench and controls spectral resolution, and a filter (3) that restricts optical radiation to pre-determined wavelength regions. Next, it reaches a collimating mirror (4) that focuses light towards the grating (5) that diffracts the light and directs it onto the focusing mirror (6) and then to the detector (7). The complete spectrum is then brought to the software.

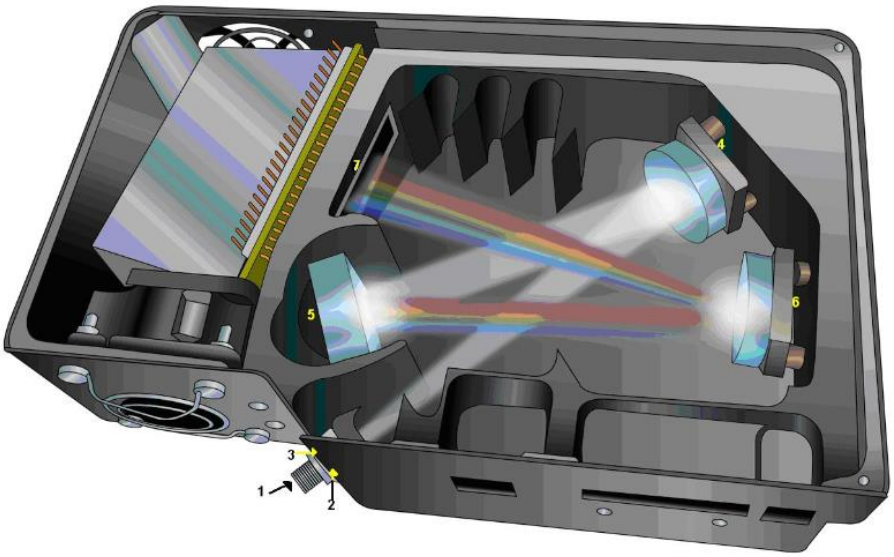


*Figure 3 - Ocean Optics NIRQuest spectrometer [7]*

Data are acquired by enclosing the end of the fibre optics to the object of interest. This device gains data from a single point in a form of an ASCII file – wavelength and a corresponding count value.

### 3.1.5. Imaging spectrometer

Hyperspectral images are produced by instruments called imaging spectrometers. The principle is similar to reflectance spectrometer, but the difference lies in the number of measured points at a single moment. Measured data are commonly combined into a 3D data cube (Figure 2).

Hyperspectral imaging sensors have a similar set-up as a reflectance spectrometer, but the detector is not a line it is a matrix. Thanks to this it provides spectral information from a line of points and not just a single one. These devices are larger, usually heavier and instead of an input fibre they are equipped with sophisticated optics, so it is possible to focus on an object placed in front of the camera.

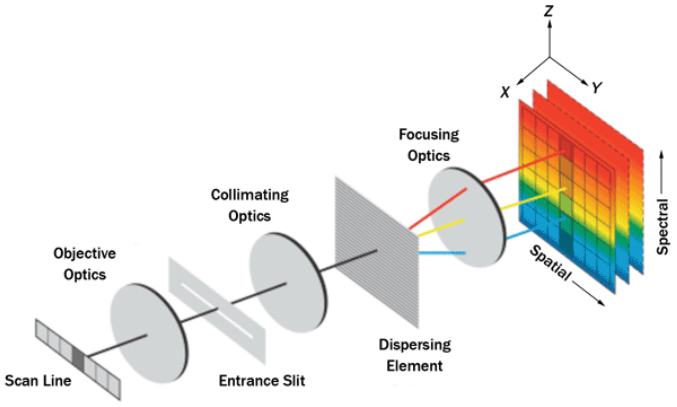


*Figure 4 - Typical push broom setup [8]*

There are two major types of imaging sensors. The first one is a „whisk broom" configuration that scans across the measurement track. In a whisk broom sensor, a mirror scans across the path reflecting the light into a single detector which collects one pixel at a time. The moving parts make this type of sensor expensive and more prone to wearing out - for example, the airborne HyMap sensor [9] spaceborne AVIRIS [10] operates using this configuration.

Second and more frequently used is a „push-broom" sensor configuration (Figure 4). It scans along the measurement track and it consists of a line of sensors arranged perpendicular to the scanning direction. Different areas of the desired object are imaged as the instrument moves. Push broom sensors are generally lighter and less expensive than their whisk broom counterparts and they can gather more light because they look at a particular area for a longer time. The light approaching the sensor is split into narrow bands by an optical dispersing element such as grating or prism and the amount of energy is measured by a detector. As an example of this technology, one can name space-borne NASA` s Hyperion [11], CASI 1500 [12] or ESA` s CHRIS [13]. Among airborne or multifunctional (also suitable for in-situ measurements) one can name Hyperspec by Headwall Photonics [14].

Hyperspectral sensors can be mounted on various platforms. Spaceborne ones are usually push-broom configuration and are the only ones that are open to the public. Hyperion data can be downloaded free of charge after registration on USGS (United States Geological Survey) web site via GloVis application [15]. CHRIS (Figure 5) data used for educational and research topics can be also downloaded free after registration, more information can be found online [16]. Spaceborne hyperspectral data are good for global analysis due to their large covered area and low spatial resolution [17].

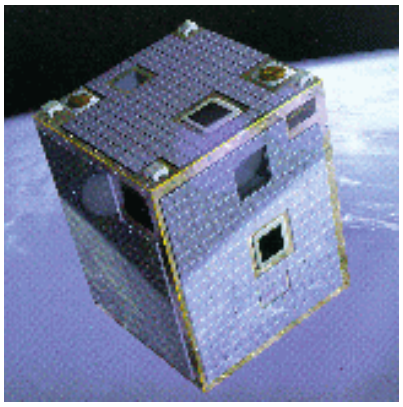

*Figure 5 – Proba satellite-carrying CHRIS hyperspectral sensor [13]*

Airborne hyperspectral data are widely used for applications in geology, agriculture, vegetation, water management, land cover detection and many others. They work perfectly on a regional or local scale; thus, one can change the spatial resolution by changing the flight height. Sensors can be either placed on aircraft/airships driven by a person or put on a UAV (Unmanned Aerial Vehicle) and be controlled by a computer. Unfortunately, these instruments are usually owned by commercial companies (Figure 6), so free downloading via web sites as mentioned above is impossible. Costs of these vary a lot depending on an instrument and an area, but as a plane needs to be used the price can be very high.


*Figure 6 – HyMap airborne hyperspectral sensor [9]*

*Figure 7 - Hyperspec multifunctional hyperspectral sensor [14]*

Multifunctional hyperspectral scanners (Figure 7) are convenient for a large variety of applications. The main benefit of these sensors is the fact that they can be used for in-situ measurements and with appropriate instruments (GPS/IMU unit, aircraft/UAV) are suitable for airborne scanning as well. This is due to their low weight and small size. These sensors are the best for specific measurements on the local scale [4].

## 3.2. Applications

There are several most important terrestrial applications of hyperspectral imaging and reflectance spectroscopy. These methods are based on a similar material characteristic so they are often used together. Reflectance spectroscopy provides valuable in-situ information for

spaceborne and airborne applications, so it is not easy to distinguish terrestrial and space/airborne hyperspectral imaging and reflectance spectroscopy method respectively. It is appropriate to emphasise, that not all applications of hyperspectral imaging and reflectance spectroscopy are mentioned in the following list.

### 3.2.1. Applications in soil mapping and land degradation

Desertification and land degradation are serious problems that must be further investigated. Hyperspectral imaging is a great help in this study because it gives global to regional image about the conditions in investigated areas. One can recognize different soils and their composition using hyperspectral imagery as well as vegetation types and their interaction [4]. As an example, one can see an application in southern Spain [18]. Also, coal fires can be detected using hyperspectral data - Zhang [19] deals with then at the Northwest China location. Soil organic carbon (SOC) as has been investigated as an indicator of land degradation and used for various analysis and monitoring [20], [21]. Reflectance spectroscopy has been used to create soil spectral libraries on local [22] [23] and global level [24].

### 3.2.2. Vegetation, agriculture and forestry applications

Many books [4], [25] and papers have been written about this topic. By hyperspectral scanning, one can determinate the amount of chlorophyll A and B which shows much about the health and vegetation stress in the field. Also, fluorescence and temperature indication regarding vegetation stress have been studied on an olive orchard [26]. Estimating crop nitrogen status is also an interesting application. Nitrogen shortage is expressed by lower chlorophyll content and leads to reduced photosynthesis rate which is not desirable on the field [4], [25]. Forest stress based on beetle attack, root rot, poor site condition or other can be also analysed using these methods [1]. Detection and analysis of specific features and structural materials like lignin [27] in wood have been studied. In practice, hyperspectral imaging and reflectance spectroscopy are used for precise agriculture for detection of contaminants e.g. heavy metals in soils [28], [29], water stress and health status [30], [31] and crop diseases [32], [33].

### 3.2.3. Applications in the food industry

Hyperspectral imaging and reflectance spectroscopy technology can be used for food quality and safety evaluation and inspection, which is a promising field of research [34]. VIS-NIR hyperspectral imaging offers the possibility, for example, of predicting the optimum stage of maturity in banana [35], monitoring the ripeness of nectarines [36], or measuring the evolution of quality parameters in peppers during maturation [37]. An interesting example is a moisture and fat analysis in salmon filets [38].

### 3.2.4. Geological applications

Spectroscopy has been used in geological applications since the mid-eighties [39]. Since then we can map the surface mineralogy and determine individual minerals or rocks. Detection of specific (rare or dangerous) materials like gold or petroleum is used as well as discovering new oil/gas reservoirs [40]. Recently several portable full-range

spectrometers for mineral identification are available on the market. These devices produce immediate on-instrument results, they include internal references to allow an easy operation and data management and also features proprietary, state-of-the-art mineral identification software for data capture in the field [41], [42].

### 3.2.5. Environmental applications

In recent years the hyperspectral imaging has been employed in the field of environment. Old ecological loads can be found using this method. *Petruchova* in [43] searched for old dumps and other not yet visible potential ecological problematic areas, thus organic materials have a very unique spectral curve, see page 220-222 in [4]. Oil spills are also investigated [44]. Sources of $CO_2$ are visible too, which can be very useful for pollution determination and further global warming research. A cuttlefish camouflage can also be analysed by using spectrometry [45]. A new approach to waste management using hyperspectral determination of materials is now evolving for electronics [46], demolition waste [47] and plastic [48], [49], [50].

### 3.2.6. Water applications

Hyperspectral imagery is a suitable technique for large-scale (airborne, spaceborne) and small-scale (in-situ measurements) monitoring of inland and coastal water quality and its advantages have been long recognised [1], [51], [52].

### 3.2.7. Cultural heritage and archaeology applications

Imaging spectroscopy is a non-destructive analysing method. It has been widely applicable in the field of archaeology and cultural heritage. Different hyperspectral instruments can be used to obtain the desired data. The application in remote sensing in archaeology allows fast acquisition of much information connected to the territory. Data about archaeological evidence, mine and quarry position, lithotype characterization, vegetation covers and types are useful for a full image of investigated area and the nature of people living there in the past [53]. The presence of structures and hollows in the top subsurface is likely to cause variations in humidity in the surface. The examination of these anomalies carried out by the use of digital processing of hyperspectral images enables the photointerpreter to determine possible signs of underground structures of archaeological interest [54], [55], [56], [57]. For discovering new archaeological sites, the integration of LiDAR and hyperspectral data can be used as seen in [58].

### 3.2.8. Art conservation applications

The hyperspectral imaging technique has been adapted to the non-destructive examination of works of art. The technique allows the art material to be distinguished by its composition, and an under-drawing can be revealed. The initial results indicate that even over limited wavelength ranges (650 – 1040 nm) and with relatively coarse spectral resolution (10 nm) a number of pigments can be distinguished. Non-destructive identification of pigments can be used to address issues of attribution, age dating, and conservation. Images of different wavelengths and false colour composites can be made to discover hidden drawing or to find out what is

under areas that are not visible yet (wine stains, ink spots, etc.) [59], [60], [61]. Not only drawing can be explored, but also old papers and books as seen in [62], [63], [64]. High-quality spectral library covering various dyes types was created [65]; unfortunately, the library is inaccessible for other researchers. Hyperspectral imaging is a part of physical techniques in the study of art, archaeology and cultural heritage as mentioned in [66], more information can be found in [67].

The analysis of paintings has been further investigated, detailed information can be found in Chapter 5.1.

### 3.2.9. Application in civil engineering and historic restoration

Determination of plaster and façade composition is a very important issue in the restoration process. The composition can help with date assessment of the building and it can also provide information about restoration processes during past years. It is desired to use non-invasive methods for these analyses since no harm damage will be done to the plaster or façade. Non-invasive methods must be verified in the laboratory before their use and a detailed methodology has to be followed.

Literature shows various methods for plaster and façade documentation and analysis. Two non-invasive methods are commonly used. It is the X-ray diffraction and Raman spectroscopy. When using X-ray diffraction, a monochromatic X ray-beam goes through the substance and beam diffraction occurs. The direction and intensity of these diffracted beams depend on an inner sample structure. It allows us to define the absolute molecule structure of the sample. This method can be used for identification of remains [59], for concrete erosion determination [68] or when combined with other methods for plaster analysis [69], [70]. Raman spectroscopy is based on the Raman phenomenon (interaction between photons and light). A laser beam is shot onto a surface, it interacts with electron and then a photon is emitted. The wavelength of this photon is measured and it provides information about the surface. This method is specially used for pigment determination of historic objects in Romania [71] and Mexico [72] or for efflorescence (soil migration) mapping in concrete [73]. These methods are very complex and due to the nature of these methods sample heating can be a big issue – intense X-ray or laser beam radiation can possibly harm the object of interest.

Reflectance spectroscopy has been already used for differentiating between anthropogenic calcite in plaster, ash, and natural calcite [74]. In this paper, the distinguishing is done using absorption peaks. In combination with other spectroscopic methods, it was used for pigment identification [75]. Urban material spectral library creation was conducted by Kotthaus et. al. [76], but without specialization to plasters and façades. Nowadays reflectance spectroscopy is not a very common method for plaster and façade analysis and that is the reason for the author's special interest. Advantages and disadvantages of the method are mentioned in Chapter 13.

More information about other spectral libraries of materials used in civil engineering can be found in Chapter 8.1

# 4. Used instruments and captured data

## 4.1. Hyperspectral imager

The unique portable hyperspectral imaging device consists of a hyperspectral sensor, Pan&Tilt unit, tripod, illumination sources and a control unit.

### 4.1.1. Hyperspectral sensor

An A-series hyperspectral VNIR camera Hyperspec VNIR manufactured by Headwall Photonics Inc. [77] is used (Figure 9). Headwall Photonics' Hyperspec imaging spectrometer platform is built on a reflective concentric, f/2 optical design. The camera is lens-based, thus equipped with a C-Mount 35mm objective and 18mm long and 25/60um wide slit. The operational wavelength ranges between 400 to 1000 nm and the focal plane size is 1004 spatial and 810 spectral bands in this range. The speed of the sensor is up to 50 full frames at 12bits with 2nm spectral resolution and the included device is a CCD. The sensor is not equipped with cooling, but it allows 2x2 binning, which was not used in this case. The imaging spectrometer has been calibrated by the manufacturer.

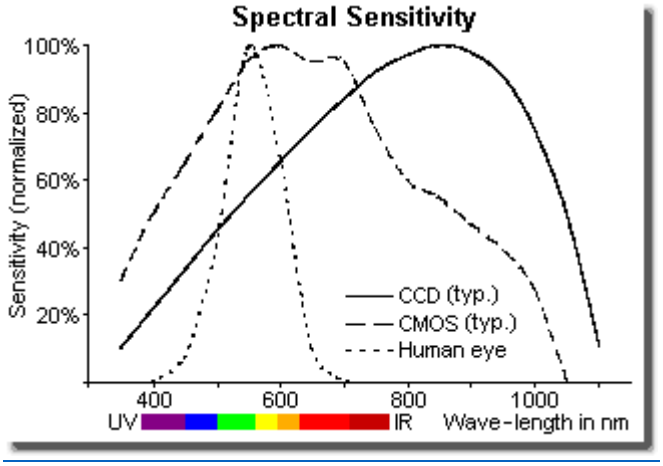


*Figure 8 – Spectral sensitivity of CCD device used in the hyperspectral imager [78]*

### 4.1.2. Pan&Tilt unit

The hyperspectral instrument is placed on a medium-size motorized moving platform designed by Headwall Photonics, Inc. named Pan&Tilt [79], which provides accurate real-time positioning of the hyperspectral equipment and is conducted via PC.

### 4.1.3. Illumination platform

The illumination platform is a unique device that has been created just for homogenous and sufficient illumination of objects of interest. Illumination plays a key role in spectral characteristics extraction because the reflectance (the amount of reflected light) is measured. It is required that the quantity of reflected light should be just enough to reach (but not exceed) the saturation level of the hyperspectral instrument. If the amount of light detected by the instrument is too low, significant noise will appear in the data. This noise cannot be mathematically corrected because it

affects dark parts of the investigated object more than the light ones. One can dispose of the noise via careful and fine illumination. This issue and its solution for the used setup is thoroughly explained in [80]. The platform is made from fine metal plate (4mm thickness) with reinforcements on both sites (2mm thickness) with two 70W ASD Illuminator Reflectance Lamps [81], one on each side of the platform. This set-up provides adequate illumination for scanned object and minimizes heat coming from illumination sources by illuminating just the scanned place since it moves with the Pan&Tilt platform.

### 4.1.4. Tripod

The setup (hyperspectral camera, Pan&Tilt unit and the illumination platform) has been placed on a strong tripod Callidus CINE 2000 to enable one to move the system and adjust the height of the camera. Special tripod head had to be created for the Pan&Tilt unit fitting.

### 4.1.5. System control

Control of the system is performed by the HDPU (Hyperspec Data Processing Unit) and using Hyperspec III. software developed by Headwall Photonics, Inc.

*Figure 9 - Hyperspectral imaging device at the Department of Geomatics, FCE, CTU in Prague*

### 4.1.6. Data type

Hyperspectral imaging data are commonly given in the form of a 3D data cube. When taken a hyperspectral image of an area or object image is given for every spectral band. In the end, we end up with as many images

as measured bands. These images compose a 3D data cube (Figure 10). The 3D data cube information resembles the reflectance spectrometer data – wavelength and a corresponding signal value. From this dataset, user can derive a spectral curve or to analyse and work with each band separately. Image processing is done using similar tools as mentioned in Chapter 3.1 and more detailed in Chapter 4.1.9, but one must consider the size of the data that can easily exceed several gigabytes.

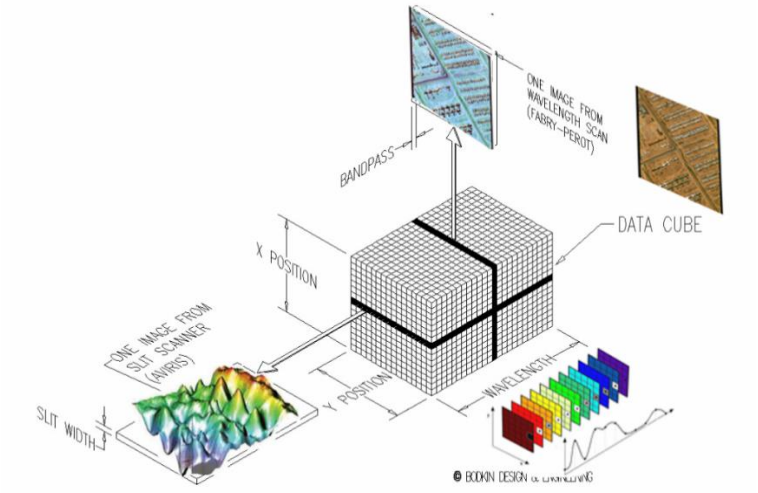


*Figure 10 – Hyperspectral data (3D cube) explanation and example [82]*

### 4.1.7. Data acquisition

Hyperspectral data are acquired using a hyperspectral sensor. Based on the sensor type the data are obtained. The key issue is to get fine, well-focused images with the appropriate geometry and spatial resolution depending on individual application. The noise level is desired to be kept at a minimum. The data acquisition itself is done using an instrument's operation software and varies with sensor types.

### 4.1.8. Data pre-processing

Hyperspectral data processing is a long process with many steps. The number of steps depends on the used sensor (spaceborne, airborne and terrestrial) and the desired outcome. The result of hyperspectral data can vary from a spectral curve comparison to pixel unmixing processes. The processing workflow always depends on an application and requested information (classification, band math, spectral curve, etc.).

Usually, the first pre-processing step is independent of the sensor and outcome. It is dark and white reference calibration. This can be done by the sensor itself (devices are equipped with a calibration workflow) or manually in the processing software. The dark calibration is usually performed by the sensor operating software by subtracting the signal of the sensor (with closed optics) from the object signal. The general-purpose method for white reference is to use an image processing software. A region of interest is created covering the white reference material in the image and mean value (for every band) is computed using statistical analysis. The entire data file is then divided by these means (since there are various means for various bands). The resulting image will then be a

reflectance image ranging from 0 to 1 (1 is the reflectance of white reference).

Geometric correction and sensor characteristics are performed according to the sensor type. When dealing with spaceborne or airborne data one need to consider radiometric correction impact. The influence of an atmosphere must be minimalized. This is usually done by atmospheric correction modules (like FLAASH in ENVI - [83]) or when in-situ measurements are conducted at the time of acquisition an empirical line correction technique can be used.

### 4.1.9. Data processing

Final processing can be performed in these steps: noise and data size removal, endmembers finding and composition determination. When dealing with reflectance spectroscopy data, the data size removal is usually not necessary. At CTU in Prague, FCE, dpt. of Geomatics an ENVI processing software is used [84].

Data size removal (dimension reduction) can be performed in processing software by Principal Component Analysis. This mathematical approach gives a result of several (tens) uncorrelated output bands. More information can be found at [85].

The Pixel Purity Index is often calculated to find appropriate endmembers for further analysis. The PPI is a processing technique designed to determine which pixels are the most spectrally unique or pure [86].

Composition determination is a very complex issue that provides information about the nature of a specific pixel. Absorption bands or peaks can be analysed to discover pixels attributes other mathematical options can be used. One can mention Spectral Feature fitting that is based on the least-squares method [87], Spectral Angle Mapper that compares a spectral angle between a test reflectance spectrum and a reference reflectance spectrum [88] or a linear spectral unmixing [89], that defines mixed endmembers in the desired pixel (Figure 11).

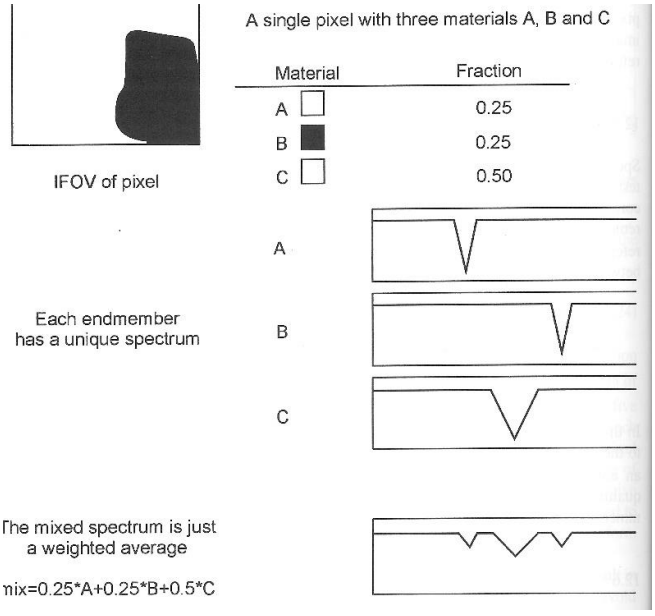


*Figure 11 – Spectral Unmixing - Different spectral classes present in a pixel [4]*

## 4.2. Reflectance Spectroscopy measuring device

Spectrometric measuring device consists of a spectrometer, illumination source, laptop with controlling software, fibre optics and a measuring probe.

### 4.2.1. Spectrometer

In 2015 a fibre optics reflectance spectrometer was purchased. The NIRQuest512-2, 5 from Ocean Optics / Ocean Insight (Figure 12), [90] works in 900 – 2500 nm spectral range. In this range 512 spectral bands are detectable. This device follows the spectral range of the VNIR Hyperspec A-series working between 400 and 1000 nm. The spectrometer is equipped with an InGaAs detector and cooling that is a necessity when using these detectors. The inner set-up is explained in Chapter 3.1.4.

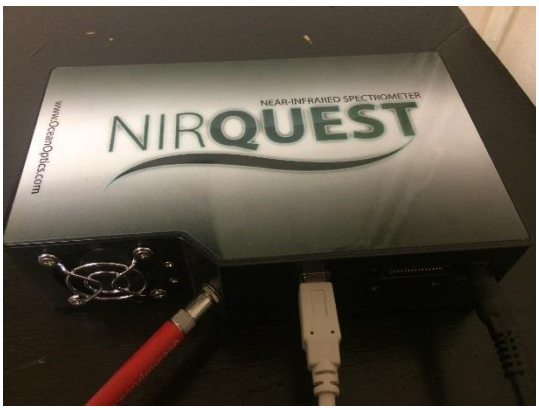


*Figure 12 - Spectrometer NIRQuest*

### 4.2.2. Illumination

Illumination of the object of interest is done by using fibre optics. An external illumination source Cool Red (Figure 13) provides an adequate light source for the 900 – 2500nm spectral range (Figure 14). An optic fibre then transfers the light into the scanning probe.

*Figure 13 - Illumination source Cool Red*

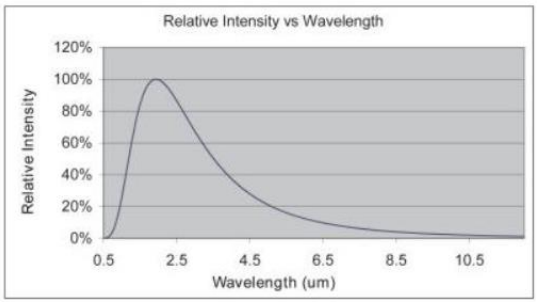


*Figure 14 - Intensity of Cool Red illumination source v and its dependence on wavelength, from [54]*

### 4.2.3. Spectroscopic measuring device

A spectroscopic measuring device (Figure 15) besides mentioned consists of a laptop with control software, fibre optics and a measuring probe. The probe [91] is composed of an optical fibre, that transfers

information into the spectrometer as well as fibres bringing illumination from an external source. End of the probe can be seen in Figure 16 and the ferrule diameter is 3,175mm and an acceptance angle of 24,8°. White reference material is a key issue for spectroscopic measurements. After several tests, it was found that Spectralon from LabSphere [92], Figure 17 will be used as a white reference.

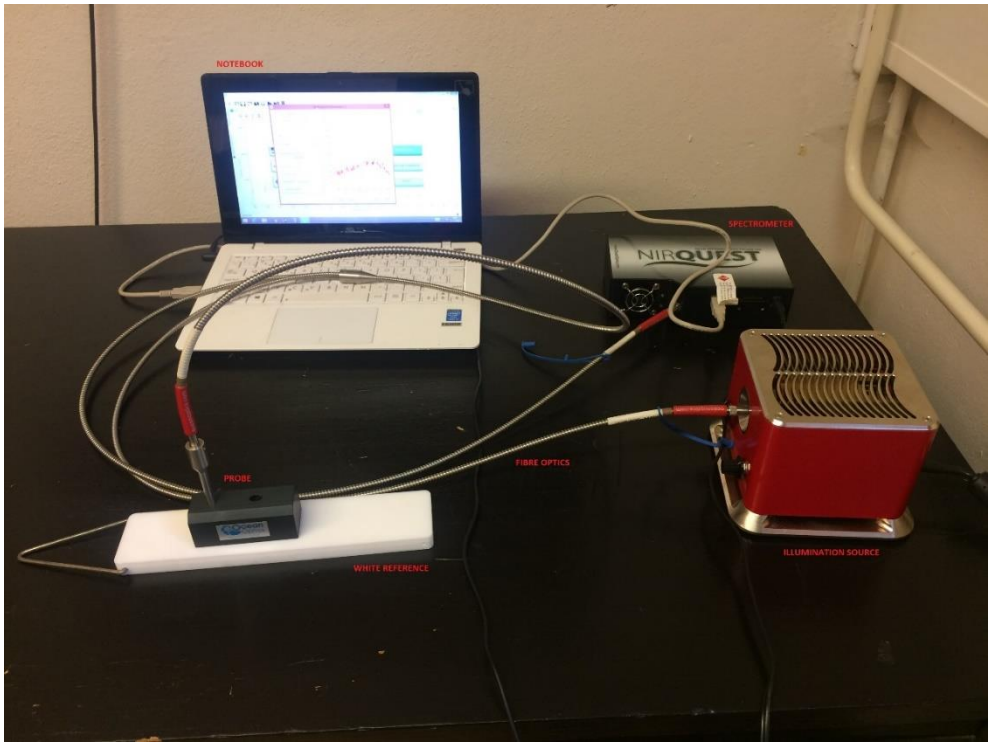


*Figure 15 - Reflectance spectrometry measuring device*

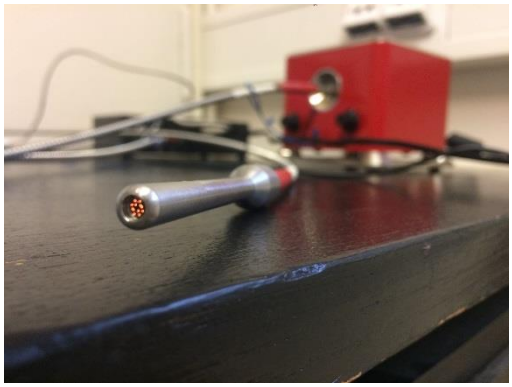

*Figure 16 - Probe on the end of fibre optics*

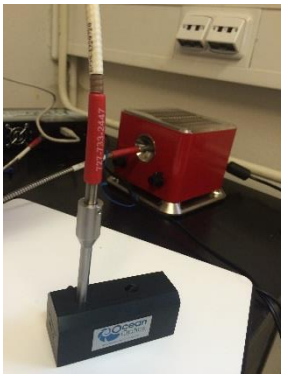

*Figure 17 – White reference calibration (Spectralon)*

### 4.2.4. Data type

Data from a reflectance spectrometer are usually given in the form of a text (ASCII) file or a table. There is information about a signal that is captured by a detector for every spectral band in an operation spectral range. These data are then processed in image processing software tools

(e.g. ENVI), in scripts written in programming languages (e.g. C++) or programming software packages (e.g. Matlab).

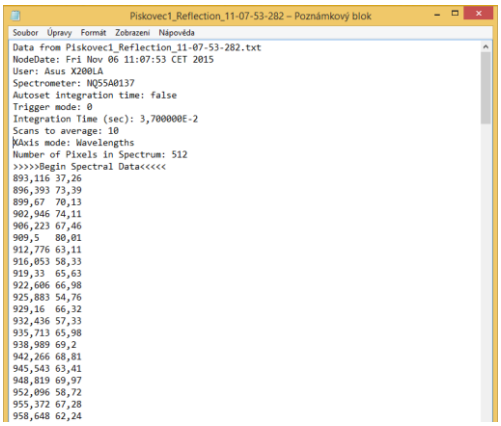


*Figure 18 - Example of reflectance spectrometer data*

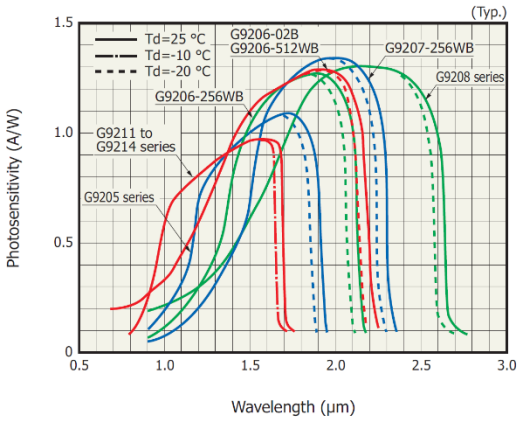


*Figure 19 – Used detector (G92087) sensitivity graph*

### 4.2.5. Data acquisition

Data were gathered using an Ocean Insight reflex probe QR600-7-VIS125BX [91] by attaching the probe end to the object of interest. The probe should be as perpendicular to the sample as possible and with a specific distance from the target. More information about probe settings and the influence of distance and angle can be found in Chapter 6.

The probe is operational using the OceanView spectrometer software version 1.6.7., that can be downloaded from [93]. Calibration is done using this software tool by setting acquisition parameters (Integration time, Number of scans to average and boxcar width) and a maximum (white reference) and minimum (dark reference) values. White reference parameters are set using a Spectralon diffuse target [92], dark reference is set by covering the probe end to eliminate any light the probe can detect. The object of interest spectral curve is then shown in the software window and the final purchase is then done using the "safe graph to file" button. To gain the best value data possible an average of 10 scans was used with a boxcar with of 2.

### 4.2.6. Pre-processing

Data were gained in the form of a text (ASCII) file and then they can be then uploaded into various processing software tools, e.g. Matlab, ENVI, QSdata. To provide valuable datasets with a spectral range from 900 to 1000nm has been cut off to eliminate a data noise. This noise is caused by a lower sensitivity of the used InGaAs detector (G9208) in this spectral range (green colour in Figure 19). Due to this fact, all reflectance spectroscopy data used to follow the 1000 – 2500nm spectral range. Since the sensitivity in longer wavelengths (around 2500nm) is sufficient, additional spectral range reduction is not needed.

Pre-processing workflow also includes data format adjustments since not all software tools can load ASCII files. This has to be done concerning the used software package.

### 4.2.7. Processing

Spectroscopy data processing is done similarly as with hyperspectral imager mentioned in Chapter 4.1.6. Concerning the nature of the acquired data only one point is analysed and unmixed. In this thesis, five methods were used to process data obtained using reflectance spectroscopy measuring device.

The pre-processed spectra of each sample is then used for a material average spectral curve calculation that is done using MATLAB software. The script was uploaded to attached CD as Appendix XIII. This tool provides information about the final/average spectrum and its statistical quality using a standard deviation computation, that provides information about data variation. Image outputs are created for better visualization and a 2,5*StdDev is shown and a maximum, minimum and average standard deviations are calculated.

#### *4.2.7.1. Spectral Angle Mapper*

Spectral Angle Mapper (SAM) is a physically-based spectral classification that uses an *n*-D angle to match pixels to reference spectra. The algorithm determines the spectral similarity between two spectra by calculating the angle between the spectra and treating them as vectors in a space with dimensionality equal to the number of bands [88].

This tool was used in two software packages – ENVI and Matlab, where a "hypersam" script was used and can be downloaded from MATLAB Hyperspectral Toolbox [94]. Results were compared and a match was found, so both tools give similar results. A Matlab script was then further used and was uploaded to an attached CD as Appendix XIV.

#### *4.2.7.2. Spectral Information Divergence*

Spectral Information Divergence (SID) is a spectral classification method that uses a divergence measure to match pixels to reference spectra. The smaller the divergence, the more likely the pixels are similar [95].

This tool was used in Matlab since it is not available in ENVI's Spectra Analyst and is available for spatial data only. MATLAB „hypersid" script was used and it can be found in an attached CD as Appendix XIV or is available online in MATLAB Hyperspectral Toolbox [94].

#### *4.2.7.3. Spectral Feature Fitting*

Spectral Feature Fitting (SFF) compares the unknown spectra and a reference spectrum using a least-squares technique. SFF is an absorption-feature-based methodology. The reference spectra are scaled to match the image spectra after the continuum is removed from both datasets [87].

This method has been used in ENVI software package in the Spectral Analyst toolbox [96].

#### *4.2.7.4. Binary Encoding*

The binary encoding technique encodes the data and endmember spectra into zeros and ones, based on whether a band falls below or above the spectrum mean, respectively.

This method has been used in ENVI software package in the Spectral Analyst toolbox [96].

#### 4.2.7.5. Non-negative Least Squares

This algorithm is included in the QSdata open-source software [97] created by prof. Ing. Aleš Čepek, CSc. It is based on non-negative least squares algorithm [98], [99] and seeks for non−negative linear coefficients whose sum is equal to one. This software package is also suitable for average spectral curve calculations, although a standard deviation of the result is missing. This issue was discussed and is planned to be added shortly. All information and abilities of this powerful open-source software tool are available online [97].

## 4.3. Instrument and captured data discussion

Two imaging spectroscopy devices were used in this thesis. The hyperspectral imager operating in 400 to 1000nm spectral range and a reflectance spectroscopy device with a 900 – 2500nm spectral range. The primary idea was to connect these spectral ranges to provide wide spectral information from visible (VIS) to short wave infrared (SWIR) wavelengths. Unfortunately, due to the nature of the devices (spatial/point) and the detector sensitivity dropping in spectral range ends (especially about 900 – 1000nm) this issue was not solved. In this range, a hyperspectral imager equipped with a CCD detector has quite high sensitivity (up to 80%, Figure 8), but the InGaAs detector used in reflectance spectroscopy device suffers from low numbers (less than 20%). The detector compatibility is visible in Figure 20. Considering these issues both devices are treated individually and the device connecting assumption may be further investigated in the future.

The reflectance value is closely dependent on illumination characteristics since it is the amount of light detected by the device. A small variation in illumination can be eliminated by calibration, but to acquire fine data with minimum noise one has to provide optimal illumination condition – uniform illumination of the entire target and correct amount of light not to saturate the device.

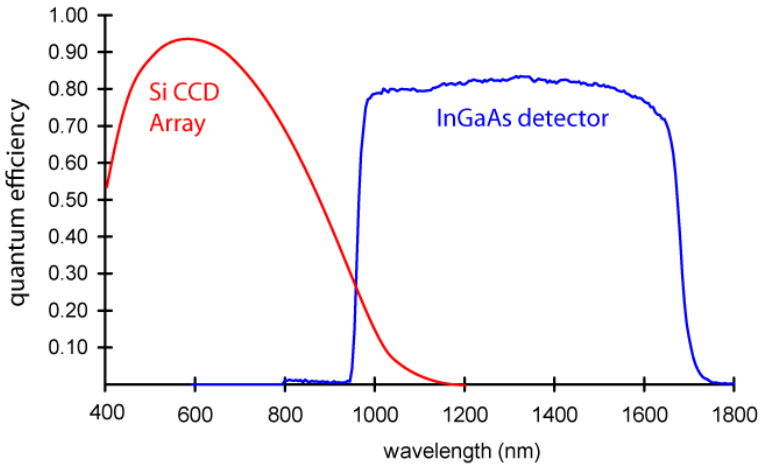


*Figure 20 – CCD vs InGaAs detector sensitivity comparison, from [100]*

# 5. Hyperspectral analysis

Hyperspectral imaging is a technique that analyses an entire light spectrum instead of assigning primary colours (red, green, blue) to each pixel. The light striking each pixel is broken down into many different spectral bands in order to provide more information about what is imaged. Following examples are just a part of possible use cases of the hyperspectral imaging and analysis technique performed by the author. More information about the application of hyperspectral imaging and reflectance spectroscopy can be found in Chapter 3.2.

## 5.1. Paintings analysis

During NAKI project (DF13P01OVV002) "New modern non-invasive methods of cultural heritage objects exploration" hyperspectral analysis of painting was performed. Pieces of art were oil paintings on a wooden desk by various authors. All paintings were borrowed from academic painter Mr Martin Martan with his kind permission. Visibility of underdrawings, paint changes and other characteristics were sought. For more information about the project see [101].

### 5.1.1. Flemish classical painting school

Two paintings from Flemish classical painting school dating in the 17$^{th}$ century were analysed. One painting was "The interior of a Mill" by David Terniers the Younger (Figure 21) and the second one was "On the road" by Thomas Van Apshoven. Paintings were documented using VNIR A-series Hyperspec hyperspectral imager (Chapter 4.1). A Principal Component Analysis (in ENVI software) was used to reduce the number of data and for the production of the false colour synthesis using band derived from PCA (Figure 23 and Figure 26). InfraRed reflectography was performed to visualize underdrawings and to compare them.

*Figure 21 - David Terniers the Younger "Interieur of a mill", painting size 48x69cm*

*Figure 22 - Painting detail - Terniers*

*Figure 23 - False colour RGB synthesis of three principal components (PC4 - red, PC - green, PC1 - blue) – Terniers*

*Figure 24 - Paintings detail as seen on IR reflectography image - Terniers*

*Figure 25- Thomas van Apshoven "On the road", painting size 76x54cm*

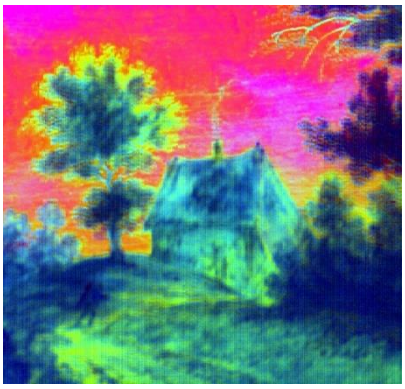

*Figure 26 - False colour RGB synthesis of the first three principal components (PC1 - red, PC2 - green, PC3 - blue) - van Apshoven*

*Figure 27 - Paintings detail as seen on IR reflectography image - van Apshoven*

Findings:

Hyperspectral analysis using the VNIR (400-1000nm) camera was performed on two 17$^{th}$ century paintings. The goal was to detect and visualize the underdrawings made by the author. Several mathematical approaches were tested and it was found that principal component analysis (PCA) can be used for this matter in certain cases. The house in *Van Apshoven's* painting is an example of an image, where PCA does not give sufficient results. When compared to IR reflectography it is not so powerful because of the data shortage in the extended infrared region. These data would allow us to go deeper into the painting and the following analysis would be attractive.

It was found, that the size of a storage jar on Ternier's painting has been changed. The original size of the jar was much smaller than the final one. This information was derived from a PCA image (Figure 23)

### 5.1.2. German painting school

A painting from an unknown author belonging to German painting school was analysed. This piece of art was created in the 19$^{th}$ century (Figure 28) and was documented in a similar way as the Flemish classical painting school objects mentioned in Chapter 5.1.1. To extend our knowledge about this piece of art cooperation with the Faculty of Electrical Engineering, CTU in Prague (Ing. Ladislava Černá – Laboratory of Photovoltaic System Diagnostics - [102]) was conducted. With the help of Ing. Černá, this painting was documented with infrared camera SWIR VGA (Figure 29) from Photonic Science [103]. This device is equipped with InGaAs detectors (resolution 640 x 512 pixels) and works in 900 – 1700 nm spectral range. The result is one image in a given spectral range since the camera is not capable of recording more spectral bands. Analysis results can be seen in Figure 30 to Figure 32.

*Figure 28 - Investigated object – Painting belonging to the German painting school*

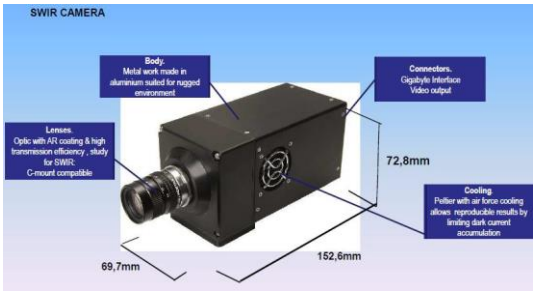


*Figure 29 – SWIR VGA camera used for the documentation of the object of interest, from [103]*

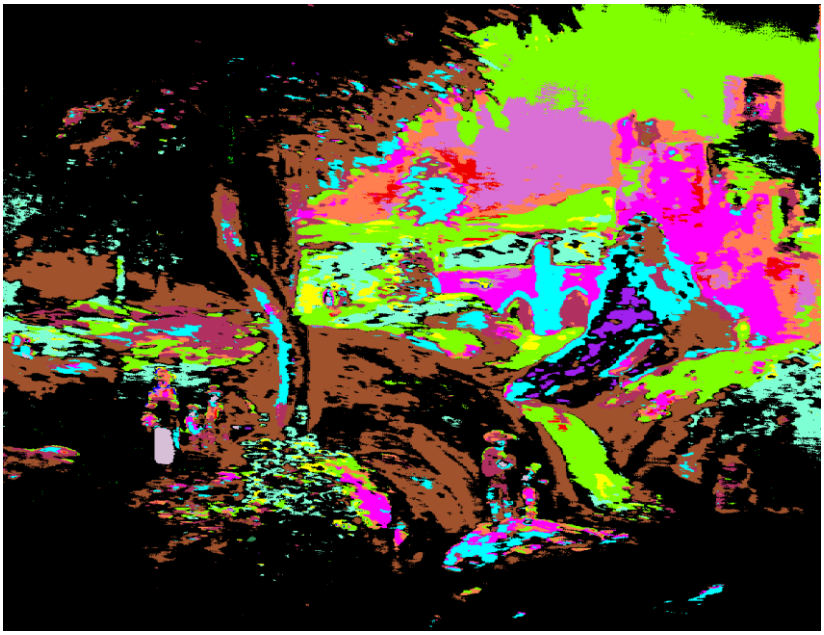

*Figure 30 – Spectral Angle Mapper classification result, 16 endmembers have been derived from the image using image processing software*

*Figure 31 - IR image from SWIR VGA camera operating in 900 – 1700 nm spectral range with highlighted points that are not visible in the visible spectrum*

*Figure 32 - Band 3 from principal component analysis with highlighted objects not visible on the original image*

Findings:

Two different instruments were used for the analysis – SWIR VGA Camera and Hyperspectral VNIR camera. SWIR VGA Camera gives a deep view into the picture showing many things that are hidden in the visible wavelengths (Figure 31). The interpretation of these object depends on the restorer. It can be due to the defect on the wooden desk, a bigger amount of paint or possibly due to the covering of unsuitable paint or an effect of the previous restoration works. Hyperspectral VNIR camera provides additional information due to a high number of spectral band and provides fine data for further mathematical analysis. Different types of classifications were performed and various pigment can be identified (Figure 30). Unfortunately, the appropriate spectral library is not at our department´ s disposal so pigments cannot be named. The data are suitable also for principal component analysis (PCA) that allows us to visualize some hidden objects (Figure 32). The limitation of this technique lies in the instrument's spectral range (400 to 1000nm). In case of the wider spectral range towards longer wavelength (SWIR), more information could be derived.

## 5.2. Biological contamination of stone

### 5.2.1. Introduction

Soil weathering and alteration can be determined by various factors, where one can mention wind, sunlight and temperature as well as rain, snow, moisture and biological contamination. The first affects the stability of the rock matrix, while the second acts through chemical corrosion of the stone forming material. Physical, chemical and biological agents act in co-association to deteriorate a stone [104]. Biodeterioration is a situation when biological material settles on a construction stone(s) of a structure and evolves there. In this case, we often deal with algae, bacteria, moss, lichens and fungi. This work is an example of how a stone affected by biodeterioration can be hyperspectraly analysed.

Sandstone has been commonly used building material in central Europe since early medieval times (Romanesque art) with a rapid expansion in the Gothic style [105]. Biological contamination is very common in sandstone and it is often created by a layer of algae together

with dust particles, soot, fungi fibres and bacteria. This coating creates a slime on its lower part that contain small stone particles. During frost circles and with changing water to ice stone particles that are covered by algae are crumbled. The crust prevents the stone from "breathing", plugs plasters pores and contributes to the disintegration of the façade surface. Expansivity of such crust in its drying out and damping is different than the expansivity of material. Similar crumbling can be seen when cyanobacterium growth is visible [106].

Biological contamination of stone - its development, minimization and treatment methods are investigated by various authors worldwide, for more information see [107], [108], [109], [110], [111], [112], [113] or [114].

### 5.2.2. The project

In the preparation phase of the Czech Ministry of Culture project DG20P02OVV021 "Stone surface topography and its application in stone element restoration field" a sandstone sample was spectrally analysed in the laboratory to determine its biological contamination. This was a preparation stage before the final project kick-off during summer/autumn 2020, where a previously chosen stone sample will be set and monitored each month over one year to analyse all changes that may occur. Next to other analytical methods hyperspectral imaging (400-1000 nm) and reflectance spectroscopy (1000 - 2500 nm) analysis will be performed during the project duration.

### 5.2.3. Test sample

The test sample was a piece of sandstone that originated from the town of Mšeno [115], the Czech Republic and is mined in Brožova skála quarry. This location has been well known for sandstone quarry since the 14th century, but the biggest peak came in around the year 1920. Nowadays this sandstone is commonly used for restoration works and also for new buildings in the Czech Republic. The test sample (Figure 33) is irregular with an approximate size of 20 x 15cm. One side of the sample is covered by biological material.

*Figure 33 – Sandstone test sample (08/2020).*

### 5.2.4. Equipment

The hyperspectral scanning system is explained in Chapter 4.1. Two 2″ Zenith polymer diffuse reflectance standards [116] with 25% and 99% reflectance were used for calibration purposes. The scanning distance was 80cm and the pixel size was approximately 1,7mm$^2$.

### 5.2.5. Time monitoring test

The goal was to monitor the above-mentioned specimen over time and to analyse possible changes in the surface. It was assumed, that biological contamination would be reduced over time due to the stone drying out.

The test was done in four following days in May 2020 in a laboratory at the Faculty of Civil Engineering, Czech Technical University in Prague. This date has been chosen because fine weather was expected and therefore the drying out was supposed to be reasonably quick due to relatively warm temperatures (around 20°C) and low humidity.

The sandstone sample was placed on a stand in front of the above-mentioned scanning system and was scanned regularly several times every day for four days in a row. These images were then pre-processed in ENVI software and a Normalized Difference Vegetation Index (NDVI) [117] has been calculated. This index has been chosen due to its nature in defining "greenness" of biological material. The chlorophyll absorbs most of the visible light, while the cell structure reflects most of the NIR light, so the more chlorophyll is present in the biological material the higher the NDVI value.

Each outcome was divided into five classes according to the NDVI number (Table 1). These classes were then treated individually and class maps were created (Figure 34 to Figure 41).

*Table 1 – NDVI number interpretation according to [118].*

| NDVI | INTERPRETATION | COLOR |
|---|---|---|
| 0,0 - 0,2 | Bare rock / almost absent density | Red |
| 0,2 - 0,4 | Low density | Green |
| 0,4 - 0,6 | Medium density | Blue |
| 0,6 - 0,8 | Dense density | Yellow |
| 0,8 - 1,0 | Very dense density | Azure |

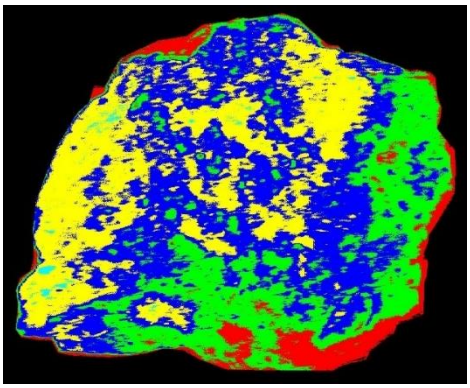

*Figure 34 – 1st-day NDVI map (6.5.2020)*

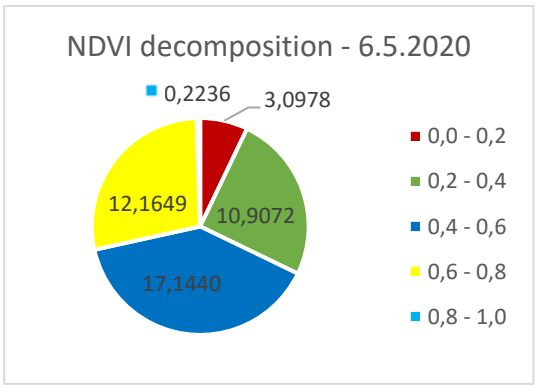


*Figure 35 – 1st-day NDVI decomposition*

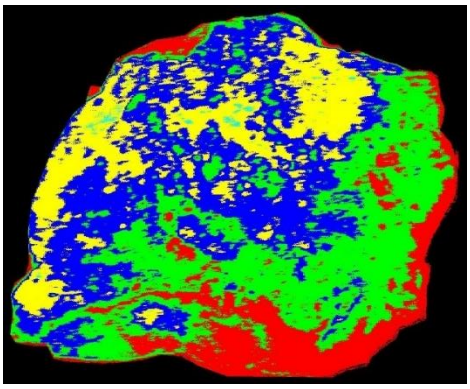

*Figure 36 – 2nd-day NDVI map (7.5.2020)*

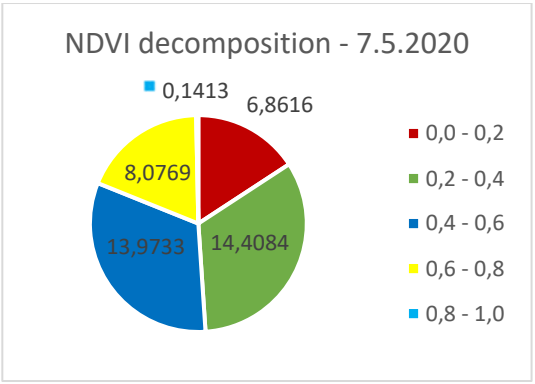


*Figure 37 – 2nd-day NDVI decomposition*

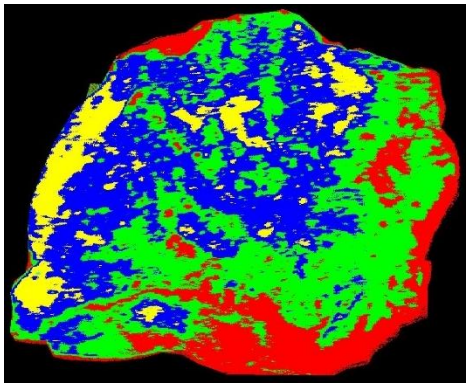

*Figure 38 – 3rd-day NDVI map (8.5.2020)*

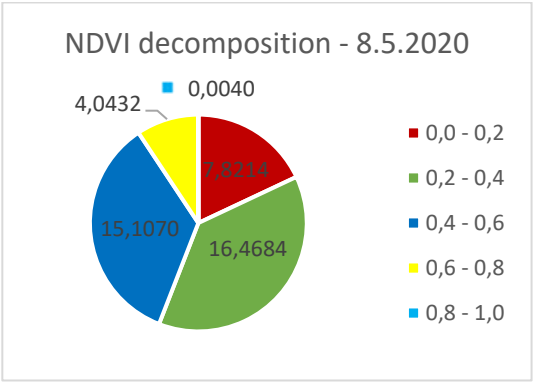


*Figure 39 – 3rd-day NDVI decomposition*

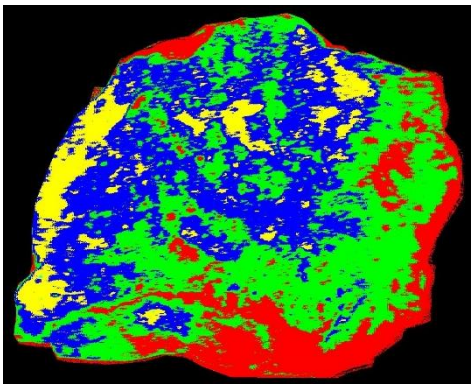

*Figure 40 – 4th-day NDVI map (8.5.2020)*

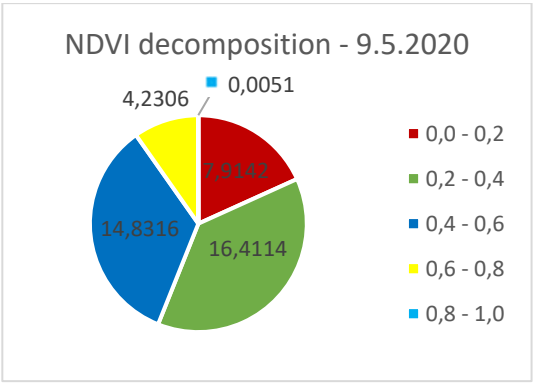


*Figure 41– 4th-day NDVI decomposition*

Results (Figure 42 to Figure 46) show significant changes over time. It can be stated, that the assumption was confirmed. Over time high (0,6 - 1,0) NDVI values decreased and the amount of lower numbers raised. This is due to the stone drying out and the amount of humidity needed by vegetation lowers. This phenomenon will be further investigated during the project mentioned in Chapter 5.2.2 and published in relevant journals.

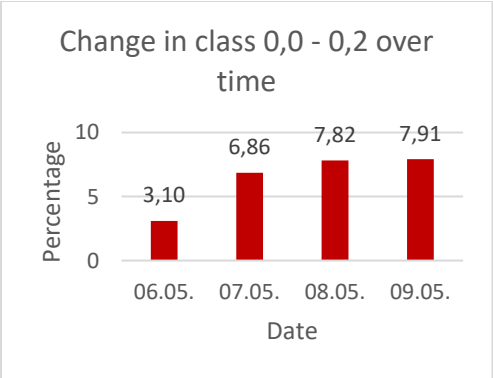


*Figure 42 – Change in class 1 (0,0-0,2) over time*

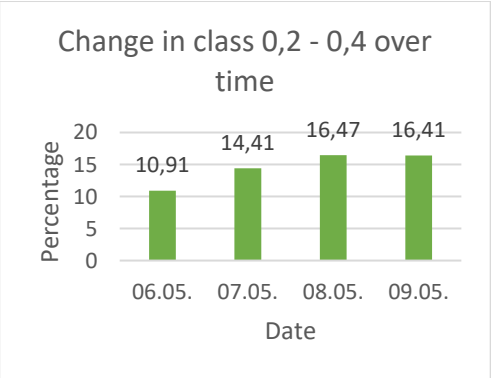


*Figure 43 – Change in class 2 (0,2 - 0,4) over time*

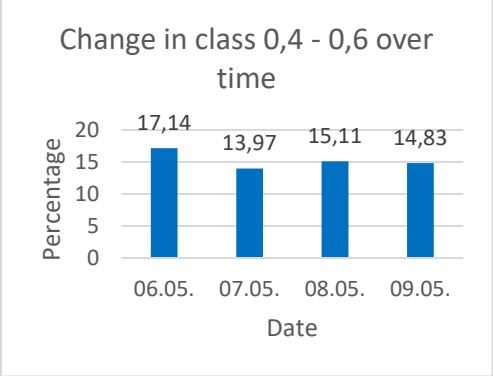


*Figure 44 – Change in class 3 (0,4 - 0,6) over time*

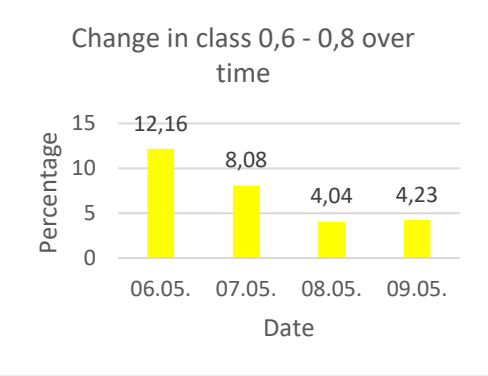


*Figure 45 - Change in class 4 (0,6 - 0,8) over time*

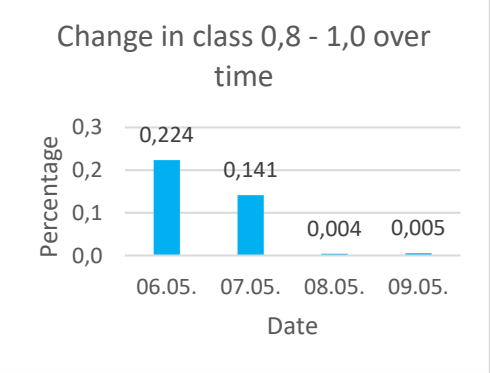


*Figure 46 - Change in class 5 (0,8 - 1,0) over time*

### 5.2.6. Hyperspectral analysis

ENVI processing software was used for the hyperspectral analysis of biologically contaminated sandstone. After pre-processing and endmember extraction a Spectral Angle Mapper was used for classification mapping. A set of 9 classes was derived (Table 2). Final result map is shown in Figure 47 and Figure 48 indicates mean spectra from each class.

*Table 2 – Classes according to derived endmembers and the deputize over the entire image (1.606.400points)*

| Class no. | Class name | Colour | Point sum | Percentage |
|---|---|---|---|---|
| 0 | Unclassified | Black | 4 939 | 0,31% |
| 1 | Vegetation 3 | Light Green | 87 784 | 5,47% |
| 2 | Vegetation 1 | Dark green | 33 384 | 2,08% |
| 3 | Mix1 | Orange Sienna | 138 557 | 8,63% |
| 4 | Rock | Dark Sienna | 51 856 | 3,23% |
| 5 | Mix2 | Dark Yellow | 2 967 | 0,19% |
| 6 | Vegetation 2 | Mid green | 36 403 | 2,27% |
| 7 | Vegetation | Brown Green | 256 397 | 15,96% |
| 8 | Masked pixels | Grey | 994 110 | 61,88% |

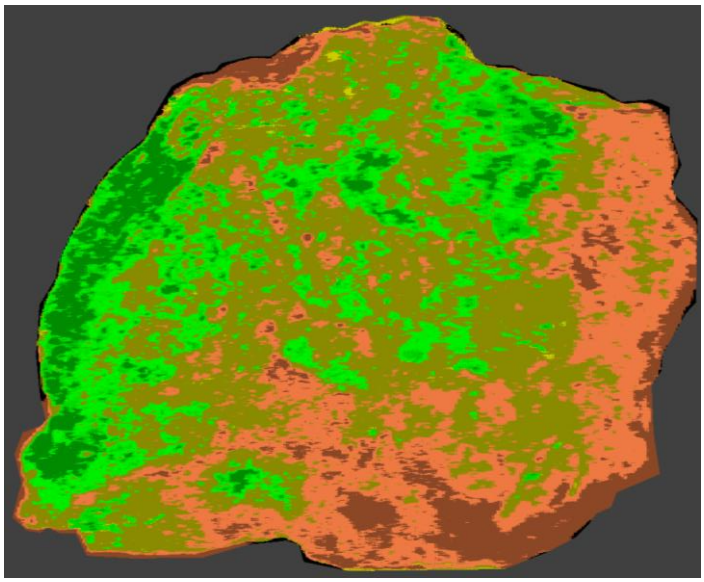

*Figure 47 – Spectral Angle Mapper map using previously defined 7 endmembers. Colours correspond to the caption of Figure 48. Part of non-classified pixels of the image was cut off for better illustrative nature*

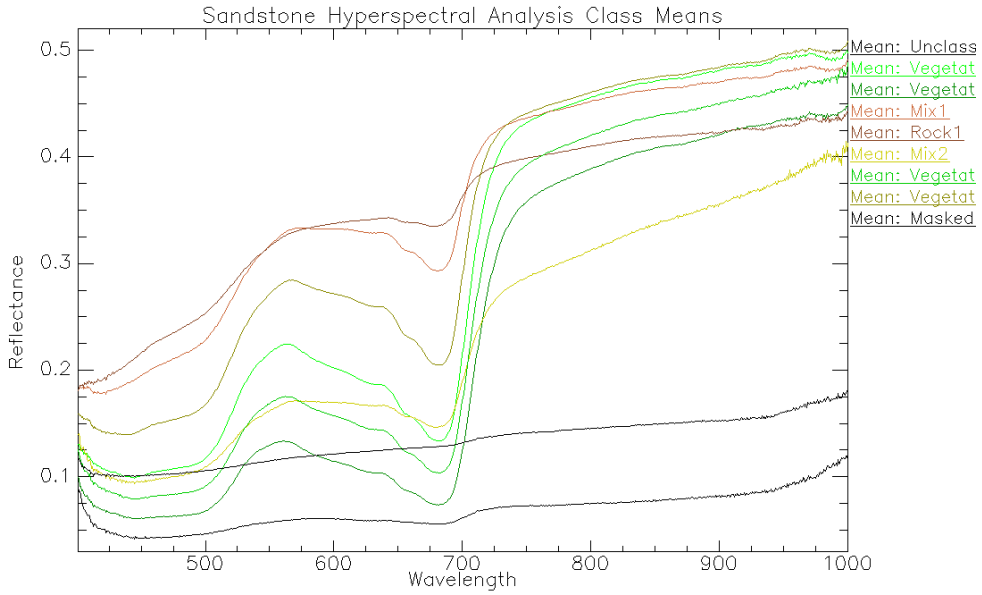


*Figure 48 – Spectral curves mean values of defined endmembers*

### 5.2.7. Biological analysis

To determine endmembers from the performed hyperspectral analysis, the sample was transported to the Czech University of Life Sciences Prague, Faculty of Environmental Sciences, Department of Ecology, where a microbiological analysis was performed by doc. RNDr. Jana Kocourková, CSc. It was found, that the sample contains tens of organic species mainly photosynthetic bacteria (cyanobacteria, blue-green algae), algae - especially fibrous algae (Ulvophyceae) that prefers a highly humid environment and mosses (Bryophytes). Furthermore, isolated fungus (Epicoccum Nigrum) was detected but compared with the sample size one can say that its occurrence is very rare.

Macro photographs were taken with the digital camera Olympus DP74 mounted on Olympus SZX 7 stereomicroscope and stacked using Olympus DeepFocus 3.5 module fitted to Promicra QuickPhoto Camera 3.2 software.

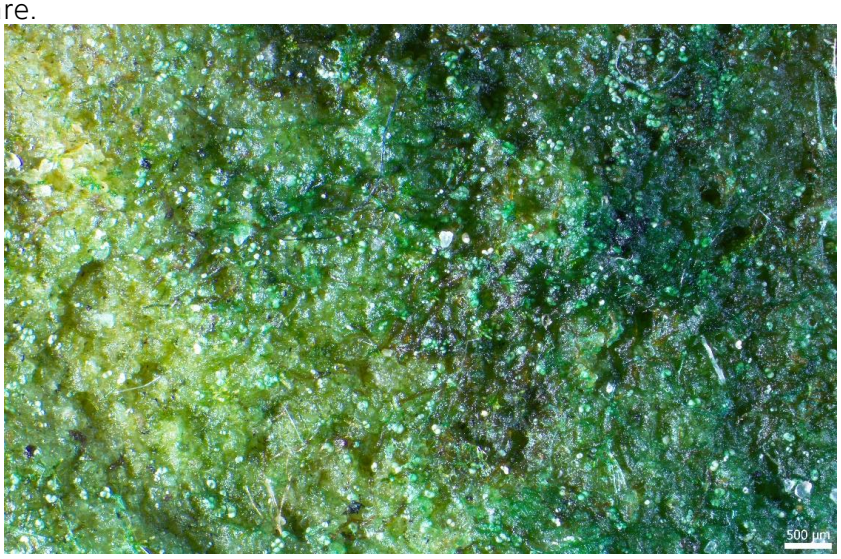


*Figure 49 – Cyanobacteria coating with green algae on the right and bottom of the image; white dots are pollen particles*

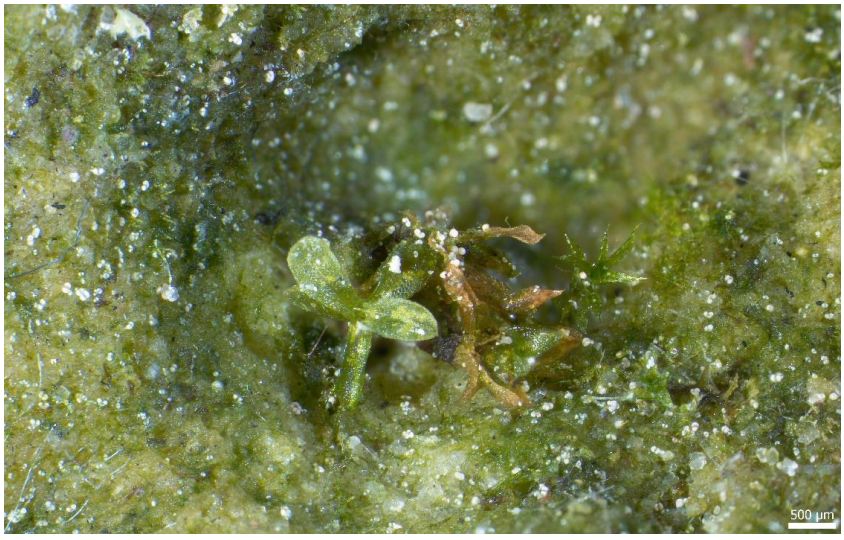


*Figure 50 – Green algae and moss. The green "flower" is a moss, brown object is a dead moss that has lost its chlorophyll; white dots are pollen particles*

### 5.2.8. Conclusion

Biologically contaminated sandstone was analysed using hyperspectral scanning system in 810 bands at wavelength range 400-1000 nm and 6 endmembers have been derived. For endmember determination, a macro microscope analysis was performed. It was found, that due to the nature of the biological material, specific species cannot be precisely ascertained thanks to a resolution issue. One pixel in the hyperspectral scan covers an area of nearly 2 $mm^2$. As seen in Figure 49 and Figure 50 this area is covered by many different species, that mix in various ways and the scanning resolution is not sufficient for species determination. Although several conclusions can be made - one can state, that Class/Endmember 5 is a rock with no vegetation and Class/Endmember 2 (vegetation1) is the darkest and therefore the densest vegetation. Classes 1 and 8 respectively are not considered to be identified on the object of interest since they stand for unclassified and masked pixels. Also, it can be concluded, that class/endmember 4 (Mix1) does have much less vegetation cover than class/endmember 6 (Mix2) since the difference in red/NIR is very small (around 10%). Classes 2,3 and 7 are similar and cover various species.

It can be concluded, that hyperspectral analysis of biologically contaminated stone provides various valuable information although it cannot distinguish individual species. It can give information about biological cover, its change over time and many more. Possibilities of this technique will be further investigated in the NAKI III. Project in the coming years.

# 6. Reflectance spectrometer test measurements

To test possibilities and limits the OceanOptics NIRQuest spectrometer several tests were performed by the author. These tests were also conducted by the necessity to create a methodology that would provide fine and time-independent measurements of various targets. They cover diverse probe to target distances and angles and give an overview of what effect these issues have.

## 6.1. Probe to target distance

It was observed, that measurements are distance-dependent due to illumination change. In this test, five test distances with a step of 2mm were used. The calibration was done using a Spectralon panel measured from a specific distance. After that three rock samples with various grain size and reflectance characteristics (Marble, Sandstone, Brick) were tested. Marble was the smoothest and sandstone was the roughest sample. Figure 51 to Figure 53 show these results.

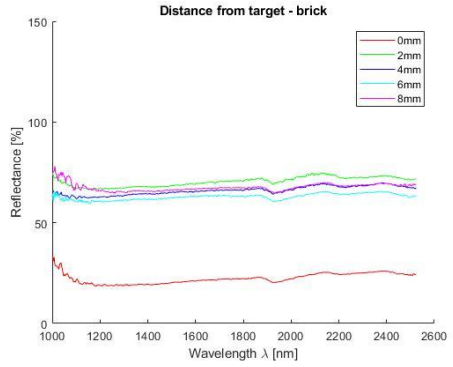


*Figure 51 – Distance from target - brick*

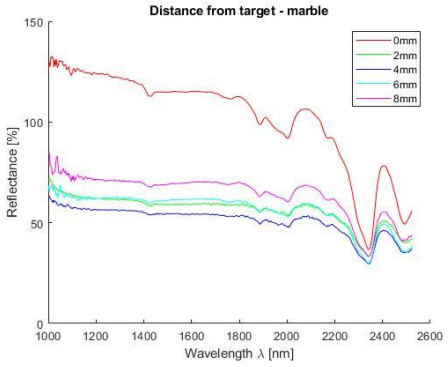


*Figure 52 - Distance from target - marble*

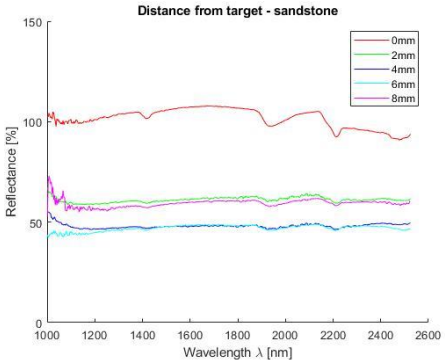


*Figure 53 - Distance from target - sandstone*

It was found, that minimum probe to target distance provides insufficient results while other distances show results with acceptable variance. Spectralon target measured with adequate angle was used for calibration, e.g. it was supposed all measurements to be even. Two samples (marble and sandstone) show the minimum distance results to be much higher while a brick sample shows much lower reflectance than other measurements. Due to this fact, all further measurements were taken from a 5mm distance from the sample and the scanning area is a circle with approximately 1mm (1,108mm) in diameter.

## 6.2. Probe to target angle

Four angles (90°, 75°, 60° and 45°) were tested to derive the influence of the measurements angle to the reflectance. This test was performed on two samples with different grain size – marble and sandstone. To test this effect flat samples were chosen. Results are shown in Figure 54 and Figure 55. Results indicate, that there is not a big difference between 90° and 75° when a sample with a smooth surface (marble) is tested. With bigger grain size the difference rises but it is still lower than 10%. When scanned using a substantially larger angle (<60°) the signal lowers distinctively and measurements are insufficient. Based on these measurements it was assumed, that it is important to measure perpendicular to the target. This can be intricate for rough surfaces, but it was tested, that a small shift does not significantly affect measurements and the variance is smaller than the measurement variance (Table 3).

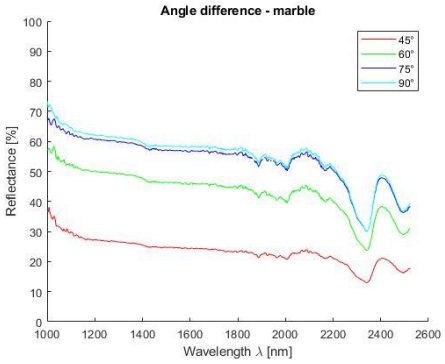


Figure 54 - Angle difference - marble

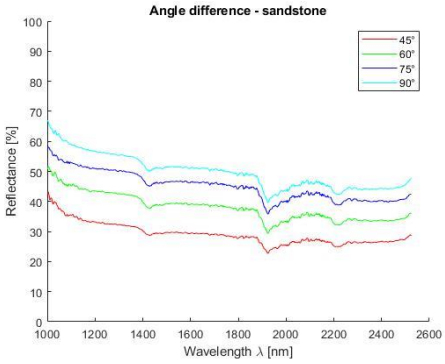


Figure 55 - Angle difference - sandstone

## 6.3. Target grain size

When analysing rock and construction material samples a variance in grain size is likely to occur and affects the reflectance values. It was observed that the bigger the grain size the bigger the reflectance variance. This can be seen by a naked eye e.g. marble vs. sandstone (Figure 56 vs. Figure 57) and it becomes more visible when a microscope is used, (Figure 58 and Figure 59). In this analysis a DinoLite AM4113ZT microscope is applied, this device is equipped with a polarization filter and a resolution of 1,3Mpix with focus on 10-70 and 200 magnification. Samples with similar composition can vary in grain size (for sandstone Chapter 9.1, 9.2 and 9.3).

Figure 56 – Mšeno sandstone sample

Figure 57 – Marble sample

Figure 58 – Mšeno sandstone sample, DinoLite microscope image, Magnification 200

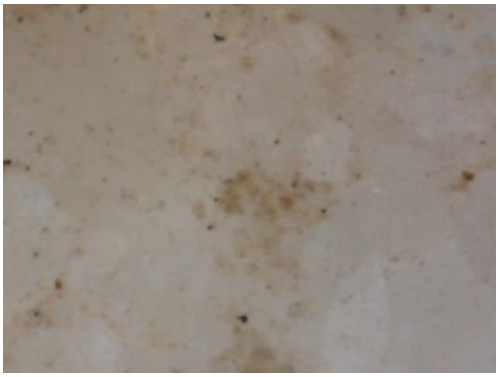

Figure 59 – Marble sample, DinoLite microscope image, Magnification 200

To demonstrate the sample shape and grain size the photogrammetric IMBR (Imaged Based Modelling and Rendering) method was used to create a 3D model of Mšeno sandstone. The model was computed from 20 images using Agisoft MetaShape software. The result was assembled from approximately 4000 triangles, but for accuracy improvement, lateral sections were cut off due to lens distortion and low precision caused by insufficient image overlapping. The final model consists of 2704 triangles representing the middle part of the model with the best achieved accuracy (Figure 60 to Figure 63).

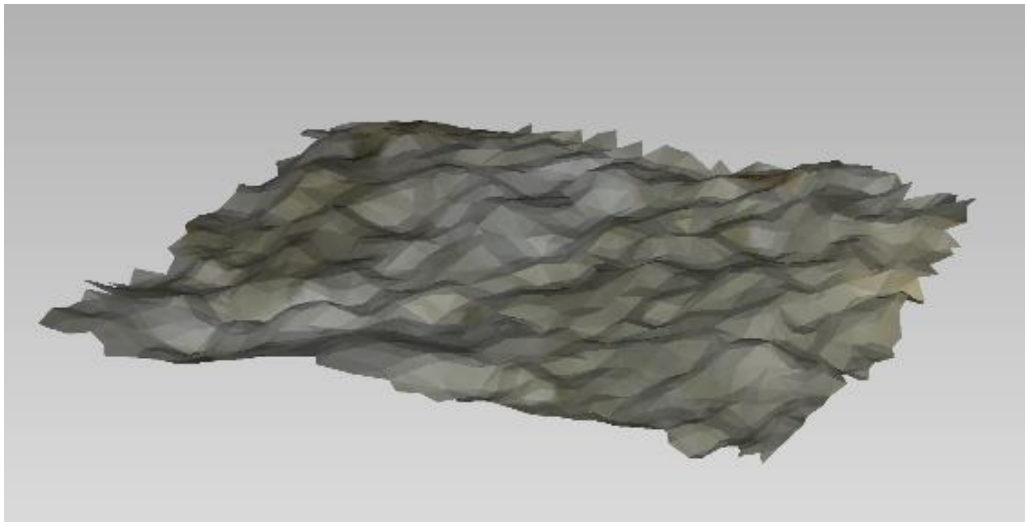

*Figure 60 - Mšeno sandstone 3D model*

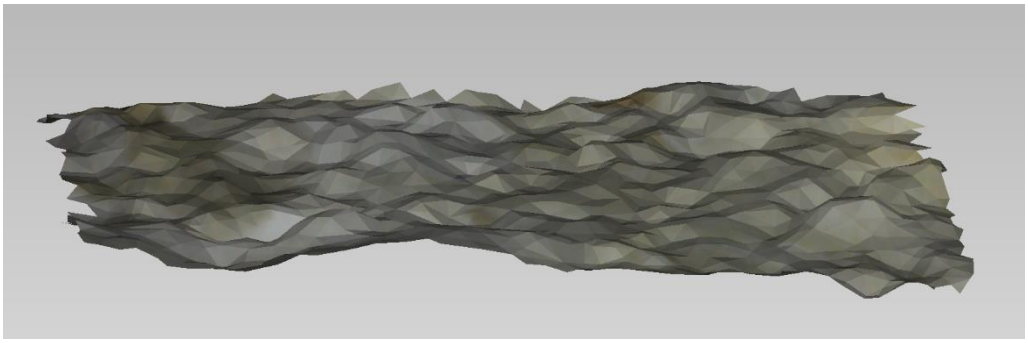

*Figure 61 – Mšeno sandstone 3D model*

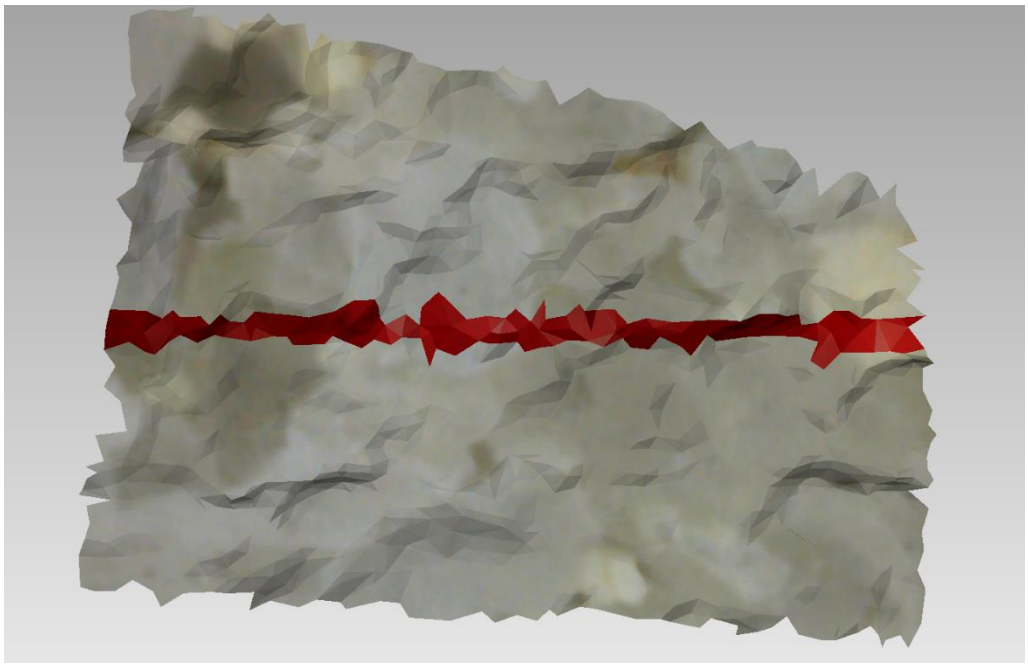

*Figure 62 – Mšeno sandstone 3D model with the highlighted cross-section*

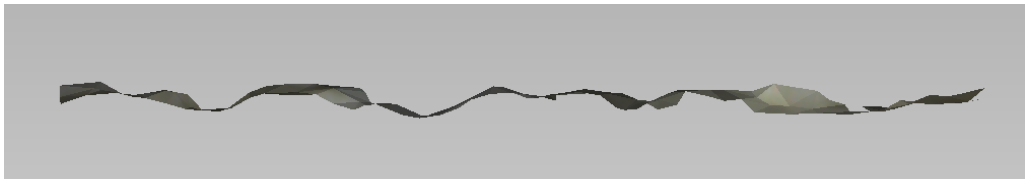

*Figure 63 – a cross-section of Mšeno sandstone 3D model*

Final spectroscopy comparison of both surfaces can be seen below. Based on mentioned tests an assumption can be made - the bigger the grain size the bigger result variance. This is due to the signal scattering and backscattering and it cannot be eliminated thanks to the nature of the individual material.

## Sandstone

Minimum standard deviation: 3.06% (for λ = 1145.286nm)
Maximum standard deviation: 3.95% (for λ = 1001.238nm)
Mean standard deviation: 3.27%

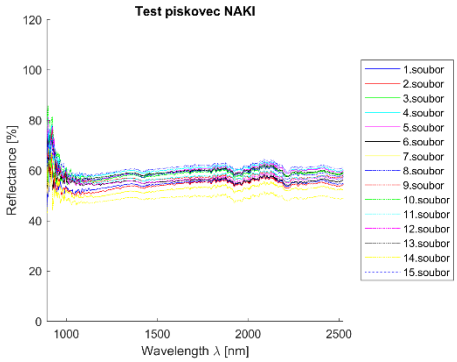


*Figure 64 - Sandstone - all measurements plot*

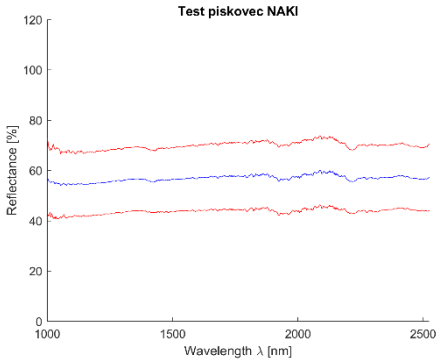


*Figure 65 – Sandstone - mean value (blue) and 2,5*standard deviation (red)*

Marble

Minimum standard deviation: 1.14% (for λ = 1435.611nm)
Maximum standard deviation: 2.88% (for λ = 1014.341nm)
Mean standard deviation: 1.62%

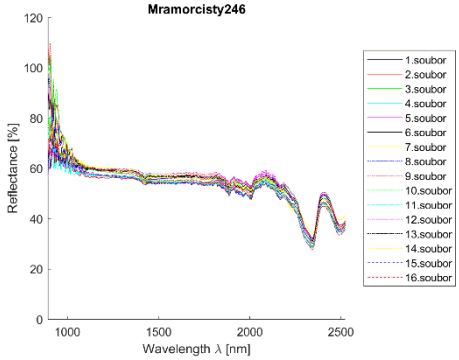


*Figure 66 – Marble - all measurements plot*

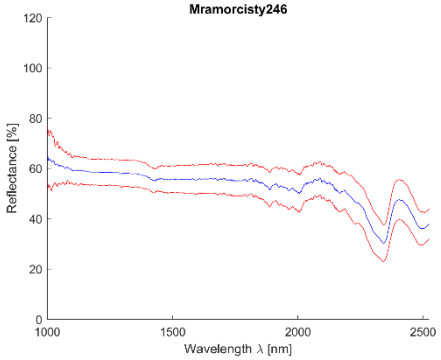


*Figure 67 - Marble - mean value (blue) and 2,5*standard deviation (red)*

# 7. Plaster and façade materials

Façade is an external wall of the building and its final treatment that protects the building from weather conditions. It is very important for building lifecycle if it is harmed it can cause significant damage to the building. To secure building walls plasters are commonly used. Plaster is a covering layer that is applied to a building inside and outside walls [119]. It creates an even smooth surface and distinguishes bumpiness of masonry. During history, plaster materials developed rapidly and the diversification is distinguishable worldwide. Due to its everyday use, it is usually composed of materials that are ordinary in a given location and their composition is analysed by various research teams, e.g. [120]. Due to its composition nature, one can divide these materials into two types – lime-based (Europe) and gypsum-based (Middle east).

## 7.1. Overview

The basic composition of plasters and mortars is very similar and these products are called mortar mixtures in general. Basic components of mortar mixtures are:

- Fillers
- Binders
- Water

Mortar mixtures contains thermally processed bindings that perform mushy and progressively hardening substance in mixture with fillers and water. Depending on compositions and additives they have different strength and plasticity

Plasters can be divided as follows:

- Brick
- Plaster
- Stucco

Classic bindings can be divided as follows:

- Air – lime, lime hydrate, gypsum
- Hydraulic – hydraulic lime, roman cement (hydraulic binding has the stability to moisture and water compared to air bindings). Natural hydraulic bindings are relatively rare (NHL). There are four bigger deposits (one in Bavaria) and they are the most convenient for historical objects use

Fillings are:

- Siliceous sand (e.g. in Bohemia)
- Sand with a proportion of non-siliceous materials, clays, slates, etc. (e.g. Italy). Clays, in general, are not suitable for mortars since they lower the strength in pressure. Clays are easily soaked and are slippery on layers and therefore plasters can start peeling off.
- Clay/Crushed brick, ash (increasing hydraulicity, strength in pressure)

## 7.2. Lime based

The most important ingredient of European plasters and mortars is a lime (calcium oxide).

The oldest findings show the use of lime in a binder (mortar) in Neolithic. The history of lime use is very old - it was used as a plaster with sand binder around an area of today's Jordan as early as 7500BC. Mortar with lime was used to connect stones in the Great Wall of China, a lime mortar was the fundamental binder of European civilizations [121] and various ingredients were added [122]. Romans made use of a volcanic product, ash, so-called "Pozzolan" that created in the mixture with a burnt lime a hydraulic binding called cementum and it was very close to what we know today as the cement which is a burnt mixture of lime with silicate (clay, sand and other additives). This binding type was forgotten after the fall of the Roman empire and it was restored in the 19$^{th}$ century. Meanwhile, lime has been used mainly as a binder in mortars and lime plasters and mortars are frequently used even nowadays. In the area of central Europe / the Czech Republic, lime has been used since the turn of the 10$^{th}$ and 11$^{th}$ century.

So-called "air mortar" is a typical representative of air binders and it is one of the lengthily used binders since the prehistoric times. When burned a burned lime (unslaked) is emerged that consists mainly of calcium oxide (CaO) created by lime ($CaCO_3$) decarbonization (calcination). Lime pieces are burned using appropriate propellant – frequently brown coal, coke, black coal (anthracite) or natural gas. Wood was also used in previous times and that is why an admixture of carbon (timber coal) can be found in older mortars. Lime (calcium oxide – CaO) contains various portions of magnesium oxide (MgO). It is made by burning clean or dolomite limes below sintering limit (1000 – 1250°C), [123].

$$CaCO_3 \rightarrow CaO + CO_2$$

By adding heat, a lime is decomposed and a carbon dioxide is created. This process is reversible – (see carbonization in further text).

Lime is slated for further employment. It is mixed with water at high temperatures (wet slaking). Calcium hydrate is also produced in lime works factories and is sold as "calcium hydrate".

$$CaO + H_2O \rightarrow Ca(OH)_2$$

Calcium hydrate with additives (e.g. sand) is mixed with water and the outcome is a mortar, that hardens slowly with the influence of air CO2 and water (carbonization).

$$Ca(OH)_2 + CO_2 + n\,H_2O \rightarrow CaCO_3 + (n-1)\,H_2O$$

Lime from various lime works factories has different quality and characteristics. They depend on the quality and abundance of limestone. It is common in practice that lime from one lime work factory is good for plastering with specific proportions and when taken the same proportions and used lime for a different factory the plaster cracks and peels after a short time. That is why other components like cement are added to the plasters [124].

Plaster and mortar composition are typical for specific time and area and additional information can then be derived from their analysis like location and time frame.

## 7.3. Hydraulic lime

Hydraulic lime is a binding prepared either by burning limestones, dolomitic limestones or carbonic marls and marlstones (rocks with natural hydraulic constituent composition) under the sintering limit (max 1250°C) or by the joint grind of hydraulic lime with convenient additives containing hydraulic oxides (artificial hydraulic lime).

Hydraulic lime must contain a minimum of 10% of hydraulic components ($SiO_2$, $Al_2O_3$, $Fe_2O_3$). According to their content hydraulic limes can be divided to:

- slightly hydraulic with 10-15% hydraulites and with minimum strength after 28 days 1,5MPa
- strongly hydraulic containing more than 15% hydraulites and minimum strength 4MPa after 28 days.

Hydraulic limes were particularly used for plasters and mortars production in foretime. From characteristics point of view, they combine attributes of air lime and cement. When compared to lime plasters they provide higher resistance to weather impacts and therefore higher lifetime period. When compared to types of cement they maintain the basic performance of cement – plasticity. There are no factories that produce hydraulic limes in the Czech Republic these days. This fact creates inconveniences in historic preservation since lime bindings used in the past always had smaller or bigger hydraulic ingredient content. Hydraulic lime for historical buildings reconstructions had to be imported from abroad.

## 7.4. Gypsum

Gypsum is produced similarly as lime by burning limestone or from energogypsum, that is created by desulphurization of combustion

products using limestone (gypsum is then actually waste of lime production).

Gypsum mineral is burned at low temperatures around 300°C by annealing or technically by thermal decomposition at temperatures 130 - 150 °C. A chemical appellation of gypsum is dihydrate of calcium sulphate (CaSO4 * 2H2O). Water is released during the thermal decomposition and a hemihydrate of calcium sulphate is created, [125].

$$CaSO_4 * 2\ H_2O \rightarrow CaSO_4 * 1/2\ H_2O + 11/2\ H_2O$$

Plaster hydration retrospectively leads to crystallization to gypsum.

$$CaSO_4 * 1/2\ H_2O + 11/2\ H_2O \rightarrow CaSO_4 * 2\ H_2O$$

# 8. Spectral Library creation

To determine historical plasters and mortars used in Central Europe a material spectral library was created. The materials were chosen concerning the area and materials used. The selection was done by doc. Ing. Zuzana Slížková, PhD from the Institute of Theoretical and Applied Mechanics of the Czech Academy of Sciences, Department of Material Research [126]. The author would like to thank Mrs Slížková for all samples and their selection.

## 8.1. Available spectral libraries

Three freely available spectral libraries provide information about building materials. These libraries are very powerful, but none of them is allocated to Central Europe, the Czech Republic, respectively. These libraries were tested and similar samples were compared. Although it was found that they are not suitable for the location of interest since common local materials are always used for mortar and plaster manufacturing.

### 8.1.1. Karlsruhe Library of Urban Materials

Karlsruhe Library of Urban Materials (KLUM), which was created in 2019, is an urban VNIR and SWIR spectral library consisting of building materials. It was created by Rebecca Ilehang and her team from the Institute of Photogrammetry and Remote Sensing (IPF), Karlsruhe Institute of Technology (KIT), Germany and it is freely available online via GitHub [127]. It is primarily intended to be used for processing data obtained by Unmanned Aerial Vehicles (UAV). The library is divided into 12 clustered classes (Asphalt, Brick, Mortar, Ceramic, Concrete, Granite, Limestone, Metal, Plaster, Sandstone, Conglomerate, Wood) and many subclasses. Samples are well defined with pictures and data were acquired using an ASD FieldSpec-4 with 350-2500nm spectral range, more information about data collection and the library itself can be found in the related paper. Due to the spectra being acquired in situ, the first processing step deals with the water vapour absorption. The spectral ranges of 1340–1450 nm, 1780–1970 nm, and 2300–2500 nm are therefore removed [128].

### 8.1.2. London Urban Micromet data Archive - the Spectral Library of impervious Urban Materials

London Urban Micromet data Archive - the Spectral Library of impervious Urban Materials (LUMA-SLUM) was created and published in 2014 by a scientist from the United Kingdom (Kotthaus et al, [76]). It provides information in a wide spectral range from VIS-SWIR (350 – 2500nm) and LWIR (8000 – 14000nm) with two different devices - HR-1024 field spectroradiometer (SVC, Spectra Vista Corporation, Poughkeepsie, NY, USA) for VIS-SWIR range and long-wave target radiance was measured with an M2000 Fourier Transform InfraRed spectrometer (FTIR, MIDAC, Westfield, MA, USA), across a spectral range of 2000 –15400 nm. This library is intended for remote sensing applications and covers 10 classes (Quartzite, Stone, Granite, Asphalt, Concrete/Cement, Brick, Roofing shingle, Roofing tiles, Metal and PVC) with several subclasses like Sandstone or Limestone that will be further analysed (Chapter 8.1.4). Only 1000 – 2500nm spectral range was used. The dataset download is available free of charge online [129].

### 8.1.3. ASTER ECOSTRESS Spectral Library

Version 1.0 of the ECOSTRESS spectral library was released on February 2, 2018 [130]. This release added over 1100 new vegetation and non-photosynthetic vegetation spectra. The ECOSTRESS spectral library is a compilation of over 3400 spectra of natural and man-made materials. These libraries were developed as a part of the ASTER and ECOSTRESS projects. The ECOSTRESS spectral library includes data from three other spectral libraries - Johns Hopkins University (JHU), Jet Propulsion Laboratory (JPL) and United States Geological Survey (USGS - Reston). It is available online free of charge after a request via https://speclib.jpl.nasa.gov/.

For the purpose of this thesis, an ASTER-perkin dataset in the 1000 – 2500nm was used. The data were gained using a Perkin-Elmer Lambda 900 UV/VIS/NIR spectrophotometer equipped with a gold-coated integrating sphere manufactured by Labsphere [131] and cover an extremely large amount of data (over 2300 spectra in 0,4 – 15,4 μm).

### 8.1.4. Library Comparison

To compare other library results with CTU Material Spectral Library two samples that are present in all three libraries were used, namely: Sandstone(s) and Limestone. The comparison was done using a MATLAB script available in Appendix XV and only 1000 – 2500nm spectral range was used. In Appendix XV all above mentioned libraries are processed.

It was found that none of the freely available spectra libraries provides similar samples, but they can be a valuable source of information in the future.

#### 8.1.4.1. Sandstone

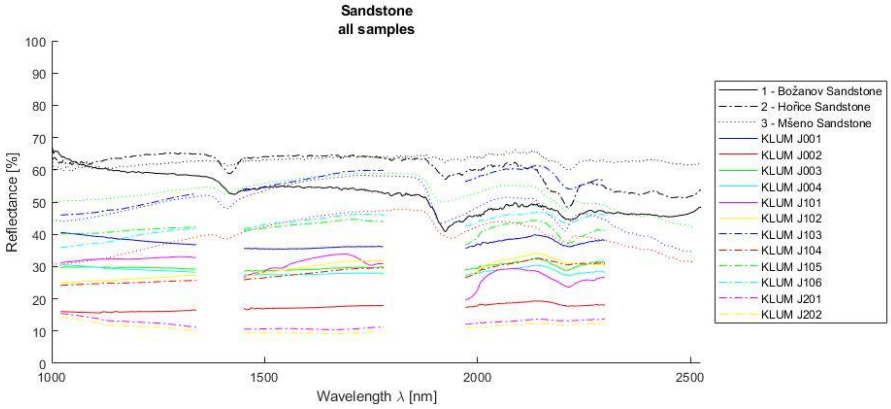


*Figure 68 – Božanov, Hořice and Mšeno sandstones compared to sandstones present in KLUM library. Codes from legend can be resolved using metadata file in [127]*

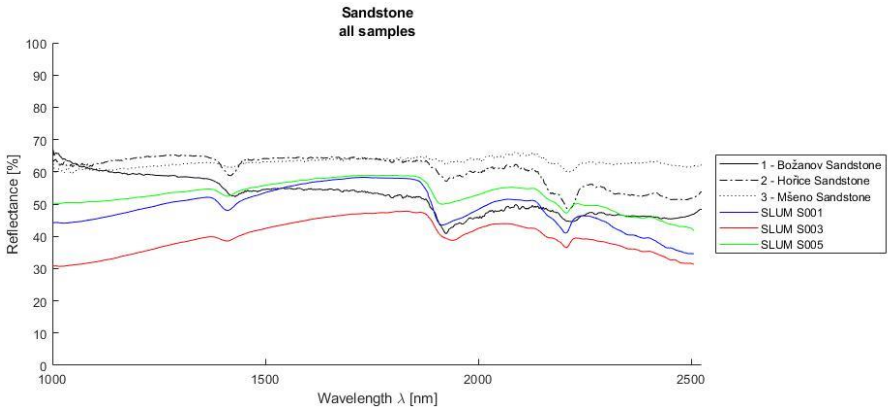


*Figure 69 - Božanov, Hořice and Mšeno sandstones compared to sandstones present in LUMA-SLUM library. Codes from legend can be resolved using metadata file in [129]*

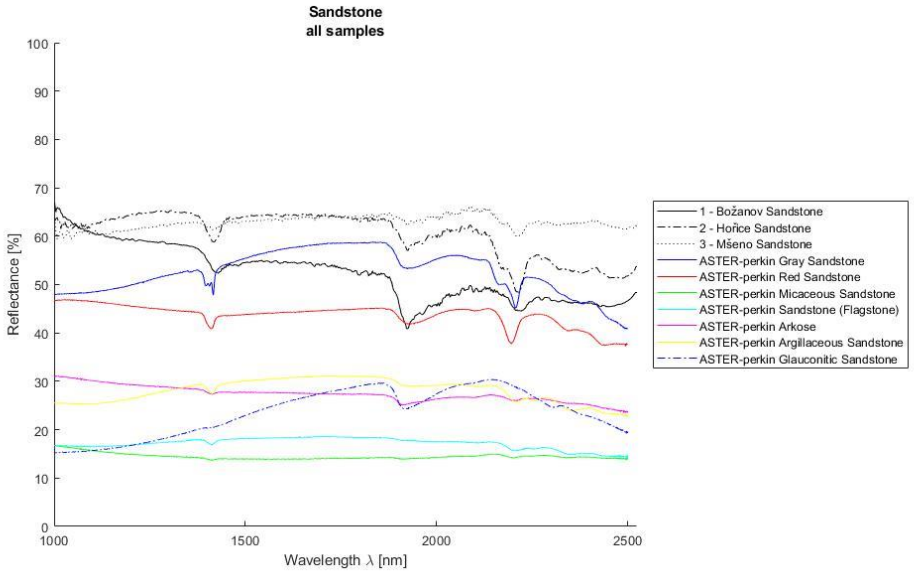


*Figure 70 - Božanov, Hořice and Mšeno sandstones compared to sandstones present in ASTER-perkin library.*

### 8.1.4.2. Limestone

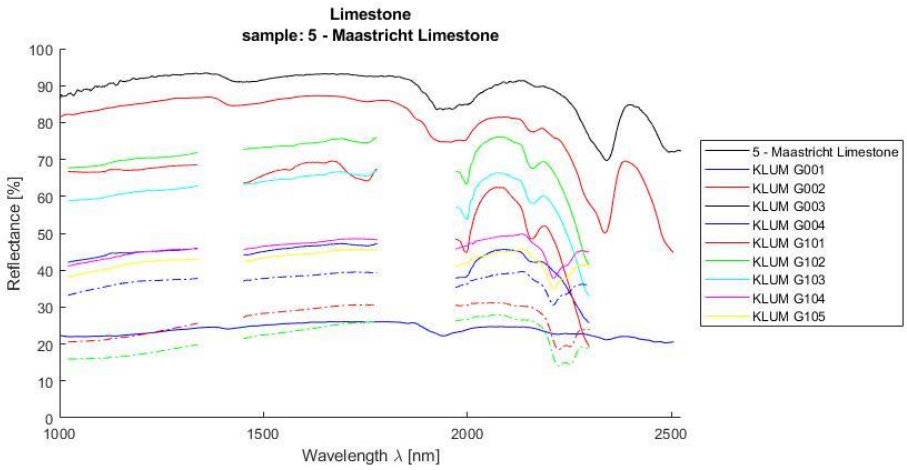


*Figure 71 – Maastricht Limestone compared to limestones present in KLUM library. Codes from legend can be resolved using metadata file in [127]*

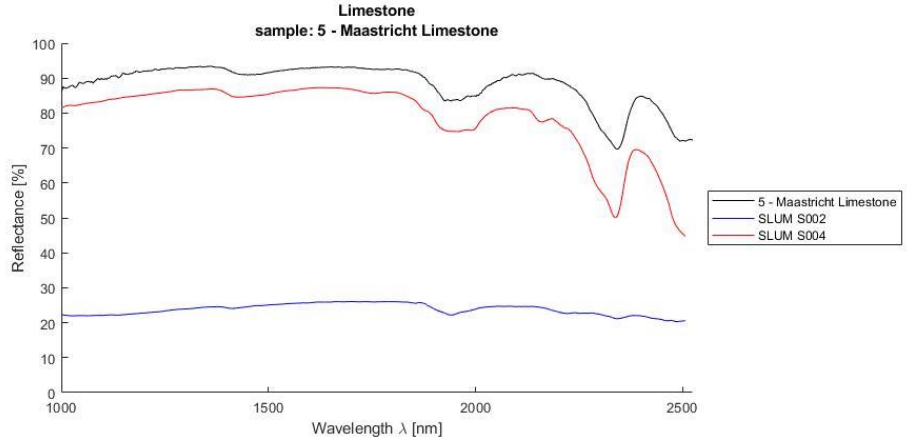


*Figure 72 – Maastricht limestone compared to limestones present in LUMA-SLUM library. Codes from legend can be resolved using metadata file in [129].*

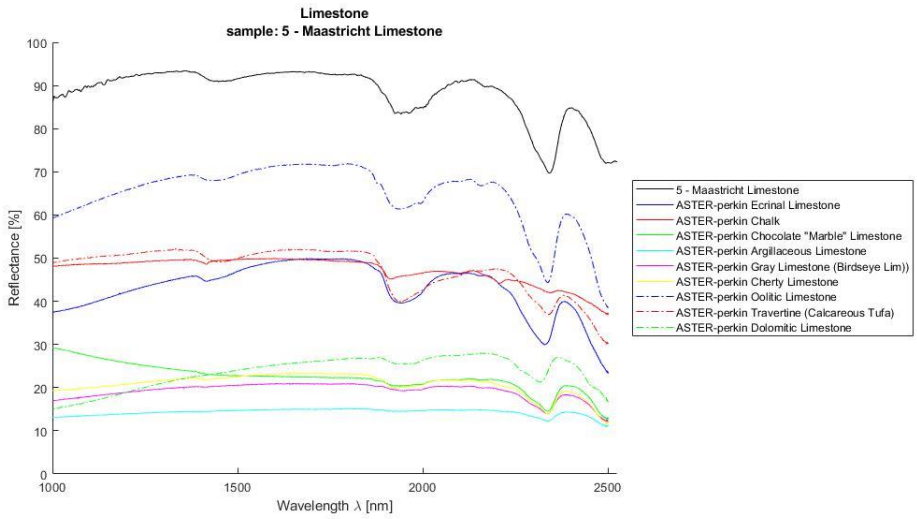


*Figure 73– Maastricht limestone compared to limestones present in ASTER library.*

## 8.2. Material Spectral Library at CTU

In order to analyse material samples from Central Europe, a CTU Material Spectral Library was created. The main goal of this library is to provide spectroscopic information about materials, that were used to produce historical and up to date plasters and mortars. This library is available after a request for all interested individuals[1]. It is included on the attached CD as Appendix XVI as well as all individual material text files.

For the spectral library creation, a CTU reflectance spectroscopy measuring device was used. It is an OceanOptics NIRQuest spectrometer with a reflectance probe, for more information see Chapter 4.2.

The spectral library consists of 20 materials, that are commonly used for plaster and mortar production in the area of Central Europe. This set was created and delivered by the Institute of Theoretical and Applied Mechanics of the Czech Academy of Sciences, Department of Material Research.

### 8.2.1. Library creation procedure

Each sample's final spectral curve was computed from a set of 15 measurements at different points. These measurements were done concerning the material to determine the nature of the sample and to provide overall information regarding its spectral signature. Each point measurement was an average of 10 individual readings.

White (Spectralon 99,9% reflectance) and dark reference calibrations were performed before and after measurement of each material. Measuring and calibration procedures are explained in detail in Chapter 4.2.5.

### 8.2.2. Data quality and processing

Each material data was processed using MATLAB scripts to determine the average spectral curve. It is an arithmetic average from all

[1] Requests should be sent to eva.matouskova@fsv.cvut.cz and will be delivered in a text format.

15 measurements. The data quality is shown using a standard deviation and a 2,5 multiple is used as a quality level determination argument. In the MATLAB script, remote measurements are excluded from calculations, although this was not needed when the library was created since point measurements were chosen very precisely and if a distant measurement occurred it was immediately replaced to provide 15 measurements for average.

Due to high noise in the spectral range 900 -1000nm caused by the device sensitivity (Chapter 4.3) the library provides information in 1000 – 2500nm spectral range.

### 8.2.3. Data verification - Scanning electron microscope (SEM) analysis

A Scanning Electron Microscope (SEM) analysis was used to verify and evaluate spectroscopy results. This is why every material sample was analysed in laboratory and element composition data were obtained. Based on Energy Dispersive Microscopy (EDS) that is a standard procedure for identifying and quantifying composition of sample areas of a micron or less. The characteristic X-rays are produced when a material is bombarded with electrons in an electron beam instrument [132].

Laboratory measurements were conducted by Ing. Jiří Němeček (jiri.nemecek.1@fsv.cvut.cz) and doc. Ing. Jiří Němeček, PhD (jiri.nemecek@fsv.cvut.cz), Department of Mechanics, Faculty of Civil Engineering, Czech Technical University in Prague [133]. A Phenom XL Desktop microscope [134] from the Nanoscience instrument company that is available at the Department of Mechanics, FCE, CTU was used [135].

The procedure steps went as follows:

- From every sample, a small part was cut and analysed.
- Samples were dusted using Au/Pd target (time 30s, plasma stream 10-20mA).
- Samples were deluged using epoxy resin, the possible occurrence of elements *C, Cl, O, H.*
- Energy Dispersive Spectroscopy (EDS) maps were created for non-powder materials (6-13) with sample dependent scale (Map resolution 128x128, pixel time 10ms). The map was not created for powder samples containing large particles due to possible errors in measured spectra and for sample consists of 99% $SiO_2$ and for samples 1-5 and 6 where the epoxy resin causes evident errors.
- On powder samples (16-20) an inaccuracy can occur due to uneven grain surface.

For additional questions regarding this method please see explanation online [136] or an electronic/paper book [137].

Available results:

- *Average Atomic Concentration* – denotes an atomic ratio at a measured point expressed in percentage. It is the quantity, that is directly measured using an electron microscope
- *Average Weight Concentration* –is computed directly from the measured spectra. It is a weight determination towards

the entire mixture weight. This quantity is computed by the microscope operational software.

- *Average Stoichiometry Weight Concentration* – shows an oxide representation ratio of the sample. Stoichiometry than says that conservation of mass law must be in force.

# 9. CTU Material spectral library

CTU Material spectral library was created by the author in 2020 and consists of 20 individual materials. It provides material spectral information as well as their analysis using an electron microscope. This library is freely available after request, more information can be found in Chapter 8.2.

## 9.1. Božanov sandstone

### 9.1.1. Sample information

The Božanov deposit is located in the north-east part of Bohemia, the Czech Republic in Broumov promontory near the Czech - Polish border close to town Božanov and is quarried by the Granit Lipnice company. The stone is lightly grey to red-brown and the grain size varies from small (less than 0,5mm) to large (up to 2mm). Božanov sandstone is harder to shape than other sandstones, but it has very good resistance towards weather conditions [138].

### 9.1.2. Spectroscopy results

The sample was documented using an ordinary mobile phone camera (Figure 74) and a digital DinoLite microscope with magnification 50 (Figure 75) and 200 (Figure 76).

*Figure 74 - Božanov sandstone sample image*

*Figure 75 – Božanov sandstone DinoLite microscope image, magnification 50*

*Figure 76 – Božanov image DinoLite microscope image, magnification 200*

Purchased reflectance spectroscopy data were processed and analysed using a MATLAB script in Appendix XIII available at enclosed CD. Analysis results are mentioned below, Figure 77 and Figure 78 shows spectral graphs of the sample.

| | |
|---|---|
| Minimum standard deviation: | 2.19% (for λ = 1096.202nm) |
| Maximum standard deviation: | 3.46% (for λ = 1004.514nm) |
| Mean standard deviation: | 2.71% |

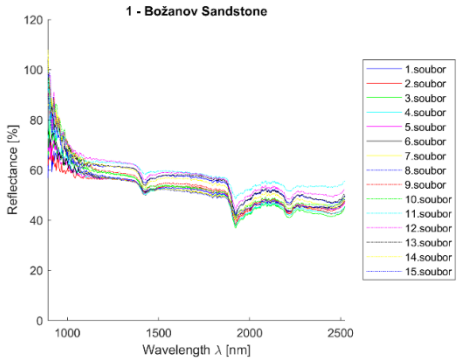


*Figure 77 - Božanov sandstone - all measurements plot*

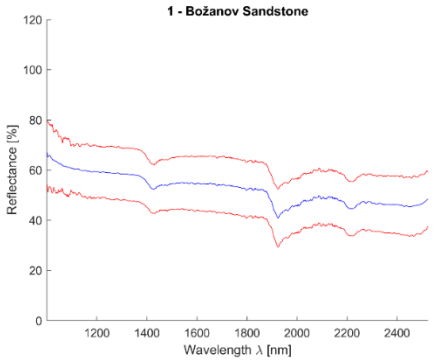


*Figure 78 - Božanov sandstone - mean value (blue) and 2,5*standard deviation (red)*

### 9.1.3. Electronic microscope findings

The sample was deluged using epoxy resin, sanded using SiC papers #2000, #4000 with water, dusted. The sample photos (Figure 79 to Figure 81) shows mainly $SiO_2$ grains – light grey colour, big pores – black colour. Particle size varies from 100 to 500 um. Dark grey colour can be seen in between grains, pores are filled with epoxy resin (chemical elements *C*, *Cl*, *O*). White grains contain *Al, K, Na* apart from *Si*.

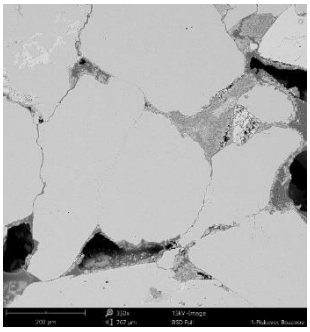

*Figure 79 – Phenom XL Desktop SEM photos - Microscopic image of the sample*

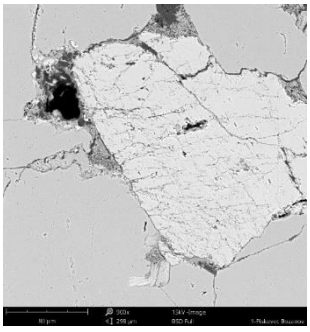

*Figure 80 - Phenom XL Desktop SEM photos - Microscopic image of the sample*

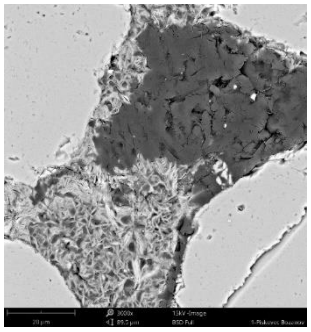

*Figure 81 - Phenom XL Desktop SEM photos - Microscopic image of the sample*

SEM results (average atomic concentration, average weight concentration and average stoichiometry weight concentration) in the form of graphs are shown in Figure 82 to Figure 84.

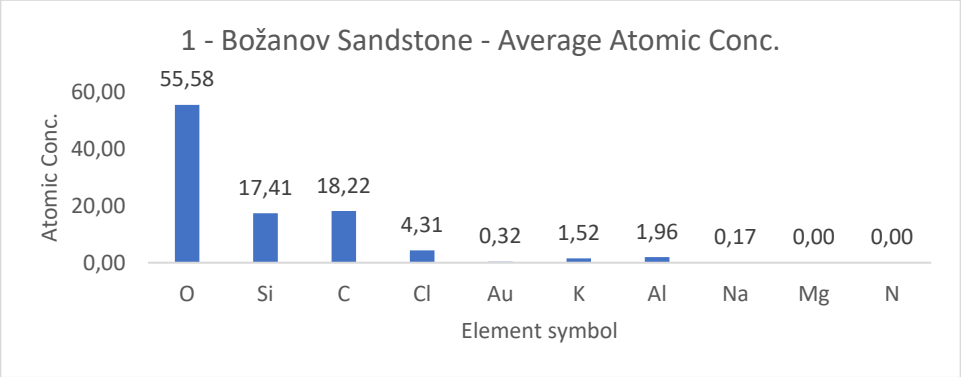


*Figure 82 – Božanov sandstone – average atomic concentration*

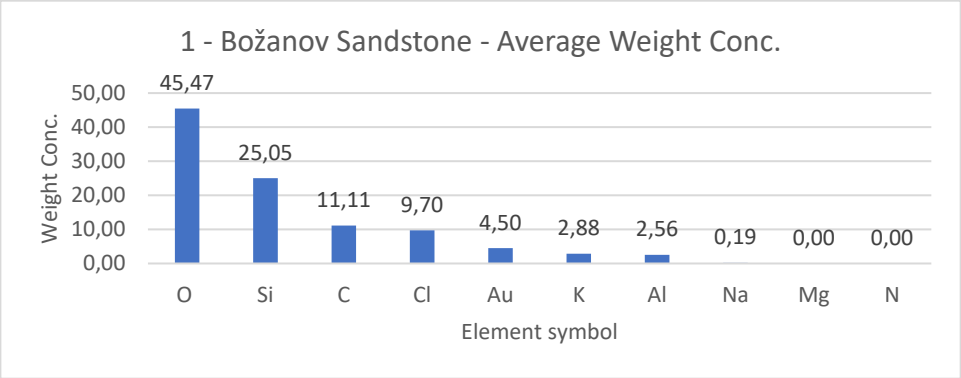


*Figure 83 – Božanov sandstone – average weight concentration*

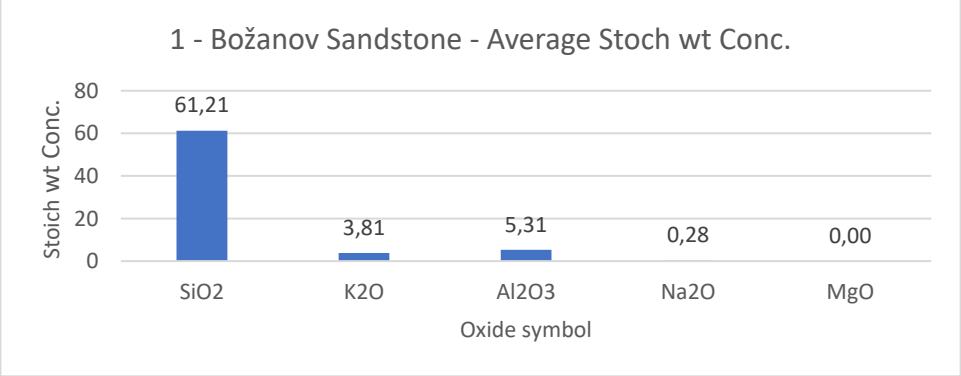


*Figure 84 – Božanov sandstone - Average Stoich wt Conc.*

## 9.2. Hořice sandstone

### 9.2.1. Sample information

Hořice sandstone is quarried on the southern hillside of Hořice ridge close to the town of Podhorní Újezd, the Czech Republic about 100km north-east from Prague and is quarried by a Kámen Ostroměř company. Mining area was created by joining three original quarries and is therefore relatively extensive. Hořice sandstone is small-grained with light ochre base coloured with copious but very delicate ferric pattern [139].

### 9.2.2. Spectroscopy results

The sample was documented using an ordinary mobile phone camera (Figure 85) and a digital DinoLite microscope with magnification 50 (Figure 86) and 200 (Figure 87).

*Figure 85 - Hořice sandstone sample image*

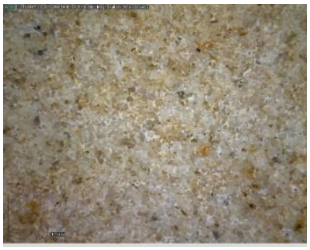

*Figure 86 - Hořice sandstone DinoLite microscope image, magnification 50*

*Figure 87 - Hořice image DinoLite microscope image, magnification 200*

Purchased reflectance spectroscopy data were processed and analysed using a MATLAB script in Appendix XII available at enclosed CD. Analysis results are mentioned below, Figure 88 and Figure 89 shows spectral graphs of the sample.

| | |
|---|---|
| Minimum standard deviation: | 1.32% (for λ = 1816.356nm) |
| Maximum standard deviation: | 2.99% (for λ = 1001.238nm) |
| Mean standard deviation: | 1.69% |

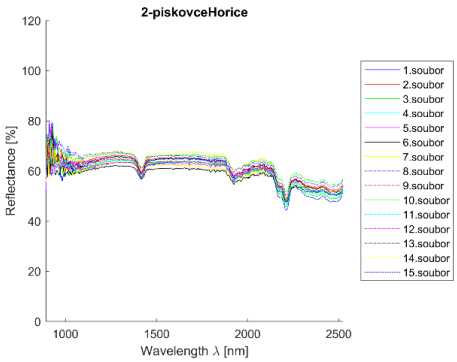


*Figure 88 - Hořice sandstone - all measurements plot*

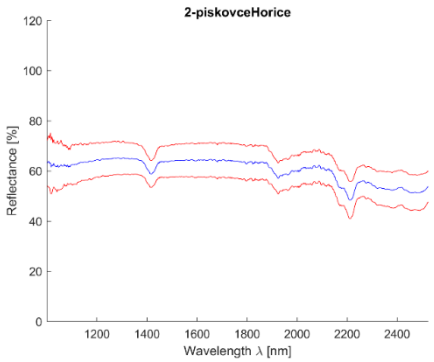


*Figure 89 - Hořice sandstone - mean value (blue) and 2,5*standard deviation (red)*

### 9.2.3. Electronic microscope findings

The sample was deluged using epoxy resin, sanded using SiC papers #2000, #4000 with water, dusted. The sample photos (Figure 90 to Figure 92) shows mainly $SiO_2$ grains – light grey colour, big pores – black colour. Particle size varies from 70 to 300 um. Dark grey colour can be seen in between grains, pores are filled with epoxy resin (chemical elements *C*, *Cl*, *O*). White grains contain *Al, K, Mg* apart from *Si*.

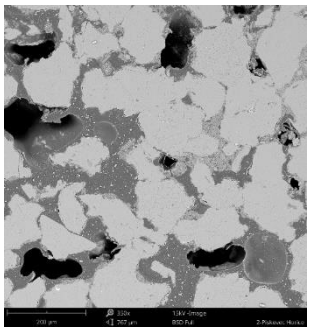

*Figure 90 - Phenom XL Desktop SEM photos - Microscopic image of the sample*

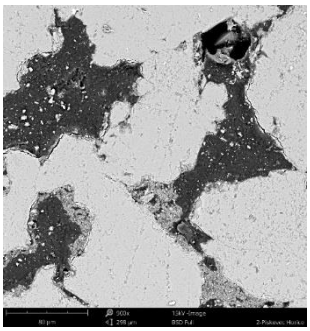

*Figure 91 - Phenom XL Desktop SEM photos - Microscope sample image*

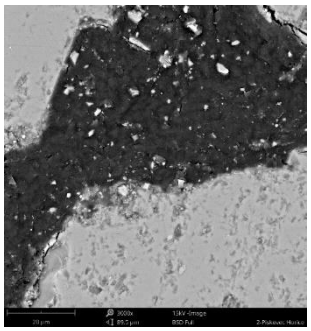

*Figure 92 - Phenom XL Desktop SEM photos - Microscopic image of the sample*

SEM results (average atomic concentration, average weight concentration and average stoichiometry weight concentration) in the form of graphs are shown in Figure 93 to Figure 95.

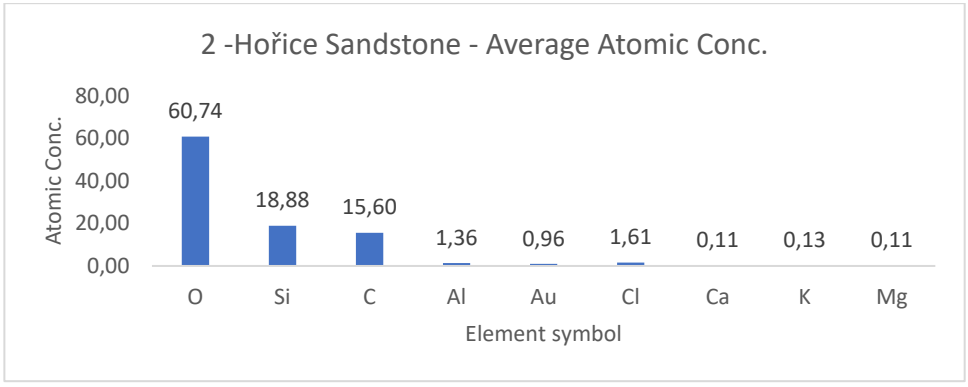


*Figure 93 - Hořice sandstone average atomic concentration*

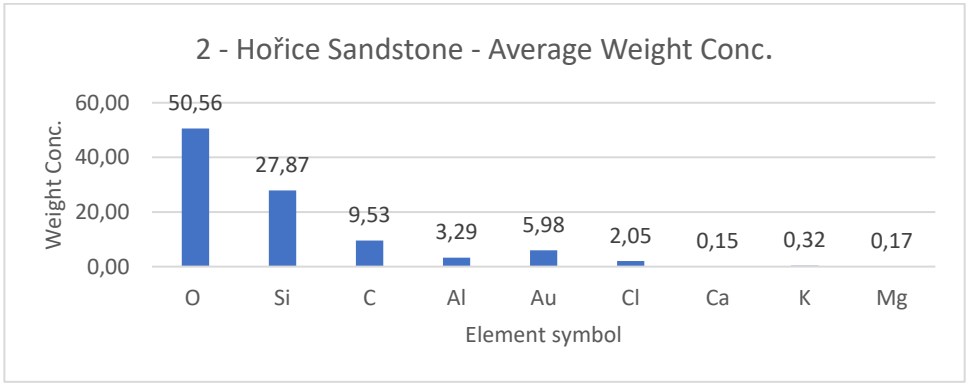


*Figure 94 - Hořice sandstone average weight concentration*

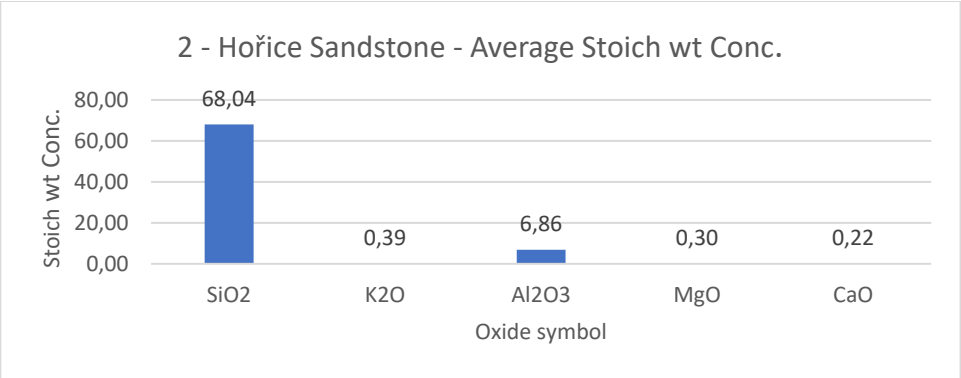


*Figure 95 - Hořice sandstone average Stoich wt conc*

## 9.3. Mšeno sandstone

### 9.3.1. Sample information

The test sample was a piece of sandstone that originated from the town of Mšeno, the Czech Republic and is mined in Brožova skála quarry. This location has been well known for a sandstone quarry since the 14th century, but the biggest boom came around the year 1920. This sandstone is nowadays commonly used for restoration works and also for new buildings in the Czech Republic [115].

### 9.3.2. Spectroscopy results

The sample was documented using an ordinary mobile phone camera (Figure 96) and a digital DinoLite microscope with magnification 50 (Figure 97) and 200 (Figure 98).


*Figure 96 – Mšeno sandstone sample image*

*Figure 97 - Mšeno sandstone DinoLite microscope image, magnification 50*

*Figure 98 - Mšeno sandstone DinoLite microscope image, magnification 200*

Purchased reflectance spectroscopy data were processed and analysed using a MATLAB script in Appendix XIII available at enclosed CD. Analysis results are mentioned below, Figure 99 and Figure 100 shows spectral graphs of the sample.

| | |
|---|---|
| Minimum standard deviation: | 1.33% (for λ = 1816.356nm) |
| Maximum standard deviation: | 3.96% (for λ = 1001.238nm) |
| Mean standard deviation: | 1.54% |

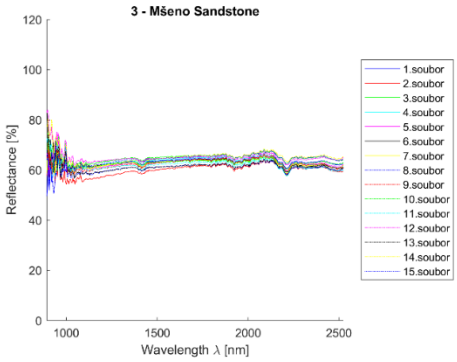


*Figure 99 - Mšeno sandstone - all measurements plot*

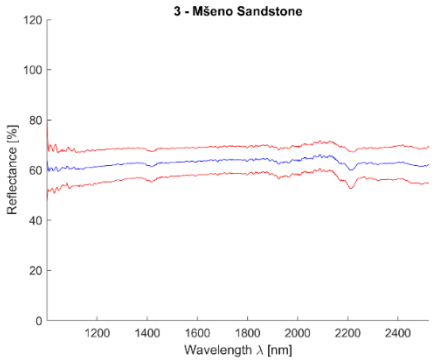


*Figure 100 - Mšeno sandstone - mean value (blue) and 2,5*standard deviation (red)*

### 9.3.3. Electronic microscope findings

The sample was deluged using epoxy resin, sanded using SiC papers #2000, #4000 with water, dusted. The sample photos (Figure 101 to Figure 103) shows mainly $SiO_2$ grains – light grey colour, big pores – black colour. Particle size varies from 100 to 300 um. Dark grey colour can be seen in between grains, pores are filled with epoxy resin (chemical elements *C*, *Cl*, *O*).

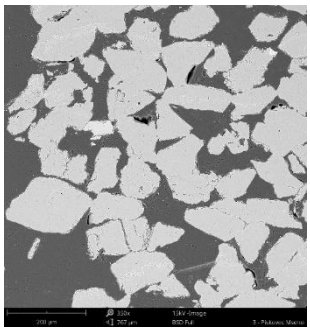

*Figure 101 - Phenom XL Desktop SEM photos - Microscope sample image*

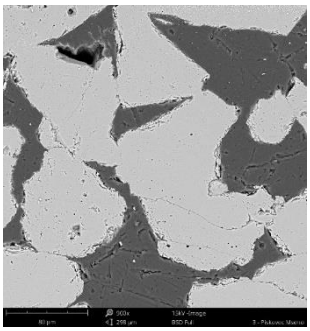

*Figure 102 - Phenom XL Desktop SEM photos - Microscope sample image*

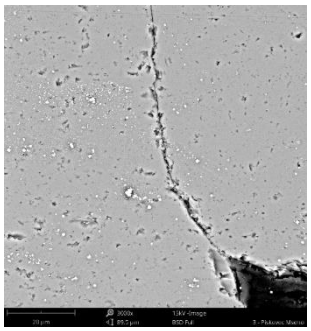

*Figure 103 - Phenom XL Desktop SEM photos - Microscope sample image*

SEM results (average atomic concentration, average weight concentration and average stoichiometry weight concentration) in the form of graphs are shown in Figure 104 to Figure 106.

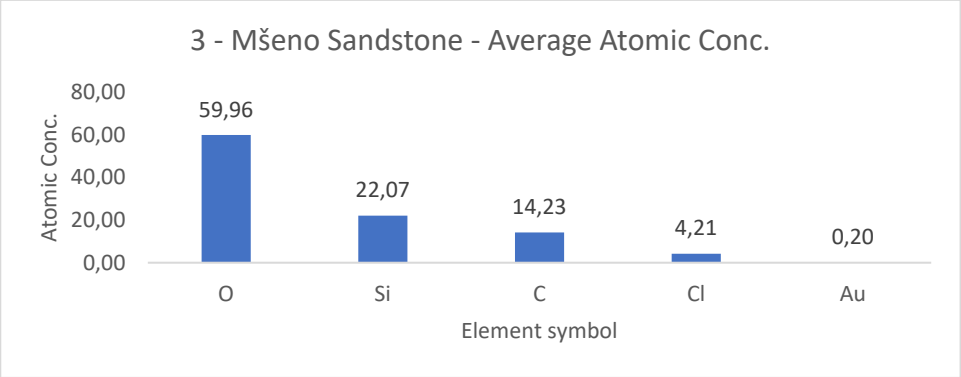


*Figure 104 - Mšeno sandstone average atomic concentration*

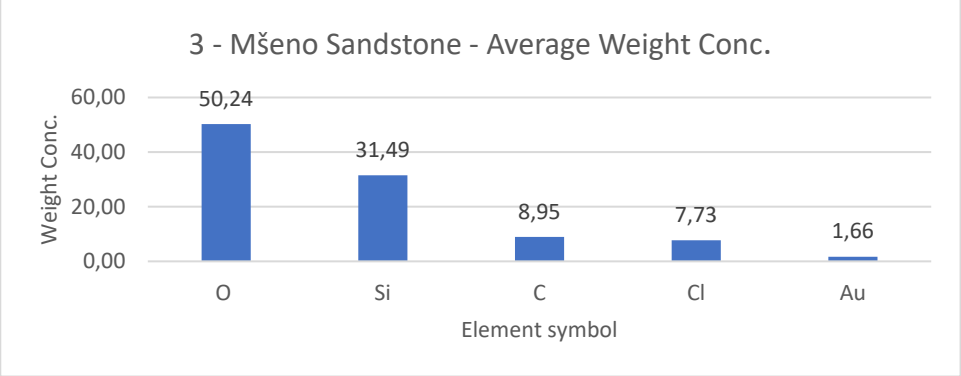


*Figure 105 - Mšeno sandstone average weight concentration*

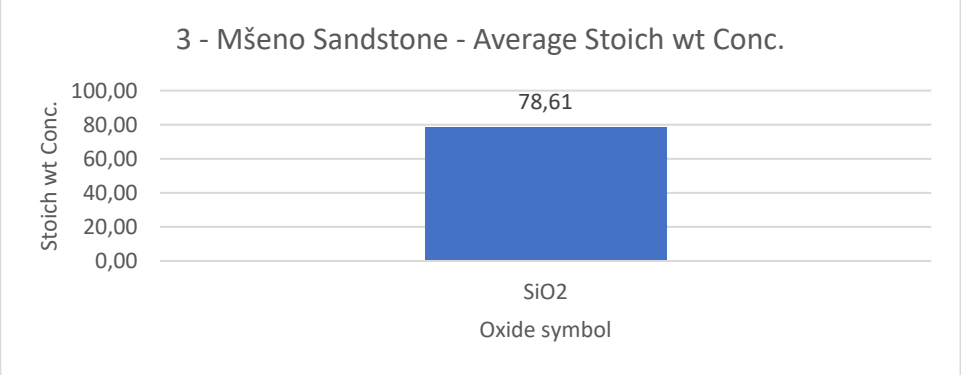


*Figure 106 - Mšeno sandstone average Stoich wt conc*

## 9.4. Quartzite

### 9.4.1. Sample information

Quartzite is a sandstone, that has been converted into a solid quartz rock. Unlike sandstones, quartzites are free from pores and have a smooth fracture [140].

### 9.4.2. Spectroscopy results

The sample was documented using an ordinary mobile phone camera (Figure 107) and a digital DinoLite microscope with magnification 50 (Figure 108) and 200 (Figure 109).

*Figure 107 – Quartzite sample image*

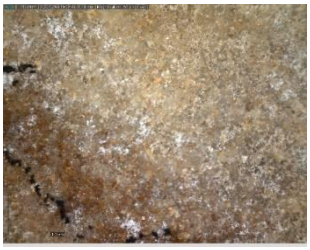

*Figure 108 – Quartzite DinoLite microscope image, magnification 50*

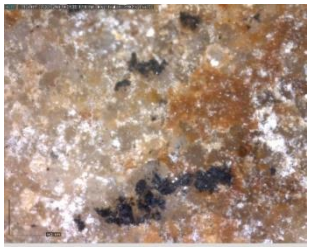

*Figure 109 – Quartzite DinoLite microscope image, magnification 50*

Purchased reflectance spectroscopy data were processed and analysed using a MATLAB script in Appendix XIII available at enclosed CD. Analysis results are mentioned below, Figure 110 and Figure 111 shows spectral graphs of the sample.

| | |
|---|---|
| Minimum standard deviation: | 1.85% (for λ = 1419.355nm) |
| Maximum standard deviation: | 2.82% (for λ = 1030.717nm) |
| Mean standard deviation: | 2.12% |

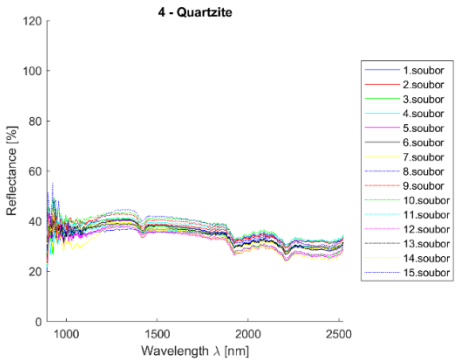


*Figure 110 Quartzite - all measurements plot*

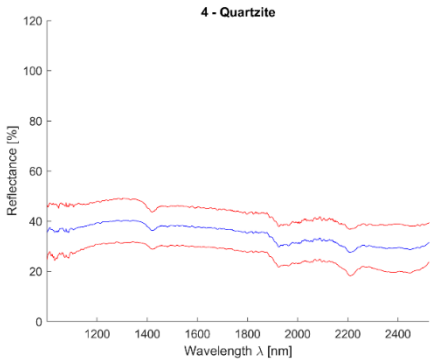


*Figure 111 - Quartzite - mean value (blue) and 2,5*standard deviation (red)*

### 9.4.3. Electronic microscope findings

The sample was deluged using epoxy resin, sanded using SiC papers #2000, #4000 with water, dusted. The sample photos (Figure 112 to Figure 114) shows closely joined $SiO_2$ grains (light grey) and porosity (black). Grain boundaries are visible with grain size varying from 50 to 200um. EDS shows that the sample constitutes from $SiO_2$ and a trace of *C*.

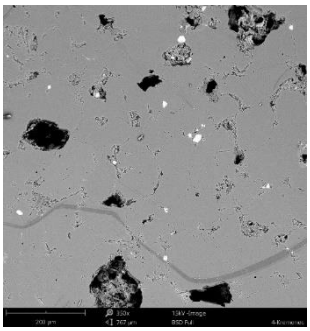

*Figure 112- Phenom XL Desktop SEM photos - Microscopic image of the sample*

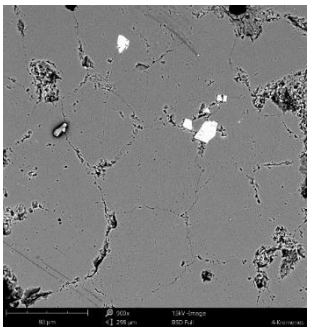

*Figure 113 - Phenom XL Desktop SEM photos - Microscope sample image*

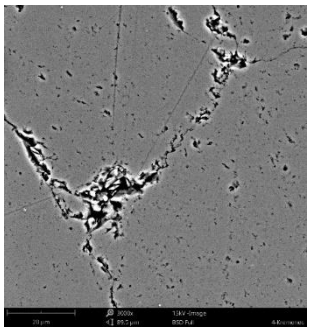

*Figure 114- Phenom XL Desktop SEM photos - Microscopic image of the sample*

SEM results (average atomic concentration, average weight concentration and average stoichiometry weight concentration) in the form of graphs are shown in Figure 115 to Figure 117.

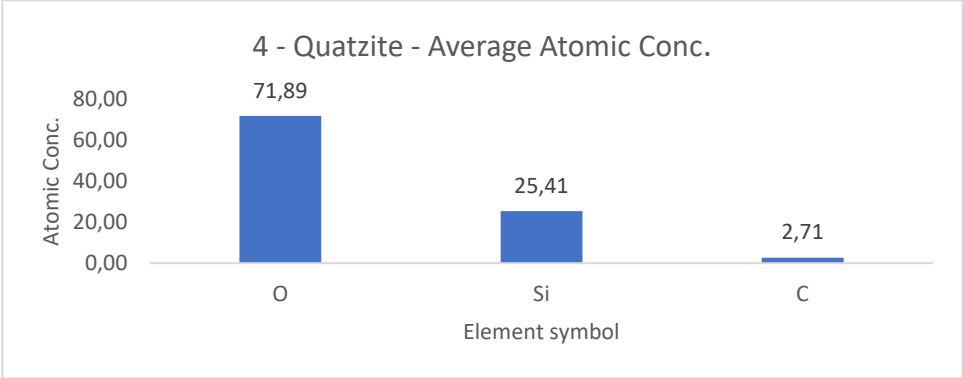


*Figure 115 - Quartzite average atomic concentration*

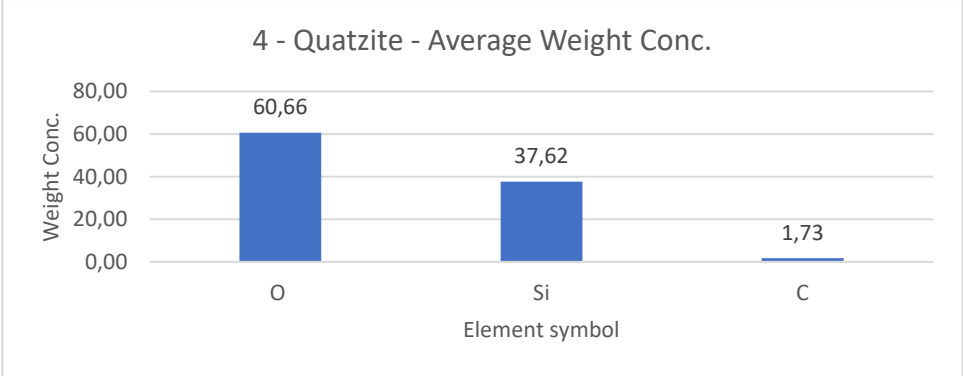


*Figure 116 – Quartzite average weight concentration*

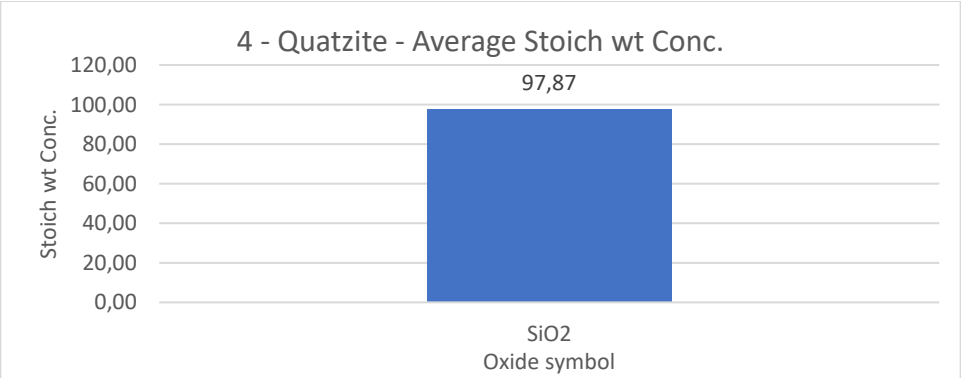


*Figure 117 - Quartzite average Stoich wt conc*

## 9.5. Maastricht limestone

### 9.5.1. Sample information

Limestone is a sedimentary rock composed mainly of calcium carbonate ($CaCO_3$). Maastricht limestone is quarried in the Maastricht formation named after the city of Maastricht that lies in the Netherlands and Belgium with thickness about 45 to 90m [141].

### 9.5.2. Spectroscopy results

The sample was documented using an ordinary mobile phone camera (Figure 118) and a digital DinoLite microscope with magnification 50 (Figure 119) and 200 (Figure 120).

*Figure 118 – Maastricht limestone sample image*

*Figure 119 – Maastricht limestone DinoLite microscope image, magnification 50*

*Figure 120 – Maastricht limestone DinoLite microscope image, magnification 200*

Purchased reflectance spectroscopy data were processed and analysed using a MATLAB script in Appendix XIII available at enclosed CD. Analysis results are mentioned below, Figure 121 and Figure 122 shows spectral graphs of the sample.

| | |
|---|---|
| Minimum standard deviation: | 1.98% (for λ = 1066.739nm) |
| Maximum standard deviation: | 3.60% (for λ = 2344.278nm) |
| Mean standard deviation: | 2.39% |

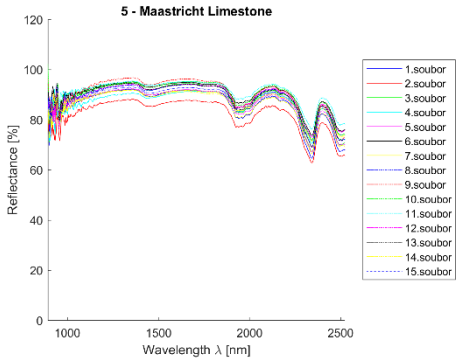


*Figure 121 – Maastricht limestone – all measurements plot*

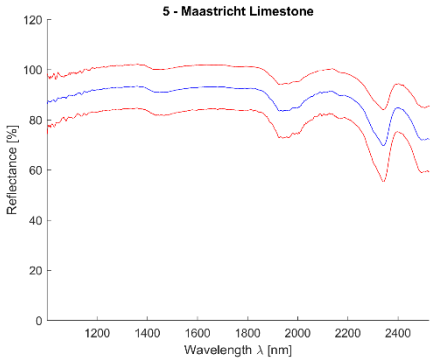


*Figure 122 – Maastricht limestone - mean value (blue) and 2,5*standard deviation (red)*

### 9.5.3. Electronic microscope findings

The sample was deluged using epoxy resin, sanded using SiC papers #2000, #4000, dusted. The sample photos (Figure 123 to Figure 125) show white grains primary from *Ca*, minority elements *Al, Mg*. Grey colour represents epoxy resin with *C, O, Cl* elements.

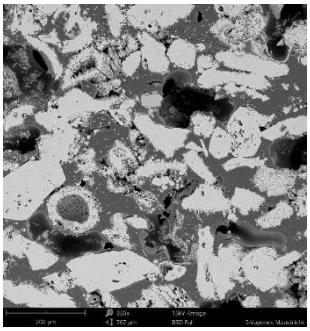

*Figure 123 - Phenom XL Desktop SEM photos - Microscope sample image*

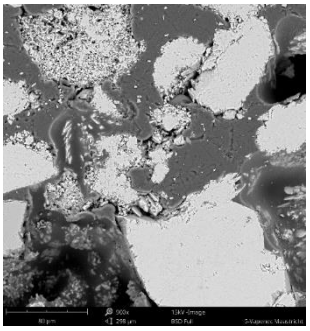

*Figure 124 - Phenom XL Desktop SEM photos - Microscope sample image*

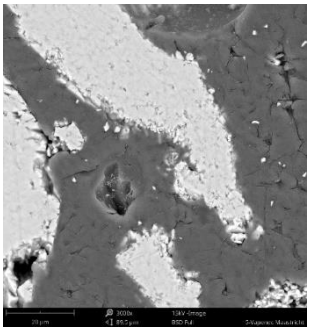

*Figure 125 - Phenom XL Desktop SEM photos - Microscope sample image*

SEM results (average atomic concentration, average weight concentration and average stoichiometry weight concentration) in the form of graphs are shown in Figure 126 to Figure 128.

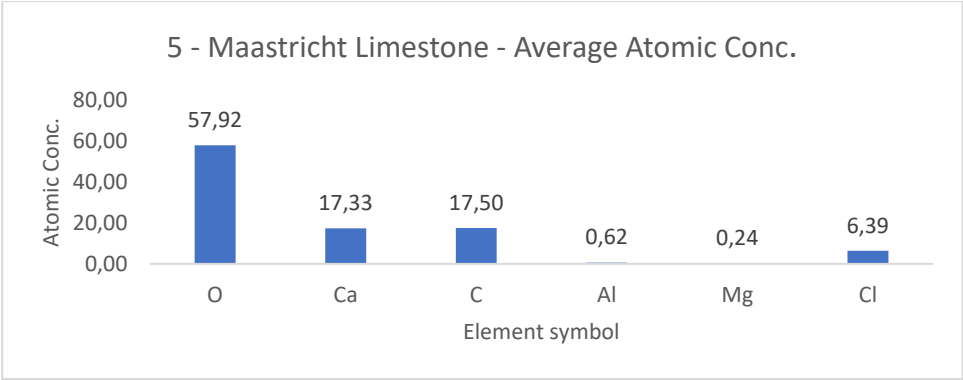


*Figure 126 – Maastricht limestone – Average atomic concentration*

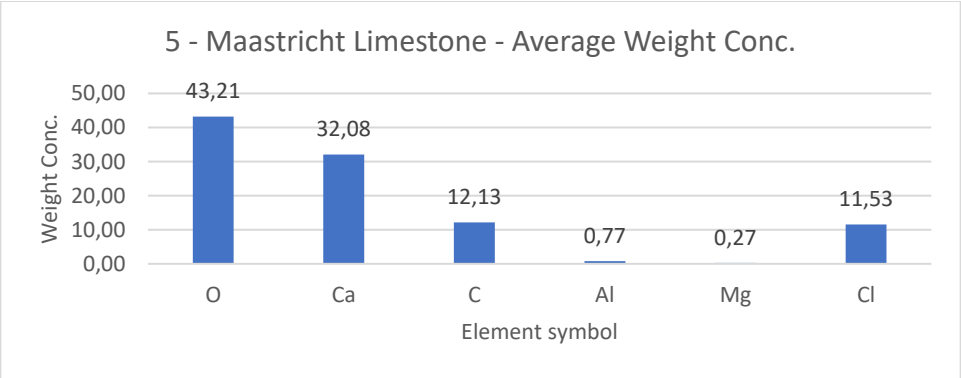


*Figure 127 – Maastricht limestone – Average weight concentration*

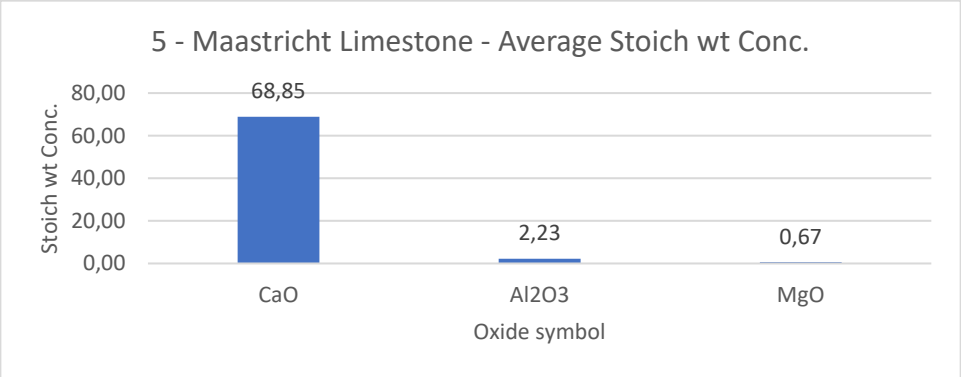


*Figure 128 – Maastricht limestone – Average Stoich wt concentration*

## 9.6. Přední Kopanina marlstone

### 9.6.1. Sample information

Marlstone is a calcium carbonate or lime-rich mud or mudstone which contains variable amounts of clays and silt. Přední Kopanina was a small village located close to Prague to the north-west and today is one of the city municipalities. Its bedrock made the village famous for the quarry of building stone. Prague buildings have been constructed using this stone since the 12$^{th}$ century and this material is still used for restoration works and new buildings in downtown Prague. Nowadays, Přední Kopanina is a natural reserve and mining is suspended [142], [143].

### 9.6.2. Spectroscopy results

The sample was documented using an ordinary mobile phone camera (Figure 129) and a digital DinoLite microscope with magnification


*Figure 129 - Marlstone sample image*

*Figure 130 - Marlstone DinoLite microscope image, magnification 50*

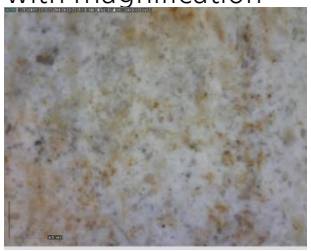

*Figure 131 - Marlstone DinoLite microscope image, magnification 200*

Purchased reflectance spectroscopy data were processed and analysed using a MATLAB script in Appendix XIII available at enclosed CD. Analysis results are mentioned below, Figure 132 and Figure 133 shows spectral graphs of the sample.

Minimum standard deviation: 1.13% (for λ = 2524.211nm)
Maximum standard deviation: 2.61% (for λ = 1033.993nm)
Mean standard deviation: 1.72%

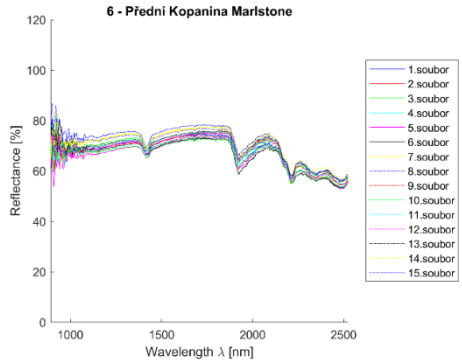


*Figure 132 - Přední Kopanina marlstone - all measurements plot*

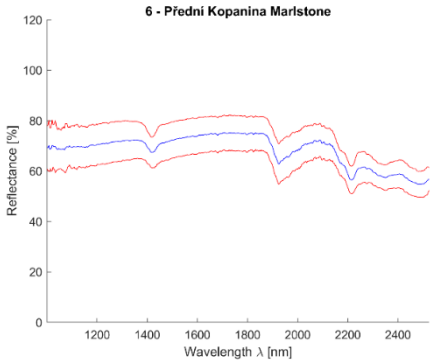


*Figure 133 - Přední Kopanina marlstone - mean value (blue) and 2,5*standard deviation (red)*

### 9.6.3. Electronic microscope findings

The sample was deluged using epoxy resin, sanded using SiC papers #2000, #4000 with water, dusted. Sample can be divided into "dark" (Figure 134 to Figure 136) and "light" parts after polishing (Figure 137 to Figure 139). "Dark" part contains a higher amount of dark grey grain (*Si*, *C*) and a smaller amount of light grey grains (*Ca*, *C*). In "light" areas is the amount of light grains (including *Ca*) significantly higher compared to those containing *Si*. Bright white areas contain iron (*Fe*) oxides and $Al_2O_3$ minor occurrence.

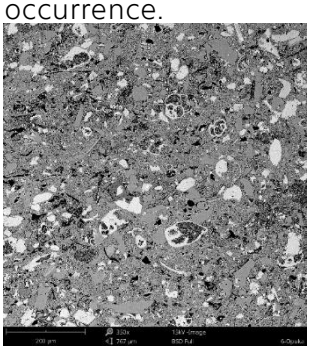

*Figure 134 - Phenom XL Desktop SEM photos - Microscope sample image*

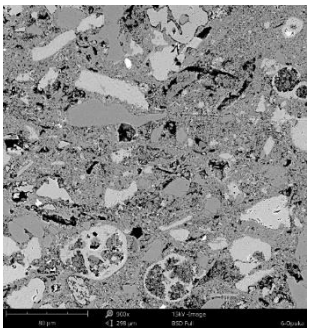

*Figure 135 - Phenom XL Desktop SEM photos - Microscope sample image*

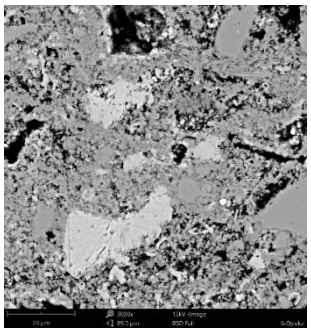

*Figure 136 - Phenom XL Desktop SEM photos - Microscope sample image*

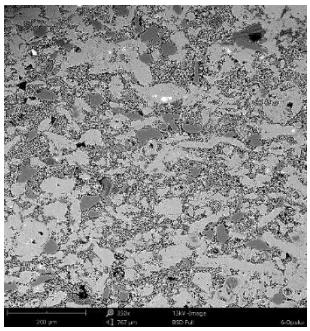

*Figure 137- Phenom XL Desktop SEM photos - Microscope sample image*

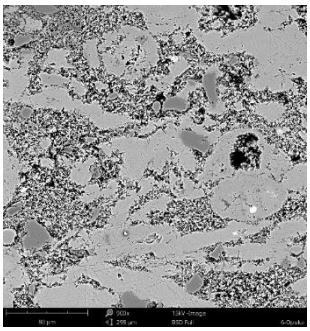

*Figure 138 - Phenom XL Desktop SEM photos - Microscope sample image*

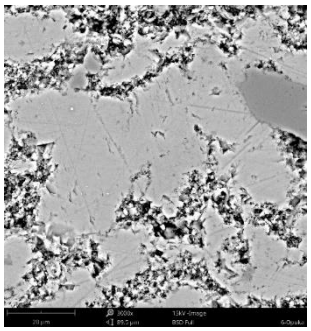

*Figure 139 - Phenom XL Desktop SEM photos - Microscope sample image*

SEM results in the form of EDS map can be seen in Figure 140 and average atomic concentration, average weight concentration and average stoichiometry weight concentration in the form of graphs are shown in Figure 141 to.Figure 143.

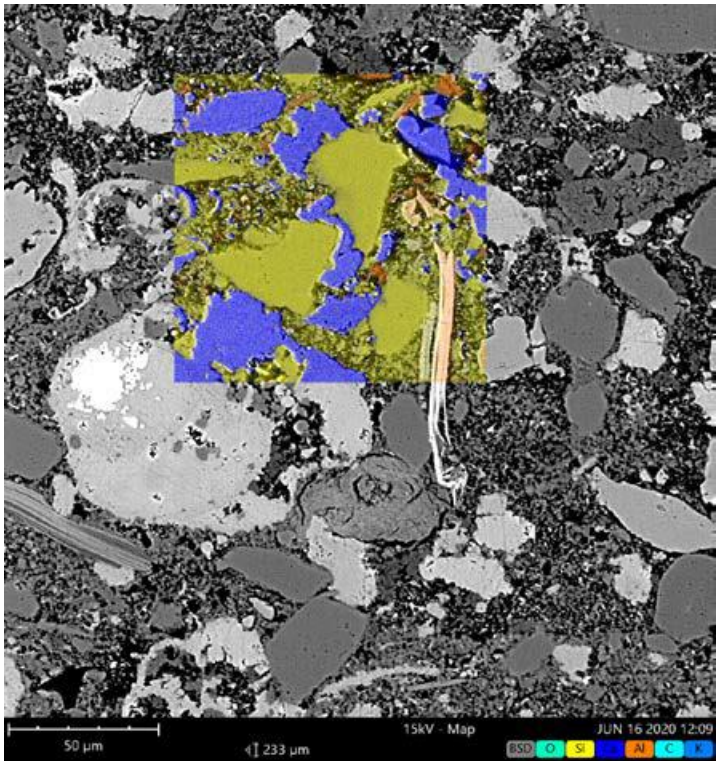


*Figure 140 - Přední Kopanina marlstone EDS map*

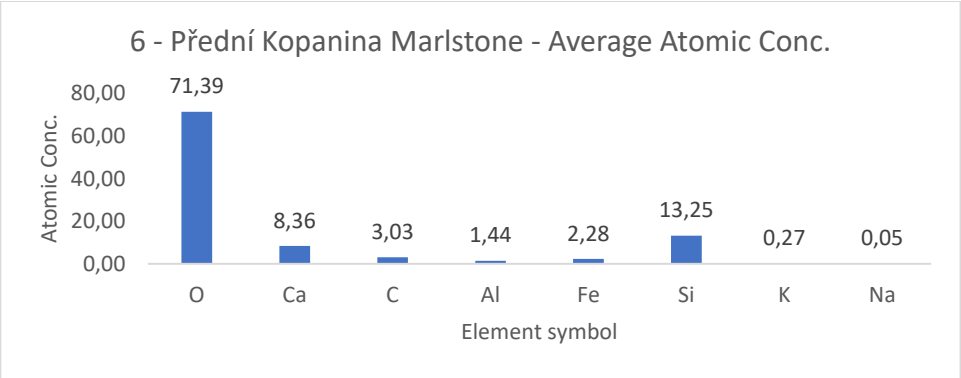


*Figure 141 - Přední Kopanina marlstone average atomic concentration*

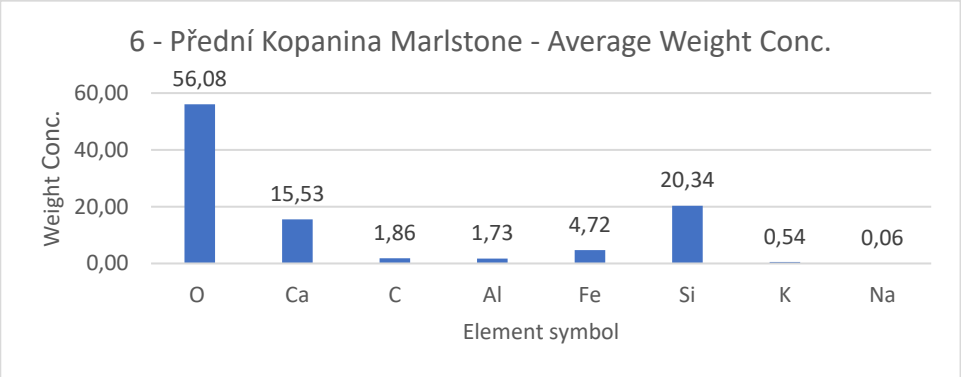


*Figure 142 - Přední Kopanina marlstone average weight concentration*

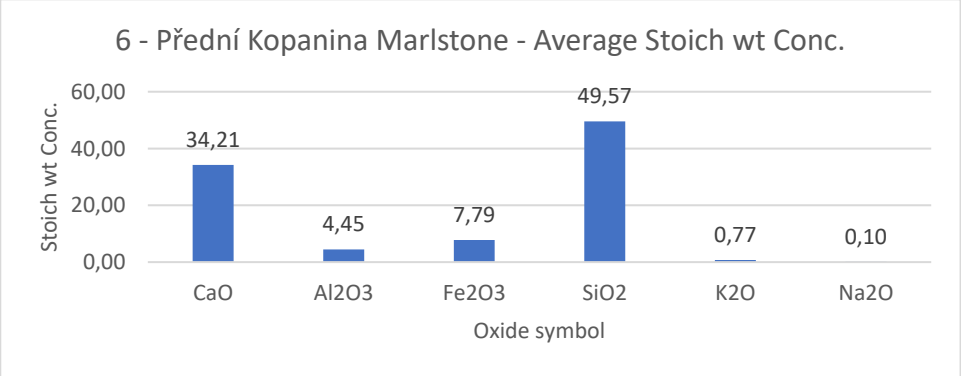


*Figure 143 - Přední Kopanina marlstone average Stoich wt conc*

## 9.7. Brick

### 9.7.1. Sample information

Brick is a structural clay product manufactured as standard units used in building construction. The brick was first produced in a sun-dried form at least 6000 years ago and was a forerunner of a wide range of structural clay products used today. It is formed from clay or shale or mixtures and burned (fired) in a kiln, or oven, to produce strength, hardness, and heat resistance [144].

### 9.7.2. Spectroscopy results

The sample was documented using an ordinary mobile phone camera (Figure 144) and a digital DinoLite microscope with magnification 50 (Figure 145) and 200 (Figure 146).

*Figure 144 – Brick sample image*

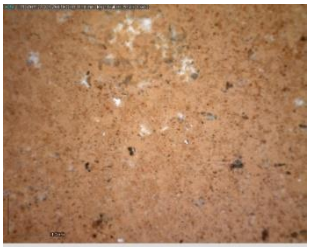

*Figure 145 – Brick DinoLite microscope image, magnification 50*

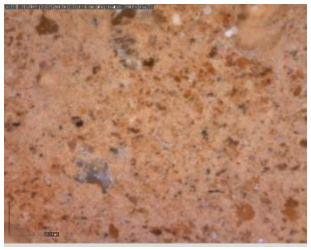

*Figure 146 – Brick DinoLite microscope image, magnification 200*

Purchased reflectance spectroscopy data were processed and analysed using a MATLAB script in Appendix XIII available at enclosed CD. Analysis results are mentioned below, Figure 147 and Figure 148 shows spectral graphs of the sample.

| | |
|---|---|
| Minimum standard deviation: | 2.12% (for λ = 1037.268nm) |
| Maximum standard deviation: | 3.01% (for λ = 1793.954nm) |
| Mean standard deviation: | 2.80% |

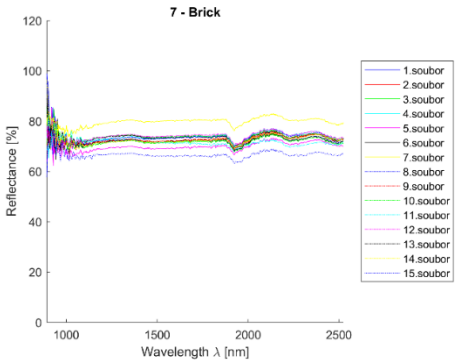


*Figure 147 - Brick - all measurements plot*

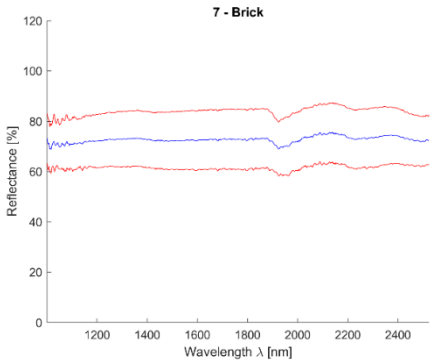


*Figure 148 - Brick - mean value (blue) and 2,5*standard devi ation (red)*

### 9.7.3. Electronic microscope findings

The sample was deluged using epoxy resin, sanded using *SiC* papers #2000, #4000 with water, dusted. SEM images (Figure 149 to Figure 151) show dark grey grains mainly comprised of $SiO_2$, $Al_2O_3$ minority. Filled with light grey matter that consists of *Al, Ca, Na, Mg, Fe* oxides, light grains consisting of various oxide compilations with considerably lower $SiO_2$ ratio.

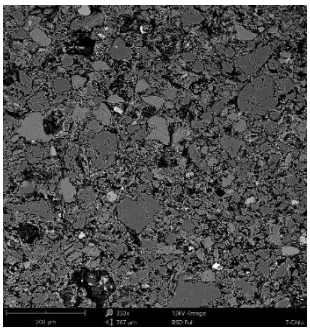

*Figure 149 - Phenom XL Desktop SEM photos - Microscope sample image*

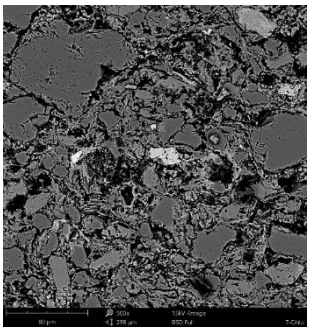

*Figure 150 - Phenom XL Desktop SEM photos - Microscope sample image*

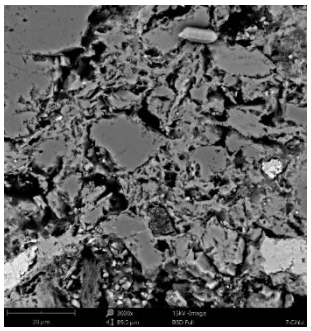

*Figure 151 - Phenom XL Desktop SEM photos - Microscope sample image*

SEM results in the form of EDS map can be seen in Figure 152 and average atomic concentration, average weight concentration and average stoichiometry weight concentration in the form of graphs are shown in Figure 153 to Figure 155.

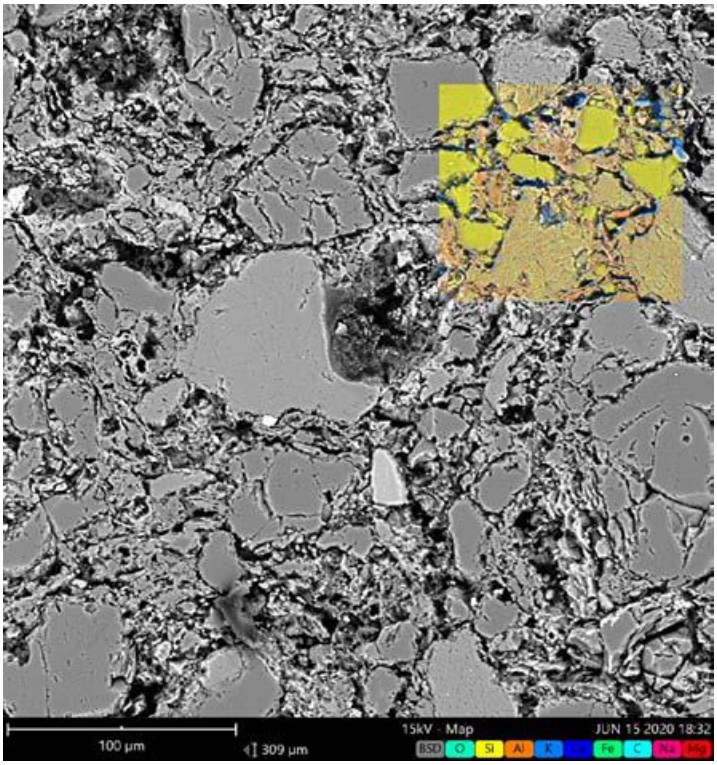


*Figure 152 - Brick - EDS map*

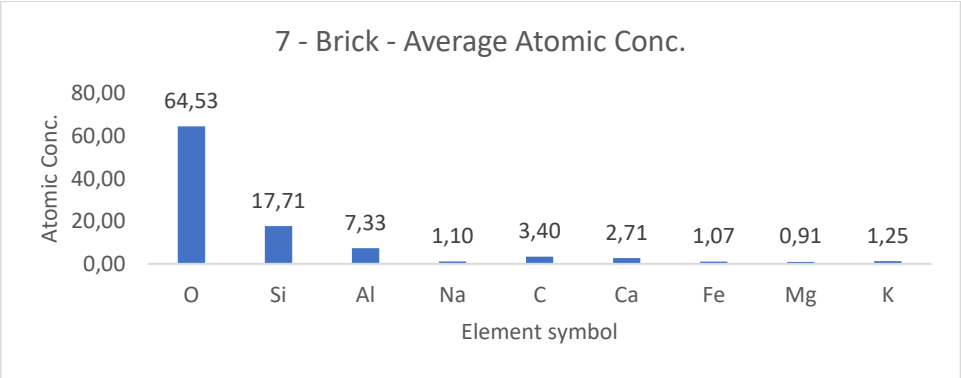


*Figure 153 - Brick average atomic concentration*

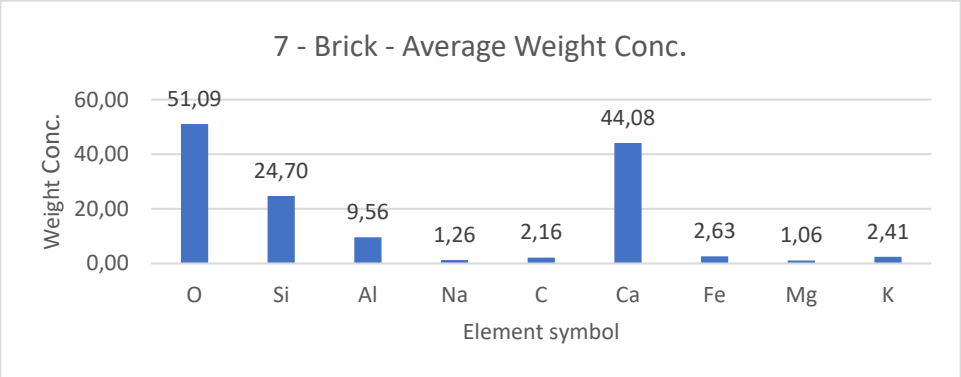


*Figure 154 -Brick average weight concentration*

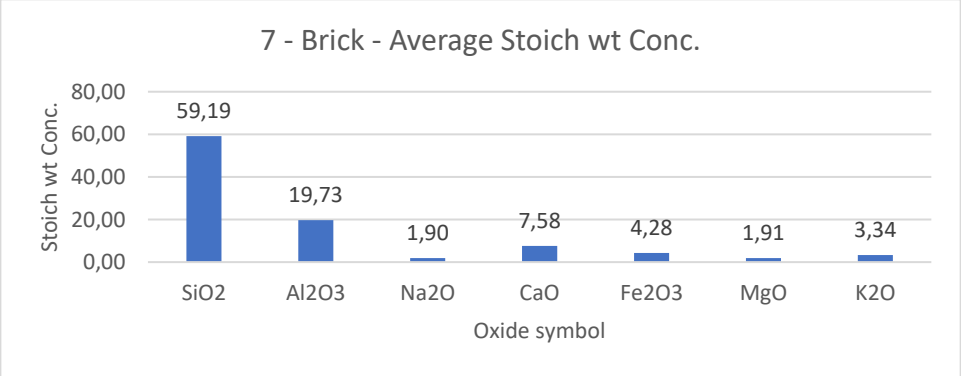


*Figure 155 - Brick average Stoich wt conc*

## 9.8. Tile

### 9.8.1. Sample information

Tile is a structural clay product manufactured as standard units used in building construction. Structural clay tile, also called terra-cotta, is a larger building unit, containing many hollow spaces (cells), and it is used mainly as a backup for brick facing or for plastered partitions. Structural clay-facing tile is often glazed when used as an exposed finish [145]. Measurements were made from the front glazed side since this side is commonly used as a façade facing.

### 9.8.2. Spectroscopy results

The sample was documented using an ordinary mobile phone camera (Figure 156) and a digital DinoLite microscope with magnification 50 (Figure 157) and 200 (Figure 158).

*Figure 156 - Tile sample image*

*Figure 157 – Tile DinoLite microscope image, magnification 50*

*Figure 158 - Tile DinoLite microscope image, magnification 200*

Purchased reflectance spectroscopy data were processed and analysed using a MATLAB script in Appendix XIII available at enclosed CD. Analysis results are mentioned below, Figure 159 and Figure 160 shows spectral graphs of the sample.

| | |
|---|---|
| Minimum standard deviation: | 1.84% (for λ = 2402.580nm) |
| Maximum standard deviation: | 3.85% (for λ = 1001.238nm) |
| Mean standard deviation: | 2.37% |

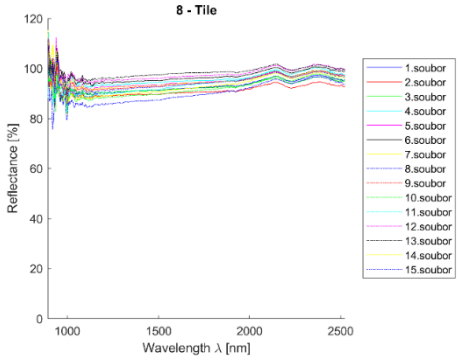


*Figure 159 - Tile - all measurements plot*

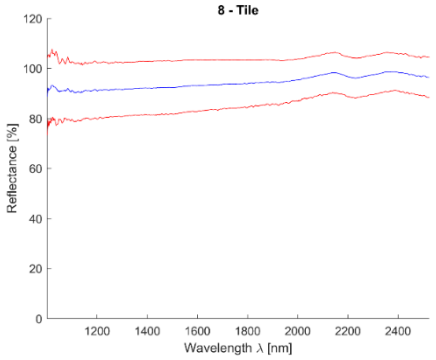


*Figure 160 – Tile - mean value (blue) and 2,5*standard deviation (red)*

### 9.8.3. Electronic microscope findings

The sample was deluged using epoxy resin, sanded using *SiC* papers #2000, #4000 with water, dusted. SEM images (Figure 161 to Figure 163) show black areas representing pores, dark sections grains with main constituent $SiO_2$ and light grey matter consisting of elements *Si, Al, Na, K* and occasionally *Mg.* EDS map shows *Ca* in pores which is a measurement error caused by the surface unevenness.

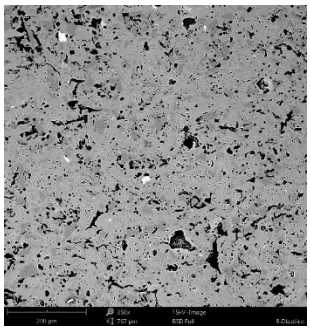

*Figure 161 - Phenom XL Desktop SEM photos - Microscope sample image*

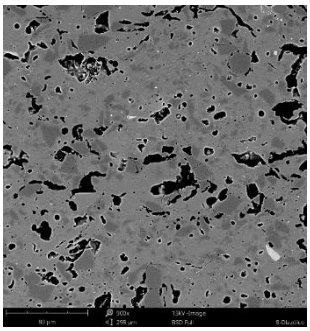

*Figure 162 - Phenom XL Desktop SEM photos - Microscope sample image*

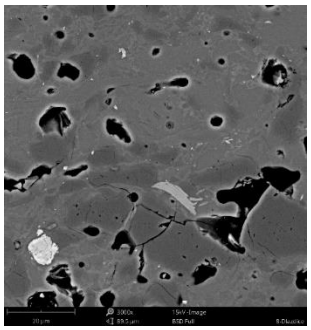

*Figure 163- Phenom XL Desktop SEM photos - Microscope sample image*

SEM results in the form of EDS map can be seen in Figure 164 and average atomic concentration, average weight concentration and average stoichiometry weight concentration in the form of graphs are shown in Figure 165 to Figure 167.

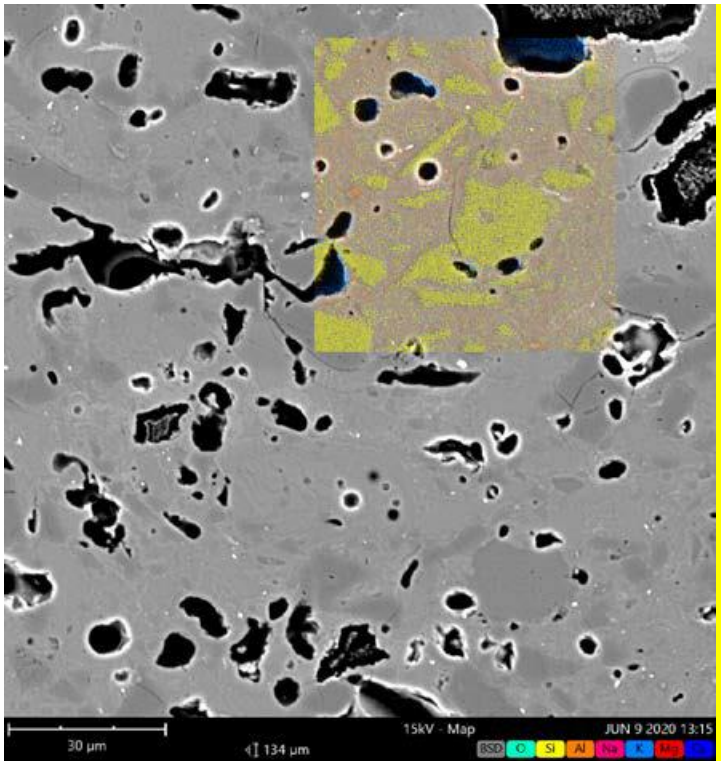


*Figure 164 - Tilt EDS map*

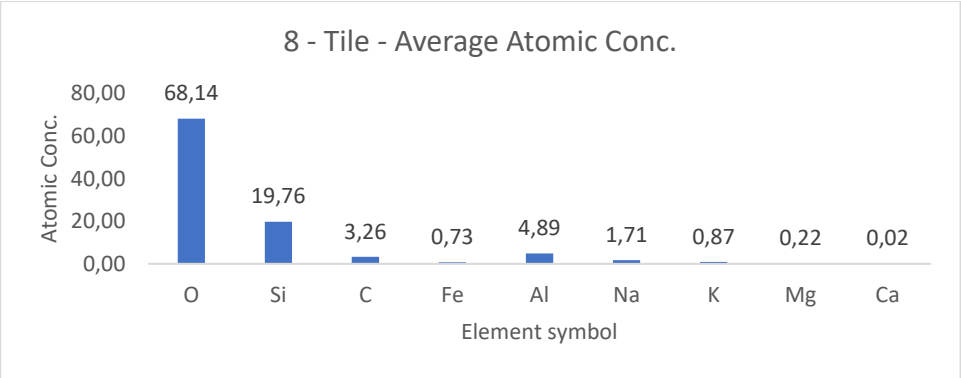


*Figure 165 - Tile average atomic concentration*

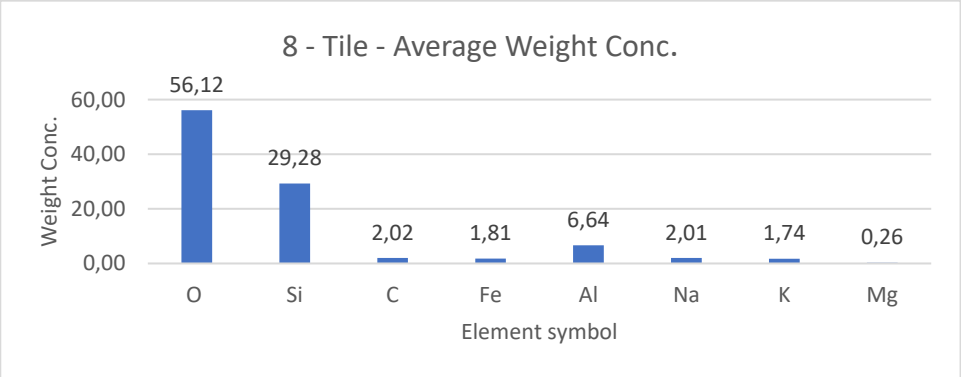


*Figure 166 - Tile average weight concentration*

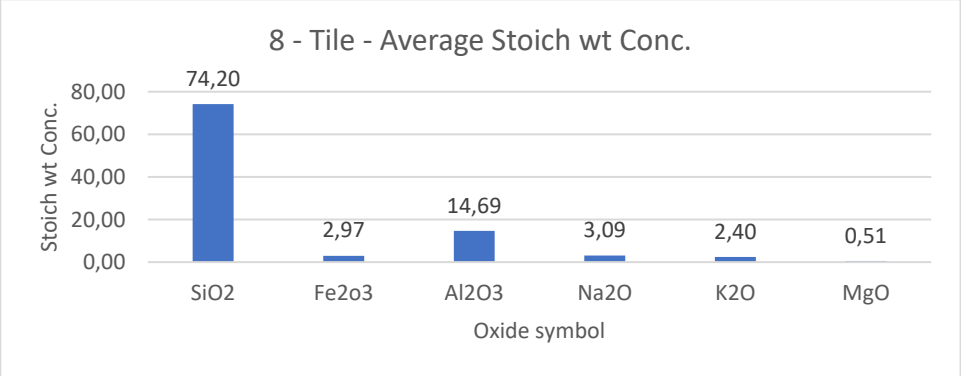


*Figure 167 - Tile average stoich wt conc*

## 9.9. Air lime mortar

### 9.9.1. Sample information

Air lime-based mortars have high porosity and wide variability in pore sizes, e.g. small and big pores are connected. These mortars are relatively not very solid but can react and adapt to building expansion in large measure. Air lime was used as a major mortar binder before the end of the 19$^{th}$ century [146].

### 9.9.2. Spectroscopy results

The sample was documented using an ordinary mobile phone camera (Figure 168) and a digital DinoLite microscope with magnification 50 (Figure 169) and 200 (Figure 170).

*Figure 168 - Air lime mortar sample image*

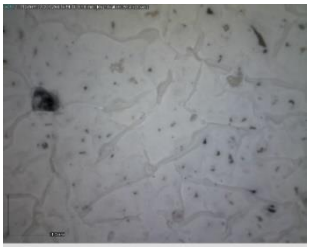

*Figure 169 – Air lime mortar DinoLite microscope image, magnification 50*

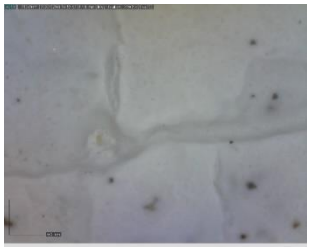

*Figure 170 - Air lime mortar DinoLite microscope image, magnification 200*

Purchased reflectance spectroscopy data were processed and analysed using a MATLAB script in Appendix XIII available at enclosed CD. Analysis results are mentioned below, Figure 171 and Figure 172 shows spectral graphs of the sample.

| | |
|---|---|
| Minimum standard deviation: | 1.60% (for λ = 2524.211nm) |
| Maximum standard deviation: | 3.08% (for λ = 1011.065nm) |
| Mean standard deviation: | 2.07% |

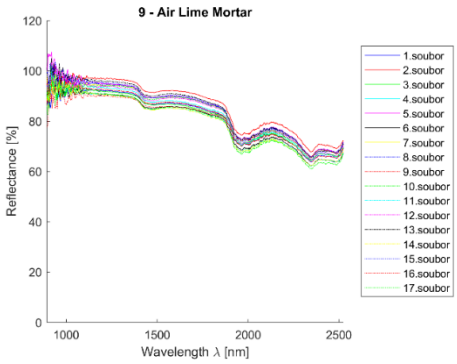


*Figure 171 - Air lime mortar - all measurements plot*

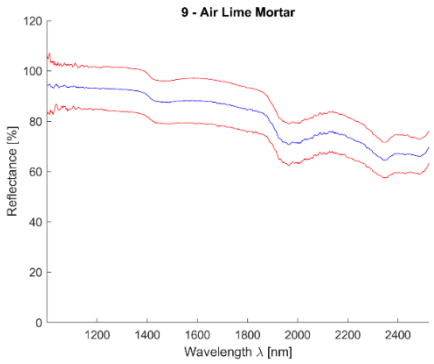


*Figure 172 - Air lime mortar - mean value (blue) and 2,5*standard deviation (red)*

### 9.9.3. Electronic microscope findings

The sample was deluged using epoxy resin, sanded using *SiC* papers #2000, #4000, dusted. EDS maps (Figure 173 to Figure 175) show aggregate grain mainly from $SiO_2$. A matrix in between grains is mostly made of *Ca* and includes a minority of *Si* and *Al*. A small amount of *C* can be found in matrix and aggregate grains. Dark grey areas in images are the epoxy resin.

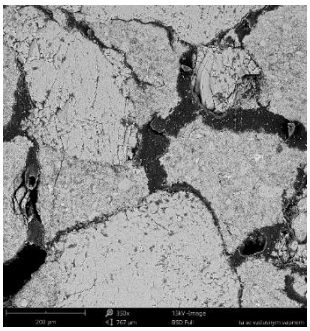

*Figure 173 - Phenom XL Desktop SEM photos - Microscope sample image*

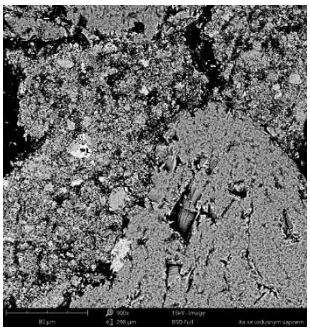

*Figure 174 - Phenom XL Desktop SEM photos - Microscope sample image*

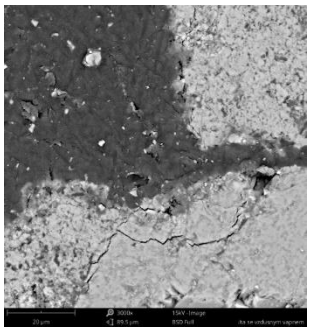

*Figure 175 - Phenom XL Desktop SEM photos - Microscope sample image*

SEM results in the form of EDS map can be seen in Figure 176 and average atomic concentration, average weight concentration and average stoichiometry weight concentration in the form of graphs are shown in Figure 177 to Figure 179.

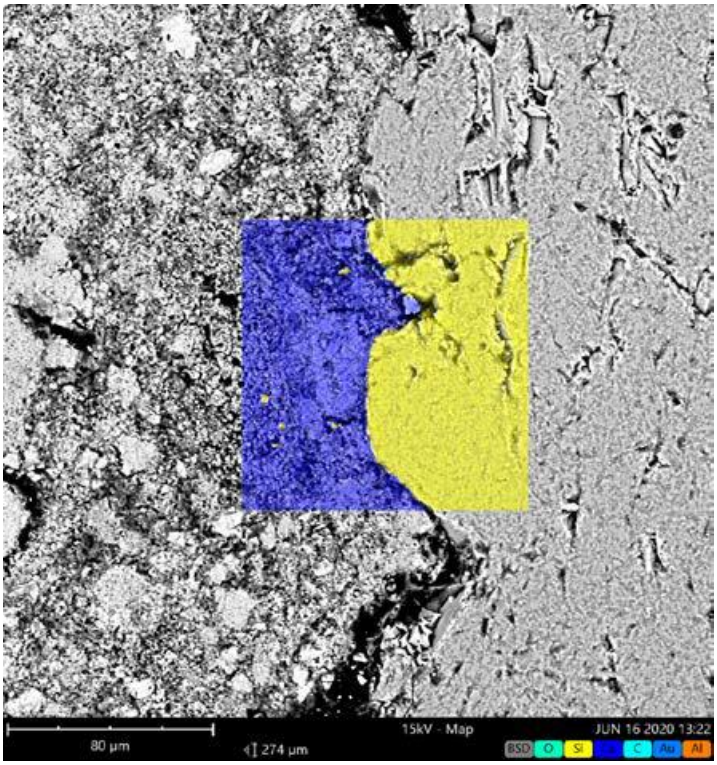


*Figure 176 - Air lime mortar EDS map*

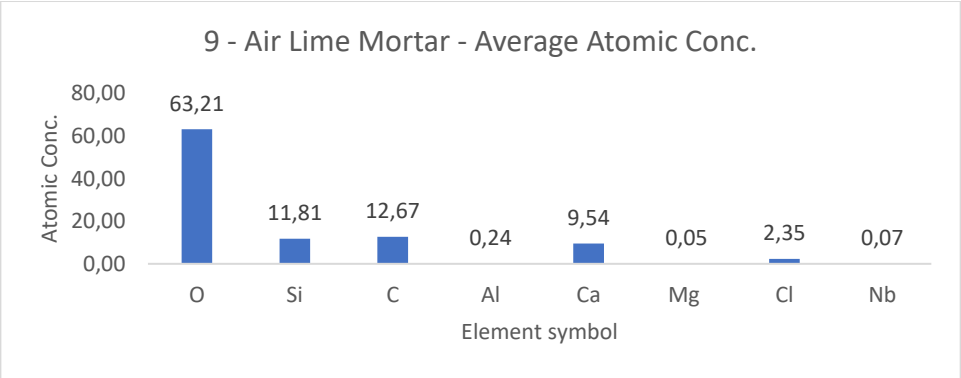


*Figure 177 - Air lime mortar average atomic concentration*

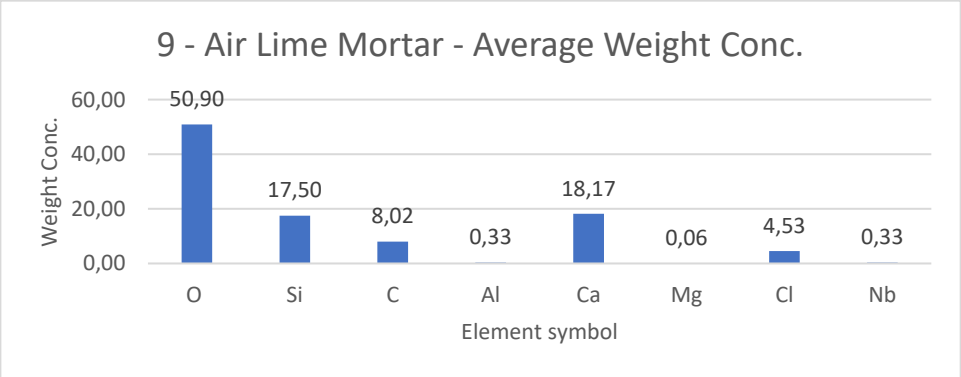


*Figure 178 - Air lime mortar average weight concentration*

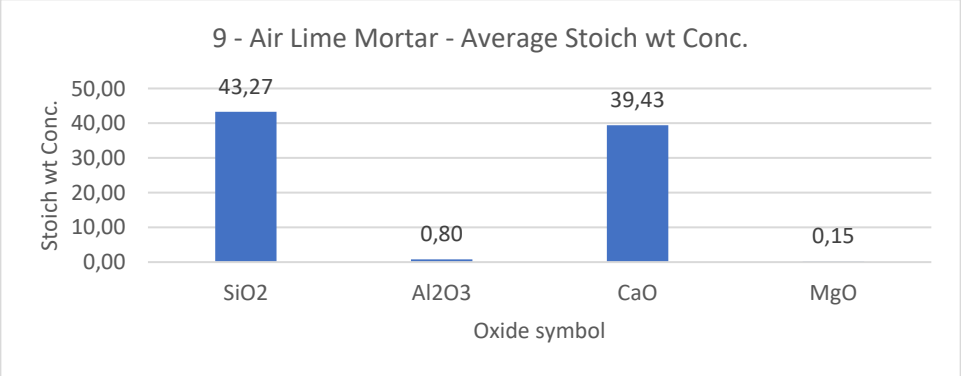


*Figure 179 - Air lime mortar average stoich wt concentration*

## 9.10. Lime + cement binder mortar

### 9.10.1. Sample information

Lime and cement binder mortars have smaller pores compared to the air lime mortars (9.9), the overall porosity is lower and therefore they have the lower soaking ability. The soaking ability has an influence on masonry humidity and drying out [146].

### 9.10.2. Spectroscopy results

The sample was documented using an ordinary mobile phone camera (Figure 180) and a digital DinoLite microscope with magnification 50 (Figure 181) and 200 (Figure 182).

*Figure 180 -Lime + cement binder mortar sample image*

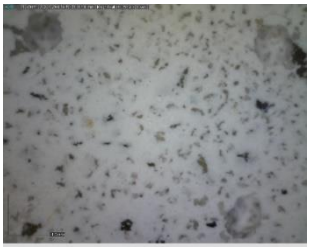

*Figure 181 - Lime + cement binder mortar DinoLite microscope image, magnification 50*

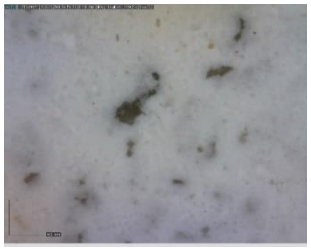

*Figure 182 - Lime + cement binder mortar DinoLite microscope image, magnification 200*

Purchased reflectance spectroscopy data were processed and analysed using a MATLAB script in Appendix XIII available at enclosed CD. Analysis results are mentioned below, Figure 183 and Figure 184 shows spectral graphs of the sample.

| | |
|---|---|
| Minimum standard deviation: | 2.17% (for λ = 1011.065nm) |
| Maximum standard deviation: | 3.23% (for λ = 2148.742nm) |
| Mean standard deviation: | 2.93% |

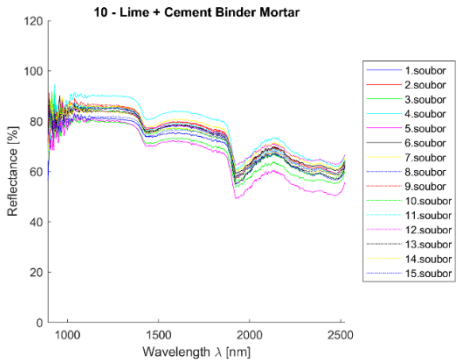


*Figure 183 - Lime + cement binder mortar - all measurements plot*

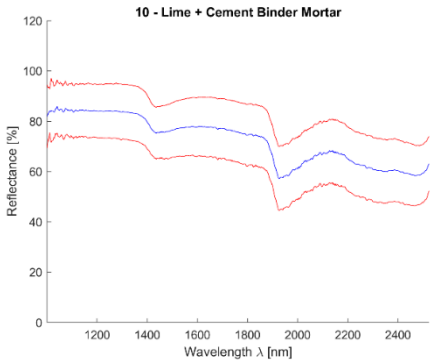


*Figure 184 - Lime + cement binder mortar - mean value (blue) and 2,5*standard deviation (red)*

### 9.10.3. Electronic microscope findings

The sample was deluged using epoxy resin, sanded using *SiC* papers #2000, #4000, dusted. EDS maps (Figure 185 to Figure 187) show aggregate grain mainly from $SiO_2$. A matrix in between grains is mostly made of *Ca* and includes a minority of *Si*. A small amount of *C* can be found in matrix and aggregate grains.

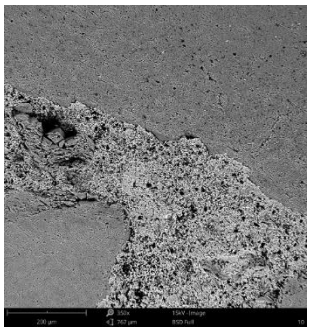

*Figure 185 - Phenom XL Desktop SEM photos - Microscope sample image*

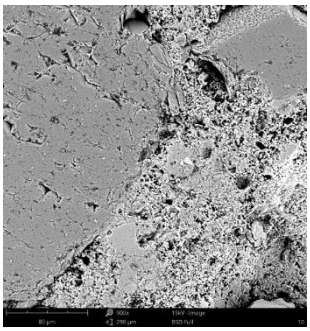

*Figure 186 - Phenom XL Desktop SEM photos - Microscope sample image*

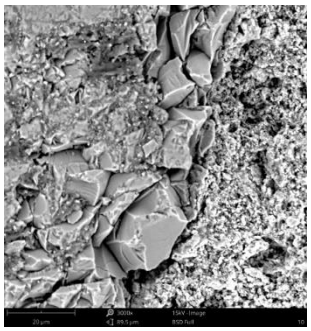

*Figure 187 - Phenom XL Desktop SEM photos - Microscope sample image*

SEM results in the form of EDS map can be seen in Figure 188 and average atomic concentration, average weight concentration and average stoichiometry weight concentration in the form of graphs are shown in Figure 189 to Figure 191.

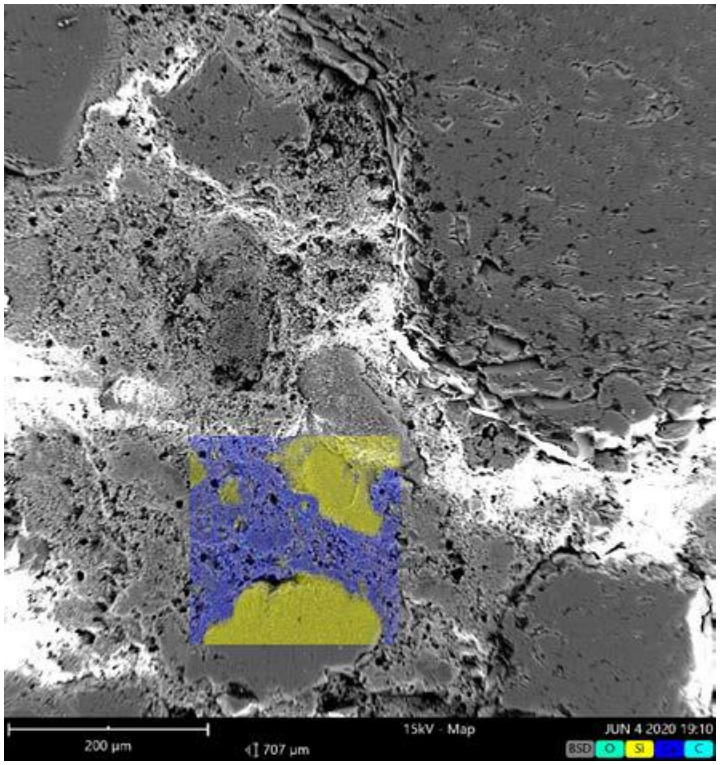


*Figure 188 - Lime + cement binder mortar EDS map*

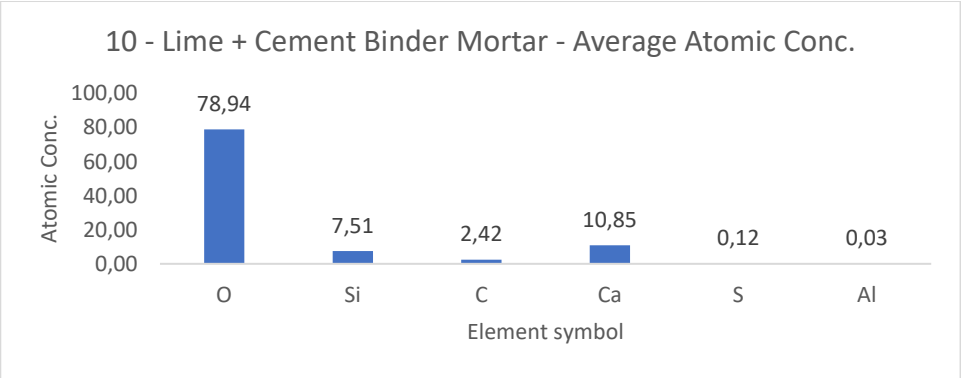


*Figure 189 - Lime + cement binder mortar average atomic concentration*

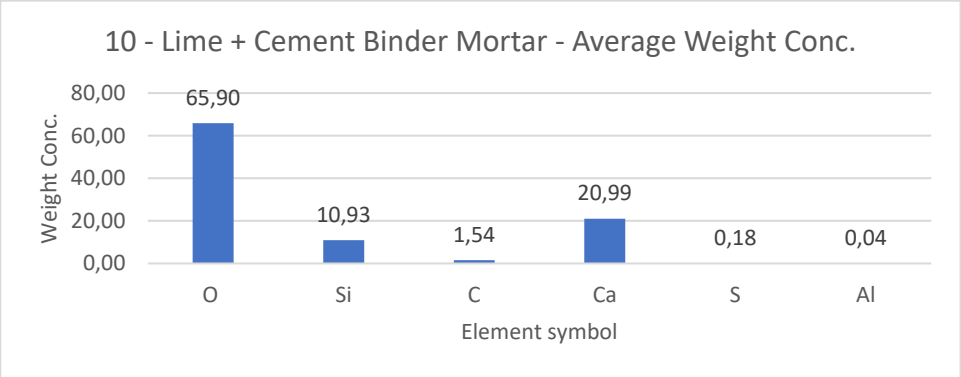


*Figure 190 - Lime + cement binder mortar average weight concentration*

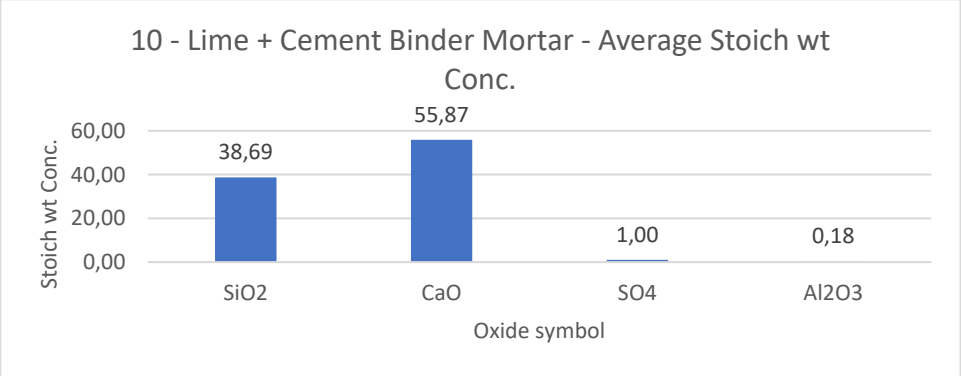


*Figure 191 - Lime + cement binder mortar average stoich wt conc*

## 9.11. Hydraulic lime mortar (NHL5)

### 9.11.1. Sample information

Hydraulic lime is a binder that shows faster hardening compared to air lime and achieves higher strength and lower soaking abilities. Hydraulic lime signified also as NHL (Natural Hydraulic Lime) is divided into categories according to final strength to NHL2, NHL3,5 and NHL5. Strong hydraulic lime is with its characteristics closer to modern cement than to air limes [146].

### 9.11.2. Spectroscopy results

The sample was documented using an ordinary mobile phone camera (Figure 192) and a digital DinoLite microscope with magnification 50 (Figure 193) and 200 (Figure 194).


*Figure 192 - Hydraulic lime mortar sample image*

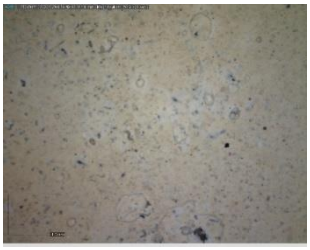

*Figure 193 - Hydraulic lime mortar DinoLite microscope image, magnification 50*

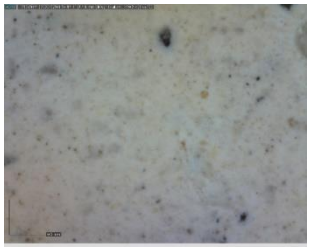

*Figure 194 - Hydraulic lime mortar DinoLite microscope image, magnification 200*

Purchased reflectance spectroscopy data were processed and analysed using a MATLAB script in Appendix XIII available at enclosed CD. Analysis results are mentioned below, Figure 195 and Figure 196 shows spectral graphs of the sample.

| | |
|---|---|
| Minimum standard deviation: | 1.41% (for λ = 1158.370nm) |
| Maximum standard deviation: | 2.37% (for λ = 1962.863nm) |
| Mean standard deviation: | 1.86% |

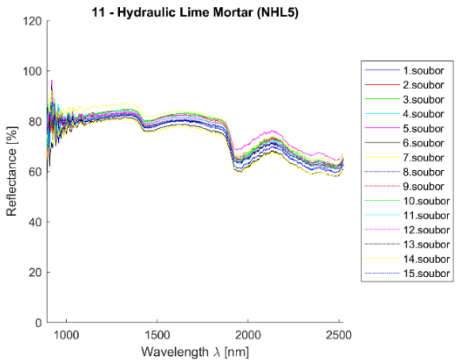


*Figure 195 - Hydraulic lime mortar - all measurements plot*

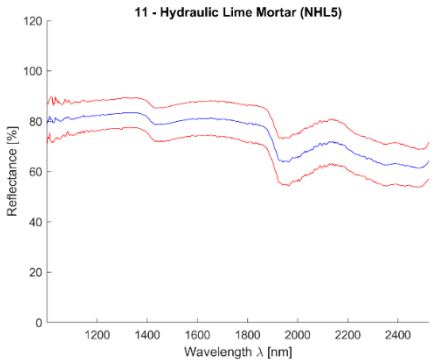


*Figure 196 – Hydraulic lime mortar - mean value (blue) and 2,5*standard deviation (red)*

### 9.11.3. Electronic microscope findings

The sample was deluged using epoxy resin, sanded using *SiC* papers #2000, #4000, dusted. EDS maps (Figure 197 to Figure 199) show aggregate grain mainly from $SiO_2$. A matrix in between grains is mostly made of *Ca* and includes a minority of *Si, Al, K and Mg*. A small amount of *C* can be found in matrix and aggregate grains.

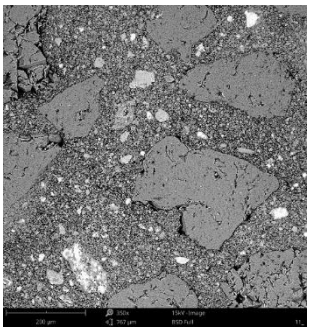

*Figure 197 - Phenom XL Desktop SEM photos - Microscope sample image*

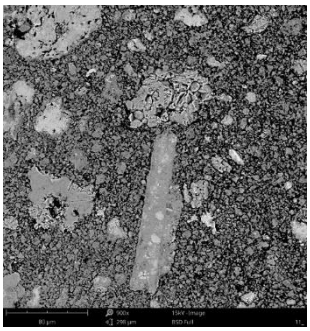

*Figure 198 - Phenom XL Desktop SEM photos - Microscope sample image*

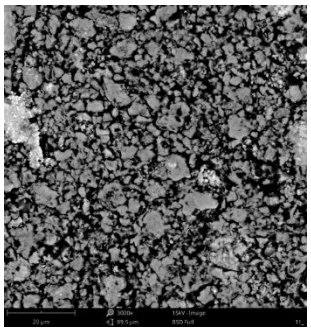

*Figure 199 - Phenom XL Desktop SEM photos - Microscope sample image*

SEM results in the form of EDS map can be seen in Figure 200 and average atomic concentration, average weight concentration and average stoichiometry weight concentration in the form of graphs are shown in Figure 201 to Figure 203.

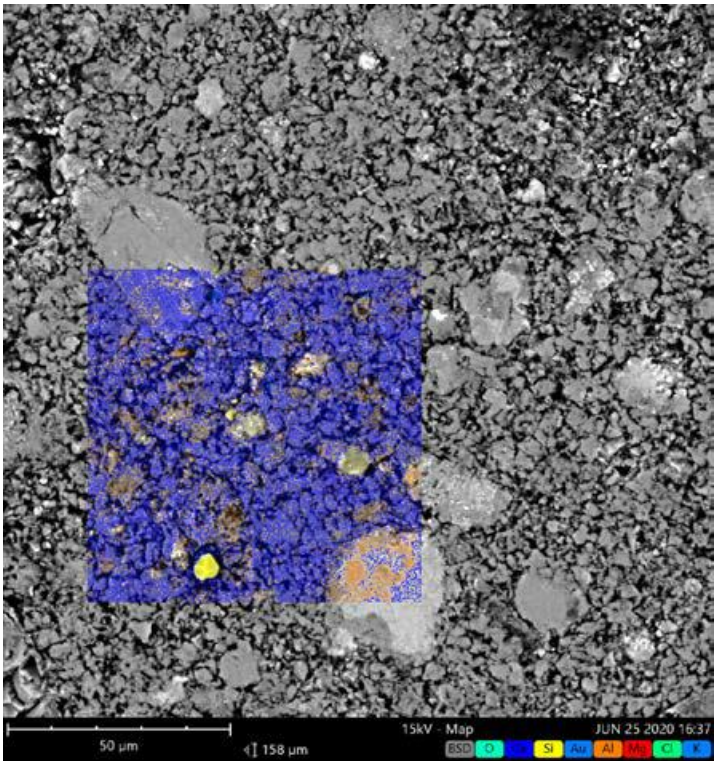


*Figure 200 - Hydraulic lime mortar EDS map*

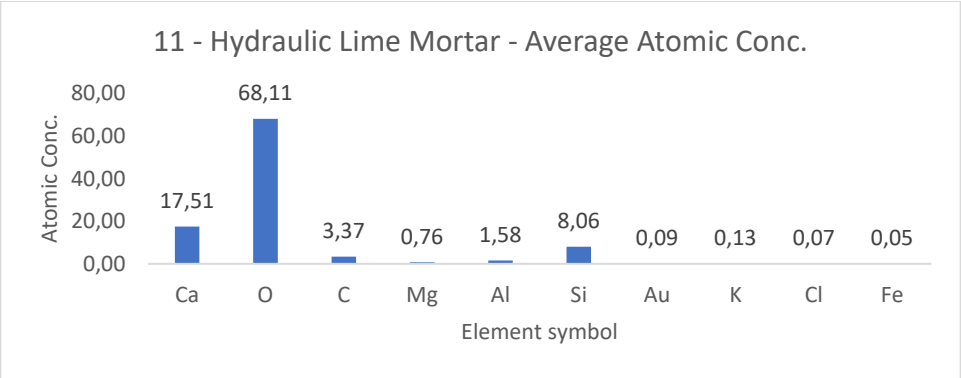


*Figure 201 - Hydraulic lime mortar average atomic concentration*

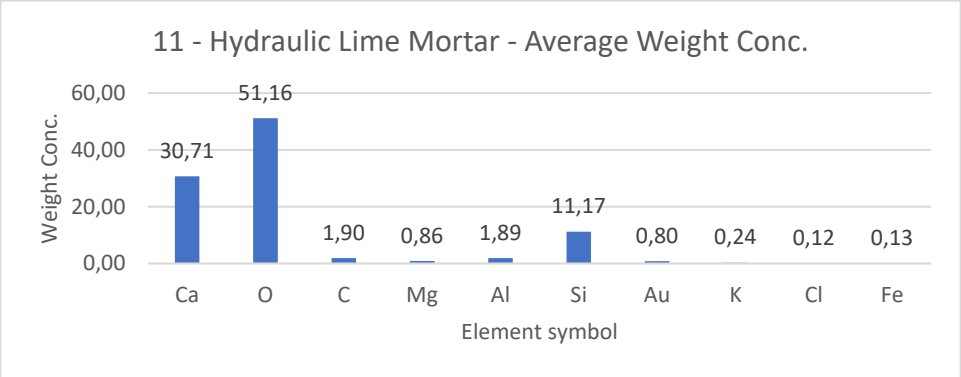


*Figure 202 - Hydraulic lime mortar average weight concentration*

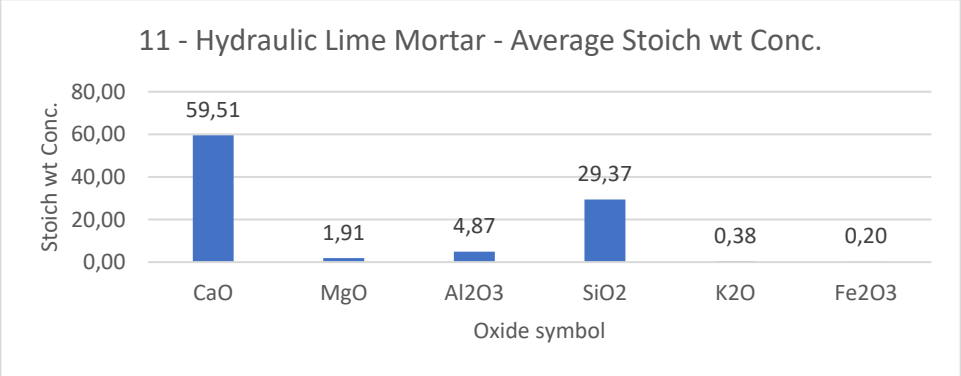


*Figure 203 - Hydraulic lime mortar average stoich wt concentration*

## 9.12. Lime + Metakaolin Binder Mortar

### 9.12.1. Sample information

Metakaolin is a highly reactive aluminium-silicon pozzolan (Chapter 7.2), that creates stable hydrate after mixing with lime and water and gives mortar hydraulic properties. After heating clay with fundamental mineral mixture kaolinite to temperatures between 500°C and 600°C a structural water loss occurs. This causes a kaolinite crystal structure deformation and a waterless reakcite form "Metakaolinit" is created. Mixed hydraulic binding on metakaolin base follows the tradition of adding heated clay into the lime mortars and it can substitute hydraulic binding using local resources. Metakaolin based binders have good compatibility with historical mortars and can be used for restoration works [147].

### 9.12.2. Spectroscopy results

The sample was documented using an ordinary mobile phone camera (Figure 204) and a digital DinoLite microscope with magnification 50 (Figure 205) and 200 (Figure 206).

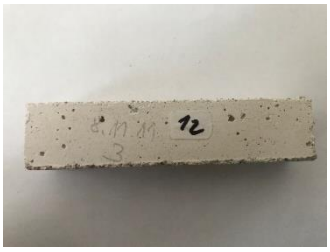


*Figure 204 - Lime + metakaolin binder mortar sample image*

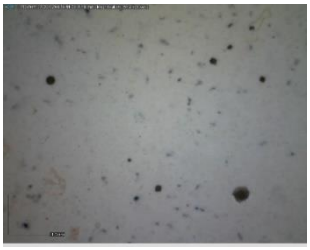

*Figure 205 - Lime + metakaolin binder mortar DinoLite microscope image, magnification 50*

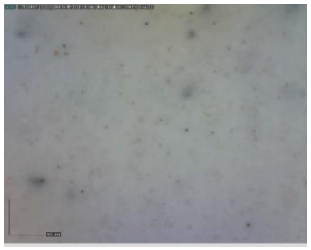

*Figure 206 - Lime + metakaolin binder mortar DinoLite microscope image, magnification 200*

Purchased reflectance spectroscopy data were processed and analysed using a MATLAB script in Appendix XIII available at enclosed CD. Analysis results are mentioned below, Figure 207 and Figure 208 shows spectral graphs of the sample.

| | |
|---|---|
| Minimum standard deviation: | 1.73% (for λ = 2481.816nm) |
| Maximum standard deviation: | 3.77% (for λ = 1001.238nm) |
| Mean standard deviation: | 2.18% |

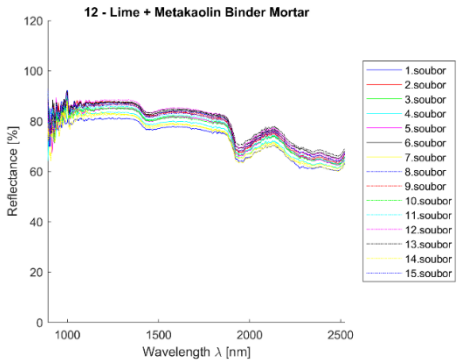


*Figure 207 - Lime + metakaolin binder mortar all measurements plot*

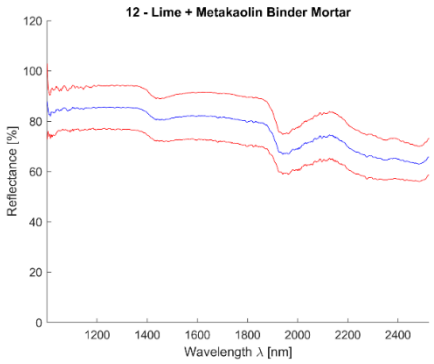


*Figure 208 - Lime + metakaolin binder mortar - mean value (blue) and 2,5*standard deviation (red)*

### 9.12.3. Electronic microscope findings

The sample was deluged using epoxy resin, sanded using *SiC* papers #2000, #4000, dusted. EDS maps (Figure 209 to Figure 211) show aggregate grain mainly from $SiO_2$. A matrix in between grains is mostly made of *Ca* and includes a minority of *Si* and *Al*. A small amount of *C* can be found in matrix and aggregate grains.

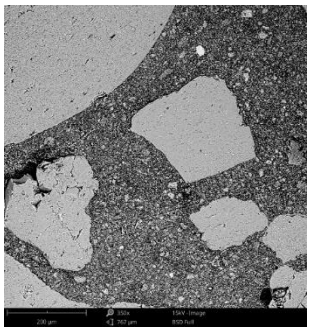

*Figure 209 - Phenom XL Desktop SEM photos - Microscope sample image*

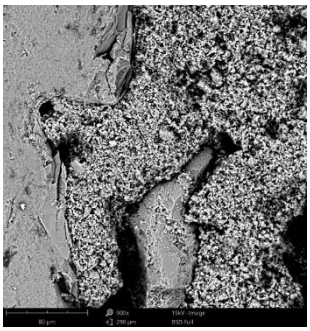

*Figure 210 - Phenom XL Desktop SEM photos - Microscope sample image*

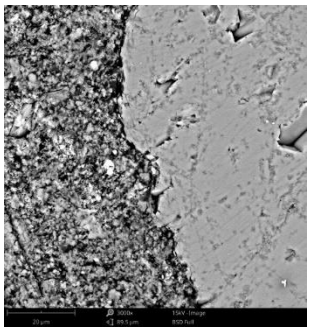

*Figure 211 - Phenom XL Desktop SEM photos - Microscope sample image*

SEM results in the form of EDS map can be seen at Figure 212 and average atomic concentration, average weight concentration and average stoichiometry weight concentration in the form of graphs are shown in Figure 213 to Figure 215.

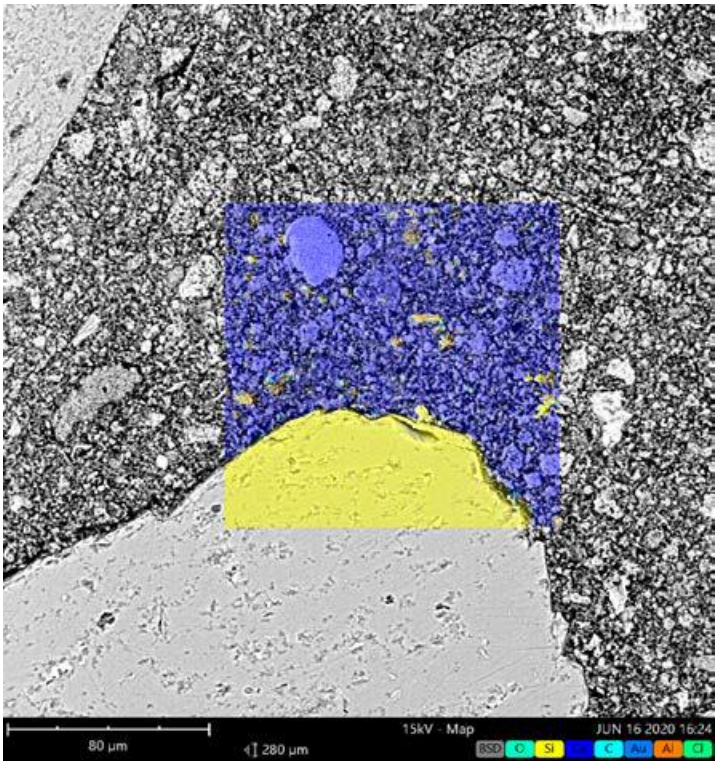


*Figure 212 - Lime + metakaolin binder mortar EDS map*

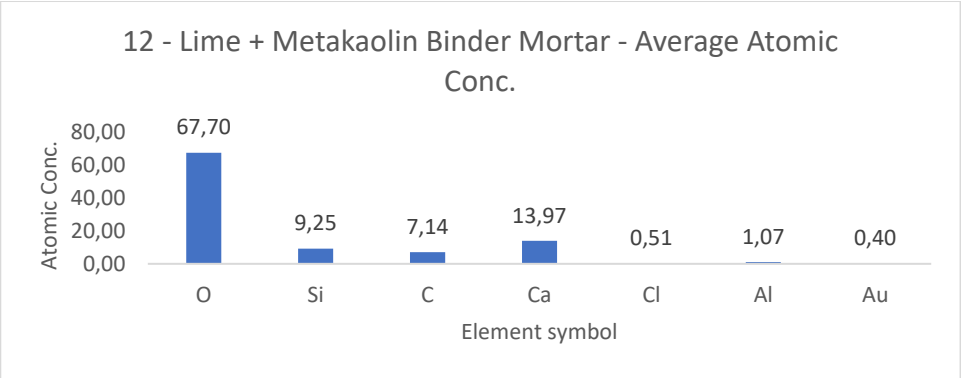


*Figure 213 - Lime + metakaolin binder mortar average atomic concentration*

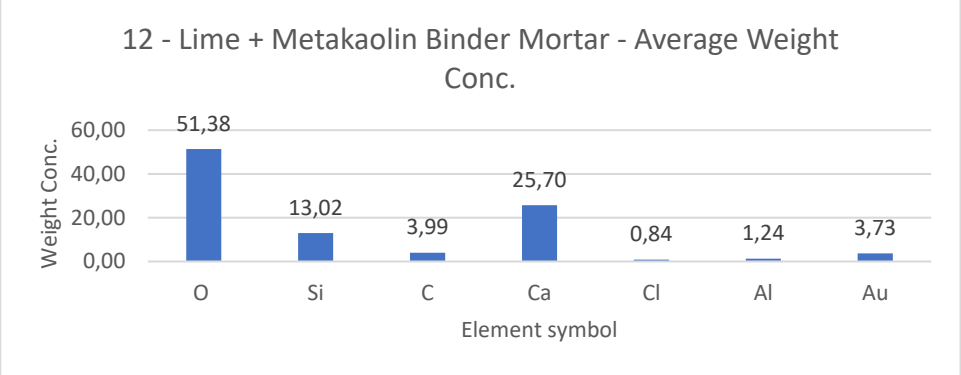


*Figure 214 - Lime + metakaolin binder mortar average weight concentration*

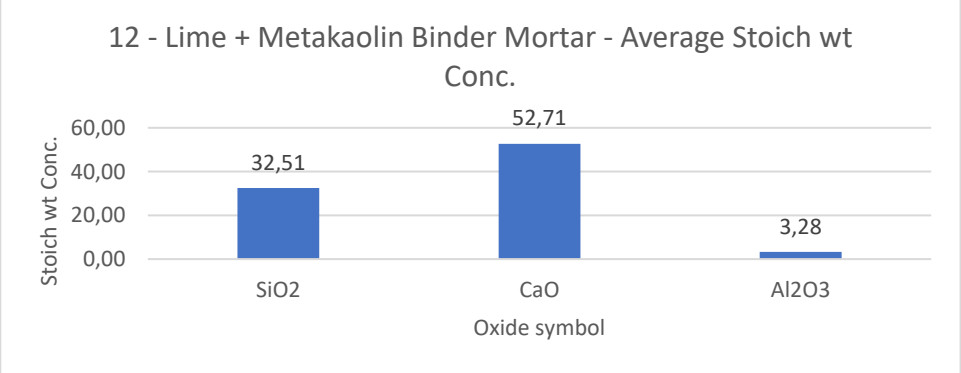


*Figure 215 - Lime + metakaolin binder mortar average stoich wt concentration*

## 9.13. Geopolymer (Střeleč sand)

### 9.13.1. Sample information

Geopolymers are inorganic, typically ceramic, materials that form long-range, covalently bonded, non-crystalline (amorphous) networks. Raw materials used in the synthesis of silicon-based polymers are mainly rock-forming minerals of geological origin, hence the name: *geopolymer* [148].

### 9.13.2. Spectroscopy results.

The sample was documented using an ordinary mobile phone camera (Figure 216) and a digital DinoLite microscope with magnification 50 (Figure 217) and 200 (Figure 218).


*Figure 216 - Geopolymer sample image*

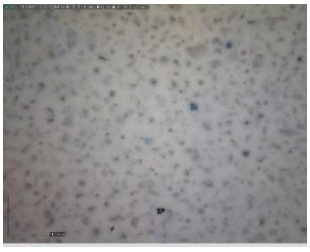

*Figure 217 - Geopolymer DinoLite microscope image, magnification 50*

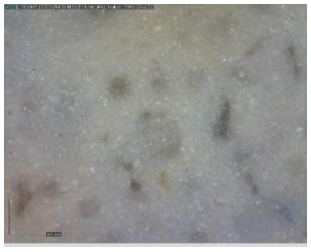

*Figure 218 - Geopolymer DinoLite microscope image, magnification 200*

Purchased reflectance spectroscopy data were processed and analysed using a MATLAB script in Appendix XIII available at enclosed CD. Analysis results are mentioned below, Figure 219 and Figure 220 shows spectral graphs of the sample.

| | |
|---|---|
| Minimum standard deviation: | 1.66% (for λ = 1011.065nm) |
| Maximum standard deviation: | 2.44% (for λ = 2126.820nm) |
| Mean standard deviation: | 2.15% |

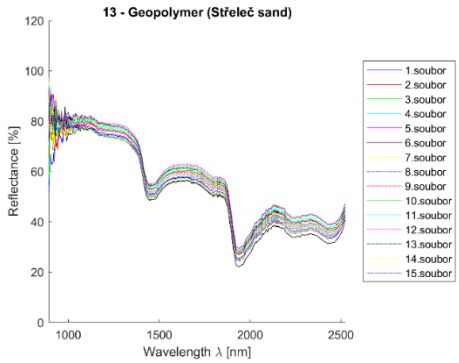


*Figure 219 - Geopolymer - all measurements plot*

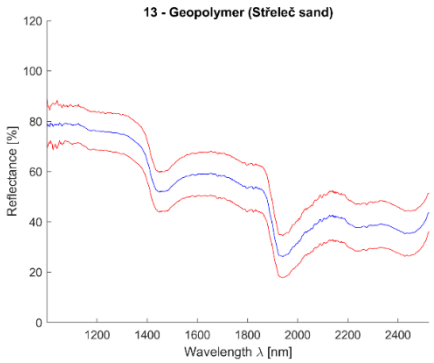


*Figure 220 - Geopolymer - mean value (blue) and 2,5*standard deviation (red)*

### 9.13.3. Electronic microscope findings

The sample was deluged using epoxy resin, sanded using *SiC* papers #2000, #4000, dusted. EDS maps (Figure 221 to Figure 223) show aggregate grain mainly from $SiO_2$. A matrix in between grains consists of *Ca*, *Si*, *Al*, *Na* and *K*.

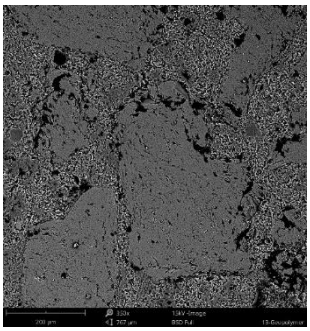

*Figure 221 - Phenom XL Desktop SEM photos - Microscope sample image*

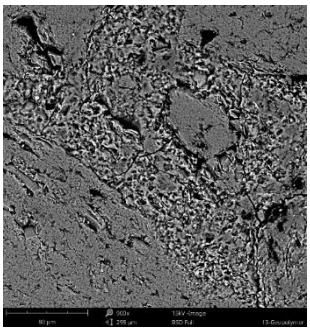

*Figure 222 - Phenom XL Desktop SEM photos - Microscope sample image*

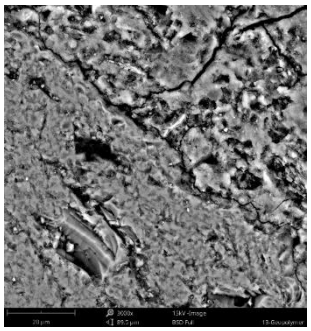

*Figure 223 - Phenom XL Desktop SEM photos - Microscope sample image*

SEM results in the form of EDS map can be seen at Figure 224 and average atomic concentration, average weight concentration and average stoichiometry weight concentration in the form of graphs are shown in Figure 225 to Figure 227.

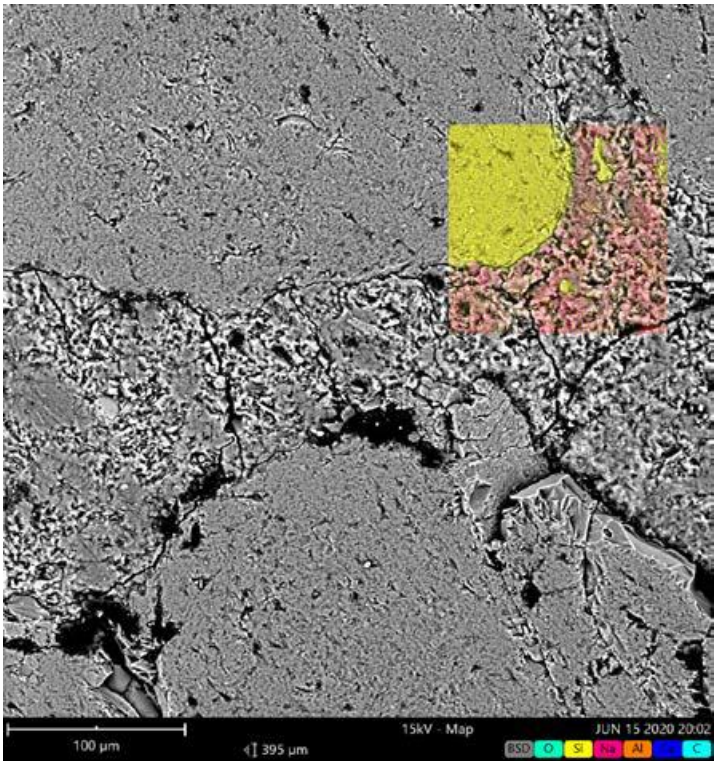


*Figure 224 - Geopolymer EDS map*

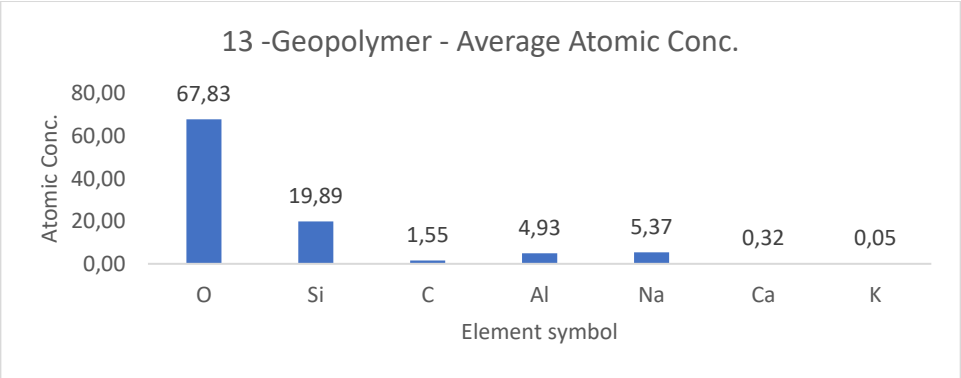


*Figure 225 - Geopolymer average atomic concentration*

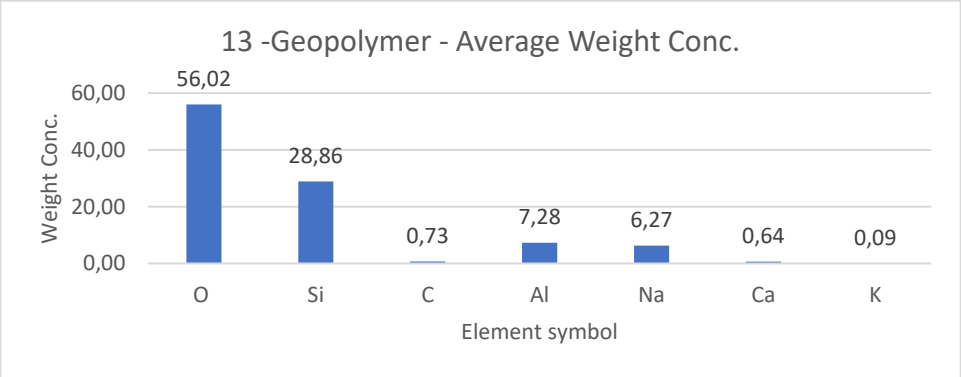


*Figure 226 - - Geopolymer average weight concentration*

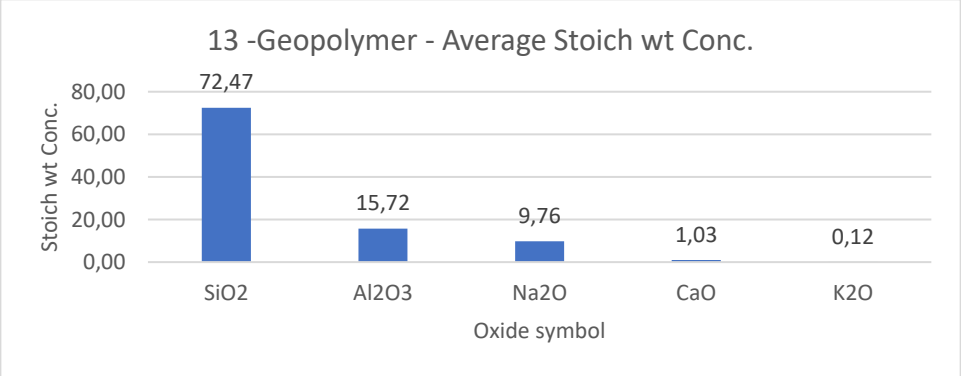


*Figure 227 - Geopolymer average stoich wt concentration*

## 9.14. Střeleč quartz sand

### 9.14.1. Sample information

This well-known quartz sand comes from the village of Střeleč, that is located about 90km northeast from Prague close to the city of Jičín. It has been quarried by a Sklopísek Střeleč company since the late 19$^{th}$ century. The company provides various types and grain sizes, more information online [149].

### 9.14.2. Spectroscopy results

The sample was documented using an ordinary mobile phone camera (Figure 228) and a digital DinoLite microscope with magnification 50 (Figure 229) and 200 (Figure 230).

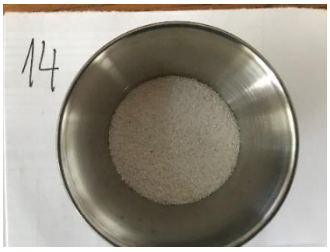


*Figure 228 - Střeleč quartz sand sample image*

*Figure 229- Střeleč quartz sand DinoLite microscope image, magnification 50*

*Figure 230 - Střeleč quartz sand DinoLite microscope image, magnification 200*

Purchased reflectance spectroscopy data were processed and analysed using a MATLAB script in Appendix XIII available at enclosed CD. Analysis results are mentioned below, Figure 231 and Figure 232 shows spectral graphs of the sample.

| | |
|---|---|
| Minimum standard deviation: | 1.33% (for λ = 1249.880nm) |
| Maximum standard deviation: | 2.84% (for λ = 1001.238nm) |
| Mean standard deviation: | 1.58% |

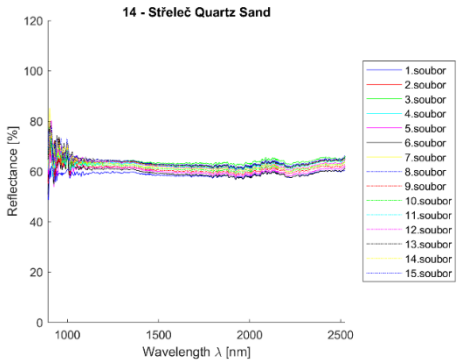


*Figure 231 - Střeleč quartz sand - all measurement plot*

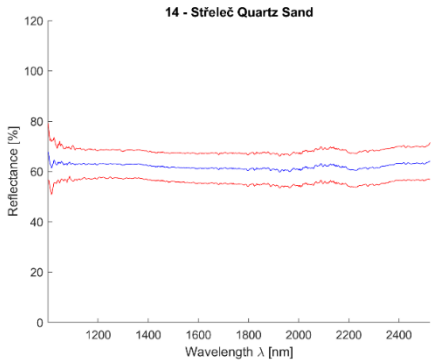


*Figure 232 - Střeleč quartz sand - mean value (blue) and 2,5*standard deviation (red)*

### 9.14.3. Electronic microscope findings

Diminutive sand particles of same size and colour. Particles attached to the disc target and dusted. Particle size varies from 100 to 400 um composed of 100% $SiO_2$. Figure 233 to Figure 235 shows the sample photos.

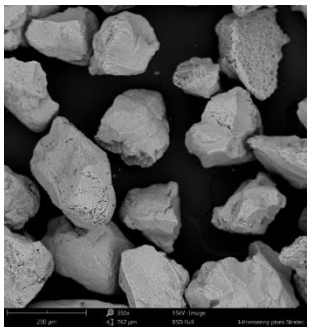

*Figure 233 - Phenom XL Desktop SEM photos - Microscope sample image*

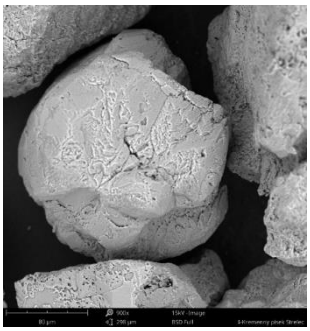

*Figure 234 - Phenom XL Desktop SEM photos - Microscope sample image*

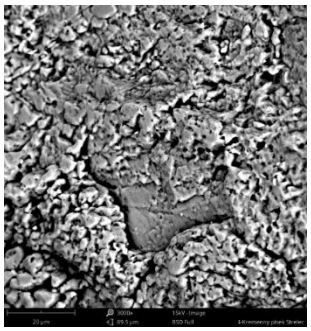

*Figure 235 - Phenom XL Desktop SEM photos - Microscope sample image*

SEM results (average atomic concentration, average weight concentration and average stoichiometry weight concentration) in the form of graphs are shown in Figure 236 to.Figure 238.

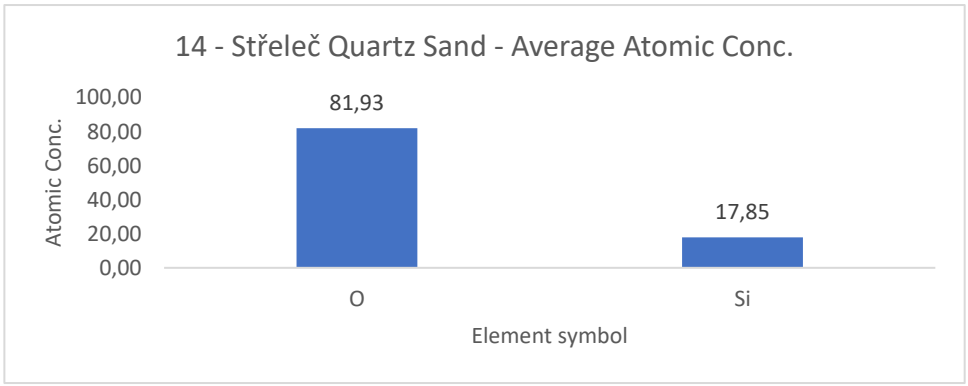


*Figure 236 - Střeleč quartz sand average atomic concentration*

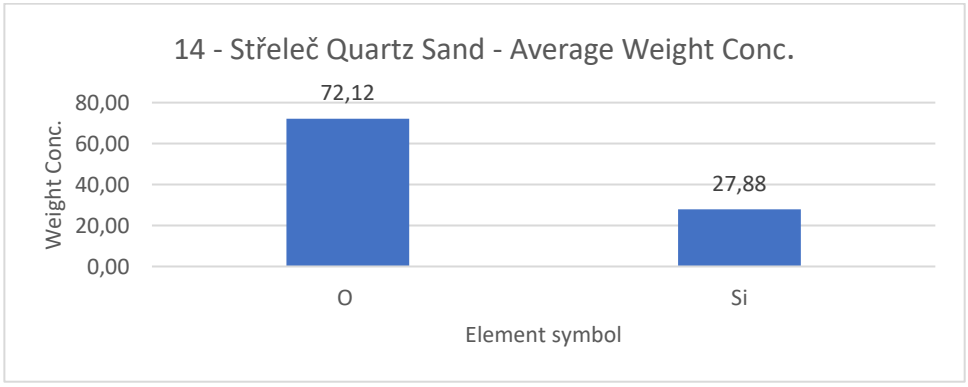


*Figure 237 - Střeleč quartz sand average atomic concentration*

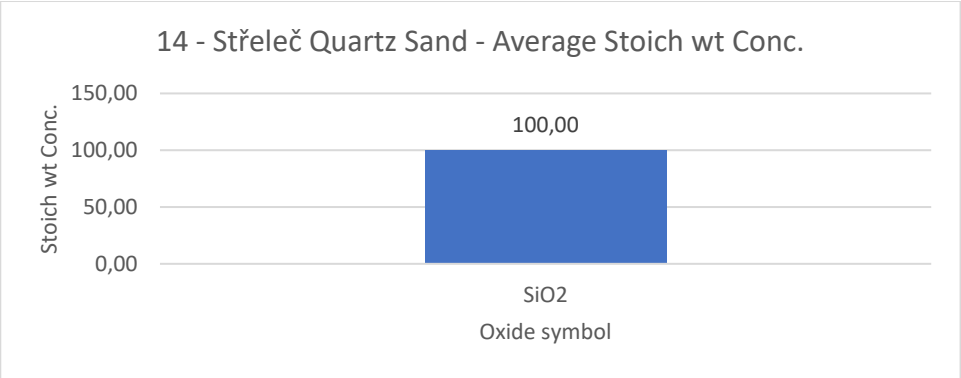


*Figure 238- Střeleč quartz sand average stoich wt concentration*

## 9.15. Borek river sand

### 9.15.1. Sample information

Borek river sand comes from the town of Borek located about 30km northeast next to the Labe river. It has been quarried since 1958 by various national companies that transferred in 1991 into Tapas Borek company that still supplies sands and stones, more information online [150].

### 9.15.2. Spectroscopy results

The sample was documented using an ordinary mobile phone camera (Figure 239) and a digital DinoLite microscope with magnification 50 (Figure 240) and 200 (Figure 241).


*Figure 239 - Borek river sand sample image*

*Figure 240 - Borek river sand DinoLite microscope image, magnification 50*

*Figure 241 - Borek river sand DinoLite microscope image, magnification 200*

Purchased reflectance spectroscopy data were processed and analysed using a MATLAB script in Appendix XIII available at enclosed CD. Analysis results are mentioned below, Figure 242 and Figure 243 shows spectral graphs of the sample.

| | |
|---|---|
| Minimum standard deviation: | 3.76% (for λ = 1030.717nm) |
| Maximum standard deviation: | 4.63% (for λ = 2359.652nm) |
| Mean standard deviation: | 4.18% |

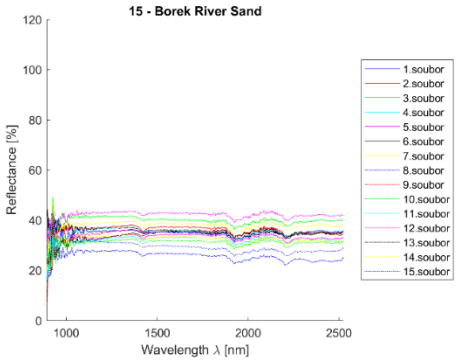


*Figure 242 - Borek river sand - all measurements plot*

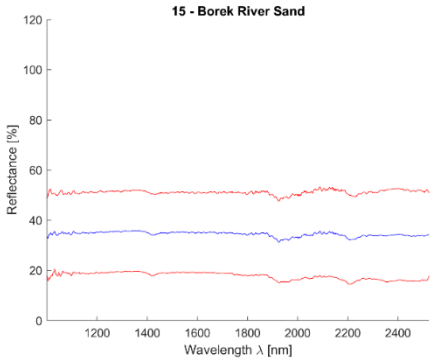


*Figure 243 - Borek river sand mean value (blue) and 2,5*standard deviation (red)*

### 9.15.3. Electronic microscope findings

Borek river sand consists of diverse size and colour aggregate grains. The sand was deluged using epoxy resin, sanded using *SiC* papers #2000, #4000 with water, dusted. SEM photos (Figure 244 to Figure 246) show light grey and white sand grains, dark grey colour represents epoxy resin. 38 single point analysis on various grains were accomplished in total. The majority of grains is from $SiO_2$, some particles include *Ca, Na, K, Mg, Al* and *Fe*.

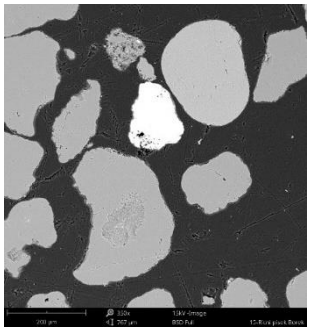

*Figure 244 - Phenom XL Desktop SEM photos - Microscope sample image*

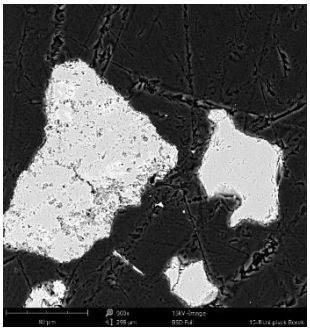

*Figure 245 - Phenom XL Desktop SEM photos - Microscope sample image*

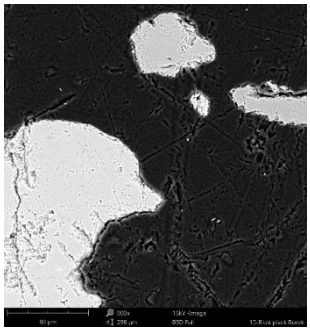

*Figure 246 - Phenom XL Desktop SEM photos - Microscope sample image*

SEM results (average atomic concentration, average weight concentration and average stoichiometry weight concentration) in the form of graphs are shown in Figure 247 to.Figure 249.

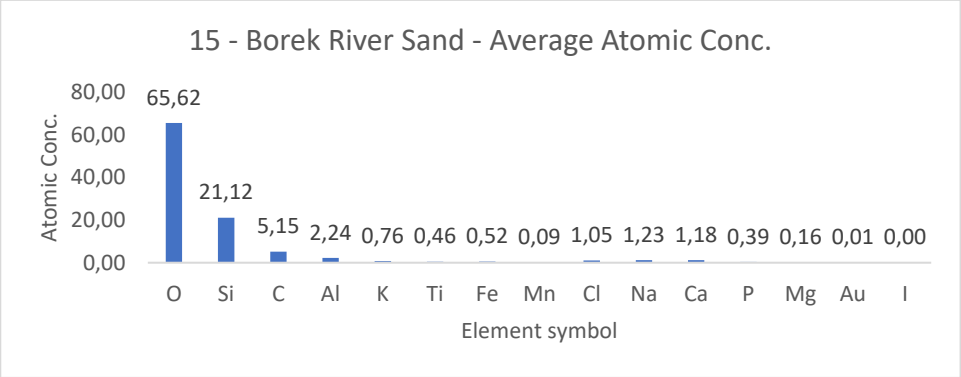


*Figure 247 - Borek river sand average Atomic concentration*

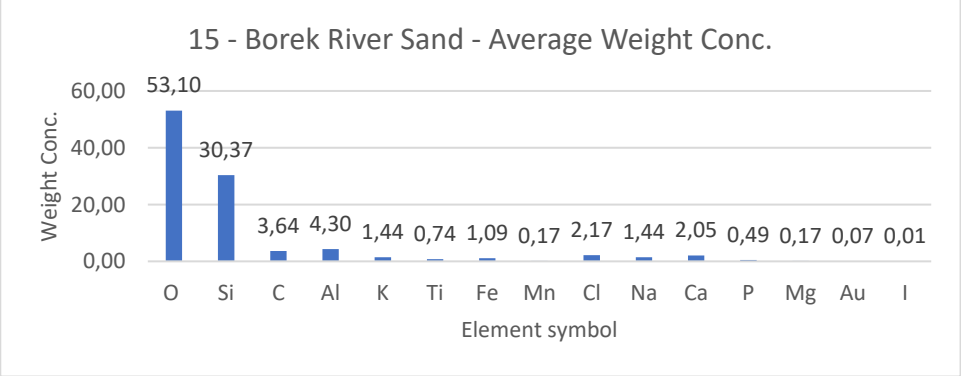


*Figure 248 - Borek river sand average weight concentration*

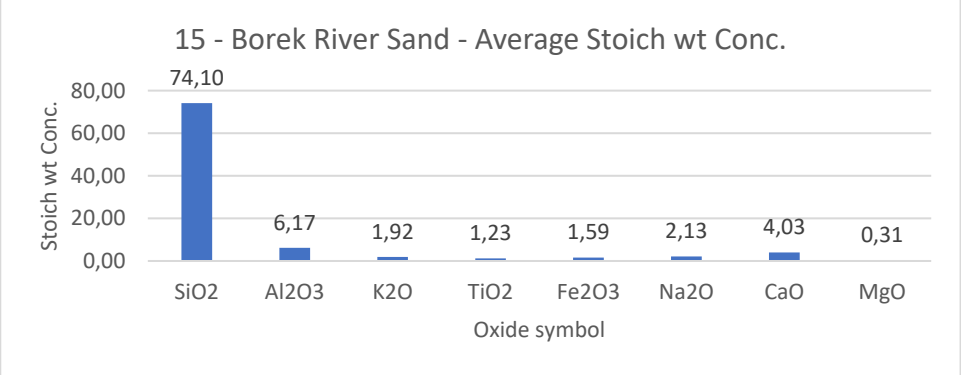


*Figure 249 - Borek river sand stoich wt concentration*

## 9.16. Čerťák lime hydrate

### 9.16.1.Sample information

Lime hydrate is an inorganic compound with the chemical formula $Ca(OH)_2$. It is a colourless crystal or white powder and it is produced when *quicklime* (calcium oxide) is mixed or slaked with water. This sample comes from "Čertovy schody lime works" that quarries lime in the area of Koněprusy and Suchomasty about 40km southwest from Prague [151].

### 9.16.2. Spectroscopy results

The sample was documented using an ordinary mobile phone camera (Figure 250) and a digital DinoLite microscope with magnification 50 (Figure 251) and 200 (Figure 252).


*Figure 250 - Čerťák lime hydrate sample image*

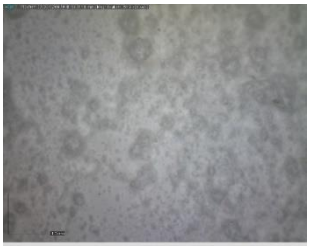

*Figure 251 - Čerťák lime hydrate DinoLite microscope image, magnification 50*

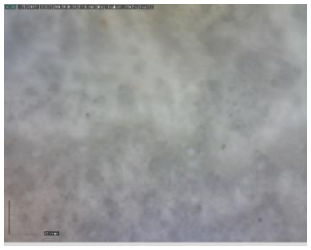

*Figure 252 - Čerťák lime hydrate DinoLite microscope image, magnification 200*

Purchased reflectance spectroscopy data were processed and analysed using a MATLAB script in Appendix XIII available at enclosed CD. Analysis results are mentioned below, Figure 253 and Figure 254 shows spectral graphs of the sample.

| | |
|---|---|
| Minimum standard deviation: | 1.68% (for λ = 2506.066nm) |
| Maximum standard deviation: | 2.99% (for λ = 1020.892nm) |
| Mean standard deviation: | 2.36% |

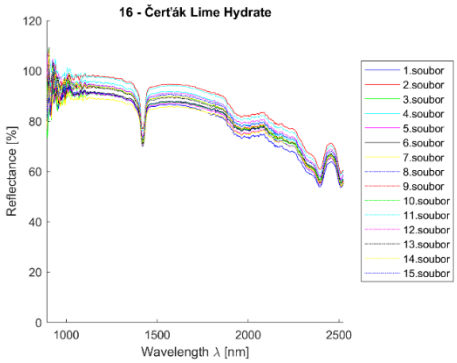


*Figure 253 - Čerťák lime hydrate - all measurements plot*

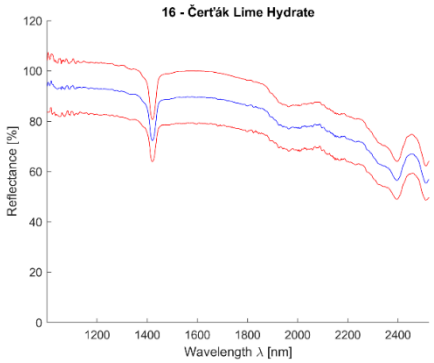


*Figure 254 - Čerťák lime hydrate mean value (blue) and 2,5*standard deviation (red)*

### 9.16.3. Electronic microscope findings

Particles attached to the disc target and dusted. Particle size up to 20 um, dominant elements *Ca and O*. Figure 255 to Figure 257 shows the sample photos.

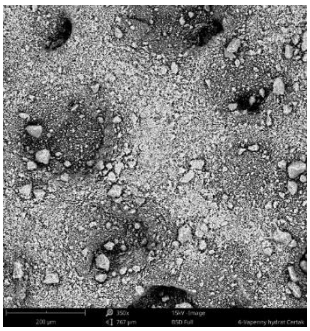

*Figure 255 - Phenom XL Desktop SEM photos - Microscope sample image*

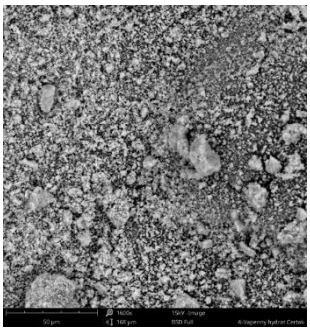

*Figure 256 - Phenom XL Desktop SEM photos - Microscope sample image*

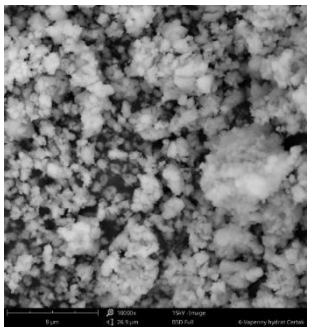

*Figure 257 - Phenom XL Desktop SEM photos - Microscope sample image*

SEM results (average atomic concentration, average weight concentration and average stoichiometry weight concentration) in the form of graphs are shown in Figure 258 to Figure 260.

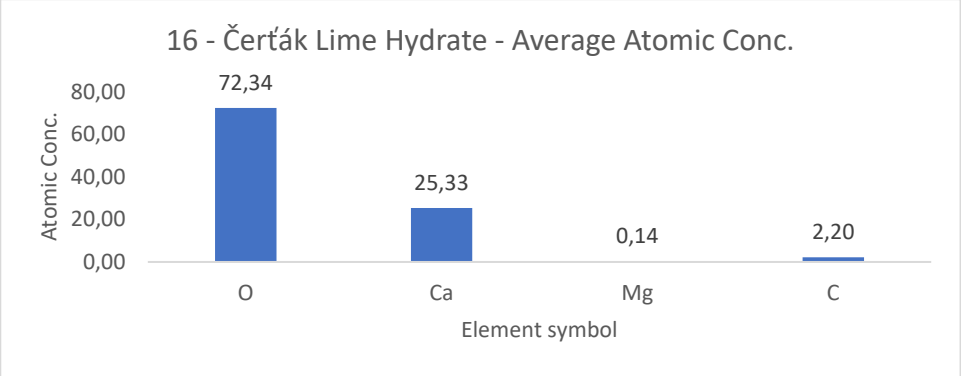


*Figure 258 - Čerťák lime hydrate average atomic concentration*

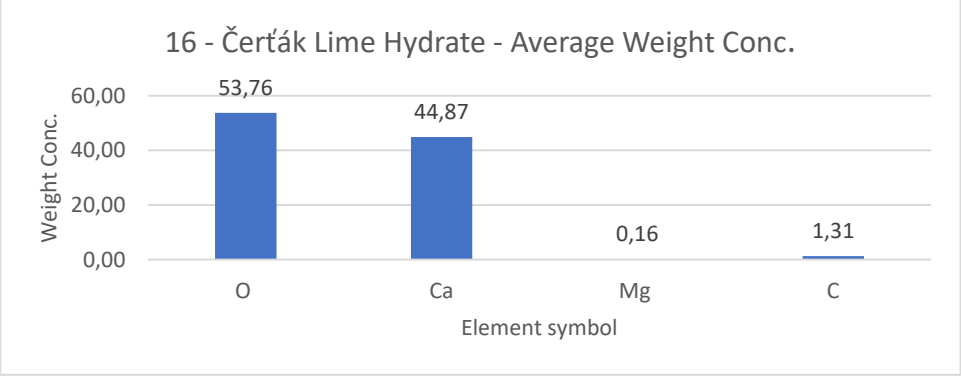


*Figure 259 - Čerťák lime hydrate average weight concentration*

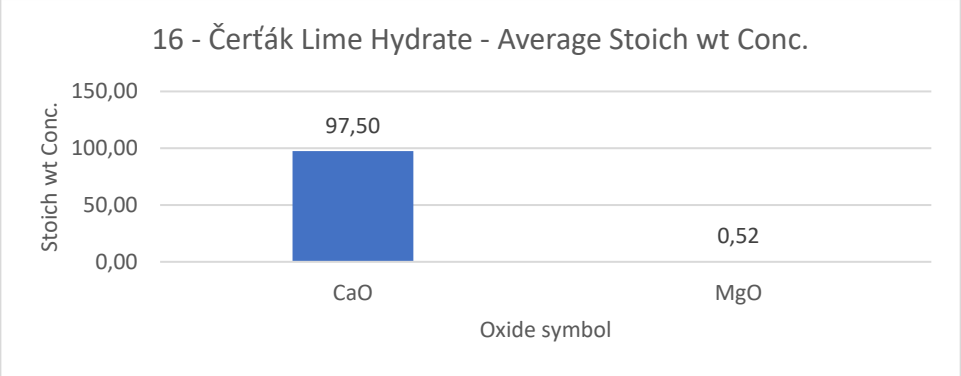


*Figure 260 - Čerťák lime hydrate average stoich wt concentration*

## 9.17. Dolomite standard

### 9.17.1. Sample information

Dolomite is a sedimentary carbonate rock that contains a high percentage of the mineral dolomite, $CaMg(CO_3)_2$. Dolomite has a stoichiometric ratio of nearly equal amounts of magnesium and calcium [152]. For spectra library creation this sample was powdered.

### 9.17.2. Spectroscopy results

The sample was documented using an ordinary mobile phone camera (Figure 261) and a digital DinoLite microscope with magnification 50 (Figure 262) and 200 (Figure 263).


*Figure 261 - Dolomite sample image*

*Figure 262 -Dolomite DinoLite microscope image, magnification 50*

*Figure 263 - Dolomite DinoLite microscope image, magnification 200*

Purchased reflectance spectroscopy data were processed and analysed using a MATLAB script in Appendix XIII available at enclosed CD. Analysis results are mentioned below, Figure 264 and Figure 265 shows spectral graphs of the sample.

| | |
|---|---|
| Minimum standard deviation: | 2.62% (for λ = 1024.167nm) |
| Maximum standard deviation: | 4.11% (for λ = 1001.238nm) |
| Mean standard deviation: | 3.27% |

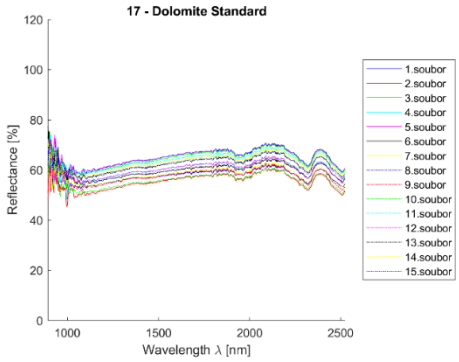


*Figure 264 – Dolomite – all measurements plot*

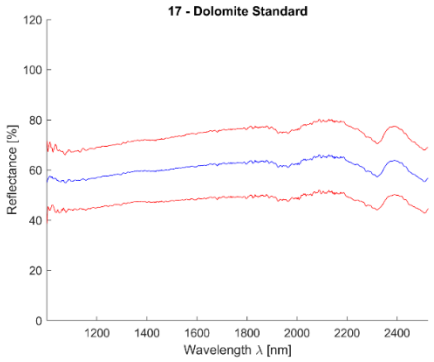


*Figure 265 - Dolomite mean value (blue) and 2,5*standard deviation (red),*

### 9.17.3. Electronic microscope findings

Particles attached to the disc target and dusted. Particle size up to 90 um, dominant elements *Ca*, *Mg* and *O*, minority elements *Al*, *Si* and *C*. Sample is pure rock Dolomite – $CaMg(CO_3)_2$. Figure 266 to Figure 268 shows the sample photos.

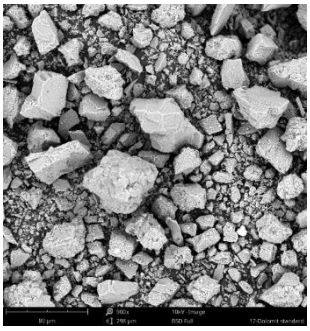

*Figure 266 - Phenom XL Desktop SEM photos - Microscopic sample image*

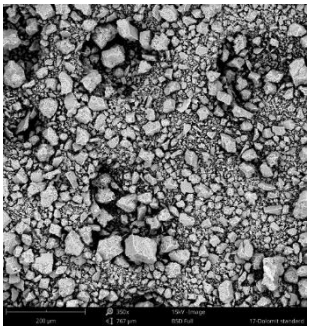

*Figure 267 - Phenom XL Desktop SEM photos - Microscopic sample image*

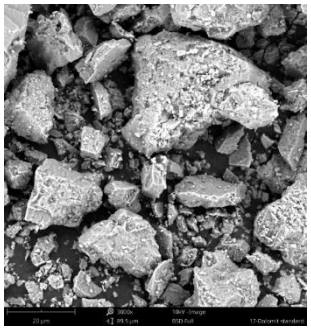

*Figure 268 - Phenom XL Desktop SEM photos - Microscopic sample image*

SEM results (average atomic concentration, average weight concentration and average stoichiometry weight concentration) in the form of graphs are shown in Figure 269 to Figure 271.

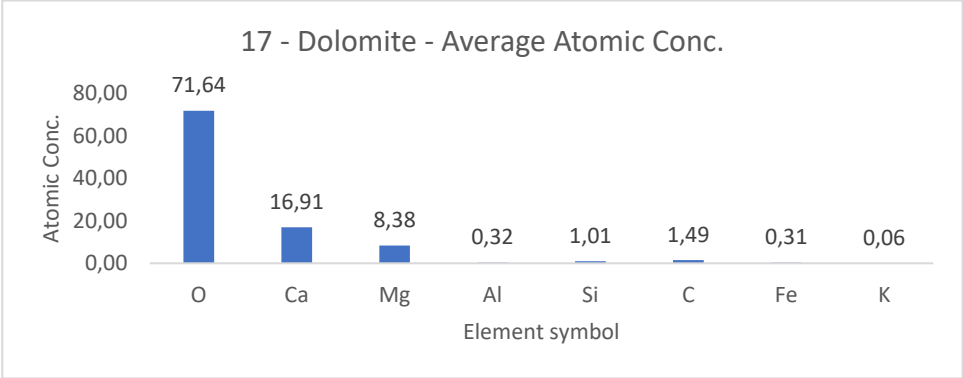


*Figure 269 - Dolomite - Average atomic concentration*

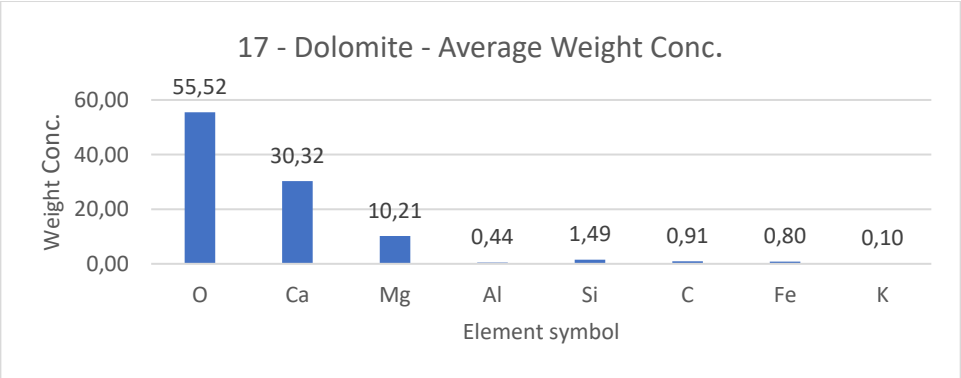


*Figure 270 - Dolomite - Average weight concentration*

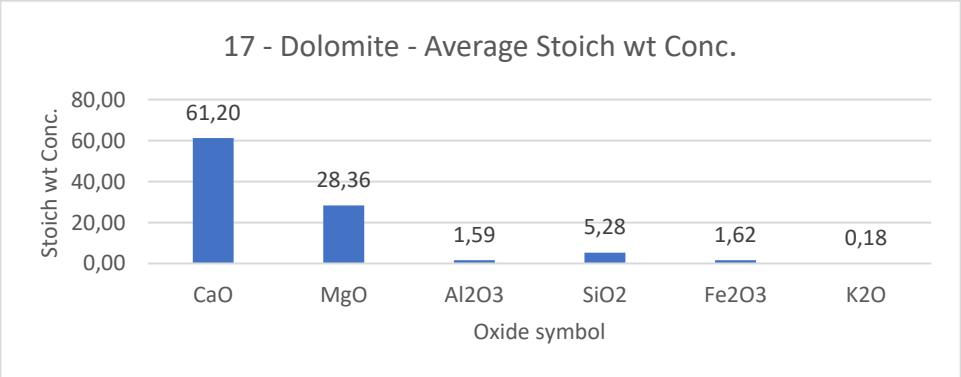


*Figure 271 – Dolomite – Average stoich wt concentration*

## 9.18. Gypsum standard

### 9.18.1. Sample information

Gypsum ($CaSO_4 \cdot 2H_2O$) is an evaporite mineral mostly found in layered sedimentary [153]. This form of gypsum is manufactured by gypsum rock heat decomposition at temperatures 130-150 °C. After mixing with water rehydration occurs and white or grey matter is created. This matter is relatively strong and solid, more information can be found in Chapter 7.4.

### 9.18.2. Spectroscopy results

The sample was documented using an ordinary mobile phone camera (Figure 272) and a digital DinoLite microscope with magnification 50 (Figure 273) and 200 (Figure 274).


*Figure 272 - Gypsum sample image*

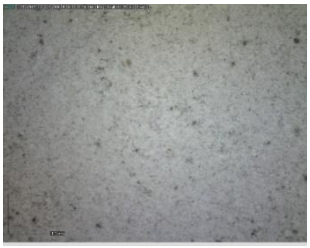

*Figure 273 - Gypsum DinoLite microscope image, magnification 50*

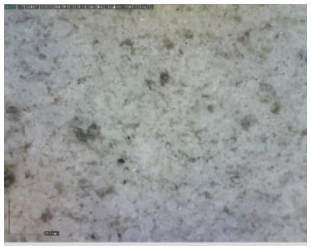

*Figure 274 - Gypsum DinoLite microscope image, magnification 200*

Purchased reflectance spectroscopy data were processed and analysed using a MATLAB script in Appendix XIII available at enclosed CD. Analysis results are mentioned below, Figure 275 and Figure 276 shows spectral graphs of the sample.

Minimum standard deviation: 2.17% (for λ = 1953.348nm)
Maximum standard deviation: 3.57% (for λ = 1697.651m)
Mean standard deviation: 3.10%

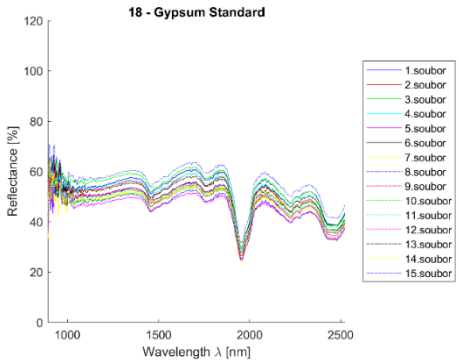


*Figure 275 – Gypsum – all measurements plot*

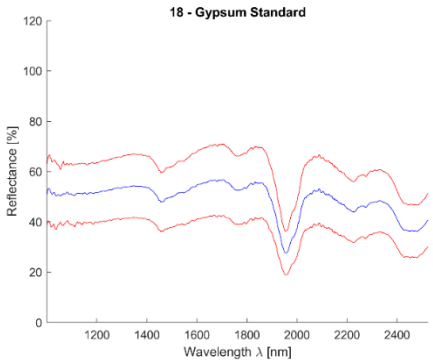


*Figure 276 - Gypsum mean value (blue) and 2,5*standard deviation (red)*

### 9.18.3. Electronic microscope findings

Particles attached to the disc target and dusted. Particle size up to 200 um, dominant elements *Ca, S* and *O*, minority elements *Al, K, Mg, Fe* and Si. Minority elements are probably contaminants or measurement was misinterpreted due to unevenness of the particle surface. Ideal values of atomic concentration *Ca* = 16,67%, *S* = 16,67%, respectively the *Ca : S* ratio should be 1 : 1. The sample is Gypsum - a calcium sulphate mineral with formula $CaSO_4*2H_2O$. Figure 277 to Figure 279 shows the sample photos.

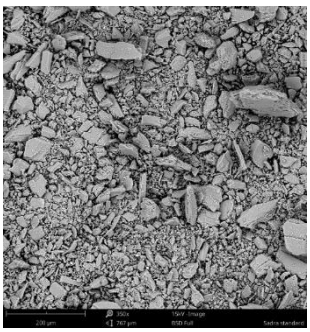

*Figure 277 - Phenom XL Desktop SEM photos - Microscopic sample image*

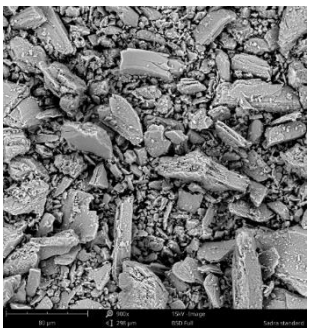

*Figure 278 - Phenom XL Desktop SEM photos - Microscopic sample image*

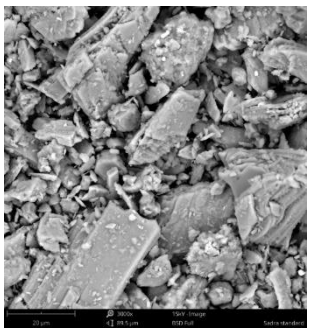

*Figure 279 - Phenom XL Desktop SEM photos - Microscopic sample image*

SEM results (average atomic concentration, average weight concentration and average stoichiometry weight concentration) in the form of graphs are shown in Figure 280 to Figure 282.

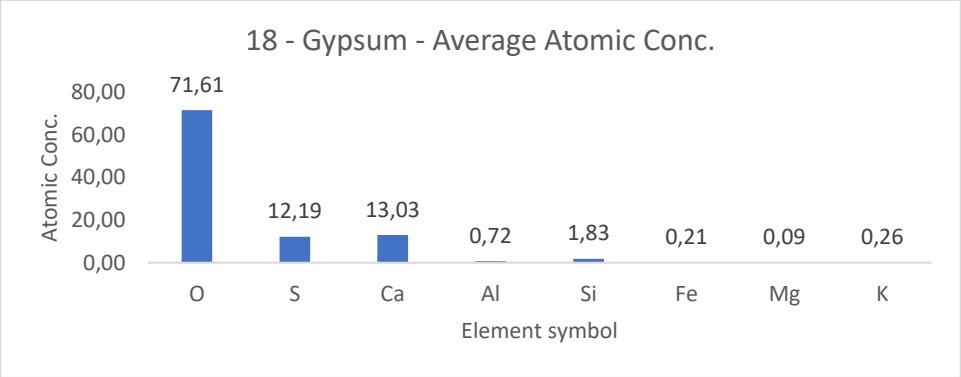


*Figure 280 – Gypsum – Average atomic concentration*

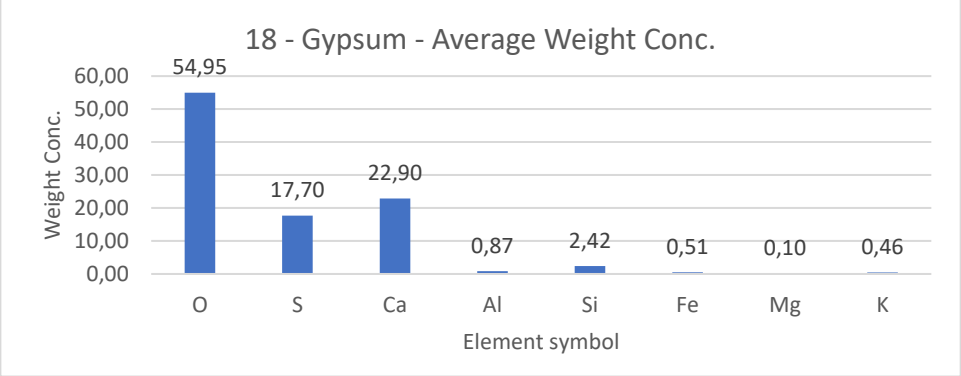


*Figure 281 – Gypsum – Average weight concentration*

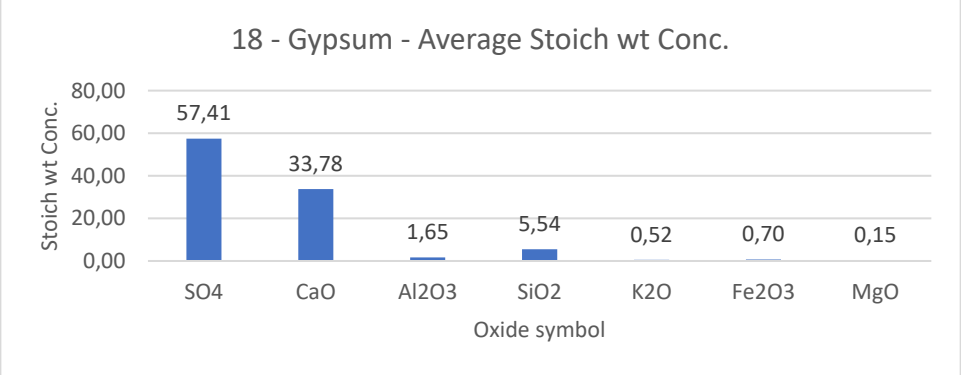


*Figure 282 – Gypsum – Average Stoich wt concentration*

## 9.19. Metakaolin L05

### 9.19.1. Sample information

Metakaolin is a highly reactive aluminium-silicon pozzolan (Chapter 7.2), that creates stable hydrate after mixing with lime and water and gives mortar hydraulic properties. After heating clay with fundamental mineral mixture kaolinite to temperatures between 500°C and 600°C a structural water loss occurs. This causes a kaolinite crystal structure deformation and a waterless reakcite form "Metakaolinite" is created [147], [154].

### 9.19.2. Spectroscopy results

The sample was documented using an ordinary mobile phone camera (Figure 283) and a digital DinoLite microscope with magnification 50 (Figure 284) and 200 (Figure 285).


*Figure 283 - Metakaolin L05 sample image*

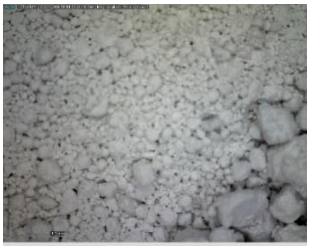

*Figure 284 - Metakaolin L05 DinoLite microscope image, magnification 50*

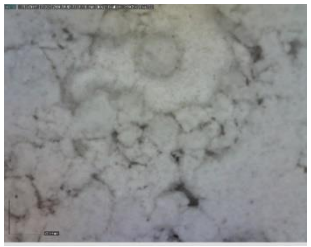

*Figure 285 - Metakaolin L05 DinoLite microscope image, magnification 200*

Purchased reflectance spectroscopy data were processed and analysed using a MATLAB script in Appendix XIII available at enclosed CD. Analysis results are mentioned below, Figure 286 and Figure 287 shows spectral graphs of the sample.

| | |
|---|---|
| Minimum standard deviation: | 2.72% (for λ = 1066.739nm) |
| Maximum standard deviation: | 3.42% (for λ = 1024.167nm) |
| Mean standard deviation: | 3.18% |

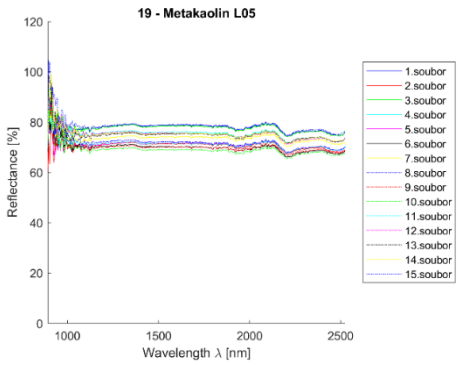


*Figure 286 – Metakaolin – All measurements plot*

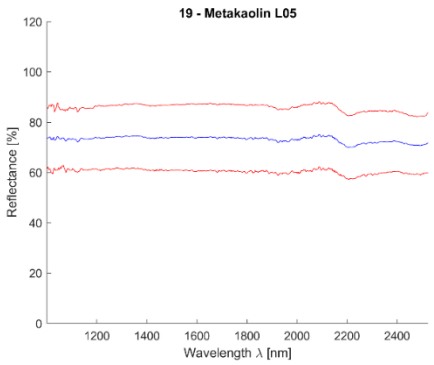


*Figure 287 - Metakaolin L05 mean value (blue) and 2,5*standard deviation (red)*

### 9.19.3. Electronic microscope findings

Particles attached to the disc target and dusted. Very small particle size up to 20 um, dominant elements *Si, Al* and *O*. Figure 288 to Figure 290 shows the sample photos.

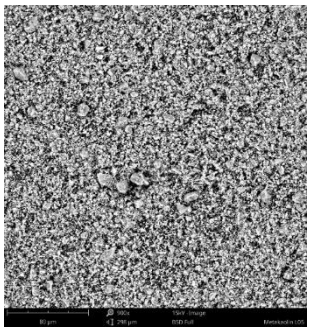

*Figure 288 - Phenom XL Desktop SEM photos - Microscopic sample image*

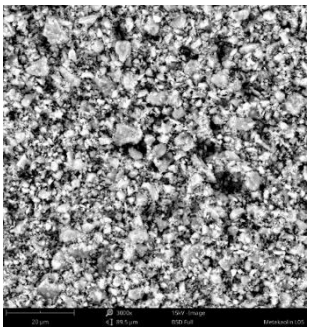

*Figure 289 - Phenom XL Desktop SEM photos - Microscopic sample image*

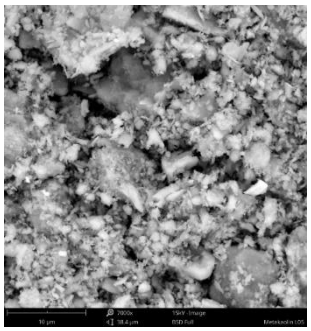

*Figure 290 - Phenom XL Desktop SEM photos - Microscopic sample image*

SEM results (average atomic concentration, average weight concentration and average stoichiometry weight concentration) in the form of graphs are shown in Figure 291 to Figure 293.

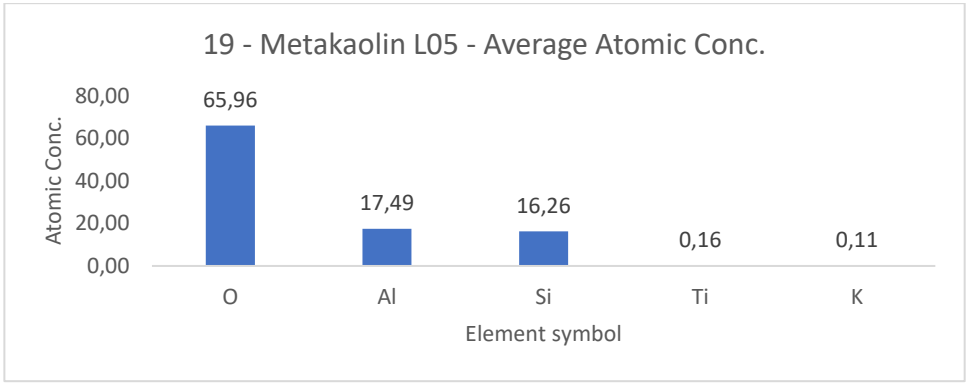


*Figure 291 - Metakaolin - Average atomic concentration*

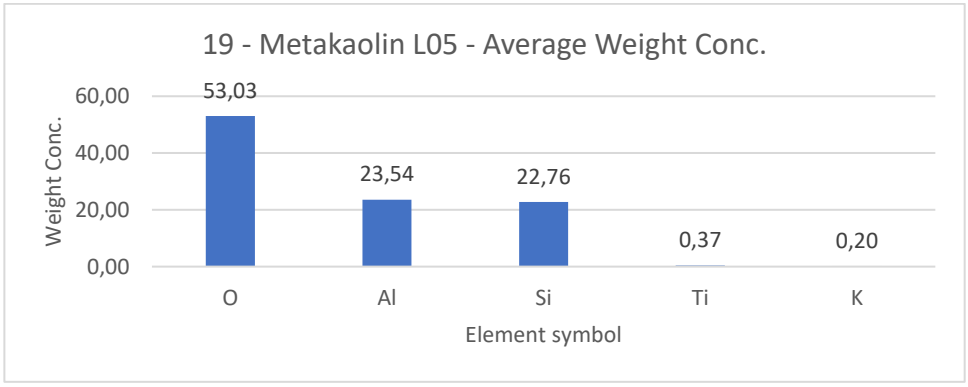


*Figure 292 - Metakaolin - Average weight concentration*

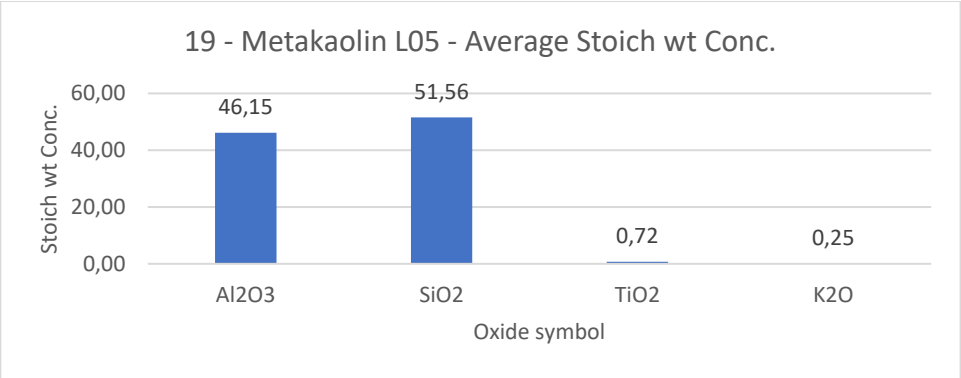


*Figure 293 - Metakaolin - Average stoich wt concentration*

## 9.20. Clay mortar (Claytec)

### 9.20.1. Sample information

Claytec is a clay mortar consisting of clay, clay soil and quartz sand manufactured by the Claytec company [155].

### 9.20.2. Spectroscopy results

The sample was documented using an ordinary mobile phone camera (Figure 294) and a digital DinoLite microscope with magnification 50 (Figure 295) and 200 (Figure 296).

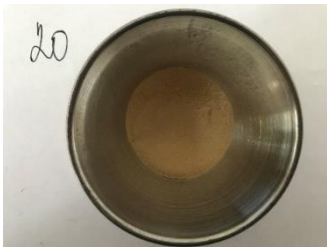


*Figure 294 - Claytec sample image*

*Figure 295 - Claytec DinoLite microscope image, magnification 50*

*Figure 296 - Claytec DinoLite microscope image, magnification 200*

Purchased reflectance spectroscopy data were processed and analysed using a MATLAB script in Appendix XIII available at enclosed CD. Analysis results are mentioned below, Figure 297 and Figure 298 shows spectral graphs of the sample.

| | |
|---|---|
| Minimum standard deviation: | 2.22% (for λ = 1063.465nm) |
| Maximum standard deviation: | 3.37% (for λ = 1004.514nm) |
| Mean standard deviation: | 2.72% |

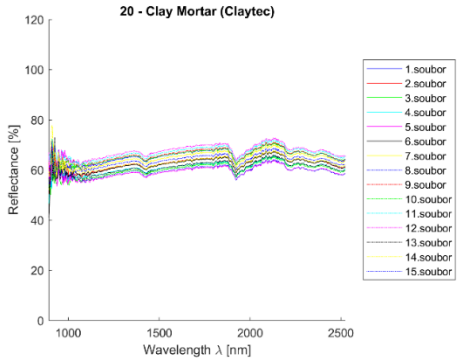


*Figure 297 – Claytec – All measurements plot*

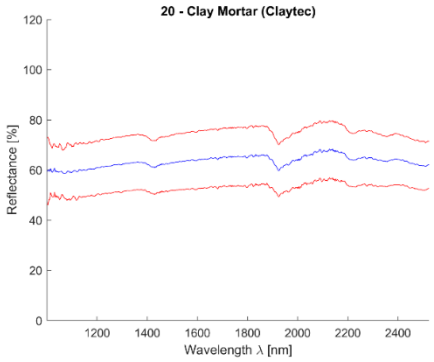


*Figure 298 - Claytec mean value (blue) and 2,5*standard deviation (red)*

### 9.20.3. Electronic microscope findings

Particles attached to the disc target and dusted. Small particle size sitting on larger ones are released during SEM/EDS analysis (Figure 299 to Figure 301). Very small particle size, particle size up to 80 um, dominant elements *Si*, *Al* and *O*, minority elements *Ca*, *Fe*, *K* and *Mg*.

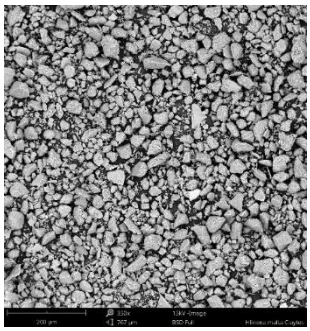

*Figure 299 - Phenom XL Desktop SEM photos - Microscopic sample image*

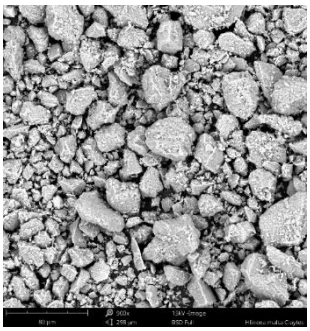

*Figure 300 - Phenom XL Desktop SEM photos - Microscopic sample image*

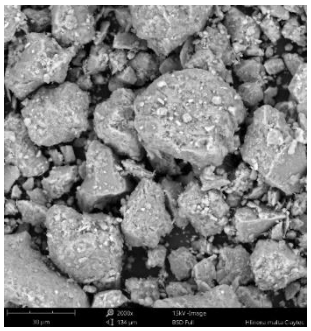

*Figure 301 - Phenom XL Desktop SEM photos - Microscopic sample image average Atomic concentration*

SEM results (average atomic concentration, average weight concentration and average stoichiometry weight concentration) in the form of graphs are shown in Figure 302 to Figure 304.

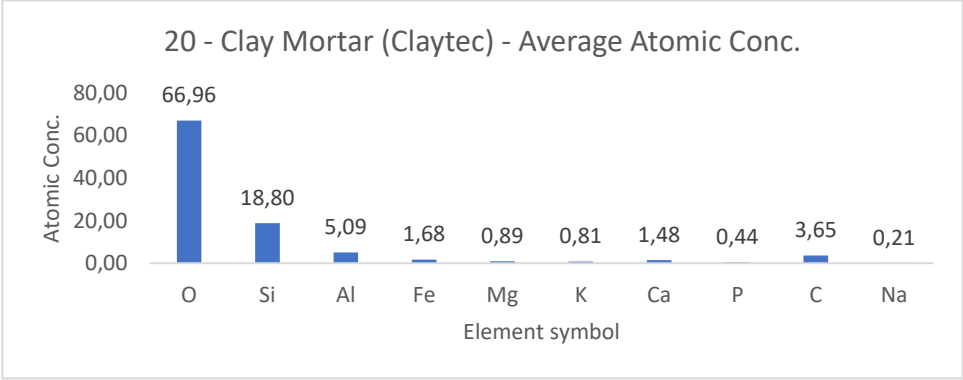


*Figure 302 - Claytec -Average atomic concentration*

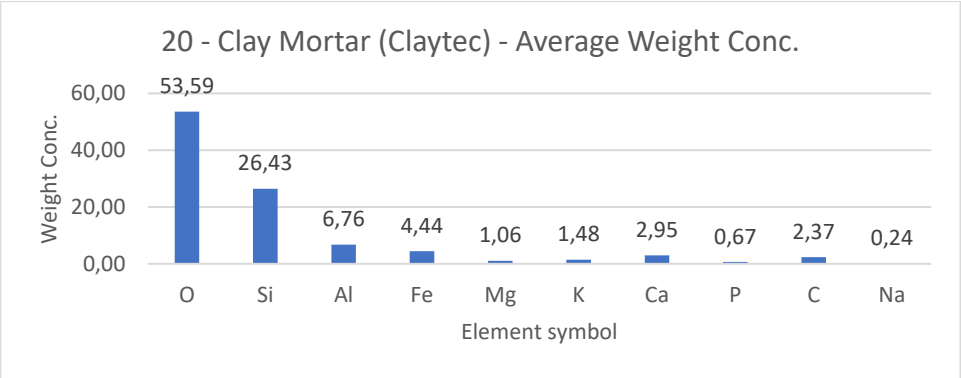


*Figure 303 - Claytec - Average weight concentration*

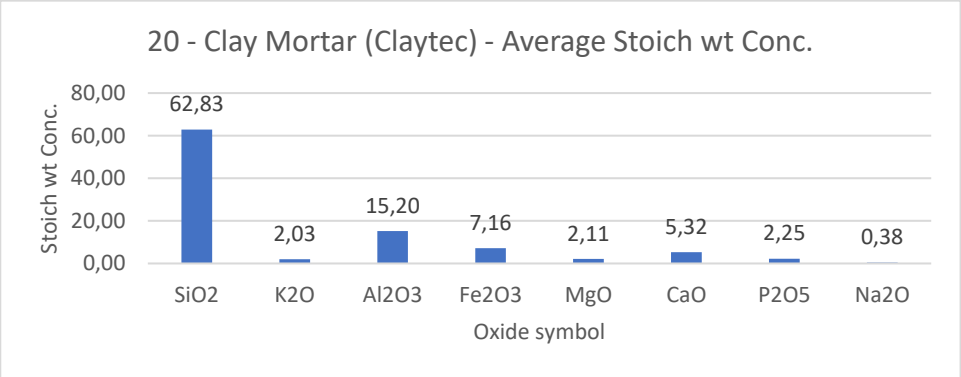


*Figure 304 - Claytec - Average Stoich wt concentration*

## 9.21. Material comparison

Twenty different materials have been added to the material spectral library (Figure 305). They were chosen to determine Czech and Central Europe composition of plasters and mortars. These materials can be divided into eight sets according to their composition and therefore spectral curve shape. Namely: lime mortars (Figure 306), limes (Figure 307), sandstones (Figure 308), quartz and sands (Figure 309), geopolymer, gypsum, marlstone (Figure 310) and other (Figure 311).

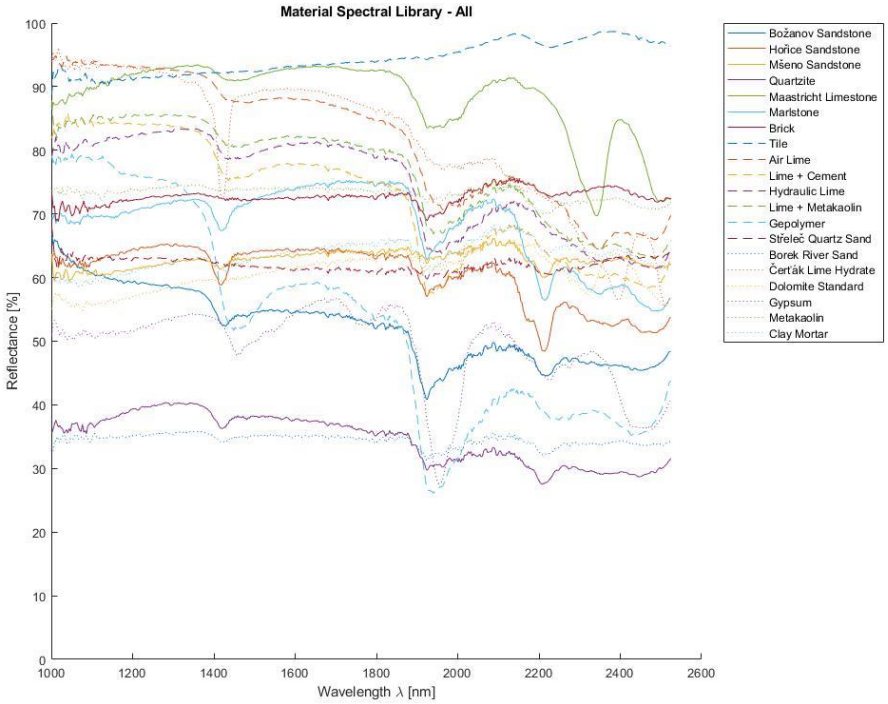


*Figure 305 – Material spectral library – All materials spectral curve*

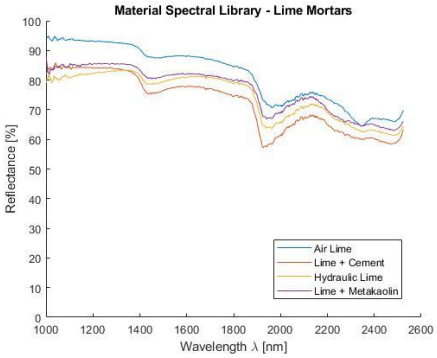


*Figure 306 – Material spectral library – Lime mortars spectral curve*

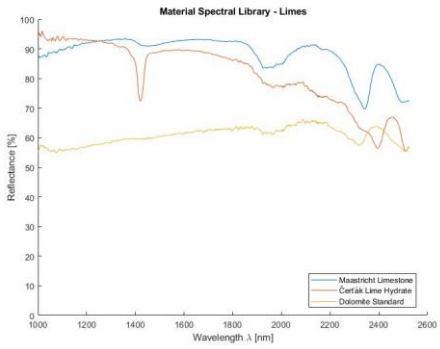


*Figure 307 – Material spectral library – Limes spectral curve*

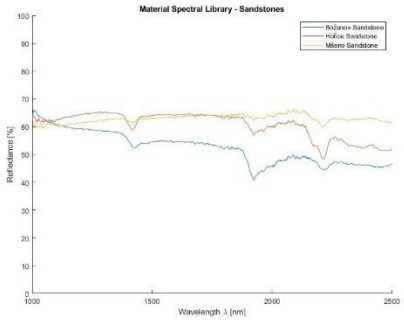


*Figure 308 – Material spectral library – Sandstones spectral curve*

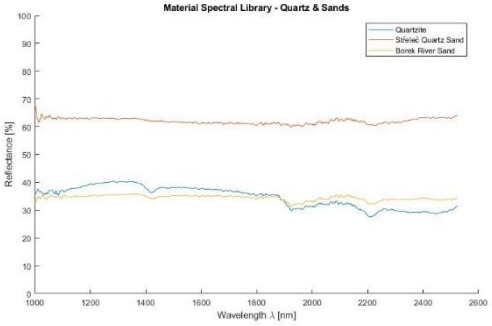


*Figure 309 – Material spectral library – Quartz & Sands spectral curve*

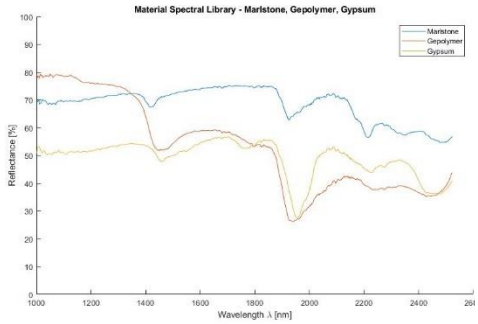


*Figure 310 – Material spectral library – Marlstone, Geopolymer and Gypsum spectral curve*

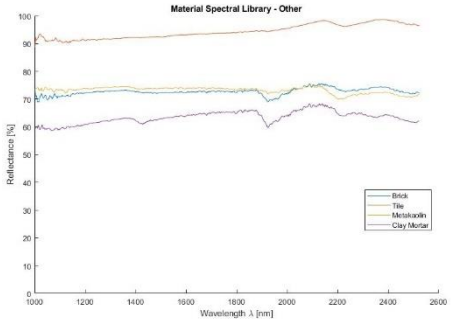


*Figure 311 – Material spectral library – Other materials spectral curve*

Table 3 shows the minimum, maximum and average standard deviation of each material. The average standard deviation lies between 1,54% (Mšeno sandstone) to 4,18% (Borek river sand). The high standard deviation of the Borek river sand sample is caused by the fact, that it is assembled by various sand grains depending on the measured point. An average standard deviation of all samples is equal to 2,45% and can be found sufficient.

*Table 3 – CTU Material Spectral Library – data quality*

| No. | Material | Standard Deviation [%] | | |
|---|---|---|---|---|
| | | Minimum | Maximum | Average |
| 1 | Božanov sandstone | 2,19 | 3,46 | 2,71 |
| 2 | Hořice sandstone | 1,32 | 2,99 | 1,69 |
| 3 | Mšeno sandstone | 1,33 | 3,96 | 1,54 |
| 4 | Quartzite | 1,85 | 2,82 | 2,12 |
| 5 | Maastricht limestone | 1,98 | 3,60 | 2,39 |
| 6 | Přední Kopanina marlstone | 1,13 | 2,61 | 1,72 |
| 7 | Brick | 2,12 | 3,01 | 2,80 |
| 8 | Tile | 1,84 | 3,85 | 2,37 |
| 9 | Air lime mortar | 1,60 | 3,08 | 2,07 |
| 10 | Lime + cement binder mortar | 2,17 | 3,23 | 2,93 |
| 11 | Hydraulic lime mortar | 1,41 | 2,37 | 1,86 |
| 12 | Lime + Metakaolin binder mortar | 1,73 | 3,77 | 2,18 |
| 13 | Geopolymer (střeleč sand) | 1,66 | 2,44 | 2,15 |
| 14 | Střeleč quartz sand | 1,33 | 2,84 | 1,58 |
| 15 | Borek river sand | 3,76 | 4,63 | 4,18 |
| 16 | Čerťák lime hydrate | 1,68 | 2,99 | 2,36 |
| 17 | Dolomite standard | 2,62 | 4,11 | 3,27 |
| 18 | Gypsum standard | 2,17 | 3,57 | 3,10 |
| 19 | Metakaolin L05 | 2,72 | 3,42 | 3,18 |
| 20 | Clay mortar (Claytec) | 2,22 | 3,37 | 2,72 |

# 10. Analyses of plasters, mortars and rock

Twelve test samples were analysed representing three sets – plasters, mortars and rock. They were originally not only from central Europe (the Czech Republic, Slovakia) but also worldwide (Iraq).

Five spectral analysis methods were conducted for each sample – Spectral Angle Mapper (SAM) in Matlab, Spectral Information Divergence (SID) in Matlab, Linear Non-Negative Least Squares (NNLS) used in QSdata programme, Spectral Feature Fitting (SFF) in ENVI software and Binary Encoding (BE) in ENVI. A detailed explanation of these methods is in Chapter 4.2.7. Due to the huge amount of data only average ranking table is shown for each sample. Results from all methods are shown in Appendix 1-11

Electron microscope findings are derived into several phases that represent areas with specific material characteristics. These phases are then called majority/minority depending on how often they can be found on a sample. Each phase was then individually analysed by experts.

## 10.1. Sample 1 - Skorkov

### 10.1.1. Sample information

The sample has been collected from the Skorkov village, the Czech Republic. Skorkov [156] is situated in Central Bohemia, about 40km northeast from Prague in a historical underground corridor probably from the Thirty-year war in the 17$^{th}$ century. This sample is presupposed to be a lime mortar.

### 10.1.2. Spectroscopy results

The sample was documented using an ordinary mobile phone camera (Figure 312) and a digital DinoLite microscope with magnification 50 (Figure 313) and 200 (Figure 314).

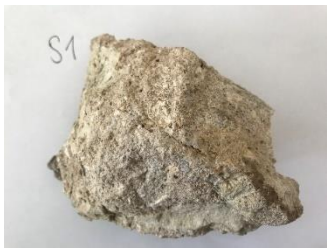


*Figure 312 - Sample 1 image*

*Figure 313 - Sample 1 DinoLite microscope image, magnification 50*

*Figure 314 - Sample 1 DinoLite microscope image, magnification 200*

Purchased reflectance spectroscopy data were processed and analysed using a MATLAB script in Appendix XIII available at enclosed CD. Analysis results are mentioned below, Figure 315 and Figure 316 shows spectral graphs of the sample.

| | |
|---|---|
| Minimum standard deviation: | 1.89% (for λ = 1011.065nm) |
| Maximum standard deviation: | 6.42% (for λ = 2344.278nm) |
| Mean standard deviation: | 4.15% |

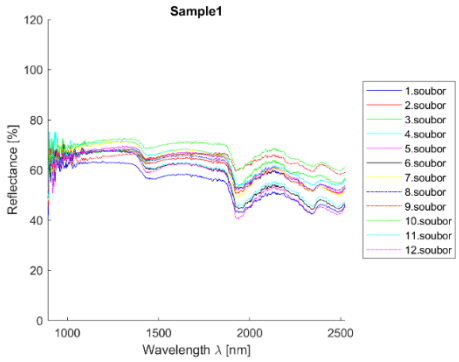


*Figure 315 – Sample 1 - all measurements plot*

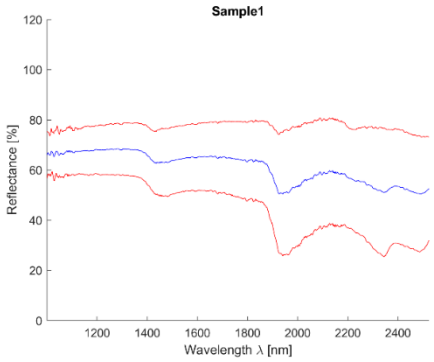


*Figure 316 – Sample 1 - mean value (blue) and 2,5*standard deviation (red)*

Table 4 shows the representation of the first ten materials derived from all methods according to their ranking. The average is an arithmetic mean of their determination ranking; standard deviation is also shown in the table to provide a level of confidence. Results of individual analysis can be found in Appendix I.

*Table 4 – Sample 1 - Average material ranking in processed analysis*

| Material | Average | Std. Dev |
|---|---|---|
| 10-Lime + Cement Binder Mortar | 4,4 | 2,2 |
| 11-Hydraulic Lime Mortar (NHL5) | 5,2 | 4,5 |
| 12-Lime + Metakaolin Binder Mortar | 5,25 | 4,5 |
| 9-Air Lime Mortar | 5,75 | 5,4 |
| 1-Božanov Sandstone | 6,75 | 0,8 |
| 2-Hořice Sandstone | 8,5 | 5,4 |
| 18-Gypsum Standard | 9 | 2,3 |
| 6-Přední Kopanina Marlstone | 9,25 | 2,2 |
| 13-Geopolymer (Střeleč sand) | 10 | 6,2 |
| 20-Clay Mortar (Claytec) | 10 | 6,6 |

Spectral curve description

The curve is more or less flat with less conspicuous water absorption band at 1450nm and more distinct at 1950nm. Reflectance value fluctuates around 50%

Individual analysis results

- SAM – correct detection of lime (lime mortars) and sand;
- SID - correct detection of lime (Dolomite) and sand, false detection of marlstone;
- NNLS – distinct representation of lime materials at the expense of sands (geopolymer); an occurrence of clay/clay mortar (due to present *Al*); false detection of gypsum;
- SFF – correct detection of lime mortars, a small amount of sands (geopolymer), the occurrence of clay (due to present *Al*); false detection of gypsum (6$^{th}$ place);
- BE – similar results as SAM - correct detection of lime (lime mortars) and sand;

- Average - Shows correctly detected lime mortars and sand, high standard deviation values.

Conclusion

The sample consists of lime and sand with smaller *Al* and *Mg* additives

### 10.1.3. Electronic microscope findings

- Phase 1 – light grey to white grains – aggregated $SiO_2$ (*Ca* minor occurrence);
- Phase 2 – matrix between grains – white areas consisting of *CaO* (*Si* minor occurrence);
- Phase 3 – dark grey matrix between grains – a high percentage of $SiO_2$; the increased proportion of *Al* and *Ca* oxides in certain points; *Mg*, *K* and *Na* minor occurrence;
- Phase 4 – Dark grey matrix, not visually visible from phase 3 shows a high proportion of *C* and *Cl* that denotes penetration of the epoxy resin into the matrix.

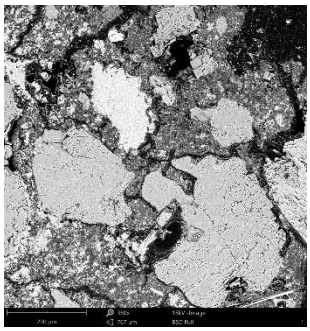

*Figure 317 - Phenom XL Desktop SEM photos - Microscopic sample image*

*Figure 318 - Phenom XL Desktop SEM photos - Microscopic sample image*

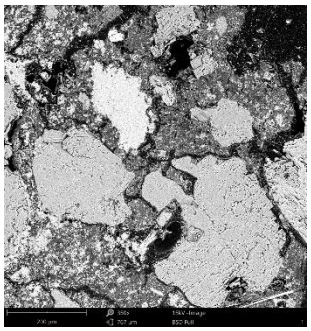

*Figure 319 - Phenom XL Desktop SEM photos - Microscopic sample image*

Figure 317 to Figure 319 shows the sample photos. SEM results (average atomic concentration, average weight concentration and average stoichiometry weight concentration) in the form of graphs are shown in Figure 320 to Figure 322.

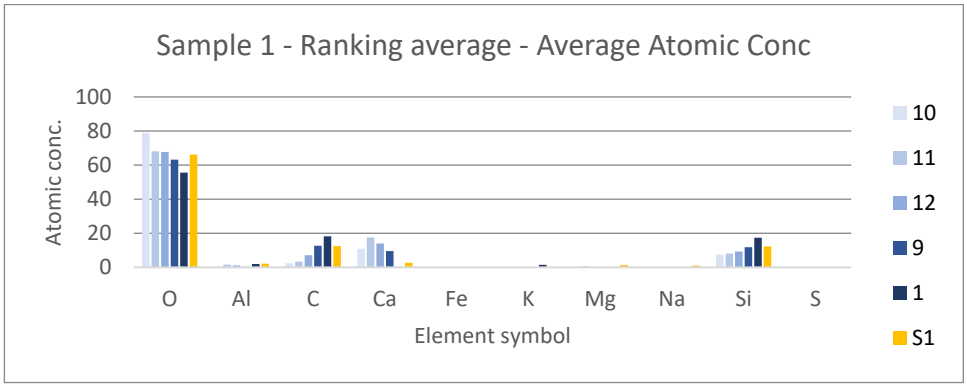


*Figure 320 – Sample 1 – Ranking average - Average atomic concentration*

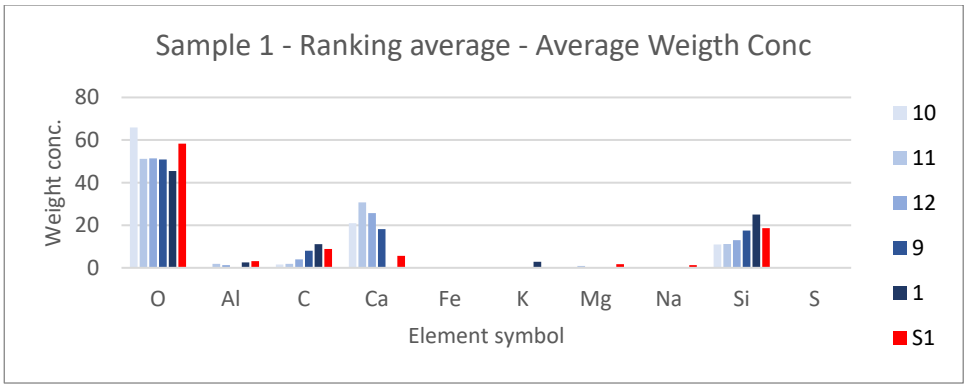


*Figure 321 - Sample 1 Ranking average - Average weight concentration*

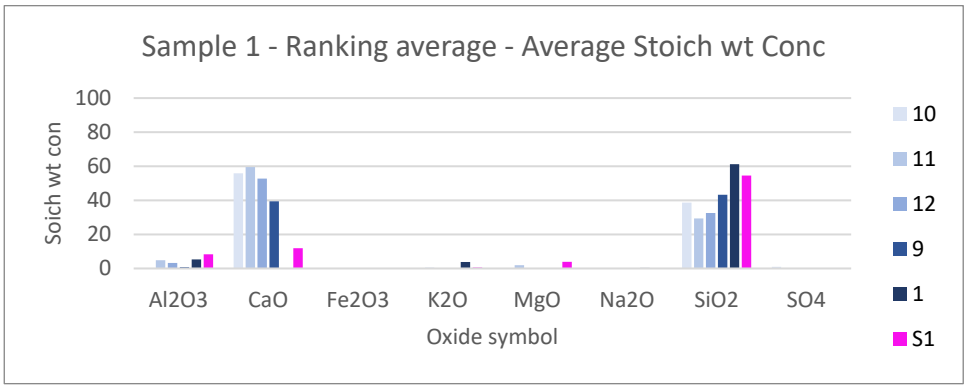


*Figure 322 - Sample 1 - Ranking average - Average stoich wt concentration*

### 10.1.4. Results comparison

Spectroscopy results indicate that sample is assembled from lime (*CaO*) and sand ($SiO_2$) with smaller *Al* and *Mg* additive. Electronic microscope results show the presence of elements *O, Si, Ca, Al* and *Mg* (also small amount of K and Na). It can be concluded, that both methods provide similar results and thus the detection can be considered satisfactory.

## 10.2. Sample 2 - Skorkov

### 10.2.1. Sample information

The sample has been collected from the Skorkov village, the Czech Republic. It comes from the same location as the sample 1 in Chapter 10.1 and is probably a bit younger (18$^{th}$ century). This sample is presupposed to be a lime plaster.

### 10.2.2. Spectroscopy results

The sample was documented using an ordinary mobile phone camera (Figure 323) and a digital DinoLite microscope with magnification 50 (Figure 324) and 200 (Figure 325).

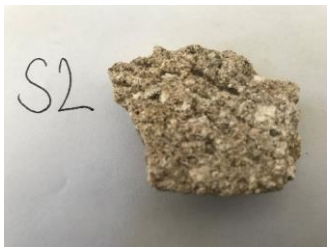


*Figure 323 - Plaster 2 sample image*

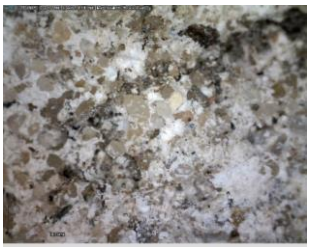

*Figure 324 - Plaster sample 2 DinoLite microscope image, magnification 50*

*Figure 325 - Plaster sample 2 DinoLite microscope image, magnification 200*

Purchased reflectance spectroscopy data were processed and analysed using a MATLAB script in Appendix XIII available at enclosed CD. Analysis results are mentioned below, Figure 326 and Figure 327 shows spectral graphs of the sample.

| | |
|---|---|
| Minimum standard deviation: | 3.08% (for λ = 2475.744nm) |
| Maximum standard deviation: | 5.05% (for λ = 1001.238nm) |
| Mean standard deviation: | 3.81% |

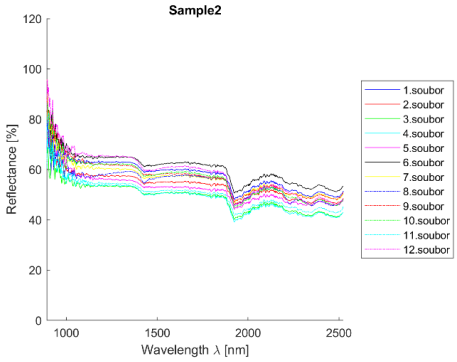


*Figure 326 - Sample 2 - all measurements plot*

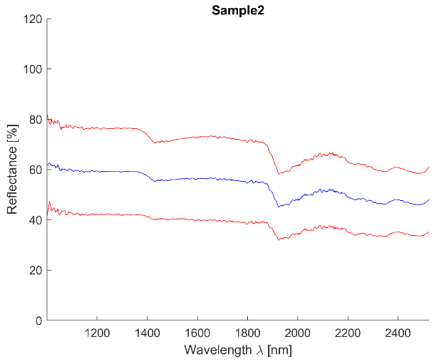


*Figure 327 - Sample 2 mean value (blue) and 2,5*standard deviation (red)*

Table 5 shows the representation of the first ten materials derived from all methods according to their ranking. The average is an arithmetic mean of their determination ranking; standard deviation is also shown in the table to provide a level of confidence. Results of individual analysis can be found in Appendix II.

*Table 5 – Sample 2 - Average material ranking in processed analysis*

| Material | Average | Std Dev |
|---|---|---|
| 1-Božanov Sandstone | 3,2 | 2,3 |
| 10-Lime + Cement Binder Mortar | 5,0 | 3,4 |
| 12-Lime + Metakaolin Binder Mortar | 5,8 | 6,4 |
| 9-Air Lime Mortar | 6,0 | 6,4 |
| 18-Gypsum Standard | 7,8 | 4,0 |
| 11-Hydraulic Lime Mortar (NHL5) | 8,2 | 6,9 |
| 2-Hořice Sandstone | 8,5 | 4,7 |
| 4-Quartzite | 9,5 | 6,6 |
| 6-Přední Kopanina Marlstone | 10,0 | 1,4 |
| 13-Geopolymer (Střeleč sand) | 10,2 | 5,5 |

Spectral curve description

The reflectance value decreases towards longer wavelengths. Water absorption bands are visible at 1450nm (less) and 1950nm (more). Reflectance value ranges from 70% to 50%.

Individual analysis results

- SAM – correct detection of lime mortar and sand;
- SID - correct detection of sand/sandstone and lime (dolomite); false detection of gypsum;
- NNLS – correct detection of lime mortar/lime and sand/sandstone;
- SFF - correct detection of lime mortar/lime and sand/sandstone; false detection of clay mortar;
- BE - correct detection of lime mortars and sand;
- Average - correct detection of lime mortars and sand; false detection of gypsum.

Conclusion

The sample consists of lime mortar and sand.

### 10.2.3. Electronic microscope findings

- Phase 1– light grey grains – aggregated $SiO_2$ ;
- Phase 2 - white matrix between grains consisting of *CaO* (*Si* minor occurrence);
- Phase 3 - dark grey matrix – a high percentage of *Si*; a smaller proportion of *Al*, *Ca* and *K* minor occurrence;
- Phase 4 - dark grey matrix, not visually visible from phase 3 shows a high proportion of *C* and *Cl* that denotes penetration of the epoxy resin into the matrix.

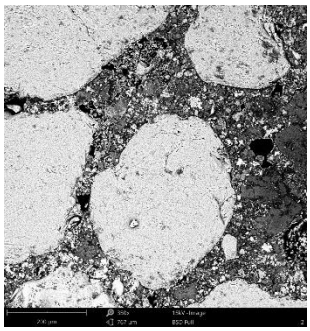

*Figure 328- Phenom XL Desktop SEM photos - Microscopic sample image*

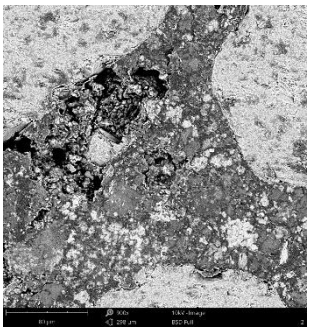

*Figure 329- Phenom XL Desktop SEM photos - Microscopic sample image*

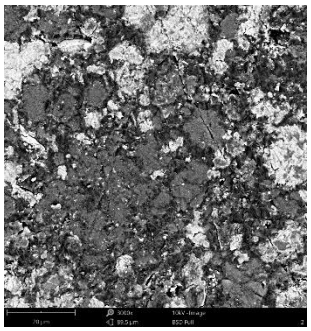

*Figure 330- Phenom XL Desktop SEM photos - Microscopic sample image*

Figure 328 to Figure 330 shows the sample photos. SEM results (average atomic concentration, average weight concentration and average stoichiometry weight concentration) in the form of graphs are shown in Figure 331 to Figure 333.

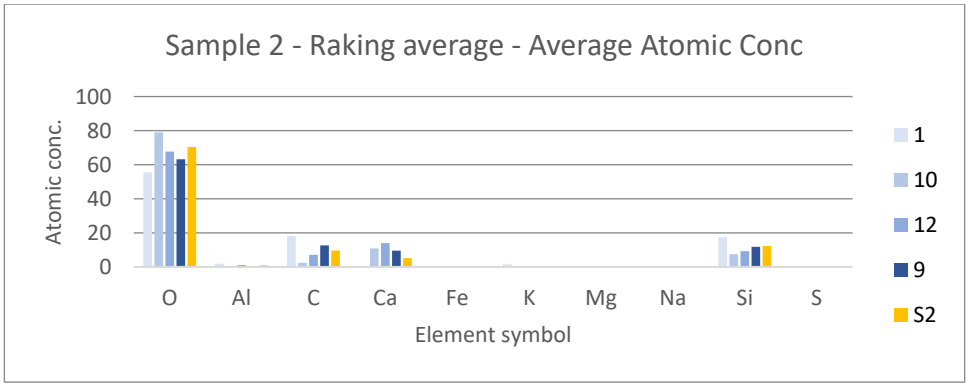


*Figure 331 – Sample 2 – Ranking average - Average atomic concentration*

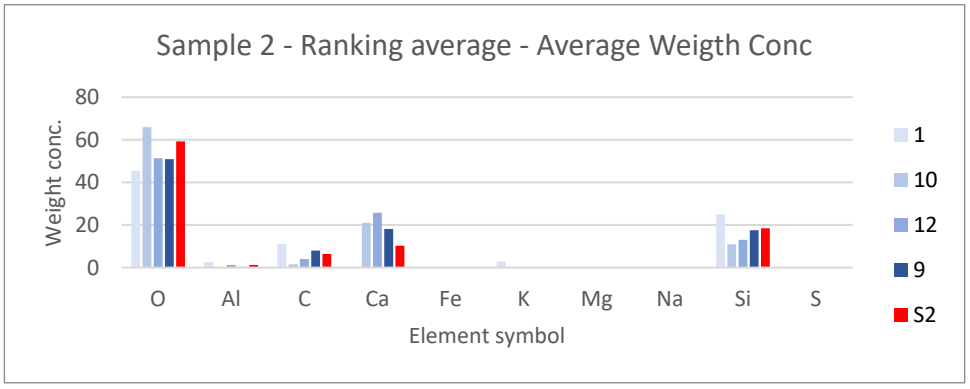


*Figure 332 – Sample 2 – Ranking average - Average weight concentration*

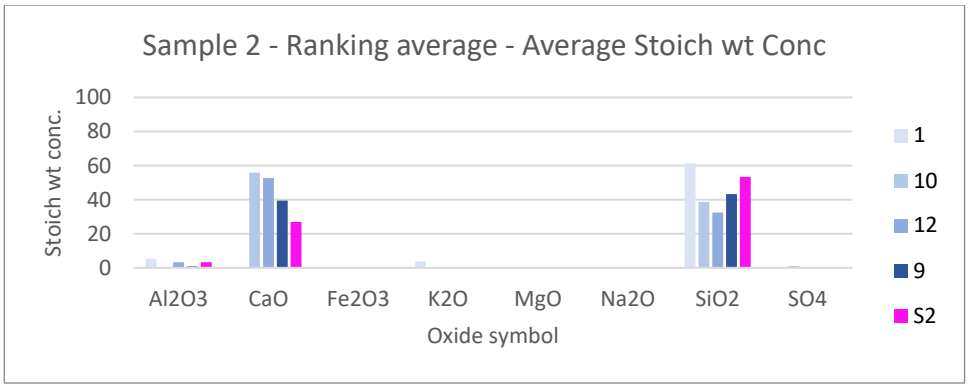


*Figure 333 - Sample 2 – Ranking average - Average stoich wt concentration*

### 10.2.4. Results comparison

Spectroscopy results indicate that the sample is assembled from lime (*CaO*) and sand ($SiO_2$). Electronic microscope results show the presence of elements *O, Si, Ca, C* and a small amount of *Al* and *K*. It can be concluded, that both methods provide similar results and thus the detection can be considered satisfactory.

## 10.3. Sample 3 - Beckov

### 10.3.1. Sample information

This sample comes from the Beckov castle, Slovakia [157]. This castle is located about 20km southwest from the city of Trenčín above the Váh river and it dates from the 17$^{th}$ century. It is presumed that the sample is the lime mortar.

### 10.3.2. Spectroscopy results

The sample was documented using an ordinary mobile phone camera (Figure 334) and a digital DinoLite microscope with magnification 50 (Figure 335) and 200 (Figure 336).

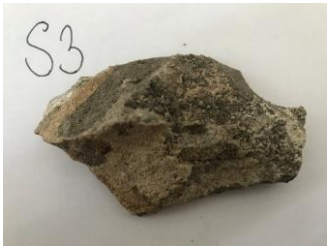


*Figure 334 - Sample 3 - sample image*

*Figure 335 - Sample 3 DinoLite microscope image, magnification 50*

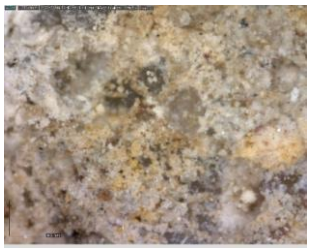

*Figure 336 - Sample 3 DinoLite microscope image, magnification 200*

Purchased reflectance spectroscopy data were processed and analysed using a MATLAB script in Appendix XIII available at enclosed CD. Analysis results are mentioned below, Figure 337 and Figure 338 shows spectral graphs of the sample.

Minimum standard deviation: 2.50% (for λ = 2524.211nm)

Maximum standard deviation: 7.69% (for λ = 1953.348nm)
Mean standard deviation: 3.77%

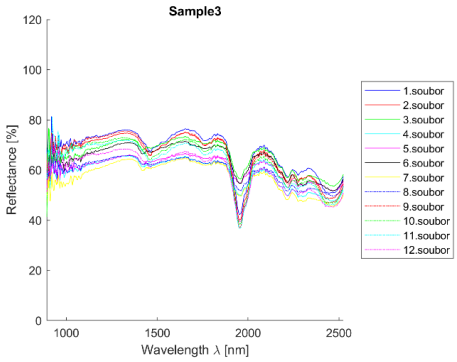


*Figure 337 – Sample 3 – All measurements plot*

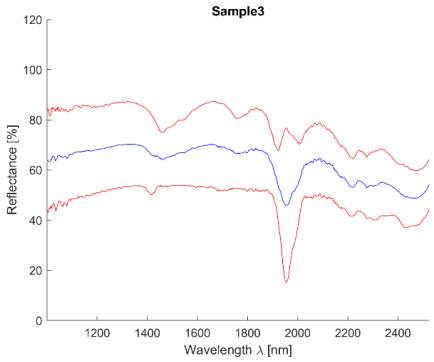


*Figure 338- Sample 3 mean value (blue) and 2,5*standard deviation (red)*

#### 10.3.2.1. Spectroscopy analysis and results

Table 6 shows the representation of the first ten materials derived from all methods according to their ranking. The average is an arithmetic mean of their determination ranking; standard deviation is also shown in the table to provide a level of confidence. Results of individual analysis can be found in Appendix III.

*Table 6 – Sample 3 - Average material ranking in processed analysis*

| Material | Average | Std Dev |
|---|---|---|
| 6-Přední Kopanina Marlstone | 3,4 | 1,1 |
| 18-Gypsum Standard | 4,0 | 5,2 |
| 2-Hořice Sandstone | 5,3 | 4,6 |
| 12-Lime + Metakaolin Binder Mortar | 5,5 | 4,5 |
| 10-Lime + Cement Binder Mortar | 6,5 | 3,1 |
| 11-Hydraulic Lime Mortar (NHL5) | 7,3 | 6,1 |
| 9-Air Lime Mortar | 8,3 | 4,6 |
| 4-Quartzite | 8,6 | 7,2 |
| 1-Božanov Sandstone | 9,5 | 1,7 |
| 19-Metakaolin L05 | 10,3 | 2,1 |

Spectral curve description

The curve oscillates around 60% reflectance with striking water absorption band at 1950nm.

Individual analysis results

- SAM - correct detection of lime mortar and sands/sandstones; false detection of gypsum; high correspondence with marlstone;
- SID - correct detection of lime mortar; high correspondence with marlstone and clay mortar;
- NNLS – false detection of gypsum (1st place); correct detection of sands and lime hydrate/geopolymer; high correspondence with marlstone;

- SFF – false detection of gypsum (1st place); correct detection of lime mortars; high correspondence with marlstone; sands/sandstones are missing;
- BE – false detection of gypsum (1st place); correct detection of lime mortars; high correspondence with marlstone; sands/sandstones are missing;
- Average - high correspondence with marlstone with small standard deviation; false detection of gypsum; correct detection of lime mortars and sand/sandstones.

Conclusion

The sample is lime with sand.

### 10.3.3. Electronic microscope findings

- Phase 1– light grey grains – aggregated $SiO_2$;
- Phase 2 - grey matrix – a high percentage of *Ca*, a lower percentage of *Si*; *Al, K, S* and *Fe* minor occurrence);
- Phase 3 – light grey matrix – a high percentage of *Ca* (higher than in phase 2); *Al, K, Si and Mg* minor occurrence;
- Phase 4 - dark grey grains: primarily consisting of *Ca*; a high percentage of *Mg*; *K, Ca* and *Al* minor occurrence;
- Phase 5 – light white areas – a higher percentage of *Ca, Al* and *Fe; Mg* and *Si* minor occurrence.

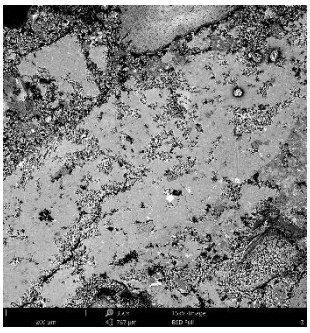

*Figure 339- Phenom XL Desktop SEM photos - Microscopic sample image*

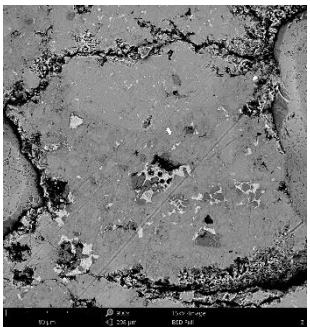

*Figure 340- Phenom XL Desktop SEM photos - Microscopic sample image*

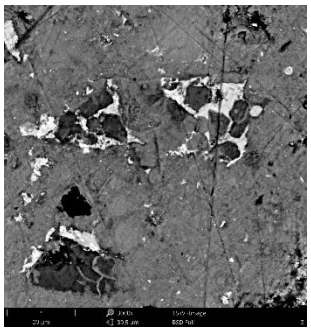

*Figure 341- Phenom XL Desktop SEM photos - Microscopic sample image*

Figure 339 to Figure 341 shows the sample photos. SEM results (average atomic concentration, average weight concentration and average stoichiometry weight concentration) in the form of graphs are shown in Figure 342 to Figure 344.

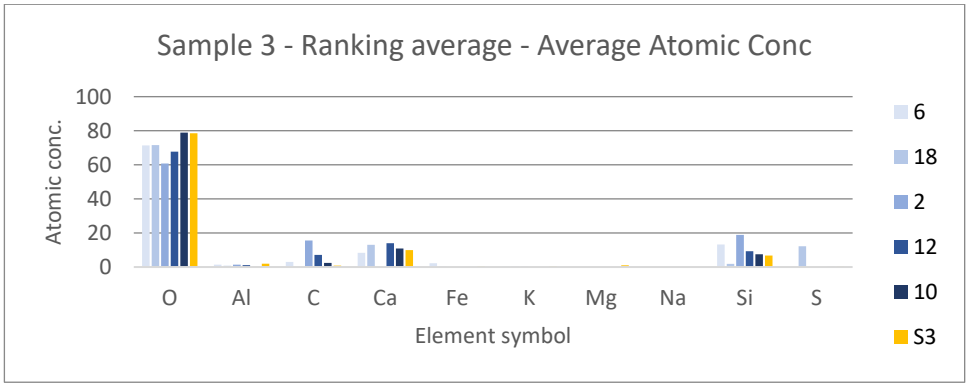


*Figure 342 – Sample 3 – Ranking average - Average atomic concentration*

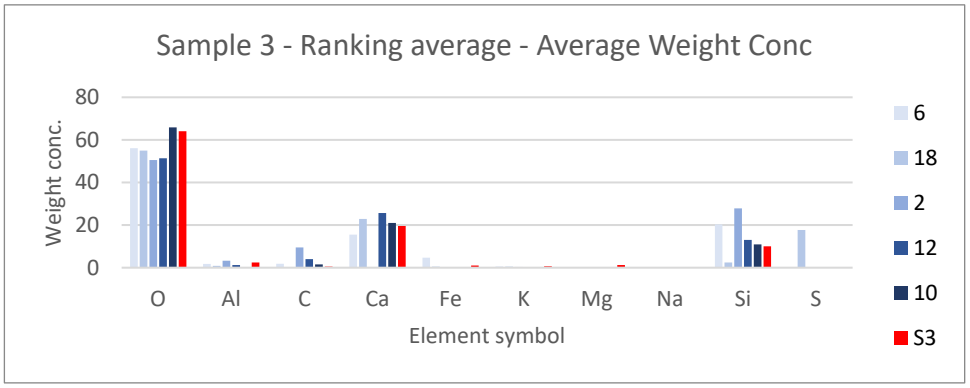


*Figure 343 – Sample 3 – Ranking average - Average weight concentration*

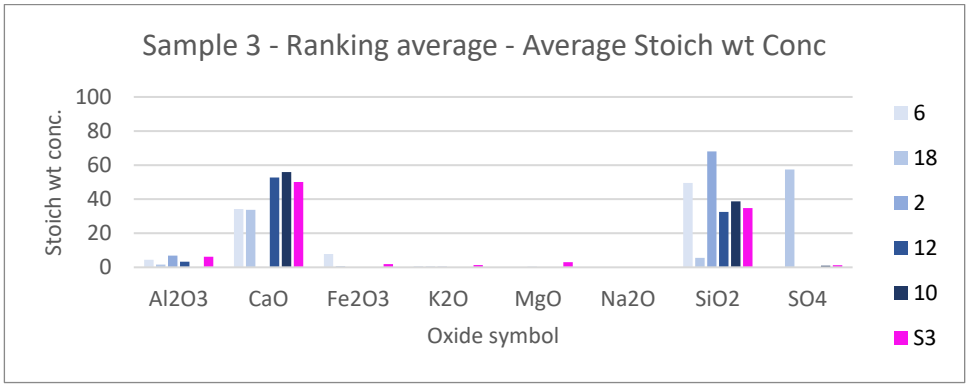


*Figure 344 – Sample 3 – Ranking average - Average stoich wt concentration*

### 10.3.4. Results comparison

Spectroscopy results indicate that the sample is assembled from lime (*CaO*) and sand ($SiO_2$), although gypsum is very high in the ranking even sometimes (NNLS, SFF, BE) on the first place that corresponds to high similarity. The detection of gypsum is incorrect thus the sample contains an only very small amount of element S. This may be due to visible water absorption band in 1920nm. Electronic microscope results show the presence of elements *O, Si, Ca* and a very small amount of *C, Al, Fe, Mg, K* and *S*. It can be concluded that spectroscopy detected incorrectly the presence of gypsum, but another composition was fine and thus the detection can be considered partially satisfactory.

## 10.4. Sample 4 - Skorkov

### 10.4.1. Sample information

The sample has been collected from the Skorkov village, the Czech Republic. It comes from the same location as the sample 1 in Chapter 10.1, dated around the 17th century. This sample is presupposed to be a calcified wood.

### 10.4.2. Spectroscopy results

The sample was documented using an ordinary mobile phone camera (Figure 345) and a digital DinoLite microscope with magnification 50 (Figure 346) and 200 (Figure 347).

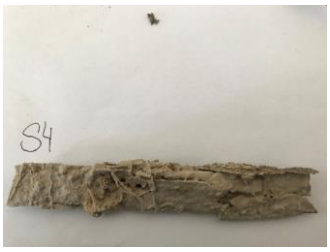


*Figure 345 - Sample 4 – sample image*

*Figure 346 - Sample 4 DinoLite microscope image, magnification 50*

*Figure 347 - Sample 4 DinoLite microscope image, magnification 200*

Purchased reflectance spectroscopy data were processed and analysed using a MATLAB script in Appendix XIII available at enclosed CD. Analysis results are mentioned below, Figure 348 and Figure 349 shows spectral graphs of the sample.

| | |
|---|---|
| Minimum standard deviation: | 2.86% (for λ = 2232.944nm) |
| Maximum standard deviation: | 5.49% (for λ = 1060.190nm) |
| Mean standard deviation: | 3.80% |

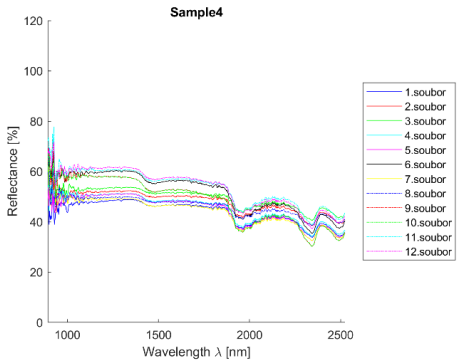


*Figure 348 – Sample 4 – All measurements plot*

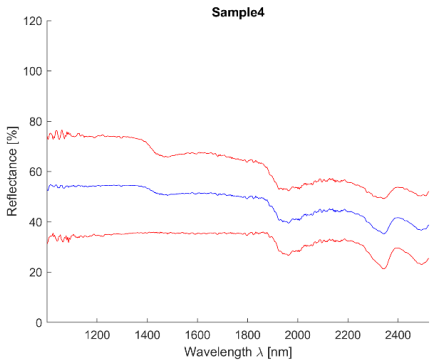


*Figure 349 - Sample 4 mean value (blue) and 2,5*standard deviation (red)*

Table 7 shows the representation of the first ten materials derived from all methods according to their ranking. The average is an arithmetic mean of their determination ranking; standard deviation is also shown in

the table to provide a level of confidence. Results of individual analysis can be found in Appendix IV.

*Table 7 – Sample 4 - Average material ranking in processed analysis*

| Material | Average | Std Dev |
|---|---|---|
| 9-Air Lime Mortar | 4,4 | 7,1 |
| 10-Lime + Cement Binder Mortar | 5,3 | 4,7 |
| 1-Božanov Sandstone | 6,0 | 3,3 |
| 4-Quartzite | 6,5 | 6,0 |
| 12-Lime + Metakaolin Binder Mortar | 6,8 | 6,2 |
| 13-Geopolymer (Střeleč sand) | 7,8 | 7,1 |
| 18-Gypsum Standard | 8,0 | 4,8 |
| 11-Hydraulic Lime Mortar (NHL5) | 8,5 | 5,9 |
| 5-Maastricht Limestone | 9,4 | 7,2 |
| 2-Hořice Sandstone | 9,5 | 5,0 |

Spectral curve description

The curve is slightly wavy with a maximum at shorter wavelengths. Almost imperceptible water absorption spectral band at 1450nm, more visible at 1950nm, noticeable at 2500mn.

Individual analysis results

- SAM - correct detection of lime mortar; only minimum of sand is present in the sample;
- SID – false detection of gypsum and sands – analysis inappropriate, cannot be used;
- NNLS – correct detection of materials consisting of lime only;
- SFF – correct detection of materials consisting of lime only;
- BE – false detection of Quartzite as a top correspondence; only minimum of sand is present in the sample; correct detection of lime mortars;
- Average - correct detection of lime-based materials; only minimum of sand is present in the sample; high standard deviation.

Conclusion

The sample is a lime plaster without sand additive.

### 10.4.3. Electronic microscope findings

- Phase 1– light grey grains – aggregated $SiO_2$ ;
- Phase 2 – white matrix – consisting mainly of *CaO* (*Si* minor occurrence);
- Phase 3 – light grey areas – wood (consisting of *C, O* and *H*);
- Phase 4 - dark grey matrix – wood and epoxy resin; Light grey matrix – aggregate + epoxy resin.

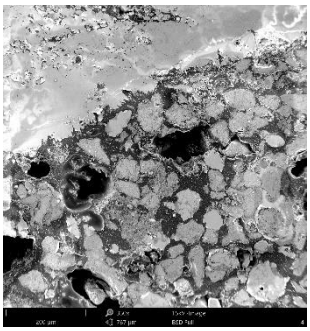

*Figure 350 - Phenom XL Desktop SEM photos - Microscopic sample image*

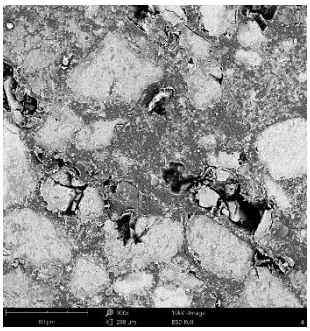

*Figure 351 - Phenom XL Desktop SEM photos - Microscopic sample image*

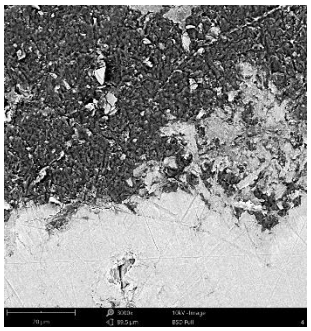

*Figure 352 - Phenom XL Desktop SEM photos - Microscopic sample image*

Figure 350 to Figure 352 shows the sample photos. SEM results (average atomic concentration, average weight concentration and average stoichiometry weight concentration) in the form of graphs are shown in Figure 353 to Figure 355.

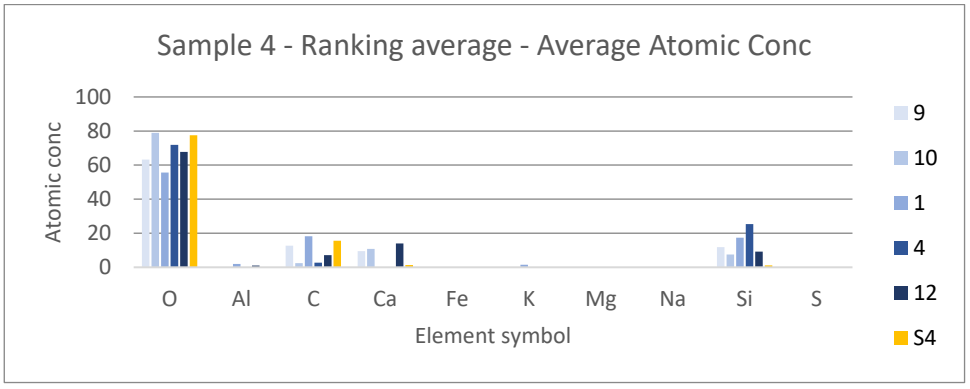


*Figure 353 – Sample 4 – Ranking average - Average atomic concentration*

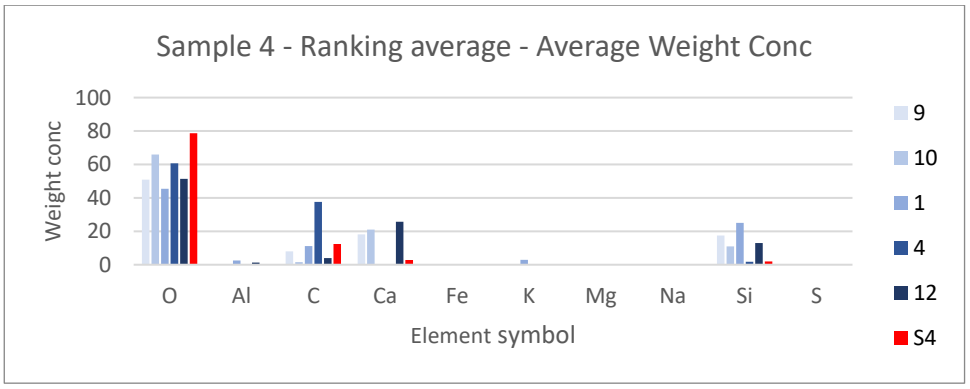


*Figure 354 – Sample 4 –Ranking average - Average weight concentration*

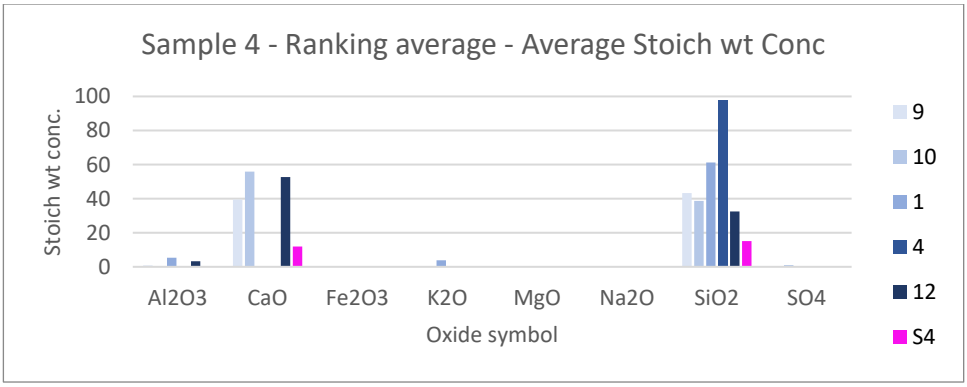


*Figure 355 – Sample 4 – Ranking average - Average Stoich wt concentration*

### 10.4.4. Results comparison

This sample is wood with pure lime (*CaO*) as shown in the microscope analysis (Chapter 10.4.3). Spectroscopy shows high similarity with lime mortars and low amount of sand. This confirms the hypothesis of pure lime-based plaster and the spectroscopy detection was correct. Wood could not be detected since it is not present in the spectral library. This sample detection is considered satisfactory.

## 10.5. Sample A - Jáchymov

### 10.5.1. Sample information

The sample has been collected in an original 19$^{th}$-century house near the town of Jáchymov, the Czech Republic. Jáchymov is located in the Ore Mountains (Krušné hory) near the Czech-German border about 20km north from Karlovy Vary. This sample is presupposed to be original lime plaster.

### 10.5.2. Spectroscopy results

The sample was documented using an ordinary mobile phone camera (Figure 356) and a digital DinoLite microscope with magnification 50 (Figure 357) and 200 (Figure 358).

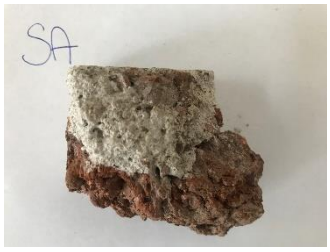


*Figure 356 – Sample A – Sample image*

*Figure 357 – Sample A - DinoLite microscope image, magnification 50*

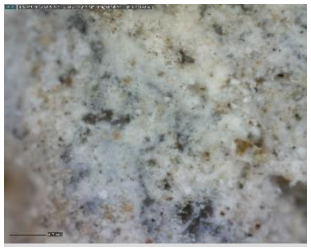

*Figure 358 – Sample A - DinoLite microscope image, magnification 200*

Purchased reflectance spectroscopy data were processed and analysed using a MATLAB script in Appendix XIII available at enclosed CD. Analysis results are mentioned below, Figure 359 and Figure 360 shows spectral graphs of the sample.

| | |
|---|---|
| Minimum standard deviation: | 1.59% (for λ = 1861.079nm) |
| Maximum standard deviation: | 3.31% (for λ = 1007.789nm) |
| Mean standard deviation: | 1.80% |

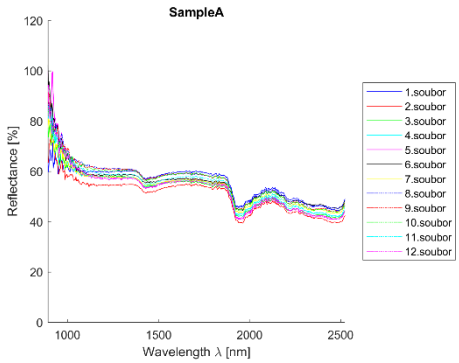


*Figure 359 – Sample A – All measurements plot*

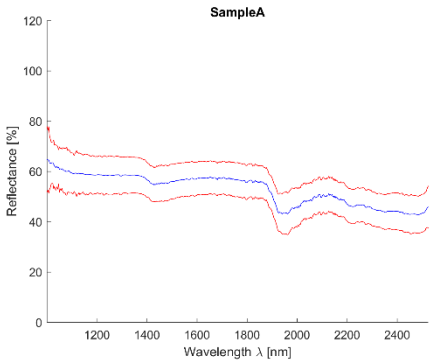


*Figure 360 - Sample A mean value (blue) and 2,5*standard deviation (red)*

Table 8 shows the representation of the first ten materials derived from all methods according to their ranking. The average is an arithmetic mean of their determination ranking; standard deviation is also shown in the table to provide a level of confidence. Results of individual analysis can be found in Appendix V.

*Table 8 – Sample A - Average material ranking in processed analysis*

| Material | Average | Std Dev |
|---|---|---|
| 1-Božanov Sandstone | 3,2 | 2,3 |
| 10-Lime + Cement Binder Mortar | 5,3 | 3,4 |
| 12-Lime + Metakaolin Binder Mortar | 5,5 | 7,1 |
| 9-Air Lime Mortar | 5,6 | 6,5 |
| 18-Gypsum Standard | 6,4 | 3,8 |
| 6-Přední Kopanina Marlstone | 8,6 | 2,9 |
| 2-Hořice Sandstone | 8,8 | 4,6 |
| 13-Geopolymer (Střeleč sand) | 9,2 | 6,3 |
| 4-Quartzite | 9,3 | 7,0 |
| 11-Hydraulic Lime Mortar (NHL5) | 9,3 | 7,8 |

Spectral curve description

The curve is similar to sandstones with perceptible water absorption band at 1450nm and more noticeable at 1950nm. The curve is relatively flat with reflectance values ranging from 40% to 60%.

Individual analysis results

- SAM - lime mortars at first 5 places;
- SID - correct detection of sandstone, false correction of gypsum; other values low;
- NNLS - correct detection of sandstone, false correction of gypsum; other values low. Difficulties with CaO detection – that's why lime hydrate and geopolymer is present with low correspondence;

- SFF – correct detection of lime mortars and sandstone. False detection of clay mortar due to high curve correspondence in water absorption features;
- BE – correct detection of lime mortars, Quartzite detected instead of sandstone;
- Average – correct detection of sands/sandstones and lime mortars; high mortar standard deviation.

Conclusion

The sample consists of lime sand (quartz) sand, the curve analogous to sandstones; detection nearly satisfactory.

### 10.5.3. Electronic microscope findings

Dominant phase

- Phase 1 – light grey grains – aggregated $SiO_2$; *Al* minor occurrence;
- Phase 2 – white grains – $SiO_2$ prominent, *MgO* and *CaO* also detected; *Al* minor occurrence;
- Phase 3 – light grey grains (slightly darker than phase 1) – *CaO* prominent; *Al, Si* and *Mg* minor occurrence;
- Phase 4 – light grey matrix – *CaO* and $Al_2O_3$ prominent; *Si, Mg, Fe, S* and *K* minor occurrence;
- Phase 5 – light grey matrix – hardly distinguishable from others *CaO* and $SiO_2$; *Al* and *K* minor occurrence.

Minor phase

- Phase 6 – bright white *Fe* particle (82% representation), the remainder is surrounding elements;
- Phase 7 – grey grain – a higher percentage of *Si, Al* and *K; Na, Mg* and *Fe* minor occurrence;
- Phase 8 – light grey matrix – A higher percentage of *Na.*

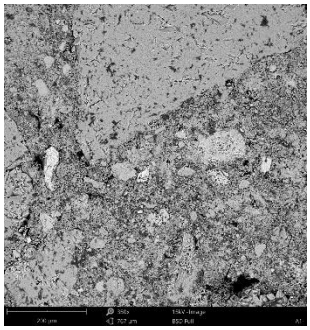

*Figure 361- Phenom XL Desktop SEM photos - Microscopic sample image*

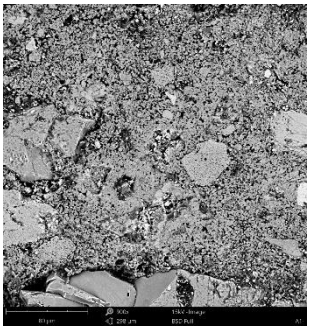

*Figure 362 - Phenom XL Desktop SEM photos - Microscopic sample image*

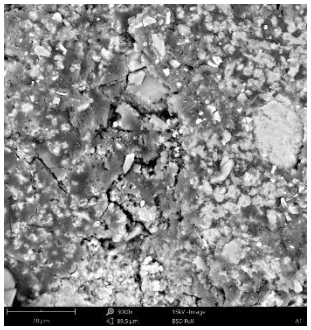

*Figure 363 - Phenom XL Desktop SEM photos - Microscopic sample image*

Figure 361 to Figure 363 shows the sample photos. SEM results (average atomic concentration, average weight concentration and average stoichiometry weight concentration) in the form of graphs are shown in Figure 364 to Figure 366.

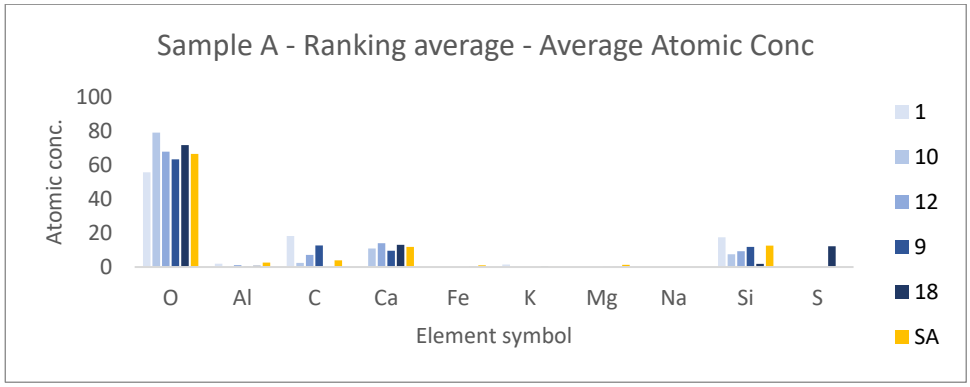


*Figure 364 – Sample A – Ranking average – Average atomic concentration*

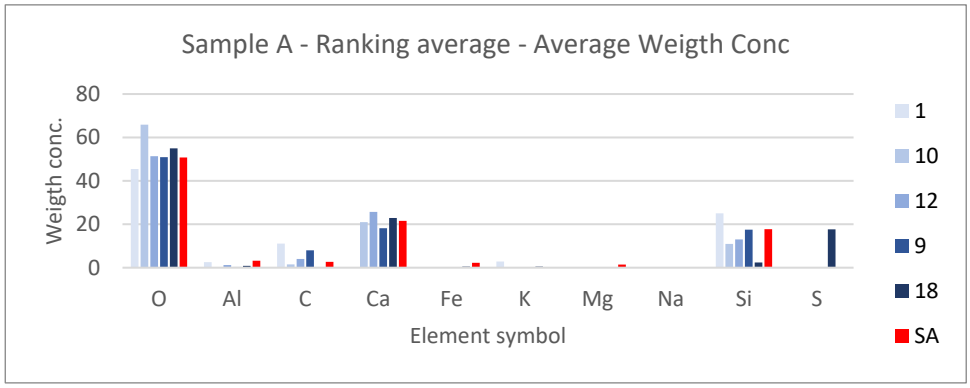


*Figure 365 – Sample A – Ranking average – Average weight concentration*

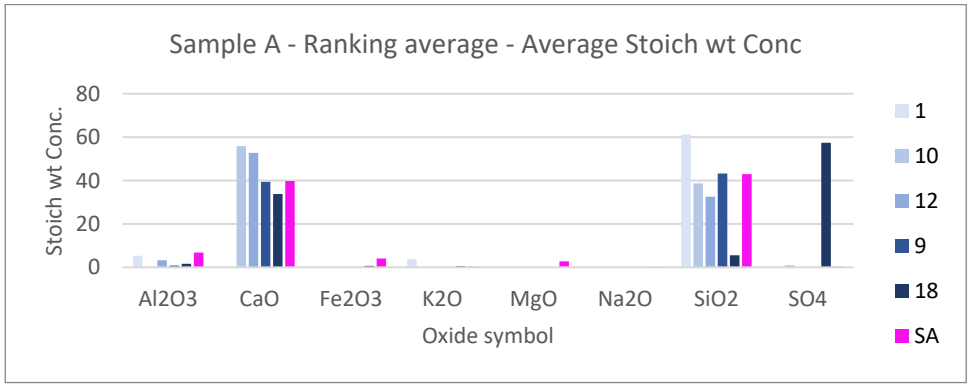


*Figure 366 – Sample A – Ranking average – Average stoich wt concentration*

### 10.5.4. Results comparison

Spectroscopy results indicate that sample is assembled from lime (*CaO*) and sand ($SiO_2$), although gypsum is present at the 5$^{th}$ place which is not current since *S* is not present in the sample based on the electron microscope. This may be due to visible water absorption band in 1920nm. Electronic microscope results show the presence of elements *O, Si, Ca, C, Mg, Al* and a small amount of *Fe, Kl* and *Na*. It can be concluded, that both methods provide similar (when gypsum is excluded) results and the detection can be considered nearly satisfactory.

## 10.6. Sample B - Koya

### 10.6.1. Sample information

This sample comes from the northern part of Kurdistan, Iraq. It was collected near the town of Koya on an archaeological site named Sheela during archaeological observation project. It is presupposed to be plaster with gypsum content.

### 10.6.2. Spectroscopy results

The sample was documented using an ordinary mobile phone camera (Figure 367) and a digital DinoLite microscope with magnification 50 (Figure 368) and 200 (Figure 369).

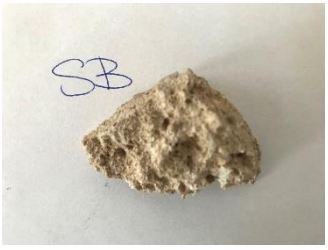


*Figure 367 – Sample B – Sample image*

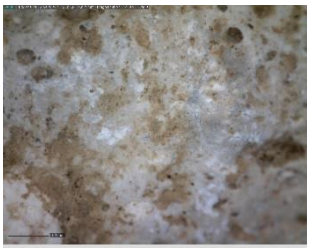

*Figure 368 – Sample B - DinoLite microscope image, magnification 50*

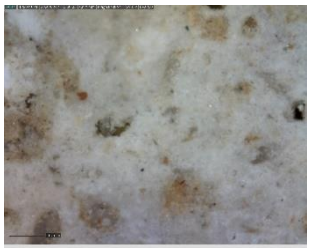

*Figure 369 – Sample B - DinoLite microscope image, magnification 200*

Purchased reflectance spectroscopy data were processed and analysed using a MATLAB script in Appendix XIII available at enclosed CD. Analysis results are mentioned below, Figure 370 and Figure 371 shows spectral graphs of the sample.

| | |
|---|---|
| Minimum standard deviation: | 1.96% (for λ = 2521.189nm) |
| Maximum standard deviation: | 5.56% (for λ = 1014.341nm) |
| Mean standard deviation: | 3.13% |

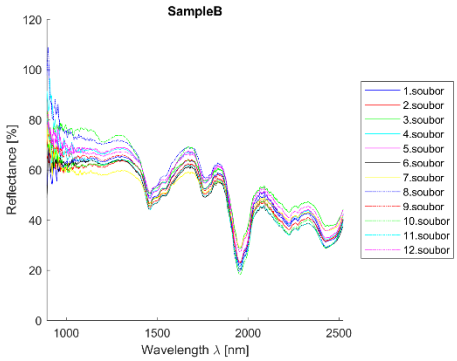


*Figure 370 – Sample B – All measurements plot*

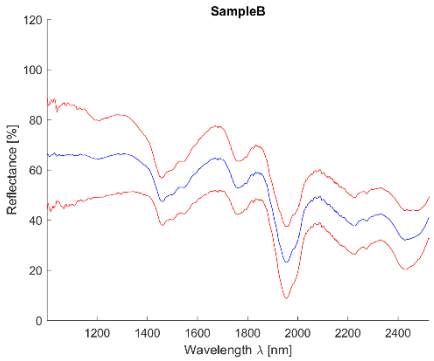


*Figure 371 - Sample B mean value (blue) and 2,5*standard deviation (red)*

Table 9 shows the representation of the first ten materials derived from all methods according to their ranking. The average is an arithmetic mean of their determination ranking; standard deviation is also shown in

the table to provide a level of confidence. Results of individual analysis can be found in Appendix VI.

*Table 9 – Sample B - Average material ranking in processed analysis*

| Material | Average | Std Dev |
|---|---|---|
| 13-Geopolymer (Střeleč sand) | 1,4 | 0,9 |
| 18-Gypsum Standard | 3,6 | 3,2 |
| 10-Lime + Cement Binder Mortar | 4,8 | 4,3 |
| 1-Božanov Sandstone | 5,3 | 1,7 |
| 4-Quartzite | 7,3 | 3,8 |
| 2-Hořice Sandstone | 8,0 | 3,5 |
| 11-Hydraulic Lime Mortar (NHL5) | 8,0 | 4,4 |
| 12-Lime + Metakaolin Binder Mortar | 8,0 | 4,8 |
| 9-Air Lime Mortar | 9,0 | 5,9 |
| 15-Borek River Sand | 10,3 | 3,6 |

Spectral curve description

The curve is considerably wavy with significant minimums in water absorption spectral bands (1450nm and 1950nm) and maximums (1300nm, 1700nm and 1850nm) with additional visible local maximums. The curve is similar to gypsum with more noticeable minimums and maximums.

Individual analysis results

- SAM – geopolymer on 1$^{st}$ place (similar curve shape), gypsum on 4$^{th}$ place – results inconclusive;
- SID - fallacious detection of geopolymer (similar curve shape), correct detection of gypsum;
- NNLS - fallacious detection of geopolymer (similar curve shape), correct detection of gypsum;
- SFF – the only analysis with gypsum at 1$^{st}$ place, other materials have significantly lower correspondence coefficients (mortars, geopolymer, sand);
- BE – results inconclusive – gypsum at 9$^{th}$ place;
- Average - false detection of geopolymer due to the similar spectral curve. The correct material – gypsum – is on 2$^{nd}$ place with a high standard deviation because of the inconclusive BE analysis, next is a lime + cement binder mortar and on 4$^{th}$ place, Božanov sandstone with reasonable standard deviation can be found.

Conclusion

The sample is gypsum mortar which was correctly determined only by SFF analysis. Other methods incorrectly detected maximum correspondence with geopolymer due to similarities in both curves, but a lower part around 1800nm is missing in geopolymer. This part is present at gypsum only when library materials are considered. Although gypsum does not have such a strong water absorption band at 1450nm. Detection is nearly satisfactory.

### 10.6.3. Electronic microscope findings

Dominant phase

- Phase 1 – dark grey grains – aggregate $SiO_2$;
- Phase 2 – light grey matrix – the majority of the sample most likely consists of $Ca_2SO_4$ with *Al* and *Si* minor occurrence.

Minor phase

- Phase 3 – light areas – *CaO* prominent; *Mg, Al, Si* and *S* minor occurrence;
- Phase 4 - bright white *Fe* particle (75% representation), the remainder is surrounding elements;
- Phase 5 – darkest grey areas – high occurrence of $SiO_2$ and *C*.

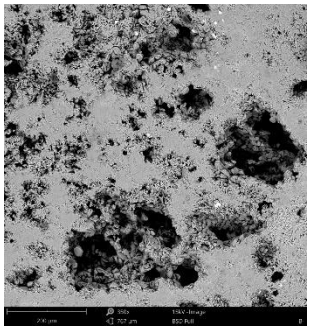

*Figure 372 - Phenom XL Desktop SEM photos - Microscopic sample image*

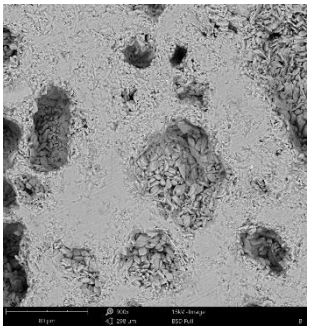

*Figure 373 - Phenom XL Desktop SEM photos - Microscopic sample image*

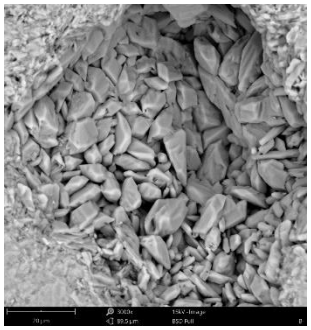

*Figure 374 - Phenom XL Desktop SEM photos - Microscopic sample image*

Figure 372 to Figure 374 shows the sample photos. SEM results (average atomic concentration, average weight concentration and average stoichiometry weight concentration) in the form of graphs are shown in Figure 375 to Figure 377.

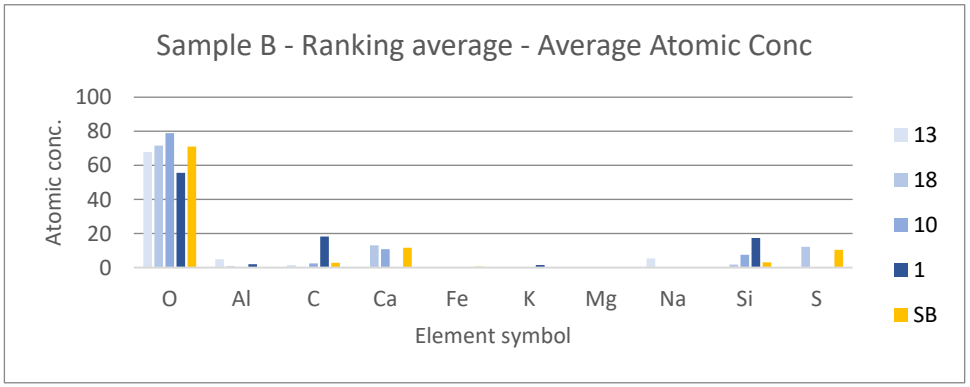


*Figure 375 - Sample B - Ranking average - Average atomic concentration*

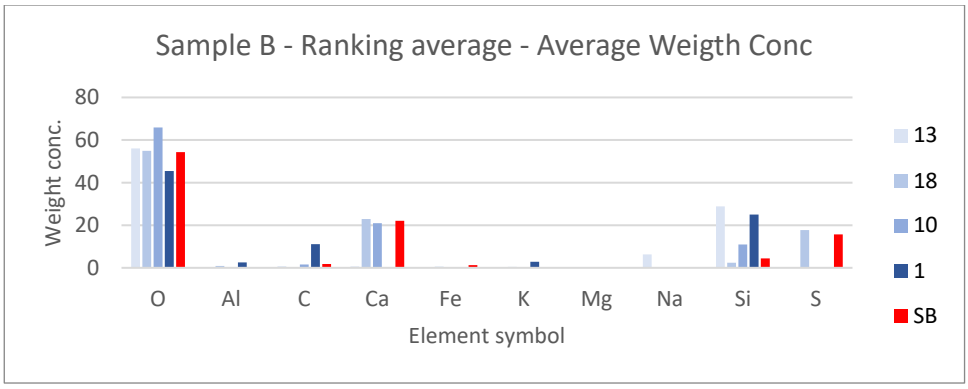


*Figure 376 – Sample B – Ranking average – Average weight concentration*

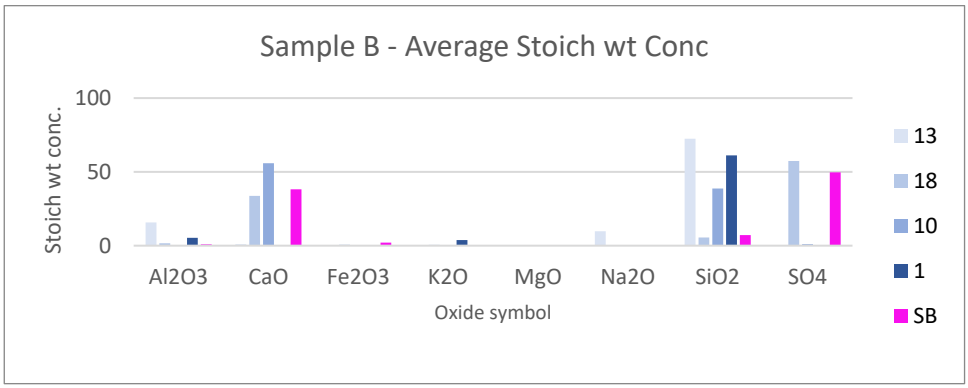


*Figure 377 – Sample B – Ranking average – Average weight concentration*

### 10.6.4. Results comparison

Spectroscopy results indicate that the sample has a high amount of gypsum present, although the main material detected is a geopolymer. This is due to the nature of the spectral curve with two water absorption features. When gypsum spectral curve is analysed the major absorption, the peak is seen. Next three materials in the ranking are sands which follow the assumption of gypsum-based mortar with sand. Electronic microscope results show the presence of $SiO_2$ and the majority of $Ca_2So_4$ with small amount of Al, Mg and Fe. It can be concluded that both methods provide similar results and the detection can be considered nearly satisfactory due to geopolymer presence. This can be solved by excluding geopolymer from the material library.

## 10.7. Sample C - Rýzmburk

### 10.7.1. Sample information

The sample has been collected in a tower of the Rýzmburk castle ruins that are situated near the Osek village, the Czech Republic and comes probably from the turn of 16$^{th}$ and 17$^{th}$ century. Osek is located in the foothills of the Ore Mountains (Krušné hory) about 15km west from the city of Teplice. This sample is presupposed to be a lime plaster with high sand content.

### 10.7.2. Spectroscopy results

The sample was documented using an ordinary mobile phone camera (Figure 378) and a digital DinoLite microscope with magnification 50 (Figure 379) and 200 (Figure 380).


*Figure 378 – Sample C – Sample image*

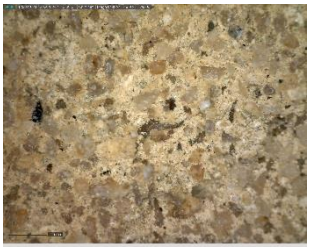

*Figure 379 – Sample C - DinoLite microscope image, magnification 50*

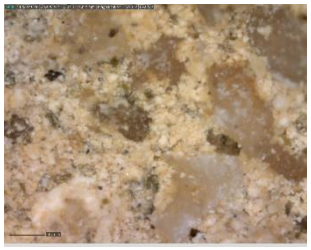

*Figure 380 – Sample C - DinoLite microscope image, magnification 200*

Purchased reflectance spectroscopy data were processed and analysed using a MATLAB script in Appendix XIII available at enclosed CD. Analysis results are mentioned below, Figure 381 and Figure 382 shows spectral graphs of the sample.

| | |
|---|---|
| Minimum standard deviation: | 3.34% (for λ = 2328.882nm) |
| Maximum standard deviation: | 9.03% (for λ = 1956.520nm) |
| Mean standard deviation: | 4.47% |

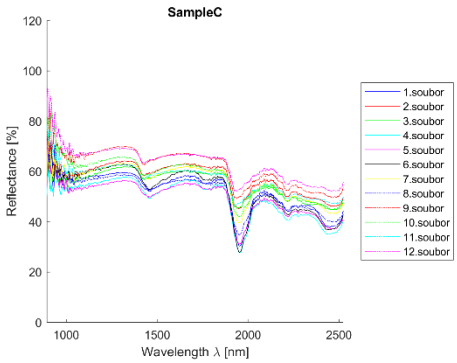


*Figure 381 – Sample C – All measurements plot*

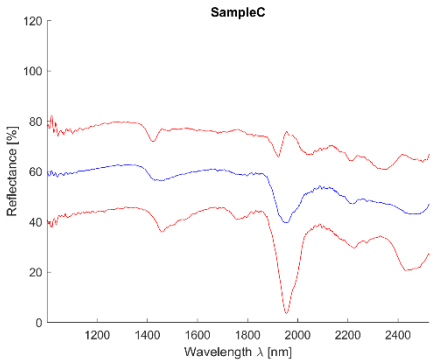


*Figure 382 - Sample C mean value (blue) and 2,5*standard deviation (red)*

Table 10 shows the representation of the first ten materials derived from all methods according to their ranking. The average is an arithmetic mean of their determination ranking; standard deviation is also shown in the table to provide a level of confidence. Results of individual analysis can be found in Appendix VII.

*Table 10 – Sample C - Average material ranking in processed analysis*

| Material | Average | Std Dev |
|---|---|---|
| 18-Gypsum Standard | 3,8 | 3,6 |
| 10-Lime + Cement Binder Mortar | 5,0 | 3,6 |
| 12-Lime + Metakaolin Binder Mortar | 5,3 | 5,9 |
| 1-Božanov Sandstone | 5,8 | 3,4 |
| 11-Hydraulic Lime Mortar (NHL5) | 6,0 | 6,0 |
| 4-Quartzite | 7,6 | 6,3 |
| 9-Air Lime Mortar | 8,0 | 6,1 |
| 2-Hořice Sandstone | 8,3 | 3,9 |
| 13-Geopolymer (Střeleč sand) | 8,8 | 6,5 |
| 6-Přední Kopanina Marlstone | 9,0 | 2,2 |

Spectral curve description

The curve reflectance ranges between 40% and 60% with visible absorption band at 1450nm and conspicuous at 1950nm. The standard deviation around 1950nm distinctly rises probably due to the inhomogeneous nature of the sample.

Individual analysis results

- SAM - correct detection of lime mortars and sands;
- SID - correct detection of sands/sandstones and dolomite/limestone; false detection of gypsum;
- NNLS - correct detection of sandstones and limestone; geopolymer can be evaluated as correct detection since it contains a lot of *CaO;*
- SFF - correct detection of sands/sandstones ($SiO_2$) and lime mortars/geopolymer (*CaO*); false detection of gypsum;
- BE - correct detection of lime mortars and quartz sand;
- Average - correct detection of sands/sandstones and lime mortars, but high standard deviation values; false detection of gypsum.

Conclusion

The sample consists of lime (*CaO*) and sand ($SiO_2$). This was correctly detected by almost all methods. False detection of gypsum (SID, NNLS and SFF) is probably due to the significant absorption feature at 1950nm. Detection is nearly satisfactory.

### 10.7.3. Electronic microscope findings

- Phase 1– light grey grains – aggregated $SiO_2$ ;
- Phase 2 – light grey areas – *CaO* and SiO2 without element minor occurrence);
- Phase 3 – light grey areas – not distinguishable from phase 2 on SEM images – *CaO* prominent; *Si, Al, K, Mg* and *Fe* minor occurrence ;
- Phase 4 – dark grey areas – epoxy resin.

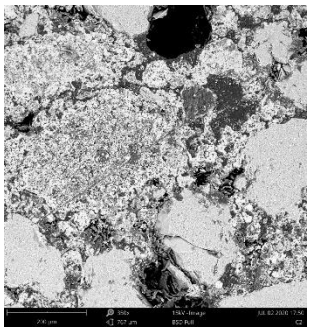

*Figure 383 - Phenom XL Desktop SEM photos - Microscopic sample image*

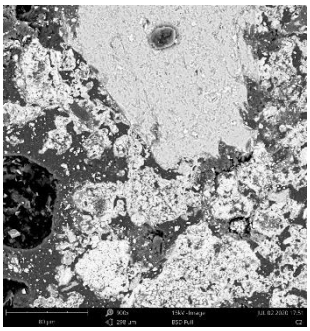

*Figure 384 - Phenom XL Desktop SEM photos - Microscopic sample image*

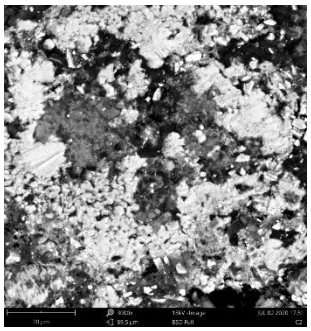

*Figure 385 - Phenom XL Desktop SEM photos - Microscopic sample image*

Figure 383 to Figure 385 shows the sample photos. SEM results (average atomic concentration, average weight concentration and average stoichiometry weight concentration) in the form of graphs are shown in Figure 386 to Figure 388.

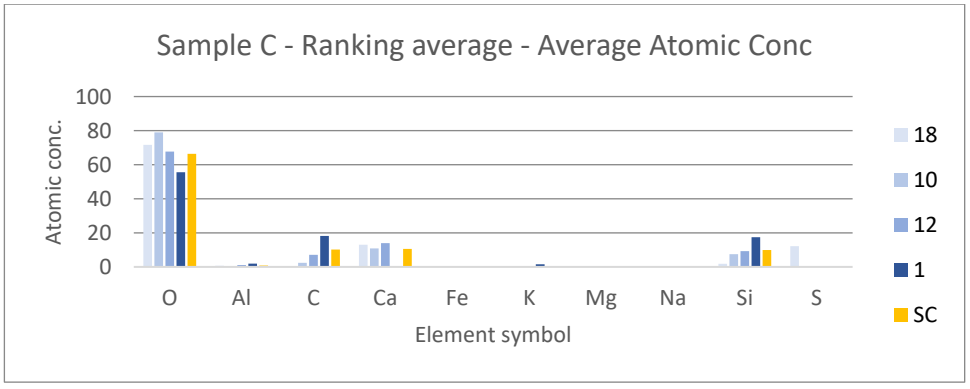


*Figure 386 – Sample C – Ranking average – Average atomic concentration*

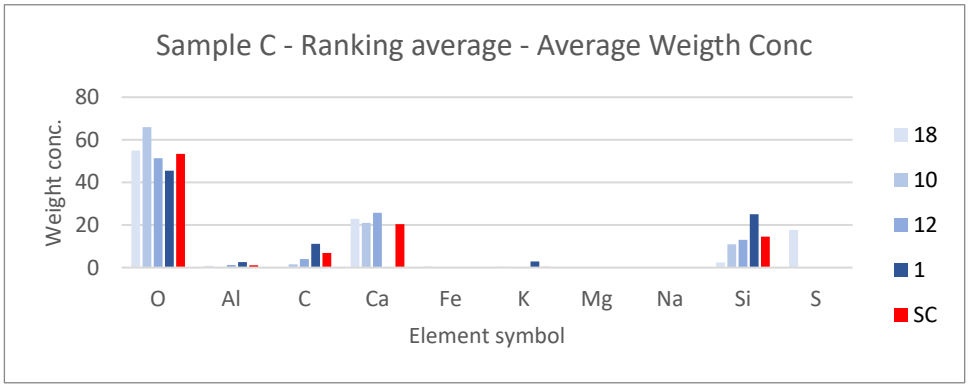


*Figure 387 – Sample C – Ranking average – Average weight concentration*

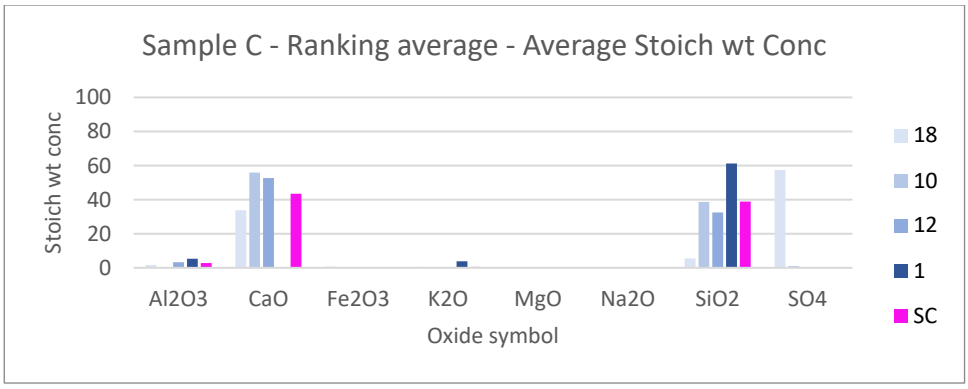


*Figure 388 – Sample C – Ranking average – Average stoich wt concentration*

### 10.7.4. Results comparison

Spectroscopy results indicate that the sample is assembled from lime (*CaO*) and sand ($SiO_2$), although gypsum is present at the 1st place which is not correct since *S* is not present in the sample based on the electron microscope. This may be due to visible water absorption band in 1920nm. Electronic microscope results show a high presence of $SiO_2$, *CaO* and a small amount of *Al, K, Mg* and *Fe*. It can be concluded that both methods provide similar (when gypsum is excluded) results and the detection can be considered nearly satisfactory.

## 10.8. Sample D - Čachtice

### 10.8.1. Sample information

This sample comes from the Čachtice castle, Slovakia [158]. This castle is located about 30km southwest from the city of Trenčín above the Váh river and comes from around the 16th century. It is presumed that the sample is lime plaster.

### 10.8.2. Spectroscopy results

The sample was documented using an ordinary mobile phone camera (Figure 389) and a digital DinoLite microscope with magnification 50 (Figure 390) and 200 (Figure 391).

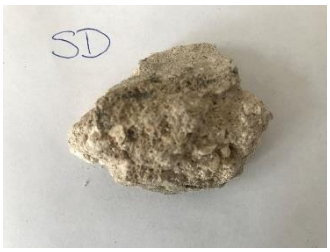


*Figure 389 – Sample D – Sample image*

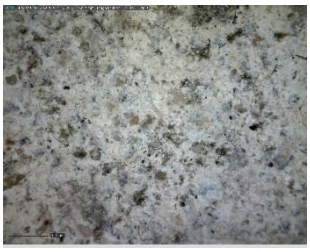

*Figure 390 – Sample D - DinoLite microscope image, magnification 50*

*Figure 391 – Sample D- - DinoLite microscope image, magnification 200*

Purchased reflectance spectroscopy data were processed and analysed using a MATLAB script in Appendix XIII available at enclosed CD.

Analysis results are mentioned below, Figure 392 and Figure 393 shows spectral graphs of the sample.

| | |
|---|---|
| Minimum standard deviation: | 3.10% (for λ = 1956.520nm) |
| Maximum standard deviation: | 5.75% (for λ = 1014.341nm) |
| Mean standard deviation: | 4.00% |

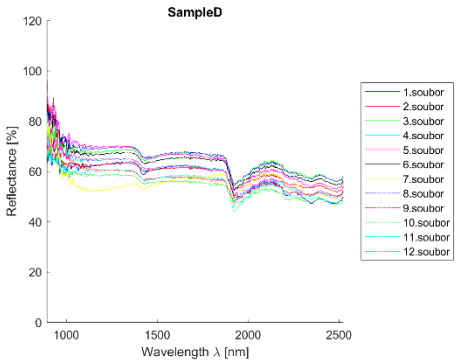


*Figure 392 – Sample D – All measurements plot*

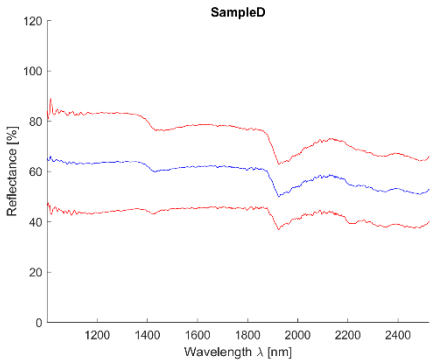


*Figure 393 - Sample D mean value (blue) and 2,5*standard deviation (red)*

Table 11 shows the representation of the first ten materials derived from all methods according to their ranking. The average is an arithmetic mean of their determination ranking; standard deviation is also shown in the table to provide a level of confidence. Results of individual analysis can be found in Appendix VIII.

*Table 11 – Sample D - Average material ranking in processed analysis*

| Material | Average | Std Dev |
|---|---|---|
| 12-Lime + Metakaolin Binder Mortar | 2,3 | 1,5 |
| 10-Lime + Cement Binder Mortar | 4,5 | 3,4 |
| 1-Božanov Sandstone | 4,6 | 2,1 |
| 9-Air Lime Mortar | 5,0 | 2,6 |
| 11-Hydraulic Lime Mortar (NHL5) | 6,5 | 7,0 |
| 2-Hořice Sandstone | 7,0 | 6,1 |
| 4-Quartzite | 7,7 | 7,6 |
| 15-Borek River Sand | 8,3 | 3,8 |
| 6-Přední Kopanina Marlstone | 8,6 | 2,1 |
| 5-Maastricht Limestone | 9,0 | 5,2 |

Spectral curve description

The curve is flat with reflectance around 60% and small absorption at 1450nm and more significant one at 1950nm. The curve is similar to sandstones and lime mortars respectively.

Individual analysis results

- SAM - correct detection of lime mortars and sands/sandstones;
- SID - correct detection of sands/sandstones and dolomite (*CaO*); curve is similar to clay mortar which can show the higher occurrence of *Al;*

- NNLS - correct detection of lime mortars and sands/sandstones and dolomite (*CaO*); curve is similar to clay mortar which can show the higher occurrence of *Al;*
- SFF - correct detection of lime mortars and sands/sandstones; curve is similar to clay mortar which can show the higher occurrence of *Al;*
- BE - correct detection of lime mortars and sands/sandstones;
- Average - correct detection of lime mortars and sands/sandstones with acceptable standard deviation values.

Conclusion

The sample consists of lime (*CaO*) and quartz sands ($SiO_2$) with a higher quantity of *Al* and lower of *K;* detection satisfactory.

### 10.8.3. Electronic microscope findings

Dominant phase

- Phase 1– light grey grains – aggregated $SiO_2$ (*Al* minor occurrence);
- Phase 2 – light grey grains – aggregated $SiO_2$ with $K_2O$ and $Al_2O_3$ additives; *Na* minor occurrence;
- Phase 3 – white matrix – predominantly *CaO; Al, Si, K* and *Mg* minor occurrence;
- Phase 4 – light grey matrix – predominantly $SiO_2$ with *CaO* and $Al_2O_3$ additives; *K, Fe, Na* and *Mg* minor occurrence;

Minor phase

- Phase 5 – light grey matrix with higher *CaO* percentage and *Fe* oxides – undistinguishable from phase 4; *Al, Si, Mg* and *Ti* minor occurrence;
- Phase 6 – dark grey areas – epoxy resin.

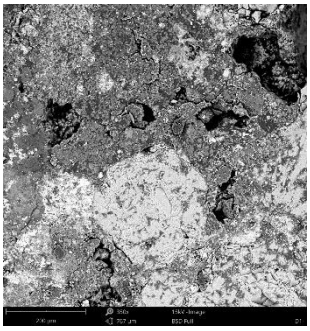

*Figure 394 - Phenom XL Desktop SEM photos - Microscopic sample image*

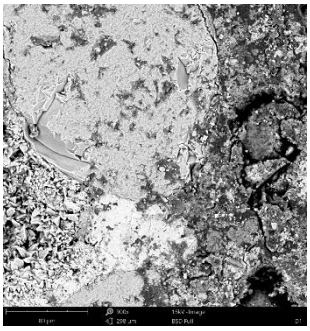

*Figure 395 - Phenom XL Desktop SEM photos - Microscopic sample image*

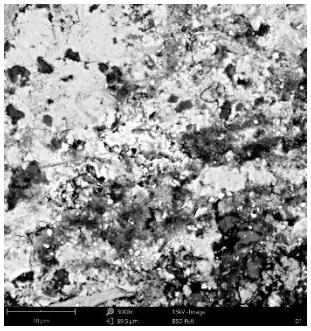

*Figure 396 - Phenom XL Desktop SEM photos - Microscopic sample image*

Figure 394 to Figure 396 shows the sample photos. SEM results (average atomic concentration, average weight concentration and average stoichiometry weight concentration) in the form of graphs are shown in Figure 397 to Figure 399.

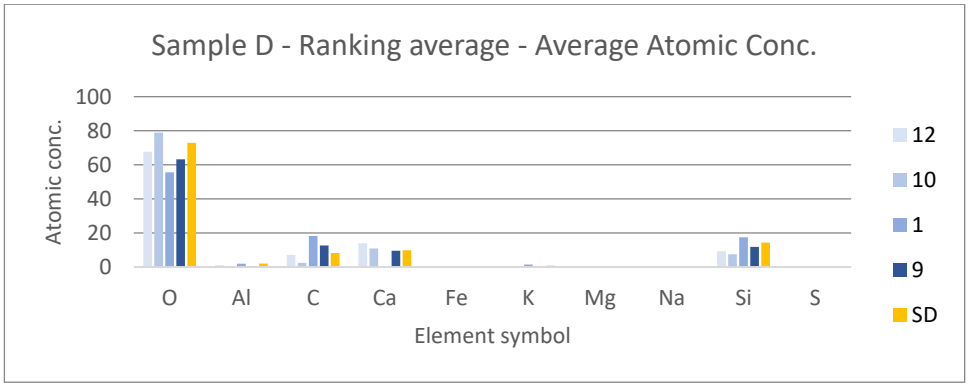


*Figure 397 – Sample D – Ranking average – Average atomic concentration*

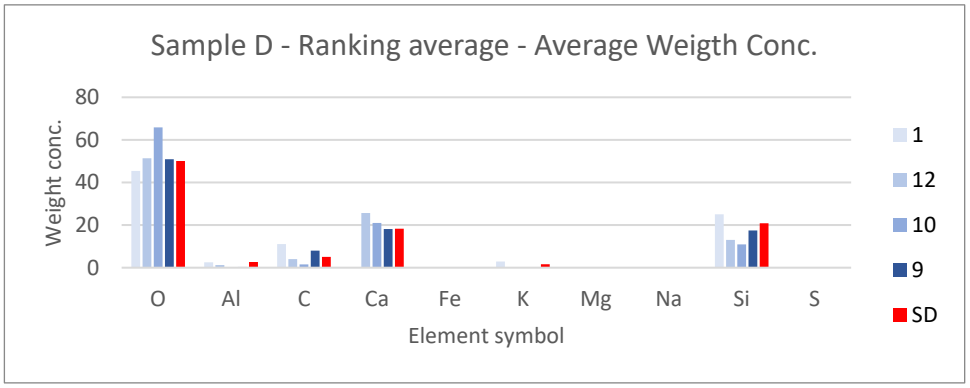


*Figure 398 – Sample D – Ranking average – Average weight concentration*

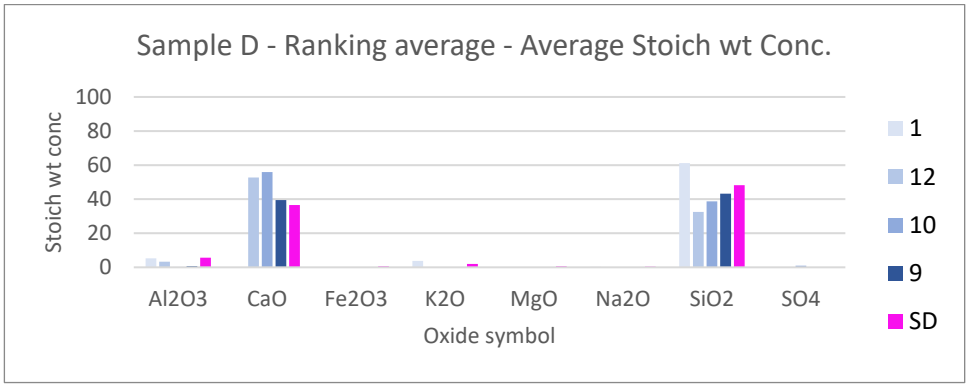


*Figure 399 – Sample D – Ranking average – Average stoich wt concentration*

### 10.8.4. Results comparison

Spectroscopy results indicate that sample is assembled from lime (*CaO*) and sand ($SiO_2$) with smaller *Al* and *K* additive. Electronic microscope results show a high presence of $SiO_2$ and *CaO* with additives $K_2O$ and $Al_2O_3$. Elements *Al, K* and *Mg* are present in minority. It can be concluded, that both methods provide similar results and thus the detection can be considered as satisfactory.

## 10.9. Sample E - Rýzmburk

### 10.9.1. Sample information

The sample has been collected from the gate of the Rýzmburk castle ruins that are situated near the Osek village, the Czech Republic and comes probably from the turn of the 16th and 17th century. Osek is located in the foothills of the Ore Mountains (Krušné hory) about 15km west from the city of Teplice. This sample is presupposed to be a lime plaster.

### 10.9.2. Spectroscopy results

The sample was documented using an ordinary mobile phone camera (Figure 400) and a digital DinoLite microscope with magnification 50 (Figure 401) and 200 (Figure 402).

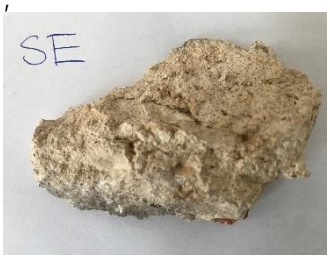


*Figure 400 – Sample E - Sample image*

*Figure 401 – Sample E - DinoLite microscope image, magnification 50*

*Figure 402 – Sample E - DinoLite microscope image, magnification 200*

Purchased reflectance spectroscopy data were processed and analysed using a MATLAB script in Appendix XIII available at enclosed CD. Analysis results are mentioned below, Figure 403 and Figure 404 shows spectral graphs of the sample.

| | |
|---|---|
| Minimum standard deviation: | 5.17% (for λ = 2512.118nm) |
| Maximum standard deviation: | 8.16% (for λ = 1956.52nm) |
| Mean standard deviation: | 7.00% |

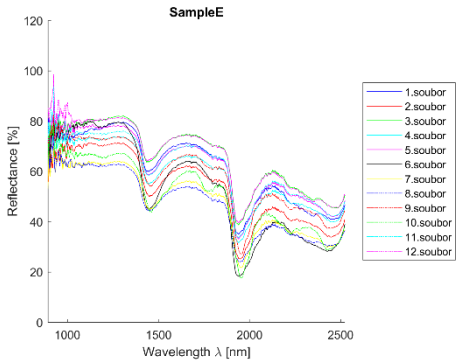


*Figure 403 – Sample E – All measurements plot*

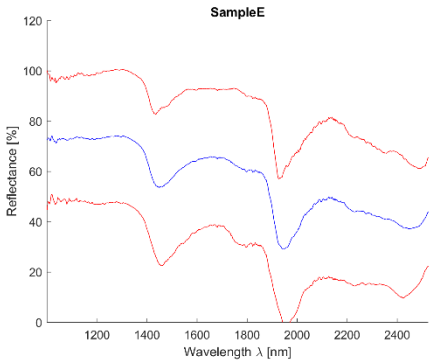


*Figure 404 - Sample E mean value (blue) and 2,5*standard deviation (red)*

Table 12 shows the representation of the first ten materials derived from all methods according to their ranking. The average is an arithmetic mean of their determination ranking; standard deviation is also shown in

the table to provide a level of confidence. Results of individual analysis can be found in Appendix IX.

*Table 12 – Sample E - Average material ranking in processed analysis*

| Material | Average | Std Dev |
|---|---|---|
| 13-Geopolymer (Střeleč sand) | 1,2 | 0,4 |
| 10-Lime + Cement Binder Mortar | 3,8 | 4,2 |
| 1-Božanov Sandstone | 5,0 | 2,4 |
| 18-Gypsum Standard | 5,4 | 3,4 |
| 9-Air Lime Mortar | 6,8 | 6,2 |
| 12-Lime + Metakaolin Binder Mortar | 7,0 | 3,7 |
| 11-Hydraulic Lime Mortar (NHL5) | 7,3 | 3,2 |
| 16-Čerťák Lime Hydrate | 8,3 | 6,2 |
| 2-Hořice Sandstone | 8,3 | 3,8 |
| 4-Quartzite | 9,0 | 5,6 |

Spectral curve description

The curve shows significant water absorption bands at 1450nm and 1950nm. The reflectance value variance is large (high standard deviation) and denotes a non-homogenous material surface

Individual analysis results

- SAM - correct detection of lime mortars and sands/sandstones
- SID - correct detection of sands/sandstones. Lime is represented by geopolymer; false detection of gypsum at 3$^{rd}$ place;
- NNLS - correct detection of sands/sandstones and in a smaller way also lime (lime hydrate, geopolymer), but the analysis does not show enough detected lime; false detection of gypsum;
- SFF - correct detection of lime mortars, but sand is missing (7$^{th}$ resp. 8$^{th}$ place with lower coefficients);
- BE – first eight materials have high similarity coefficients and sands/sandstones and lime mortars were determined correctly;
- Average - correct detection of lime mortars and sands/sandstones; geopolymer provides information on *CaO* presence and have significant water absorption bands; false detection of gypsum.

Conclusion

The sample is lime (*CaO*) with sand with *Al* ($Al_2O_3$) and *Na* additive; detection partially satisfactory.

### 10.9.3. Electronic microscope findings

- Phase 1 – light grey grains – aggregated $SiO_2$ ;
- Phase 2 – light grey to the white matrix – primarily *CaO*; *Si, Na* and *Al* minor occurrence;
- Phase 3 – light grey to the white matrix – not distinguishable on SEM image from phase 2 - predominantly *CaO* with *SiO2* additive; *K, Mg, Na* and *Al* minor occurrence;

- Phase 4 – dark grey matrix between grains – predominantly $SiO_2$ with $CaO$ and $Al_2O_3$ additives; *K, Mg, Na, K, Fe, P* and *Ti* minor occurrence.

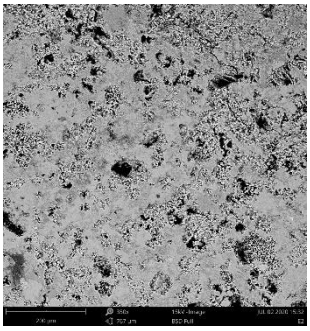

*Figure 405 - Phenom XL Desktop SEM photos - Microscopic sample image*

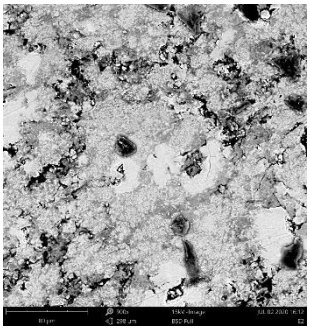

*Figure 406 - Phenom XL Desktop SEM photos - Microscopic sample image*

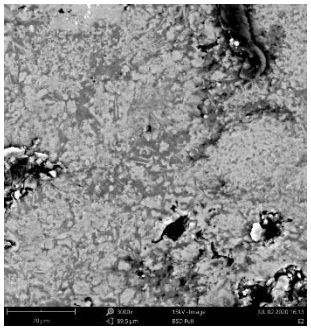

*Figure 407 - Phenom XL Desktop SEM photos - Microscopic sample image*

Figure 405 to Figure 407 shows the sample photos. SEM results (average atomic concentration, average weight concentration and average stoichiometry weight concentration) in the form of graphs are shown in Figure 408 to Figure 410.

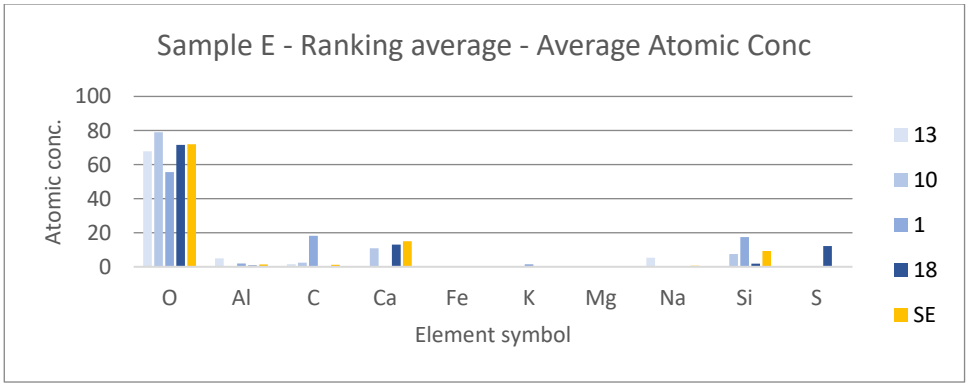


*Figure 408 – Sample E – Ranking average – Average atomic concentration*

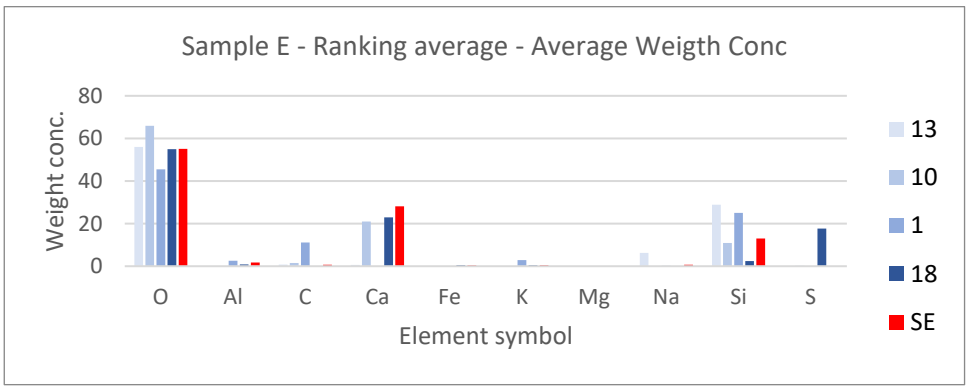


*Figure 409 – Sample E – Ranking average – Average weight concentration*

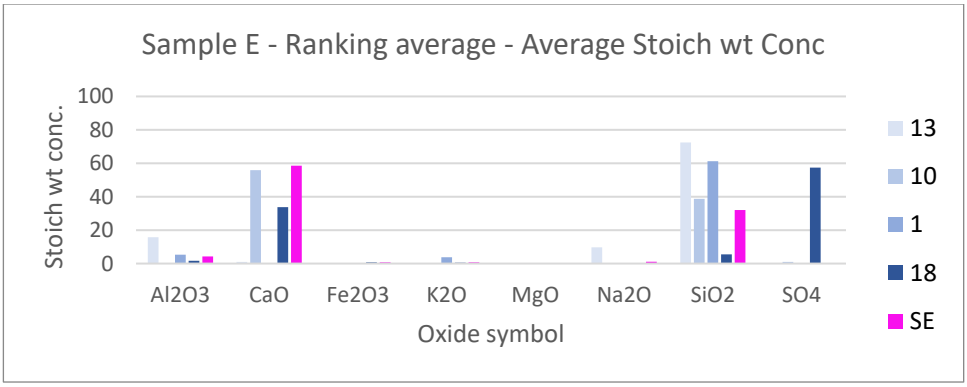


*Figure 410 – Sample E – Ranking average – Average stoich wt concentration*

### 10.9.4. Results comparison

Spectroscopy results indicate Geopolymer and Gypsum on 1st and 4th place in the ranking, but there is no presence of S in the electron microscope results. This may be due to visible water absorption band in 1450 and 1920nm respectively. Electronic microscope results show a high presence of $SiO_2$ and *CaO* with additive elements *Na, Al, K* and *Mg*. It can be concluded, that apart of Geopolymer and Gypsum detection both methods provide similar results and thus the detection can be considered partly satisfactory.

## 10.10. Sample FA - Cheb

### 10.10.1. Sample information

The sample has been collected from the Cheb castle that is located in the so-called city and is probably from the 18th century. The city of Cheb is located in Western Bohemia near the Czech-German border about 50km from Karlovy Vary. This sample is presupposed to be a baroque lime plaster.

### 10.10.2. Spectroscopy results

The sample was documented using an ordinary mobile phone camera (Figure 411) and a digital DinoLite microscope with magnification 50 (Figure 412) and 200 (Figure 413).

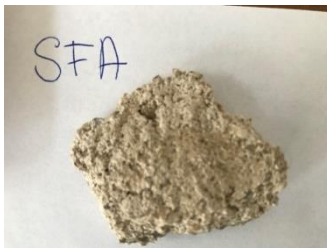


*Figure 411 – Sample FA – Sample image*

*Figure 412 – Sample FA - DinoLite microscope image, magnification 50*

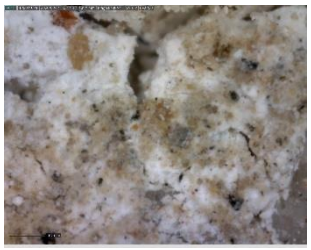

*Figure 413 – Sample FA - DinoLite microscope image, magnification 200*

Purchased reflectance spectroscopy data were processed and analysed using a MATLAB script in Appendix XIII available at enclosed CD. Analysis results are mentioned below, Figure 414 and Figure 415 shows spectral graphs of the sample.

Minimum standard deviation: 2.82% (for λ = 2490.917nm)
Maximum standard deviation: 4.51% (for λ = 1681.556nm)
Mean standard deviation: 3.86%

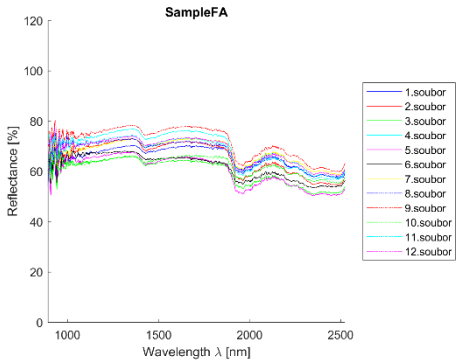


*Figure 414 – Sample FA – All measurements plot*

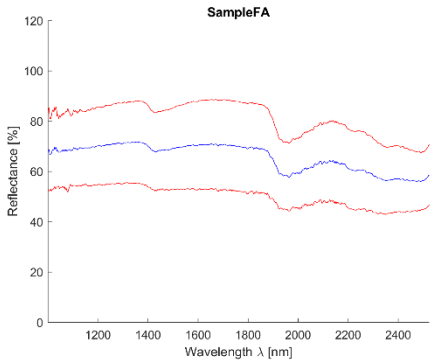


*Figure 415 - Sample FA mean value (blue) and 2,5*standard deviation (red)*

Table 13 shows the representation of the first ten materials derived from all methods according to their ranking. The average is an arithmetic mean of their determination ranking; standard deviation is also shown in the table to provide a level of confidence. Results of individual analysis can be found in Appendix X.

*Table 13 – Sample FA - Average material ranking in processed analysis*

| Material | Average | Std Dev |
|---|---|---|
| 12-Lime + Metakaolin Binder Mortar | 4,3 | 4,5 |
| 10-Lime + Cement Binder Mortar | 5,0 | 2,9 |
| 11-Hydraulic Lime Mortar (NHL5) | 5,4 | 6,7 |
| 6-Přední Kopanina Marlstone | 6,0 | 4,3 |
| 9-Air Lime Mortar | 6,8 | 4,5 |
| 2-Hořice Sandstone | 7,0 | 5,4 |
| 4-Quartzite | 9,2 | 7,3 |
| 1-Božanov Sandstone | 9,3 | 2,1 |
| 20-Clay Mortar (Claytec) | 9,6 | 7,8 |
| 18-Gypsum Standard | 10,8 | 4,0 |

Spectral curve description

The curve reflectance range varies from 60 to 70% with visible but not very substantial water absorption bands in 1450nm and more significant at 1950nm.

Individual analysis results

- SAM - correct detection of lime mortars/limestone and sands/sandstones;
- SID - significantly highest correspondence to marlstone (*AI*); other materials have much lower similarity coefficient; correct detection of sands/sandstones; Clay mortar detected (*AI*);
- NNLS - correct detection of lime mortars, striking detection of marlstone; little sands/sandstones;

- SFF - correct detection of lime mortars; geopolymer detected because of *CaO* and clay mortar due to *Al;*
- BE - correct detection of lime mortars and sands/sandstones;
- Average – lime mortars and marlstone were correctly detected with sufficient standard deviations.

Conclusion

The sample is lime (*CaO*) with sand ($SiO_2$) and small Al additive; detection satisfactory.

### 10.10.3. Electronic microscope findings

Dominant phase

- Phase 1 – light grey grains – aggregated $SiO_2$; *Al* minor occurrence;
- Phase 2 – a bit lighter grey grains – aggregated $SiO_2$ *and* $Al_2O_3$*; K, Mg, Na* and *Fe* minor occurrence;
- Phase 3 – light matrix between grain consists mainly of *CaO; Si, Al* and *Mg* minor occurrence.

Minor phase

- Phase 4 – light white particles of *Ti*; *Al* and *Si* minor occurrence;
- Phase 5 – dark grey areas – epoxy resin.

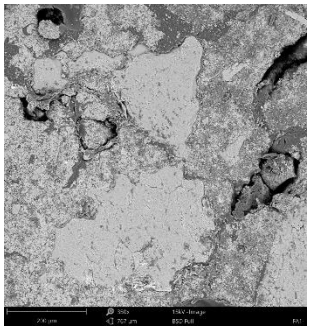

*Figure 416 - Phenom XL Desktop SEM photos - Microscopic sample image*

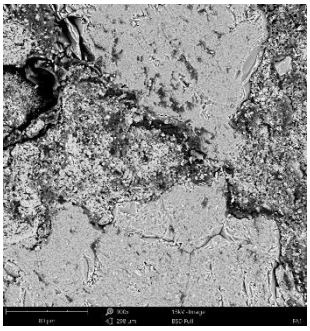

*Figure 417 - Phenom XL Desktop SEM photos - Microscopic sample image*

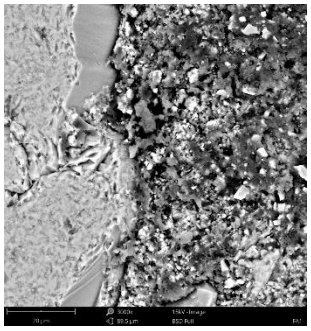

*Figure 418 - Phenom XL Desktop SEM photos - Microscopic sample image*

Figure 233 to Figure 418 shows the sample photos. SEM results (average atomic concentration, average weight concentration and average stoichiometry weight concentration) in the form of graphs are shown in Figure 419 to Figure 421.

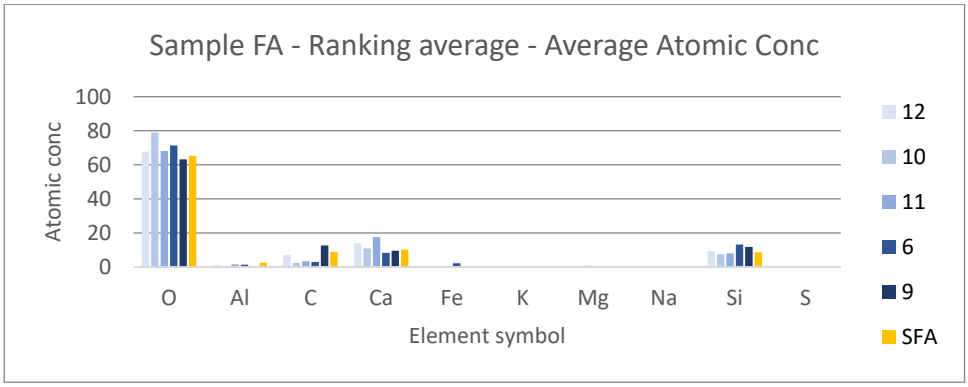


*Figure 419 – Sample FA – Ranking average – Average atomic concentration*

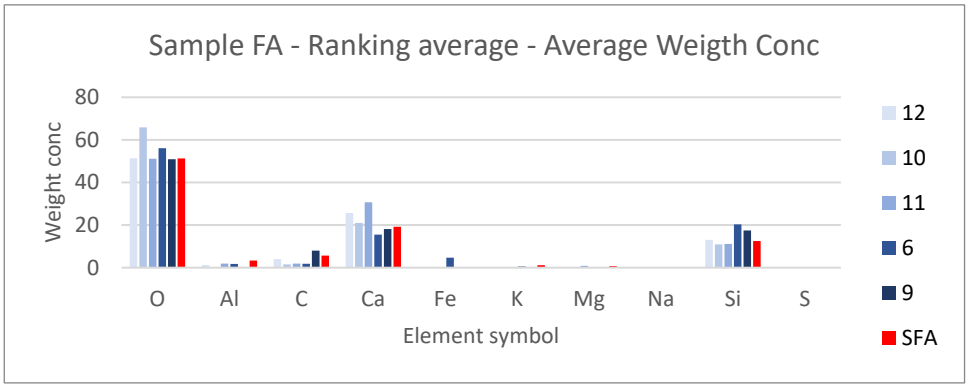


*Figure 420 – Sample FA – Ranking average – Average weight concentration*

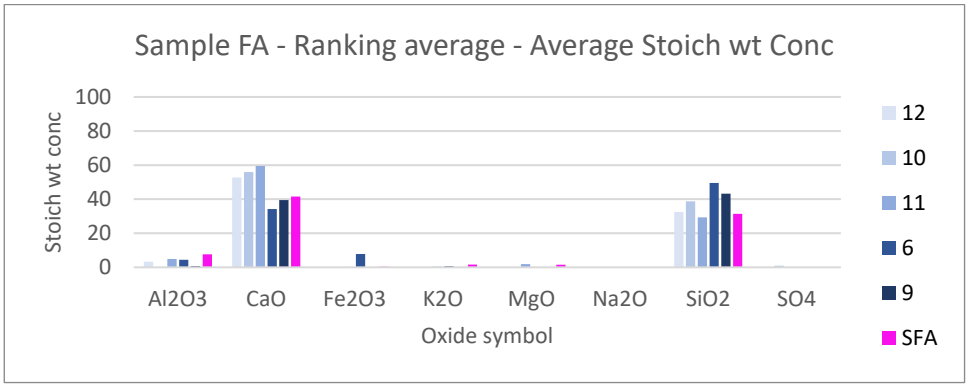


*Figure 421 – Sample FA – Ranking average – Average stoich wt concentration*

### 10.10.4. Results comparison

Spectroscopy results indicate that sample is assembled from lime (*CaO*) and sand ($SiO_2$) with smaller *Al* additive. Electronic microscope results show a high presence of $SiO_2$ and *CaO* with $Al_2O_3$ additive, elements *Mg*, *Na*, *K* and *Fe* are present in minority and a small amount of *Ti* was found. It can be concluded that both methods provide similar results and thus the detection can be considered satisfactory.

## 10.11. Sample FB - Cheb

### 10.11.1. Sample information

The sample has been collected from the Cheb castle that is located in the city of Cheb and is probably from the 18th century. The city of Cheb is located in Western Bohemia near the Czech-German border about 50km from Karlovy Vary. This sample is presupposed to be a baroque lime plaster.

### 10.11.2. Spectroscopy results

The sample was documented using an ordinary mobile phone camera (Figure 422) and a digital DinoLite microscope with magnification 50 (Figure 423) and 200 (Figure 424).

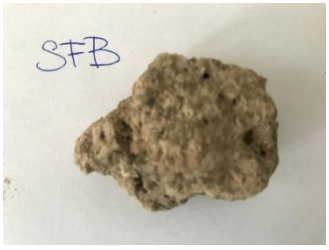


*Figure 422 – Sample FB - Sample Image*

*Figure 423 – Sample FB - DinoLite microscope image, magnification 50*

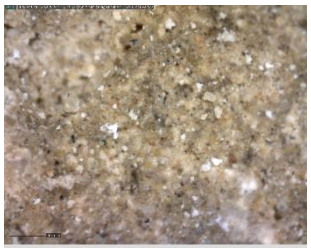

*Figure 424 - Sample FB - DinoLite microscope image, magnification 200*

Purchased reflectance spectroscopy data were processed and analysed using a MATLAB script in Appendix XIII available at enclosed CD. Analysis results are mentioned below, Figure 425 and Figure 426 shows spectral graphs of the sample.

| | |
|---|---|
| Minimum standard deviation: | 3.27% (for λ = 2463.588nm) |
| Maximum standard deviation: | 5.65% (for λ = 1678.336nm) |
| Mean standard deviation: | 4.76% |

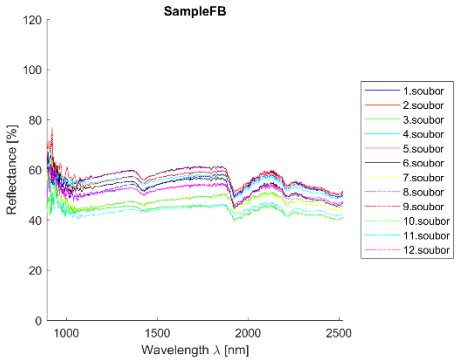


*Figure 425 – Sample FB – All measurements plot*

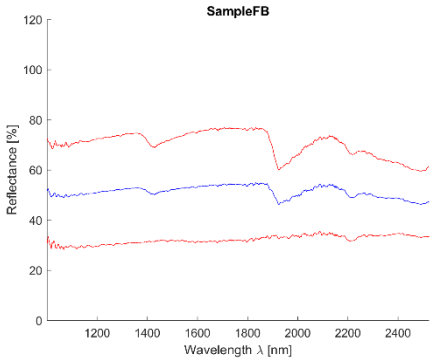


*Figure 426 - Sample FB mean value (blue) and 2,5*standard deviation (red)*

Table 14 shows the representation of the first ten materials derived from all methods according to their ranking. The average is an arithmetic mean of their determination ranking; standard deviation is also shown in

the table to provide a level of confidence. Results of individual analysis can be found in Appendix XI.

*Table 14 – Sample FB - Average material ranking in processed analysis*

| Material | Average | Std Dev |
|---|---|---|
| 15-Borek River Sand | 5,0 | 3,8 |
| 18-Gypsum Standard | 5,6 | 5,7 |
| 3-Mšeno Sandstone | 6,0 | 2,2 |
| 20-Clay Mortar (Claytec) | 6,2 | 7,0 |
| 19-Metakaolin L05 | 6,8 | 5,7 |
| 6-Přední Kopanina Marlstone | 7,2 | 3,6 |
| 2-Hořice Sandstone | 7,8 | 5,5 |
| 1-Božanov Sandstone | 8,5 | 7,6 |
| 7-Brick | 9,3 | 5,7 |
| 17-Dolomite Standard | 10,0 | 5,7 |

Spectral curve description

The curve is flat with visible water absorption band at 1450nm and more significant at 1950nm, reflectance varying around 50%.

Individual analysis results

- SAM - correct detection of sands/sandstones also correspondence to brick (contains *Al* and *Mg*) and clay mortar (*Al* and *Mg*) was found;
- SID - correct detection of sands/sandstones and material containing *CaO* (Dolomite); false detection of gypsum;
- NNLS – the highest resemblance was found with clay mortar (contains *Al* and *Mg*); correct detection of sands/sandstones and lime mortar; false detection of gypsum;
- SFF – the highest resemblance was found with clay mortar (contains *Al* and *Mg*); correct detection of sands/sandstones and lime mortar; a correspondence to brick (*Al* and *Mg*) was found; false detection of gypsum;
- BE – correct detection of sands/sandstones; a correspondence to metakaolin (*CaO*) and marlstone (*Al*) was found; false detection of gypsum;
- Average – value variance is high as is the standard deviation. This sample is not a pure composition of library material.

Conclusion

The sample consists of lime (*CaO*) and sands ($SiO_2$) with *Al* and *Mg* additives; detection satisfactory.

### 10.11.3. Electronic microscope findings

Dominant phase

- Phase 1– light grey grains – aggregated $SiO_2$; *Al, Ca* and *K* minor occurrence;
- Phase 2 – darker grains – aggregated $SiO_2$ and $Al_2O_3$; *Mg, Ca, K* and *Fe* minor occurrence;

- Phase 3 – light matrix between grain consists mainly of *CaO; Si, Al, Fe* and *Mg* minor occurrence.

Minor phase

- Phase 4 – light white particles of *Fe*; *Al* and *Si* minor occurrence;
- Phase 5 – dark grey areas – epoxy resin.

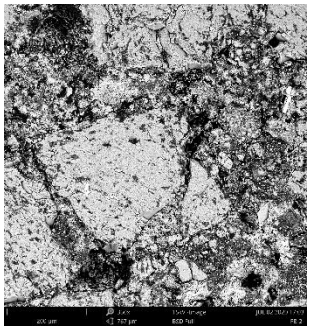

*Figure 427 - Phenom XL Desktop SEM photos - Microscopic sample image*

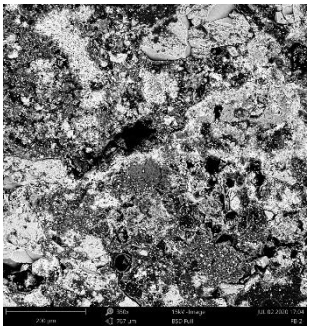

*Figure 428 - Phenom XL Desktop SEM photos - Microscopic sample image*

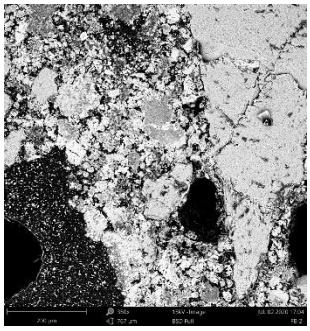

*Figure 429 - Phenom XL Desktop SEM photos - Microscopic sample image*

Figure 427 to Figure 429 shows the sample photos. SEM results (average atomic concentration, average weight concentration and average stoichiometry weight concentration) in the form of graphs are shown in Figure 430 to Figure 432.

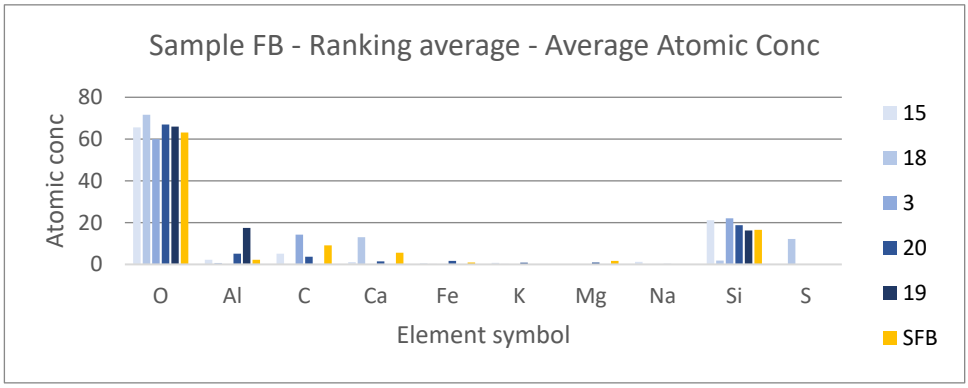


*Figure 430 – Sample FB – Ranking average – Average atomic concentration*

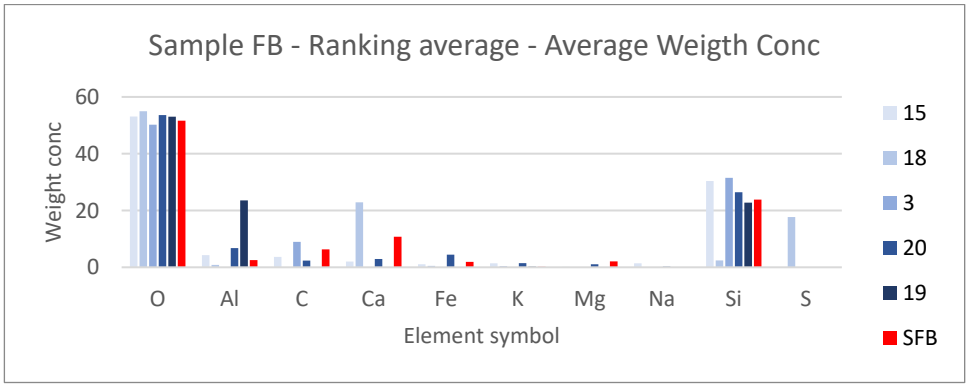


*Figure 431 – Sample FB – Ranking average – Average weight concentration*

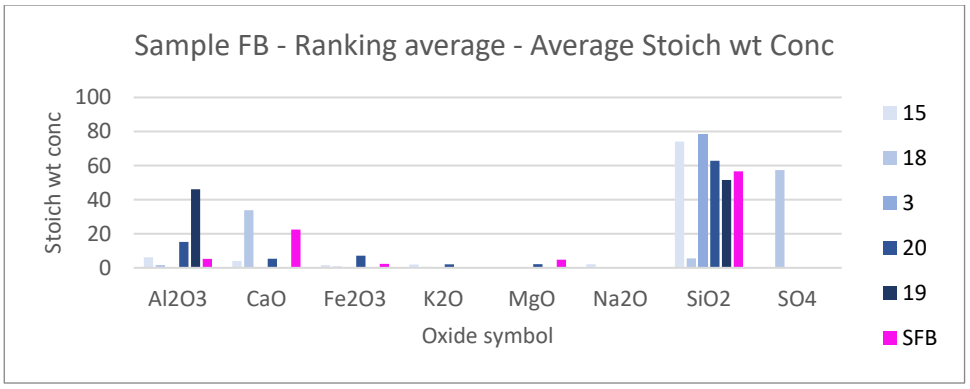


*Figure 432 – Sample FB – Ranking average – Average stoich wt concentration*

### 10.11.4. Results comparison

Spectroscopy results indicate that sample is assembled from lime (*CaO*) and sand ($SiO_2$) with smaller *Al* additive. Electronic microscope results show a high presence of $SiO_2$ and *CaO* with $Al_2O_3$ additive, elements *Mg, K* and *Fe* are present in minority. It can be concluded, that both methods provide similar results and thus the detection can be considered satisfactory.

## 10.12. Rock sample 1

### 10.12.1. Sample information

The sample was received from Mr Cihla for the NAKI III. Project (Chapter 5.2.2) and was used for the Biological contamination of stone (Chapter 5.2). This sample was dried and then used for the spectroscopy analysis. The sample is a Mšeno Sandstone.

### 10.12.2. Spectroscopy results

The sample was documented using an ordinary mobile phone camera (Figure 433) and a digital DinoLite microscope with magnification 50 (Figure 434) and 200 (Figure 435).

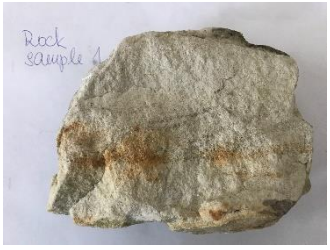


*Figure 433 – Rock sample 1 – Sample image*

*Figure 434 – Rock sample 1 - DinoLite microscope image, magnification 50*

*Figure 435 – Rock sample 1 - DinoLite microscope image, magnification 200*

Purchased reflectance spectroscopy data were processed and analysed using a MATLAB script in Appendix XIII available at enclosed CD. Analysis results are mentioned below, Figure 436 and Figure 437 shows spectral graphs of the sample.

Minimum standard deviation: 3.06% (for λ = 1145.286nm)
Maximum standard deviation: 3.95% (for λ = 1001.238nm)
Mean standard deviation: 3.27%

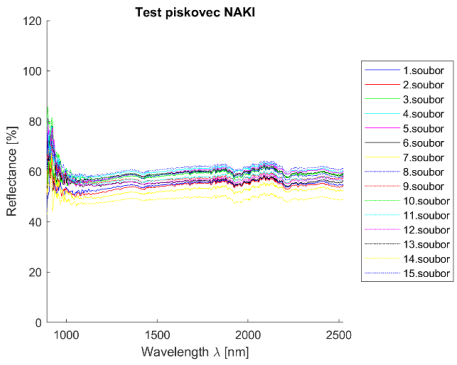


*Figure 436 – Rock sample 1 – all measurements plot*

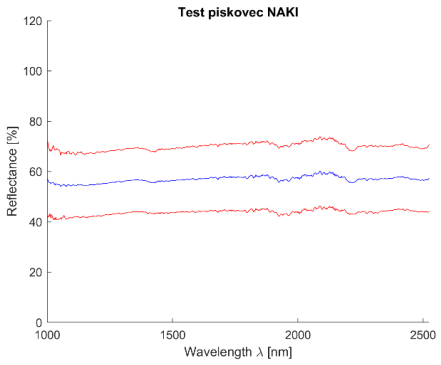


*Figure 437 – Rock sample 1 mean value (blue) and 2,5*standard deviation (red)*

Table 15 shows the representation of the first ten materials derived from all methods according to their ranking. The average is an arithmetic mean of their determination ranking; standard deviation is also shown in the table to provide a level of confidence. Results of individual analysis can be found in Appendix XII.

*Table 15 – Rock sample 1- Average material ranking in processed analysis*

| Material | Average | Std Dev |
|---|---|---|
| 3-Mšeno Sandstone | 1,80 | 1,10 |
| 20-Clay Mortar (Claytec) | 3,40 | 2,07 |
| 17-Dolomite Standard | 4,40 | 2,88 |
| 7-Brick | 4,75 | 2,99 |
| 14-Střeleč Sand Quartz | 5,40 | 4,22 |

Spectral curve description

The curve is flat with reflectance around 60% without bigger divergence.

Individual analysis results

- SAM – correctly detected Mšeno sandstone on 1st place, a big difference between 1st and 2nd ;
- SID - false detection of dolomite at 1st place, Střeleč quartz sand 2nd and Mšeno sandstone 3rd because Mšeno sandstone contains a lot of quartz sand;
- NNLS – correctly detected Mšeno sandstone on 1st place, but there was not a big difference between other materials (clay mortar, Střeleč quartz sand, dolomite) ;
- SFF - correctly detected Mšeno sandstone on 1st, not a big difference between 2nd Střeleč quartz sand because Mšeno sandstone contains a lot of quartz sand;
- BE -f detection of dolomite at 1st place, Mšeno sandstone 3rd ;

- Average - correctly detected Mšeno sandstone on 1st place, a big difference between 1st and 2nd.

Conclusion

The sample is Mšeno sandstone

### 10.12.1. Results comparison

This sample is pure Mšeno sandstone and was added into analysis to test the workflow. It was found that the detection is satisfactory since the assumption was confirmed and this sample was detected as Mšeno sandstone.

# 11. Plaster analysis evaluation

Eleven plasters were analysed using spectroscopy and electron microscope techniques in order to find possibilities of reflectance spectroscopy and its ability to determine the composition of plasters and mortars. It was found that reflectance spectroscopy can provide powerful information, but results must be interpreted with care and they are not unequivocal.

Lime mortars' spectral signature has high vicinity among all four samples and hence the differentiation is lower. Geopolymer is often interchanged with gypsum and vice versa. Since water absorption features [159] were not removed from the spectra, gypsum and geopolymer are often incorrectly mentioned in the material decomposition. The influence of these spectral features is strongly material dependent and provides additional information about materials and samples. The majority of samples consists of sand and lime mixture with different percentage of each. These small differences were not always detected and this is the main limitation of the spectroscopy method. Analysis using continuum removal [160] was also tested but not further used. It is more of a visualization method that highlights extremes and hence can be compared to histogram stretching - [161] method used for remote sensing data.

Table 16 shows the minimum, maximum and average standard deviation of each sample. The quality of spectroscopy detection depends mainly on the correctness of detected material, standard deviation is a derivative outcome. The average standard deviation lies between 1,80% (Sample A) to 7,00% (Sample E). The high standard deviation of Sample E is caused by the fact, that it is assembled by different materials that have variable spectral signatures and are very inhomogeneous. An average standard deviation of all samples is equal to 3,99% and can be found sufficient.

*Table 16 – Sample measurements – Data and detection quality*

| Sample | Standard Deviation [%] | | | Spectroscopy detection quality |
|---|---|---|---|---|
| | Minimum | Maximum | Average | |
| 1 | 1,89 | 6,42 | 4,15 | Satisfactory |
| 2 | 3,08 | 5,05 | 3,81 | Satisfactory |
| 3 | 2,50 | 7,69 | 3,77 | Partially satisfactory |
| 4 | 2,86 | 5,49 | 3,80 | Satisfactory |
| A | 1,59 | 3,31 | 1,80 | Nearly satisfactory |
| B | 1,96 | 5,56 | 3,13 | Nearly satisfactory |
| C | 3,34 | 9,03 | 4,47 | Nearly satisfactory |
| D | 3,10 | 5,75 | 4,00 | Satisfactory |
| E | 5,17 | 8,16 | 7,00 | Partially satisfactory |
| FA | 2,82 | 4,51 | 3,86 | Satisfactory |
| FB | 3,27 | 5,65 | 4,76 | Satisfactory |
| Rock 1 | 3,06 | 3,95 | 3,27 | Satisfactory |

# 12. Decision tree

Next to spectroscopy analysis, a decision tree approach was also tested. This method, commonly used for multispectral remote sensing data [162], chooses previously defined thresholds, that should be fulfilled to categorize sample into a specific previously defined class. With the spectroscopy data, the possibilities on threshold definition rise and can become very precise and pointing at specific attributes of spectral curves.

## 12.1. Class definition

For this thesis, eight classes were set. Namely – Geopolymer, Gypsum, Lime mortars, Limes, Marlstone, Sandstone, Quartz and Unidentified. These classes were chosen based on the CTU Material Spectral Library (Chapter 9) and individual characteristics of their spectral signatures. All twenty materials were divided into these eight classes as follows:

- Geopolymer
  - Geopolymer (Střeleč sand), no.13
- Gypsum
  - Gypsum Standard, no. 18
- Lime mortars
  - Air lime mortar, no.9
  - Lime + Cement Binder Mortar, no. 10
  - Hydraulic Lime Mortar, no. 11
  - Lime + Metakaolin Binder Mortar, no. 12
- Limes
  - Maastricht Limestone, no. 5
  - Čerťák Lime Hydrate, no. 16
  - Dolomite Standard, no. 17
- Marlstone
  - Přední Kopanina Marlstone, no. 6

- Sandstone
  - Božanov Sandstone, no. 1
  - Hořice Sandstone, no. 2
  - Mšeno sandstone, no. 3
- Quartz
  - Quartzite, no. 4
  - Střeleč Quartz Sand, no. 14
  - Borek River Sand, no. 15
  - Clay Mortar, no. 20
- Unidentified
  - Brick, no. 7
  - Tile, no. 8
  - Metakaolin, no. 19

## 12.2. Threshold settings

To classify each material into the correct class, seven thresholds had to be set. These limits were chosen concerning the nature of material individual spectral signature. Maximum and minimum values in specific spectral range, as well as the reflectance, were considered. These boundaries were then tuned up using the CTU Material Spectral Library to assure that all material present in the library will be present in the correct class. This was an issue with Clay mortar (no. 20), that was integrated into "Other" class at first, but then it was found out, that due to its high amount of quartz sand present in the mixture it cannot be spectrally distinguished from the "Quartz" class and therefore it was moved and classes were set as mentioned in Chapter 12.1.

The thresholds for individual classes were set as follows:

1. Geopolymer
   - In spectral range 1250 – 1600nm the Max – Min value ≤ 20
   - In spectral range 1800 – 2100nm the Max – Min value ≤ 28
2. Gypsum
   - In spectral range 1800 – 2100nm the Max – Min value ≥ 28
3. Lime mortars
   - Average reflectance over an entire spectral range between 60 and 90%
   - In spectral range 1300 – 1500nm the Max – Min value ≥ 4
   - In spectral range 1800 – 2100nm the Max – Min value ≥ 10
4. Limes
   - In spectral range 2300 – 2500nm the Max – Min value ≥ 6

5. Marlstone
    - In spectral range 1300 – 1450nm the Max – Min value ≥ 4
    - In spectral range 1800 – 2000nm the Max – Min value ≥ 10
    - In spectral range 2000 – 2250nm the Max – Min value ≥ 10
6. Sandstone
    - Average reflectance over an entire spectral range between 45 and 70%
    - In spectral range 2100 – 2300nm the Max – Min value ≥ 5
7. Quartz
    - Average reflectance over the entire spectral range is smaller than 70%
    - Max – Min value over the entire spectral range ≤ 13

If a sample does not fulfil any threshold it will be included in the „Unidentified" class.

## 12.3. Data processing and results

Data were processed using MATLAB script available on a CD as Appendix XVII. and the flowchart is shown in Figure 438. Results are expressed in the form of a text file (Figure 439).

When results shown in Figure 439 were compared to outcomes derived from the electron microscope available for every sample it can be concluded, that the decision tree provides relevant results. Samples A, C, D and 2 were assigned to class "Sandstone" since there is a lot of sand particles included in the mixture. Samples FA, 1 and 3 were assigned to the class "Lime mortar" which corresponds with electron microscope findings. Sample B was correctly included into "Gypsum" class and Sample 4 matched the "Lime" class since it is pure *CaO* on wood. Sample E was classified as "Geopolymer" which is the only incorrect result and it is caused by the fact, that the sample is very inhomogeneous with visible water absorption spectral bands that are similar to geopolymer.

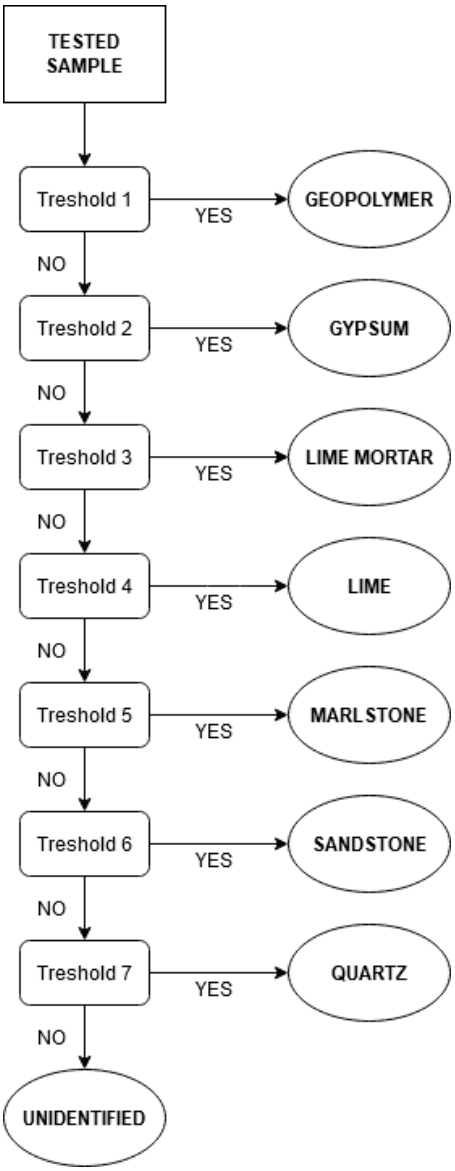


*Figure 438 – Decision tree results in a text file*

| sample | material group |
|---|---|
| SampleA | sandstone |
| SampleB | gypsum |
| SampleC | sandstone |
| SampleD | sandstone |
| SampleE | geopolymer |
| SampleFA | lime mortar |
| SampleFB | sandstone |
| Sample1 | lime mortar |
| Sample2 | sandstone |
| Sample3 | lime mortar |
| Sample4 | lime |

*Figure 439 – Decision tree flowchart*

# 13. Discussion

Various terrestrial applications of the hyperspectral and spectroscopy data were introduced and conducted. Hyperspectral methods were used for non-invasive painting analysis and biological contamination of stone. Possibilities and limitation of spectroscopy were tested for mortar and plaster determination and a material spectral library was created.

It was found that hyperspectral data can be a powerful tool for painting analysis and can show information that is not visible to the human eye like underdrawings or even material composition. Using a hyperspectral scanning sensor provides unique datasets that can be analysed in different ways depending on the expected result. A principal component analysis results can be used (Chapter 5.1) or the data can be further processed and an endmember extraction can be accomplished together with final mapping (using e.g. spectral angle mapper, Chapter 5.2).

The main limitation of this method lies in the sensor characteristics like available spectral range, spectral and spatial resolution, data quality (e.g. amount of noise). The imaging sensor available at FCE, CTU (Chapter 4.1) provides good quality data in a spectral range 400 – 1000nm which is sufficient for the majority of vegetation analysis, but the lack of information in SWIR (up to 2500nm) limits the possibility for closer material analysis since the major information lies in this spectral range. Even though very interesting outcomes were created with biological contamination of stone like vegetation time monitoring or endmember mapping. These possibilities will be further investigated in the ongoing Czech Ministry of Culture project (NAKI III - Stone surface topography and its application in stone element restoration field).

Spectroscopic analysis of plasters and mortar materials is introduced in the second part of the thesis. Based on provided material samples, a CTU Material Spectra Library was created and it is available online after request on Laboratory of Photogrammetry, Department of Geomatics, Czech Technical University in Prague web page (http://lfgm.fsv.cvut.cz/CTU.html). This library includes 20 materials that were chosen to define historical plaster and mortar composition used in the area of Central Europe (the Czech Republic). This library was then tested on 11 plaster and mortar samples. To verify this method an electron microscope results were confronted to determine the composition of individual materials and samples. It was found that reflectance spectroscopy can be a powerful tool when treated with care and vigilant. In general, test samples were determined correctly, the results are closely analysed in Chapter 11. The majority of samples consists of sand (*SiO2*) and lime (*CaO*) mixture with a different percentage of each. These small differences were not always detected and this is the main limitation of this method. A decision tree approach for material composition detection of plaster and mortar samples was tested in this thesis (Chapter 12). Materials were separated into eight classes and these thresholds were then applied to plaster and mortar samples. Results show the fine determination of samples into specific classes that correspond to results given by the electron microscope and spectroscopy analysis.

The analysis was performed in various software tools like a MATLAB script language, open-source QSdata software and ENVI software. The biggest benefit of the script language and the opensource software is that it is visible how the variables are computed and parameters can be adjusted. An ENVI software tool has a user-friendly interface and some analysis explanation can be found online, but full control over the processing chain is not enabled. Due to the above mentioned the best computing software cannot be derived and was not the main purpose of this thesis.

The power of the reflectance spectroscopy method lies in its repeatability that is assured by the calibration procedure. The CTU Material Spectral Library can be used by various researchers worldwide. If a different reflectance spectroscopy device is employed, the user selects the spectral range that corresponds to the operating range of the device used. Its limitation is the spectral range (1000 – 2500nm) - it may occur that due to a small overlap between the spectral range of the CTU Material Spectral Library and users' device there might be a restraint in the application. This

can be solved by enlarging the spectral library spectral range with a new device.

In the future research, the author would like to focus on enlarging the material spectral library for a more specific material determination not only for plasters and mortars but also for other historical building materials towards their higher variability.

## 14. Aims and objectives fulfilment

The first objective was to explore and test possibilities of hyperspectral imaging on close-range analysis in the laboratory to prepare the CTU hyperspectral system for future in-situ use. It can be stated that the research fully met this objective since the author has processed the laboratory measurements. The author proved that the CTU hyperspectral imaging system is operational and ready for in-situ measurements that will be performed in the location of Charles Bridge, Prague, the Czech Republic. With respect to the methodology capabilities mentioned earlier (Chapter 4.1 and 5) this system will be used for historical stone time monitoring that will start as soon as the epidemic situation allows.

The second objective was to create and examine spectral characteristics of selected materials that will be used for their determination in the Central Europe region using reflectance spectroscopy. It can be concluded that the research met this objective. The CTU material spectral library with twenty in-depth analysed materials was created and evaluated. Scanning electron microscope analysis method was used for thorough validation. This spectral library was tested on eleven historical plaster, mortar and stone samples and it is now available online after request (Chapter 8.2).

The author has met all aims of the dissertation.

## 15. Conclusion

This study focuses on the use of hyperspectral imaging and reflectance spectroscopy. Basic principles were explained and different instrument types were described in the first part. Major applications were presented and one can state that hyperspectral imaging and reflectance spectroscopy are very perspective methods and will be used a lot in future research and work in many diverse topics.

Hyperspectral imaging was used for non-invasive documentation of historical paintings and biological determination of stone. These methods provide valuable results like material composition that help to understand the nature of the object of interest and can provide information that is not visible at the beginning.

Reflectance spectroscopy was used to derive plaster and mortar material composition based on the created material spectral library. It is a unique set of material spectral information that is directed to Central Europe and becomes the basis for future enlargement. Various analysis were performed and compared. It was found that the spectroscopy method is suitable for use in the historical heritage documentation field. It is not expected to obtain precise results regarding the material composition of man-made mixtures (mortars, plasters) using reflectance spectroscopy. Many of them contain similar additives and/or the additives are much alike

(e.g. sand of various quality and composition). European mortars traditionally contain lime. This method is therefore very useful for mineral and rock types in geology.

The author believes that the use of non-invasive cultural heritage object documentation will play a key role in the future. When documenting historical objects, owners will prefer non-invasive techniques since they do not damage the object of interest. Nowadays methodologies of these techniques should be created, in order to be widely used by the public in days to come.

# 16. References


[1] BORENGASSER, Marcus, William HUNGATE a Russel WATKINS. *Hyperspectral Remote Sensing: Principles and Applications*. 1. CRC Press, 2007. ISBN 978-1566706544.

[2] ROBINSON, Heath. Spectral Reflectance. *Humbolt state university* [online]. Arcata, California, USA: Humbolt state university, 2019 [cit. 2020-09-24]. Dostupné z: http://gsp.humboldt.edu/OLM/Courses/GSP_216_Online/lesson2-1/reflectance.html

[3] MEER, Freek a Steven JONG, ed. *Imaging Spectrometry* [online]. 1. Dordrecht: Springer Netherlands, 2002 [cit. 2020-08-24]. Remote Sensing and Digital Image Processing. ISBN 978-1-4020-0194-9. Dostupné z: doi:10.1007/978-0-306-47578-8

[4] HUANG, Hui, Li LIU a Michael NGADI. Recent Developments in Hyperspectral Imaging for Assessment of Food Quality and Safety. *Sensors* [online]. 2014, 14(4), 7248-7276 [cit. 2020-08-24]. ISSN 1424-8220. Dostupné z: doi:10.3390/s140407248

[5] InGaAs linear image sensors. In: *Hamamatsu* [online]. [cit. 2020-08-24]. Dostupné z: https://www.hamamatsu.com/resources/pdf/ssd/g9211-256s_etc_kmir1011e.pdf

[6] SMITH, Randal B. Introduction to hyperspectral imaging: Intro to hypersp. In: *MicroImages, Inc.* [online]. [cit. 2020-08-24]. Dostupné z: https://www.microimages.com/documentation/Tutorials/hyprspec.pdf

[7] NIRQuest Installation and Operation Manual. *OceanOptics* [online]. [cit. 2020-08-24]. Dostupné z: http://oceanoptics.com//wp-content/uploads/nirquest.pdf

[8] DELL'ENDICE, Francesco, Jens NIEKE, Benjamin KOETZ, Michael SCHAEPMAN a Klaus ITTEN. Improving radiometry of imaging spectrometers by using programmable spectral regions of interest. *ISPRS Journal of Photogrammetry and Remote Sensing* [online]. 2009, 64(6), 632-639 [cit. 2020-08-24]. ISSN 09242716. Dostupné z: doi:10.1016/j.isprsjprs.2009.05.007

[9] HyMap. *HyVista Corporation* [online]. [cit. 2020-08-24]. Dostupné z: http://www.hyvista.com/technology/sensors/hymap/

[10] AVIRIS. *AVIRIS* [online]. NASA Jet Propulsion Laboratory [cit. 2020-08-24]. Dostupné z: https://aviris.jpl.nasa.gov/documents/aviris_task.html

[11] *Earth Observing-1 Extended Mission* [online]. Geological Survey (U.S.), 2005 [cit. 2020-08-24]. Dostupné z: doi:10.3133/fs20053060

[12] *CASI1500* [online]. Calgary, Alberta, Canada: ITRES Research Limited, 2010 [cit. 2020-08-25]. Dostupné z: https://www.linkfast.com.tw/upload/files/CASI-1500.pdf

[13] *Proba 1* [online]. European Space Agency [cit. 2020-08-24]. Dostupné z: https://earth.esa.int/web/guest/missions/esa-operational-eo-missions/proba/

[14] Hyperspectral sensors. *Headwall Photonics* [online]. USA: Headwall Photonics, 2020 [cit. 2020-08-25]. Dostupné z: https://www.headwallphotonics.com/hyperspectral-sensors

[15] *GloVis* [online]. USGS [cit. 2020-08-24]. Dostupné z: https://glovis.usgs.gov/

[16] How to access ESA data. *Earth Online: Earth Observation information discovery platform* [online]. [cit. 2020-08-25]. Dostupné z: https://earth.esa.int/web/guest/data-access/how-to-access-esa-data

[17] SHIPPERT, Peg. Introduction toHyperspectral Image Analysis. *Online journal of space commmunication* [online]. [cit. 2020-08-25]. ISSN 1542-0639A. Dostupné z: https://spacejournal.ohio.edu/pdf/shippert.pdf

[18] SHRESTHA, D.P., D.E. MARGATE, F. MEER a H.V. ANH. Analysis and classification of hyperspectral data for mapping land degradation: An application in southern Spain. *International Journal of Applied Earth Observation and Geoinformation* [online]. 2005, 7(2), 85-96 [cit. 2020-08-25]. ISSN 03032434. Dostupné z: doi:10.1016/j.jag.2005.01.001

[19] ZHANG, Xiangmin. *Coal fires in Northwest China: detection, monitoring, and prediction using remote sensing data*. 58. [Hebei Province, China: X. Zhang, 1998. ITC publication (Enschede, Netherlands), no. 58. ISBN 90-616-4144-6.

[20] BARTHèS, Bernard G. a Jean-Luc CHOTTE. Infrared spectroscopy approaches support soil organic carbon estimations to evaluate land degradation. *Land Degradation & Development* [online]. [cit. 2020-09-24]. ISSN 1085-3278. Dostupné z: doi:10.1002/ldr.3718

[21] WARD, Kathrin J., Sabine CHABRILLAT, Carsten NEUMANN a Saskia FOERSTER. A remote sensing adapted approach for soil organic carbon prediction based on the spectrally clustered LUCAS soil database. *Geoderma* [online]. 2019, 353, 297-307 [cit. 2020-09-24]. ISSN 00167061. Dostupné z: doi:10.1016/j.geoderma.2019.07.010

[22] BRODSKÝ, L., A. KLEMENT, V. PENÍŽEK, R. KODEŠOVÁ a L. BORŮVKA. Building soil spectral library of the Czech soils for quantitative digital soil mapping. *Soil and Water Research* [online]. 2011, 6(4), 165-172 [cit. 2020-03-18]. ISSN 18015395. Dostupné z: doi:10.17221/24/2011-SWR

[23] DEMATTê, José A.M., André Carnieletto DOTTO, Ariane F.S. PAIVA et al. The Brazilian Soil Spectral Library (BSSL): A general view, application and challenges. *Geoderma* [online]. 2019, 354 [cit. 2020-09-24]. ISSN 00167061. Dostupné z: doi:10.1016/j.geoderma.2019.05.043

[24] VISCARRA ROSSEL, R.A., T. BEHRENS, E. BEN-DOR et al. A global spectral library to characterize the world's soil. *Earth-Science Reviews* [online]. 2016, 155(2016), 198-230 [cit. 2020-03-18]. ISSN 00128252. Dostupné z: doi:10.1016/j.earscirev.2016.01.012

[25] THENKABAIL, Prasad, J. LYON a Alfredo HUETE. *Hyperspectral remote sensing of vegetation*. Boca Raton, FL: CRC Press, 2012. ISBN 14-398-4537-9.

[26] ZARCO-TEJADA, P.J., V. GONZÁLEZ-DUGO a J.A.J. BERNI. Fluorescence, temperature and narrow-band indices acquired from a UAV platform for water stress detection using a micro-hyperspectral imager and a thermal camera. *Remote Sensing of Environment* [online]. 2012, 117, 322-337 [cit. 2020-08-25]. ISSN 00344257. Dostupné z: doi:10.1016/j.rse.2011.10.007

[27] KUPKOVA, Lucie, Marketa POTUCKOVA, Michaela BURICOVA, Veronika KOPACKOVA, Zuzana LHOTAKOVA a Jana ALBRECHTOVA. Determination of lignin content in Norway spruce foliage using NIR spectroscopy and hyperspectral data. In: *2012 IEEE International Geoscience and Remote Sensing Symposium* [online]. IEEE, 2012, s. 4190-4193 [cit. 2020-09-24]. ISBN 978-1-4673-1159-5. Dostupné z: doi:10.1109/IGARSS.2012.6351745

[28] MOHAMED, E. S., A. M. ALI, M. A. EL SHIRBENY, Afaf A. ABD EL RAZEK a I. Yu. SAVIN. Near infrared spectroscopy techniques for soil contamination assessment in the Nile Delta. *Eurasian Soil Science* [online]. 2016, 49(6), 632-

639 [cit. 2020-09-24]. ISSN 1064-2293. Dostupné z: doi:10.1134/S1064229316060065

[29] SIEBIELEC, Grzegorz, Gregory W. MCCARTY, Tomasz I. STUCZYNSKI a James B. REEVES. Near- and Mid-Infrared Diffuse Reflectance Spectroscopy for Measuring Soil Metal Content. *Journal of Environmental Quality* [online]. 2004, 33(6), 2056-2069 [cit. 2020-09-24]. ISSN 00472425. Dostupné z: doi:10.2134/jeq2004.2056

[30] GONZÁLEZ-FERNÁNDEZ, Ana Belén, José Ramón RODRÍGUEZ-PÉREZ, Victoriano MARCELO a José B. VALENCIANO. Using field spectrometry and a plant probe accessory to determine leaf water content in commercial vineyards. *Agricultural Water Management* [online]. 2015, 156, 43-50 [cit. 2020-09-24]. ISSN 03783774. Dostupné z: doi:10.1016/j.agwat.2015.03.024

[31] KÖKSAL, Eyüp Selim, Yetkin GÜNGÖR a Yusuf Ersoy YILDIRIM. Spectral reflectance characteristics of sugar beet under different levels of irrigation water and relationships between growth parameters and spectral indexes. *Irrigation and Drainage* [online]. 2011, 60(2), 187-195 [cit. 2020-09-24]. ISSN 15310353. Dostupné z: doi:10.1002/ird.558

[32] WEST, Jonathan S., Cedric BRAVO, Roberto OBERTI, Dimitri LEMAIRE, Dimitrios MOSHOU a H. Alastair MCCARTNEY. T HE P OTENTIAL OF O PTICAL C ANOPY M EASUREMENT FOR T ARGETED C ONTROL OF F IELD C ROP D ISEASES. *Annual Review of Phytopathology* [online]. 2003, 41(1), 593-614 [cit. 2020-09-24]. ISSN 0066-4286. Dostupné z: doi:10.1146/annurev.phyto.41.121702.103726

[33] MARTINELLI, Federico, Riccardo SCALENGHE, Salvatore DAVINO et al. Advanced methods of plant disease detection. A review. *Agronomy for Sustainable Development* [online]. 2015, 35(1), 1-25 [cit. 2020-09-24]. ISSN 1774-0746. Dostupné z: doi:10.1007/s13593-014-0246-1

[34] CHO, Yong-Jin. *Emerging technologies for food quality and food safety evaluation*. Boca Raton: CRC Press, 2011. ISBN 978-143-9815-243.

[35] RAJKUMAR, P., N. WANG, G. EIMASRY, G.S.V. RAGHAVAN a Y. GARIEPY. Studies on banana fruit quality and maturity stages using hyperspectral imaging. *Journal of Food Engineering* [online]. 2012, 108(1), 194-200 [cit. 2020-09-24]. ISSN 02608774. Dostupné z: doi:10.1016/j.jfoodeng.2011.05.002

[36] GOWEN, A, C ODONNELL, P CULLEN, G DOWNEY a J FRIAS. Hyperspectral imaging – an emerging process analytical tool for food quality and safety control. *Trends in Food Science & Technology* [online]. 2007, 18(12), 590-598 [cit. 2020-09-24]. ISSN 09242244. Dostupné z: doi:10.1016/j.tifs.2007.06.001

[37] SCHMILOVITCH, Ze'ev, Timea IGNAT, Victor ALCHANATIS, Janna GATKER, Viacheslav OSTROVSKY a József FELFÖLDI. Hyperspectral imaging of intact bell peppers. *Biosystems Engineering* [online]. 2014, 117, 83-93 [cit. 2020-09-24]. ISSN 15375110. Dostupné z: doi:10.1016/j.biosystemseng.2013.07.003

[38] ZHU, Fengle, Hailiang ZHANG, Yongni SHAO, Yong HE a Michael NGADI. Mapping of Fat and Moisture Distribution in Atlantic Salmon Using Near-Infrared Hyperspectral Imaging. *Food and Bioprocess Technology* [online]. 2014, 7(4), 1208-1214 [cit. 2020-08-25]. ISSN 1935-5130. Dostupné z: doi:10.1007/s11947-013-1228-z

[39] GOETZ, Alexander, Gregg VANE, Jerry SOLOMON a Barrett ROCK. Imaging Spectrometry for Earth Remote Sensing. *Science*. 1985, 228(4704), 1147-1153.

[40] ANDREOLI, G., B. BULGARELLI a D. TARCHI. Hyperspectral Analysis of Oil and Oil-Impacted Soils for Remote Sensing Purposes. *European Commision - Joint Research Centre* [online]. European Communities, 2007, , 1-36 [cit. 2020-08-25]. ISSN 1018-5593. Dostupné z: https://publications.jrc.ec.europa.eu/repository/bitstream/111111111/5106/1/6875%20-%20EUR%2022739%20-%20hyperspectral__23-05-2007__rev2.pdf

[41] ASD TerraSpec Halo Mineral Identifier. *Malvern Pananalytical* [online]. Malvern Panalytical Ltd, 2020 [cit. 2020-09-24]. Dostupné z: https://www.malvernpanalytical.com/en/products/product-range/asd-range/terraspec-range/terraspec-halo-mineral-identifier

[42] Field Portable Spectrometers for Mineral Identification and Analysis in Mining Exploration. *Spectral Evolution* [online]. Haverhill, MA 01835 USA: Spectral Evolution, 2020 [cit. 2020-09-24]. Dostupné z: https://spectralevolution.com/products/hardware/field-portable-spectrometers-for-mining/

[43] PETRUCHOVÁ, Jana. *Využití hyperspektrálního snímkování v oblasti detekce kontaminovaných míst: Analýza a vytvořenní metodiky*. Praha, 2010.. PhD Thesis. CTU in Prague, Faculty of Civil Engineering. Vedoucí práce Ing. Růžena Zimová, Ph.D.

[44] ALAM, Mohammad a Paheding SIDIKE. Trends in oil spill detection via hyperspectral imaging. In: *2012 7th International Conference on Electrical and Computer Engineering* [online]. IEEE, 2012, s. 858-862 [cit. 2020-08-25]. ISBN 978-1-4673-1436-7. Dostupné z: doi:10.1109/ICECE.2012.6471686

[45] AKKAYNAK, Derya, Justine ALLEN, Lydia MÄTHGER, Chuan-Chin CHIAO a Roger HANLON. Quantification of cuttlefish (Sepia officinalis) camouflage: a study of color and luminance using in situ spectrometry. *Journal of Comparative Physiology A* [online]. 2013, 199(3), 211-225 [cit. 2020-08-25]. ISSN 0340-7594. Dostupné z: doi:10.1007/s00359-012-0785-3

[46] CANDIANI, Gabriele, Nicoletta PICONE, Loredana POMPILIO, Monica PEPE a Marcello COLLEDANI. Characterization of Fine Metal Particles Derived from Shredded WEEE Using a Hyperspectral Image System: Preliminary Results. *Sensors* [online]. 2017, 17(5) [cit. 2020-09-24]. ISSN 1424-8220. Dostupné z: doi:10.3390/s17051117

[47] VO-DINH, Tuan, Robert A. LIEBERMAN, Günter G. GAUGLITZ, Frank HOLLSTEIN, Íñigo CACHO, Sixto ARNAIZ a Markus WOHLLEBE. *Challenges in automatic sorting of construction and demolition waste by hyperspectral imaging* [online]. In: . 98620J- [cit. 2020-09-24]. Dostupné z: doi:10.1117/12.2220769

[48] CALVINI, Rosalba, Giorgia ORLANDI, Giorgia FOCA a Alessandro ULRICI. Development of a classification algorithm for efficient handling of multiple classes in sorting systems based on hyperspectral imaging. *Journal of Spectral Imaging* [online]. [cit. 2020-09-24]. ISSN 2040-4565. Dostupné z: doi:10.1255/jsi.2018.a13

[49] MORONI, Monica, Alessandro MEI, Alessandra LEONARDI, Emanuela LUPO a Floriana MARCA. PET and PVC Separation with Hyperspectral Imagery. *Sensors* [online]. 2015, 15(1), 2205-2227 [cit. 2020-09-24]. ISSN 1424-8220. Dostupné z: doi:10.3390/s150102205

[50] BONIFAZI, Giuseppe, Giuseppe CAPOBIANCO a Silvia SERRANTI. A hierarchical classification approach for recognition of low-density (LDPE) and high-density polyethylene (HDPE) in mixed plastic waste based on short-wave infrared (SWIR) hyperspectral imaging. *Spectrochimica Acta Part A: Molecular and Biomolecular Spectroscopy* [online]. 2018, 198, 115-

122 [cit. 2020-09-24]. ISSN 13861425. Dostupné z: doi:10.1016/j.saa.2018.03.006

[51] BAGHERI, Sima. *Hyperspectral Remote Sensing of Nearshore Water Quality* [online]. Cham: Springer International Publishing, 2017 [cit. 2020-09-24]. SpringerBriefs in Environmental Science. ISBN 978-3-319-46947-8. Dostupné z: doi:10.1007/978-3-319-46949-2

[52] KUDELA, Raphael M., Sherry L. PALACIOS, David C. AUSTERBERRY, Emma K. ACCORSI, Liane S. GUILD a Juan TORRES-PEREZ. Application of hyperspectral remote sensing to cyanobacterial blooms in inland waters. *Remote Sensing of Environment* [online]. 2015, 167, 196-205 [cit. 2020-09-24]. ISSN 00344257. Dostupné z: doi:10.1016/j.rse.2015.01.025

[53] ARDISSONE, P., P. BOCCARDO a E. BORGOGNO MONDINO. DIGITAL IMAGES PROCESSING OF HYPERSPECTRAL AIRBORNE DATA: A CULTURAL HERITAGE EXAMPLE. In: *CIPA: Heritage documentation*. 2005.

[54] EMMOLO, D., V. FRANCO, M. LO BRUTTO, P. ORL a B. VILLA. *HYPERSPECTRAL TECHNIQUES AND GIS FOR ARCHAEOLOGICAL INVESTIGATION* [online]. [cit. 2020-08-25]. Dostupné z: http://citeseerx.ist.psu.edu/viewdoc/summary?doi=10.1.1.118.2016

[55] CAVALLI, Rosa, Francesca COLOSI, Angelo PALOMBO, Stefano PIGNATTI a Maurizio POSCOLIERI. Remote hyperspectral imagery as a support to archaeological prospection. *Journal of Cultural Heritage* [online]. 2007, 8(3), 272-283 [cit. 2020-08-25]. ISSN 12962074. Dostupné z: doi:10.1016/j.culher.2007.03.003

[56] BASSANI, Cristiana, Rosa CAVALLI, Roberto GOFFREDO, Angelo PALOMBO, Simone PASCUCCI a Stefano PIGNATTI. Specific spectral bands for different land cover contexts to improve the efficiency of remote sensing archaeological prospection: The Arpi case study. *Journal of Cultural Heritage* [online]. 2009, 10, 41-48 [cit. 2020-08-25]. ISSN 12962074. Dostupné z: doi:10.1016/j.culher.2009.09.002

[57] CAVALLI, Giorgio Antonino LICCIARDI a Jocelyn CHANUSSOT. Detection of Anomalies Produced by Buried Archaeological Structures Using Nonlinear Principal Component Analysis Applied to Airborne Hyperspectral Image. *IEEE Journal of Selected Topics in Applied Earth Observations and Remote Sensing* [online]. 2013, 6(2), 659-669 [cit. 2020-09-24]. ISSN 1939-1404. Dostupné z: doi:10.1109/JSTARS.2012.2227301

[58] COREN, Franco, Domenico VISINTINI, Guido PREARO a Paolo STERZAI. *INTEGRATING LIDAR INTENSITY MEASURES AND HYPERSPECTRAL DATA FOR EXTRACTING OF CULTURAL HERITAGE* [online]. 2005 [cit. 2020-08-25]. Dostupné z: https://www.researchgate.net/publication/228949213_Integrating_LiDAR_intensity_measures_and_hyperspectral_data_for_extracting_of_cultural_heritage

[59] ATTAS, Michael, Edward CLOUTIS, Catherine COLLINS, Douglas GOLTZ, Claudine MAJZELS, James MANSFIELD a Henry MANTSCH. Near-infrared spectroscopic imaging in art conservation: investigation of drawing constituents. *Journal of Cultural Heritage* [online]. 2003, 4(2), 127-136 [cit. 2020-08-25]. ISSN 12962074. Dostupné z: doi:10.1016/S1296-2074(03)00024-4

[60] MANSFIELD, James, Michael ATTAS, Claudine MAJZELS, Edward CLOUTIS, Cathy COLLINS a Henry MANTSCH. Near infrared spectroscopic reflectance imaging: a new tool in art conservation. *Vibrational Spectroscopy* [online]. 2002, 28(1), 59-66 [cit. 2020-08-25]. ISSN 09242031. Dostupné z: doi:10.1016/S0924-2031(01)00145-X

[61] CUCCI, Constanza, Andrea CASINI, Marcello PICOLLO, Marco POGGESI a Lorenzo STEFANI. A HYPER-SPECTRAL SCANNER FOR HIGH QUALITY IMAGE SPECTROSCOPY: DIGITAL DOCUMENTATION AND SPECTROSCOPIC CHARACTERIZATION OF POLYCHROME SURFACES. *The Open Access NDT Database: The Web's Largest Database of NondestructiveTesting (NDT)* [online]. 2011, , 1-7 [cit. 2020-08-25]. Dostupné z: https://www.ndt.net/article/art2011/papers/CUCCI%20-%20NDT%2031.pdf

[62] GOLTZ, Douglas, Michael ATTAS, Gregory YOUNG, Edward CLOUTIS a Maria BEDYNSKI. Assessing stains on historical documents using hyperspectral imaging. *Journal of Cultural Heritage* [online]. 2010, 11(1), 19-26 [cit. 2020-08-25]. ISSN 12962074. Dostupné z: doi:10.1016/j.culher.2009.11.003

[63] PADOAN, R., Th. STEEMERS, M. KLEIN, B. AALDERINK a G. DE BRUIN. QUANTITATIVE HYPERSPECTRAL IMAGING OF HISTORICAL DOCUMENTS: TECHNIQUE AND APPLICATIONS. In: *9th International Conference on NDT of Art*. Jerusalem, Izrael, 2008, s. 1-10. Dostupné z: https://www.ndt.net/article/art2008/papers/097Padoan.pdf

[64] RICCIARDI, Paola, John DELANEY, Michelle FACINI, Jason ZEIBEL, Marcello PICOLLO, Suzanne LOMAX a Murray LOEW. Near Infrared Reflectance Imaging Spectroscopy to Map Paint Binders In Situ on Illuminated Manuscripts. *Angewandte Chemie* [online]. 2012, 124(23), 5705-5708 [cit. 2020-08-25]. ISSN 00448249. Dostupné z: doi:10.1002/ange.201200840

[65] MONTAGNER, Cristina, Mauro BACCI, Susanna BRACCI, Rachel FREEMAN a Marcello PICOLLO. Library of UV–Vis–NIR reflectance spectra of modern organic dyes from historic pattern-card coloured papers. *Spectrochimica Acta Part A: Molecular and Biomolecular Spectroscopy* [online]. 2011, 79(5), 1669-1680 [cit. 2020-08-25]. ISSN 13861425. Dostupné z: doi:10.1016/j.saa.2011.05.033

[66] CREAGH, Dudley a David BRADLEY. *Physical Techniques in the Study of Art, Archaeology and Cultural Heritage*. 2. Nederlands: Elsevier Science, 2007. ISBN 9780444528568.

[67] AMIGO, José Manuel. *Hyperspectral Imaging*. 1. Nederlands: Elsevier Science, 2020. ISBN 978-0-444-63977-6.

[68] KÖLIÖ, Arto, Mari HONKANEN, Jukka LAHDENSIVU, Minnamari VIPPOLA a Matti PENTTI. Corrosion products of carbonation induced corrosion in existing reinforced concrete facades. *Cement and Concrete Research* [online]. 2015, 78, 200-207 [cit. 2020-08-25]. ISSN 00088846. Dostupné z: doi:10.1016/j.cemconres.2015.07.009

[69] ANDERSON, Emma, Matthew ALMOND a Wendy MATTHEWS. Analysis of wall plasters and natural sediments from the Neolithic town of Çatalhöyük (Turkey) by a range of analytical techniques. *Spectrochimica Acta Part A: Molecular and Biomolecular Spectroscopy* [online]. 2014, 133, 326-334 [cit. 2020-08-25]. ISSN 13861425. Dostupné z: doi:10.1016/j.saa.2014.04.072

[70] SINGH, M., S. VINODH KUMAR a Sujata WAGHMARE. Characterization of 6–11th century A.D decorative lime plasters of rock cut caves of Ellora. *Construction and Building Materials* [online]. 2015, 98, 156-170 [cit. 2020-08-25]. ISSN 09500618. Dostupné z: doi:10.1016/j.conbuildmat.2015.08.039

[71] BUZGAR, Nicolae, Andrei BUZATU, Andrei-Ionuţ APOPEI a Vasile COTIUGă. In situ Raman spectroscopy at the Voroneţ Monastery (16th century, Romania): New results for green and blue pigments. *Vibrational Spectroscopy* [online]. 2014, 72, 142-148 [cit. 2020-08-25]. ISSN 09242031. Dostupné z: doi:10.1016/j.vibspec.2014.03.008

[72] VANDENABEELE, P., S. BODÉ, A. ALONSO a L. MOENS. Raman spectroscopic analysis of the Maya wall paintings in Ek'Balam, Mexico. *Spectrochimica Acta Part A: Molecular and Biomolecular Spectroscopy* [online]. 2005, 61(10), 2349-2356 [cit. 2020-08-25]. ISSN 13861425. Dostupné z: doi:10.1016/j.saa.2005.02.034

[73] MORILLAS, Héctor, Maite MAGUREGUI, Josu TREBOLAZABALA a Juan MADARIAGA. Nature and origin of white efflorescence on bricks, artificial stones, and joint mortars of modern houses evaluated by portable Raman spectroscopy and laboratory analyses. *Spectrochimica Acta Part A: Molecular and Biomolecular Spectroscopy* [online]. 2015, 136, 1195-1203 [cit. 2020-08-25]. ISSN 13861425. Dostupné z: doi:10.1016/j.saa.2014.10.006

[74] CHU, Vikki, Lior REGEV, Steve WEINER a Elisabetta BOARETTO. Differentiating between anthropogenic calcite in plaster, ash and natural calcite using infrared spectroscopy: implications in archaeology. *Journal of Archaeological Science* [online]. 2008, 35(4), 905-911 [cit. 2020-08-25]. ISSN 03054403. Dostupné z: doi:10.1016/j.jas.2007.06.024

[75] CHEILAKOU, Eleni, Michail TROULLINOS a Maria KOUI. Identification of pigments on Byzantine wall paintings from Crete (14th century AD) using non-invasive Fiber Optics Diffuse Reflectance Spectroscopy (FORS). *Journal of Archaeological Science* [online]. 2014, 41, 541-555 [cit. 2020-08-25]. ISSN 03054403. Dostupné z: doi:10.1016/j.jas.2013.09.020

[76] KOTTHAUS, Simone, Thomas SMITH, Martin WOOSTER a C.S.B. GRIMMOND. Derivation of an urban materials spectral library through emittance and reflectance spectroscopy. *ISPRS Journal of Photogrammetry and Remote Sensing* [online]. 2014, 94, 194-212 [cit. 2020-08-25]. ISSN 09242716. Dostupné z: doi:10.1016/j.isprsjprs.2014.05.005

[77] Hyperspectral sensors. *Headwall Photonics* [online]. USA: Headwall Photonics, 2020 [cit. 2020-08-25]. Dostupné z: https://www.headwallphotonics.com/hyperspectral-sensors

[78] CCD spectral sensitivity. *ResearchGate* [online]. ResearchGate GmbH, 2011 [cit. 2020-08-26]. Dostupné z: https://www.researchgate.net/figure/3-Spectral-sensitivity-graph-of-CCD-sensor-CMOS-sensor-and-human-eye-3-Width-is-5mm_fig3_216533561

[79] Pan&Tilt. *Headwall Photonics* [online]. USA: Headwall Photonics, 2020 [cit. 2020-08-25]. Dostupné z: https://www.headwallphotonics.com/products

[80] MATOUŠKOVÁ, Eva, Martina FALTÝNOVÁ a Karel PAVELKA. Influence of illumination and white reference material for hyperspectral imaging of cultural heritage objects. In: *14th International Multidisciplinary Scientific Geoconference SGEM 2014*. III. Sofia: STEF92 Technology Ltd., 2014, s. 199-206. ISBN 978-619-7105-12-4. ISSN 1314-2704.

[81] ASD Illuminator reflectance lamp. *AZO materials* [online]. [cit. 2020-08-25]. Dostupné z: https://www.azom.com/equipment-details.aspx?EquipID=5409

[82] Graphical representation of the 3D hyperspectral datacube and the acquisition parameters of existing systems. *ResearchGate* [online]. ResearchGate, 2009 [cit. 2020-08-25]. Dostupné z: https://www.researchgate.net/figure/Graphical-representation-of-the-3D-hyperspectral-datacube-and-the-acquisition-parameters_fig1_252773266

[83] Fast Line-of-sight Atmospheric Analysis of Hypercubes (FLAASH). *L3Harris geospatial* [online]. L3Harris geospatial, 2020 [cit. 2020-08-25]. Dostupné z: https://www.harrisgeospatial.com/docs/FLAASH.html

[84] ENVI. *L3Harris geospatial* [online]. L3Harris geospatial, 2020 [cit. 2020-08-25]. Dostupné z: https://www.harrisgeospatial.com/Software-Technology/ENVI

[85] Principal Components Analysis. *L3Harris geospatial* [online]. L3Harris geospatial, 2020 [cit. 2020-08-25]. Dostupné z: https://www.harrisgeospatial.com/docs/PrincipalComponentAnalysis.html

[86] Pixel Purity Index. *L3Harris geospatial* [online]. L3Harris geospatial, 2020 [cit. 2020-08-25]. Dostupné z: https://www.harrisgeospatial.com/docs/PixelPurityIndex.html

[87] Spectral Feature Fitting. *L3Harris geospatial* [online]. L3Harris geospatial, 2020 [cit. 2020-08-25]. Dostupné z: http://www.exelisvis.com/docs/SpectralFeatureFitting.html

[88] Spectral Angle Mapper. *L3Harris geospatial* [online]. L3Harris geospatial, 2020 [cit. 2020-08-25]. Dostupné z: https://www.harrisgeospatial.com/docs/SpectralAngleMapper.html

[89] Linear Spectral Unmixing. *L3Harris geospatial* [online]. L3Harris geospatial, 2020 [cit. 2020-08-25]. Dostupné z: https://www.harrisgeospatial.com/docs/LinearSpectralUnmixing.html

[90] *Ocean Insight* [online]. Ocean Insight, 2020 [cit. 2020-08-25]. Dostupné z: https://www.oceaninsight.com/

[91] Fibre optics probe. *Ocean Insight* [online]. Ocean Insight, 2020 [cit. 2020-08-26]. https://www.oceaninsight.com/products/fibers-and-probes/probes/reflectionbackscatter-probes/qr600-7-vis125bx/?qty=1

[92] Spectralon - Diffuse Reflectance Targets. *Labsphere* [online]. Labsphere, 2020 [cit. 2020-08-25]. Dostupné z: http://labsphere.com/labsphere-products-solutions/materials-coatings-2/targets-standards/diffuse-reflectance-standards/

[93] OceanView Spectrometer Operating Software. *Ocean Insight* [online]. Ocean Insight, 2020 [cit. 2020-08-26]. Dostupné z: https://www.oceaninsight.com/support/software-downloads/

[94] Matlab Hyperspectral Toolbox. *MathWorks* [online]. The MathWorks, Inc., 2017 [cit. 2020-08-26]. Dostupné z: https://www.mathworks.com/matlabcentral/fileexchange/61630-matlab-hyperspectral-toolbox

[95] Spectral Information Divergence. *L3Harris geospatial* [online]. L3Harris geospatial, 2020 [cit. 2020-08-26]. Dostupné z: https://www.harrisgeospatial.com/docs/SpectralInformationDivergence.html

[96] Spectral Analyst. *L3Harris geospatial* [online]. L3Harris geospatial, 2020 [cit. 2020-08-26]. Dostupné z: https://www.harrisgeospatial.com/docs/SpectralAnalyst.html

[97] QSdata. *SourceForge* [online]. Slashdot Media, 2020 [cit. 2020-08-26]. Dostupné z: https://sourceforge.net/projects/qsdata/

[98] GAGALOWICZ, André a Wilfried PHILIPS. *Computer analysis of images and patterns: 11th international conference, CAIP 2005, Versailles, France, September 5-8, 2005 : proceedings*. New York: Springer, 2005. ISBN 978-3-540-28969-2.

[99] CHANG, Chein-I a Chein-I CHANG. *Hyperspectral data processing: algorithm design and analysis*. 1. Hoboken, NJ: Wiley-Interscience, 2013. ISBN 978-0-471-69056-6.

[100] Electroluminescence. *PV Education* [online]. Sensors Unlimited, a Collins Aerospace Company, 2020 [cit. 2020-08-26]. Dostupné z: https://www.pveducation.org/pvcdrom/characterisation/electroluminescence

[101] The NAKI project - New modern methods of non-invasive cultural heritage object documentation. *Laboratory of photogrammetry, CTU in Prague* [online]. Prague: CTU in Prague, 2019 [cit. 2020-08-25]. Dostupné z: http://lfgm.fsv.cvut.cz/naki/index.html

[102] Laboratory of Photovoltaic Systems Diagnostics. *Faculty of Electrical Engineering, Czech Technical University in Prague* [online]. Prague: Czech Technical University in Prague, 2020 [cit. 2020-08-25]. Dostupné z: http://pasan.feld.cvut.cz/

[103] *Photonics Science* [online]. United Kingdom: Photonics Science, 2020 [cit. 2020-08-25]. Dostupné z: https://photonicscience.com/

[104] WARSCHEID, Th. a J. BRAAMS. Biodeterioration of stone: a review. *International Biodeterioration & Biodegradation* [online]. 2000, 46(4), 343-368 [cit. 2020-08-18]. ISSN 09648305. Dostupné z: doi:10.1016/S0964-8305(00)00109-8

[105] Historické způsoby opracování kamene, metody průzkumu a kritéria výběru náhradního kamene kvádrového zdiva. *Katedra Geotechniky, FSv, ČVUT v Praze* [online]. Praha: FSv, +CVUT v Praze, 2013 [cit. 2020-08-18]. Dostupné z: https://departments.fsv.cvut.cz/k135/naki/Library/GRAFICKE%20PRILOHY%202013/g-18__publikace__historicke__zpusoby__opracovani__kamene.pdf

[106] Biologické napadení stavebních materiálů. *Izolace.cz* [online]. Praha: A.W.A.L. - PRO, s.r.o., 2006 [cit. 2020-08-18]. Dostupné z: https://www.izolace.cz/clanky/biologicke-napadeni-stavebnich-materialu/

[107] ADAN, Olf a Robert SAMSON. *Fundamentals of Mold Growth in Indoor Environments and Strategies for Healthy Living*. 1. Wageningen: Wageningen Academic Publishers, 2011. ISBN 978-90-8686-722-6.

[108] CANEVA, Giulia a Salvador ORNELLA. Biodeterioration of Stone. *The Deterioration and Conservation of Stone: Notes from the International Venetian Courses on Stone Restoration*. 1988, , 182-234.

[109] GRIFFIN, P.S., N. INDICTOR a R.J. KOESTLER. The Biodeterioration of Stone: a Review of Deterioration Mechanisms, Conservation Case Histories, and Treatment. *International Biodeterioration* [online]. 1991, 28(1), 187-207 [cit. 2020-08-18]. Dostupné z: doi:10.1016/0265-3036(91)90042-P

[110] MARTÍNEZ-MARTÍNEZ, Javier, David BENAVENTE, Miguel GOMEZ-HERAS, Luz MARCO-CASTAñO a M. GARCÍA-DEL-CURA. Non-linear decay of building stones during freeze–thaw weathering processes. *Construction and Building Materials* [online]. 2013, 38, 443-454 [cit. 2020-08-18]. ISSN 09500618. Dostupné z: doi:10.1016/j.conbuildmat.2012.07.059

[111] MCNAMARA, Christopher a Ralph MITCHELL. Microbial deterioration of historic stone. *Frontiers in Ecology and the Environment* [online]. 2005, 3(8), 445-451 [cit. 2020-08-18]. ISSN 1540-9295. Dostupné z: doi:10.1890/1540-9295(2005)003[0445:MDOHS]2.0.CO;2

[112] SCHEERER, Stefanie, Otto ORTEGA-MORALES a Christine GAYLARDE. *Chapter 5 Microbial Deterioration of Stone Monuments—An Updated Overview* [online]. Elsevier, 2009, , 97-139 [cit. 2020-08-18]. Advances in Applied Microbiology. ISBN 9780123747884. Dostupné z: doi:10.1016/S0065-2164(08)00805-8

[113] SMITH, B.J., M. GOMEZ-HERAS a S. MCCABE. Understanding the decay of stone-built cultural heritage. *Progress in Physical Geography: Earth and Environment* [online]. 2008, 32(4), 439-461 [cit. 2020-08-18]. ISSN 0309-1333. Dostupné z: doi:10.1177/0309133308098119

[114] WELTON, , RYAN G, Simon CUTHBERT, Roger MCLEAN, Andrew HURSTHOUSE a John HUGES. A Preliminary Study of the Phycological Degradation of Natural Stone Masonry. *Environmental Geochemistry and Health*. 2003, 25(1), 139-45.

[115] *Mšenské pískovce* [online]. Mšenské lázně: Mšenské pískovce spol. s.r.o., 2014 [cit. 2020-08-18]. Dostupné z: https://www.msenskepiskovce.cz

[116] Zenith Polymer® Diffuse Reflectance Standards. *Sphere Optics* [online]. SphereOptics GmbH, 2017 [cit. 2020-08-26]. Dostupné z: https://sphereoptics.de/en/wp-content/uploads/sites/3/2014/03/SphereOptics-Diffuse-Reflectance-Standards-Targets-Materials-Zenith-Polymer.pdf

[117] NDVI. *L3Harris geospatial* [online]. L3Harris geospatial, 2020 [cit. 2020-08-25]. Dostupné z: https://www.harrisgeospatial.com/docs/NDVI.html

[118] NDVI. *Agricolus* [online]. Perugia, Italy: Agricolus S.r.l., 2020 [cit. 2020-08-26]. Dostupné z: https://www.agricolus.com/en/indici-vegetazione-ndvi-ndmi-istruzioni-luso/

[119] SVOBODA, Lukáš, Zdenka BAŽANTOVÁ, Milan MYŠKA, Jaroslav NOVÁK, Zdeněk TOBOLKA, Roman VÁVRA, Alena VIMMROVÁ a Jaroslav VÝBORNÝ. *Stavební hmoty*. 3. Praha: ČVUT v Praze, 2013. ISBN 978-80-2604-972-2.

[120] OLESON, John, Christopher BRANDON, Steven CRAMER, Roberto CUCITORE, Emanuele GOTTI a Robert HOHLFELDER. The ROMACONS Project: a Contribution to the Historical and Engineering Analysis of Hydraulic Concrete in Roman Maritime Structures. *International Journal of Nautical Archaeology* [online]. 2004, 33(2), 199-229 [cit. 2020-08-24]. ISSN 10572414. Dostupné z: doi:10.1111/j.1095-9270.2004.00020.x

[121] NEČAS, Radovan. Ultramarin pro vápenné nátěry. *TZB-info.cz* [online]. 2016 [cit. 2020-08-24]. Dostupné z: https://stavba.tzb-info.cz/beton-malty-omitky/13732-ultramarin-pro-vapenne-natery

[122] NEČAS, Radovan, Martin BOHÁČ a Vladimír PERSAŇ. Vliv historických přísad na vlastnosti vápenných kaší a malt. *TZB-info.cz* [online]. 2013 [cit. 2020-08-24]. Dostupné z: https://stavba.tzb-info.cz/beton-malty-omitky/10511-vliv-historickych-prisad-na-vlastnosti-vapennych-kasi-a-malt

[123] OŽANOVÁ, Lucie. *Rekonstrukce výrobních postupů historických malt a omítek* [online]. Brno, 2008 [cit. 2020-08-24].. Barchelor thesis. Masaryk university, Faculty of Science. Dostupné z: https://is.muni.cz/th/lmoqo/Rekonstrukce_vyrobnich_postupu_historickych_malt_a_omitek.pdf. Barchelor thesis. Masaryk university, Faculty of Science.

[124] PROŠKOVÁ, Pavlína. *Srovnávání vlastností vápna připravovaného tradiční technologií s průmyslově vyrobenými produkty* [online]. Pardubice, 2008 [cit. 2020-08-24].. Barchelor thesis. University of Pardubice, Faculty of restoration. Dostupné z: https://dk.upce.cz/bitstream/handle/10195/32779/proskovap_srovnavani%20vlastnosti_RT_2008.pdf;jsessionid=8CFB024FAFBA34D2A7EE093D03869208?sequence=1. Barchelor thesis. University of Pardubice, Faculty of restoration.

[125] KOLOUCHOVÁ, Eliška. *MATERIÁLY PRO OBNOVU OMÍTEK HISTORICKÝCH STAVEB* [online]. Brno, 2013 [cit. 2020-08-24].. Barchelor's thesis. Brno university of technology, Institute of Chemistry. Dostupné z: https://www.vutbr.cz/www_base/zav_prace_soubor_verejne.php?file_id=73169. Barchelor's thesis. Brno university of technology, Institute of Chemistry.

[126] *Institute of Theoretical and Applied Mechanics of the Czech Academy of sciences* [online]. Praha 9: The Czech Academy of Sciences, Centre of Administration and Operations of CAS, 2020 [cit. 2020-08-27]. Dostupné z: http://www.itam.cas.cz/oddeleni/materialoveho_vyzkumu/

[127] KLUM_library. *GitHub* [online]. GitHub, Inc., 2020 [cit. 2020-08-27]. Dostupné z: https://github.com/rebeccailehag/KLUM_library

[128] ILEHAG, Rebecca, Andreas SCHENK, Yilin HUANG a Stefan HINZ. KLUM: An Urban VNIR and SWIR Spectral Library Consisting of Building Materials. *Remote Sensing* [online]. 2019, 11(18) [cit. 2020-03-18]. ISSN 2072-4292. Dostupné z: doi:10.3390/rs11182149

[129] *LUMA-SLUM download* [online]. Urban Meteorology at University of Reading [cit. 2020-08-27]. Dostupné z: https://urban-meteorology-reading.github.io/SLUM

[130] *ECOSTRESS Spectral Library* [online]. California, USA: California Institute of Technology, 2017 [cit. 2020-08-27]. Dostupné z: https://speclib.jpl.nasa.gov/

[131] BALDRIDGE, A.M., S.J. HOOK, C.I. GROVE a G. RIVERA. The ASTER spectral library version 2.0. *Remote Sensing of Environment* [online]. 2009, 113(4), 711-715 [cit. 2020-08-27]. ISSN 00344257. Dostupné z: doi:10.1016/j.rse.2008.11.007

[132] Energy Dispersive Microscopy (EDS). *PennState Material Research Institute* [online]. The Pennsylvania State University Materials Research Institute: PennState Material Research Institute, 2020 [cit. 2020-08-31]. Dostupné z: https://www.mri.psu.edu/materials-characterization-lab/characterization-techniques/energy-dispersive-spectroscopy-eds

[133] *Department of Mechanics, Faculty of Civil Engineering, Czech Technical University in Prague* [online]. Praha: Department of Mechanics, Faculty of Civil Engineering, Czech Technical University in Prague, 2020 [cit. 2020-08-31]. Dostupné z: https://mech.fsv.cvut.cz/web/index.php?&lang=en

[134] Phenom XL. *NanoScience Instruments* [online]. Nanoscience Instruments, 2020 [cit. 2020-08-31]. Dostupné z: https://www.nanoscience.com/products/scanning-electron-microscopes/phenom-xl/

[135] Vytvoření infrastruktury pro inovovaný doktorský studijní program Fyzikální a materiálové inženýrství. *Faculty of Civil Engineering, Czech Technical University in Prague* [online]. Prague: Faculty of Civil Engineering, Czech Technical University in Prague, 2020 [cit. 2020-08-31]. Dostupné z: https://web.fsv.cvut.cz/aktuality/437/

[136] Quantitative EDS X-ray microanalysis using SEM. *MyScope: Microscopy Training* [online]. Australia, 2020 [cit. 2020-08-31]. Dostupné z: https://myscope.training/legacy/analysis/eds/quantitative/

[137] GOLDSTEIN, Joseph, Dale NEWBURY, Patrick ECHLIN, David JOY, Charles LYMAN, Eric LIFSHIN, Linda SAWYER a Joseph MICHAEL. *Scanning Electron Microscopy and X-ray Microanalysis* [online]. Boston, MA: Springer US, 2003 [cit. 2020-08-31]. ISBN 978-1-4613-4969-3. Dostupné z: doi:10.1007/978-1-4615-0215-9

[138] Božanov sandstone. *Granit Lipnice* [online]. Dolní Město, Czech Republic: Granit Lipnice s.r.o., 2020 [cit. 2020-08-26]. Dostupné z: http://www.granit-lipnice.cz/tezene-materialy/bozanovsky-piskovec/

[139] Hořice sandstone. *Kámen Ostroměř* [online]. Kámen Ostroměř s.r.o., 2017 [cit. 2020-08-26]. Dostupné z: https://www.piskovce.cz/lom-podhorni-ujezd

[140] Quartzite. *Encyclopedia Britannica* [online]. Encyclopædia Britannica, Inc., 2020 [cit. 2020-08-26]. Dostupné z: https://www.britannica.com/science/quartzite

[141] Maastricht limestone. *National Commission for Stratigraphy Belgium* [online]. [cit. 2020-08-26]. Dostupné z: https://ncs.naturalsciences.be/cretaceous/maastricht-formation-maa

[142] Přední Kopanina. *Dekorační kameny, vápence a vybrané písky ČR* [online]. Research Institute of Inorganic Chemistry and Jan Evangelista Purkyně University in Ústí nad Labem [cit. 2020-08-26]. Dostupné z: http://kamenolomy.fzp.ujep.cz/index.php?page=record&id=379&tab=lom

[143] Přední Kopanina. *Přední Kopanina* [online]. [cit. 2020-08-26]. Dostupné z: http://www.prednikopanina.cz/opukove-lomy/

[144] Brick. *Encyclopedia Britannica* [online]. Encyclopædia Britannica, Inc., 2020 [cit. 2020-08-26]. Dostupné z: https://www.britannica.com/technology/brick-building-material

[145] Tile. *Encyclopedia Britannica* [online]. Encyclopædia Britannica, Inc., 2020 [cit. 2020-08-26]. Dostupné z: https://www.britannica.com/technology/brick-building-material

[146] Lime mortars. *The National Heritage Institute* [online]. Prague: The National Heritage Institute, 2020 [cit. 2020-08-26]. Dostupné z: https://netusene-souvislosti.npu.cz/pamatky/netusene-souvislosti/ke-stazeni/ZDICI%20%20MALTY%20MICHO%202.pdf

[147] SLÍŽKOVÁ, Zuzana. VÝVOJ SMĚSNÉHO HYDRAULICKÉHO POJIVA NA BÁZI METAKAOLINU. *Studio AXIS* [online]. Studio AXIS, 2020 [cit. 2020-08-27]. Dostupné z: https://www.google.com/search?client=firefox-b-d&q=malta+s+pojivem+vapno+metakaolin#

[148] MACKENZIE, K.J.D. a M. WELTER. Geopolymer (aluminosilicate) composites: synthesis, properties and applications. *Advances in Ceramic Matrix Composites* [online]. Elsevier, 2014, s. 445-470 [cit. 2020-08-27]. ISBN 9780857091208. Dostupné z: doi:10.1533/9780857098825.3.445

[149] *Sklopísek Střeleč* [online]. Střeleč: Sklopísek Střeleč, 2017 [cit. 2020-08-27]. Dostupné z: https://glassand.eu/

[150] *Tapas Borek* [online]. Tapas Borek [cit. 2020-08-27]. Dostupné z: http://www.tapasborek.cz/

[151] *Vápenka Čertovy schody* [online]. [cit. 2020-08-27]. Dostupné z: https://www.lhoist.com/cs__cs

[152] Dolomite. *Czech Geological Survey* [online]. Czech Geological Survey [cit. 2020-08-27]. Dostupné z: http://www.geology.cz/aplikace/encyklopedie/term.pl?dolomit

[153] *Gypsum* [online]. [cit. 2020-08-27]. Dostupné z: https://geology.com/minerals/gypsum.shtml

[154] Mefisto L05. *České Lupkové Závody a.s.* [online]. [cit. 2020-08-27]. Dostupné z: http://www.cluz.cz/cz/mefisto-l05

[155] *Claytec* [online]. CLAYTEC e.K., 2020 [cit. 2020-08-27]. https://www.claytec.de/en

*Skorkov* [online]. Skorkov: Obec Skorkov, 2020 [cit. 2020-08-27]. [156] Dostupné z: https://www.skorkov.cz/

*Hrad Beckov* [online]. [cit. 2020-08-27]. Dostupné z: [157] http://www.hrad-beckov.sk/

*Čachtický hrad* [online]. [cit. 2020-08-27]. Dostupné z: [158] https://cachtickyhrad.eu/

CURCIO, Joseph a Charles PETTY. The Near Infrared Absorption [159] Spectrum of Liquid Water. *Journal of the Optical Society of America* [online]. 1951, 41(5) [cit. 2020-09-22]. ISSN 0030-3941. Dostupné z: doi:10.1364/JOSA.41.000302

CLARK, Roger a Ted ROUSH. Reflectance spectroscopy: Quantitative [160] analysis techniques for remote sensing applications. *Journal of Geophysical Research: Solid Earth* [online]. 1984, 89(7), 6329-6340 [cit. 2020-09-22]. ISSN 01480227. Dostupné z: doi:10.1029/JB089iB07p06329

ALPARSLAN, E a Mr. FUATINCE. Image enhancement by local [161] histogram stretching. *IEEE Transactions on Systems, Man, and Cybernetics*. 1981, -11(), 376-385.

WU, Chialin, David LANDGREBE a Philip SWAIN. *THE DECISION* [162] *TREEAPPROACH TO CLASSIFICATION*. May 1. https://ntrs.nasa.gov/citations/19750021455: NASA, 1975.

## 17. List of Appendix

- Appendix I. – Individual analysis results of Sample 1
- Appendix II. – Individual analysis results of Sample 2
- Appendix III. – Individual analysis results of Sample 3
- Appendix IV. – Individual analysis results of Sample 4
- Appendix V. – Individual analysis results of Sample A
- Appendix VI. – Individual analysis results of Sample B
- Appendix VII. – Individual analysis results of Sample C
- Appendix VIII. – Individual analysis results of Sample D
- Appendix IX. – Individual analysis results of Sample E
- Appendix X. – Individual analysis results of Sample FA
- Appendix XI. – Individual analysis results of Sample FB
- Appendix XII. – Individual analysis results of Rock sample 1
- Appendix XIII. – Measured data processing (CD only)
- Appendix XIV. – SAM/SID calculations (CD only)
- Appendix XV. - Spectral libraries - KLUM, SLUM, ASTER (CD only)
- Appendix XVI. - CTU Material Spectral Library (CD only)